UNIVERSITY OF SOUTHAMPTON

Faculty of Engineering, Science and Mathematics

Optoelectronics Research Centre

Direct and inverse design of microstructured optical fibres

by

Francesco Poletti

A thesis submitted for the degree of
Doctor of Philosophy

May 2007

UNIVERSITY OF SOUTHAMPTON

ABSTRACT

FACULTY OF ENGINEERING, SCIENCE AND MATHEMATICS
OPTOELECTRONICS RESEARCH CENTRE

Doctor of Philosophy

Direct and inverse design of microstructured optical fibres

by Francesco Poletti

Microstructured optical fibres, where an arrangement of air holes running longitudinally along the fibre guides light in either a solid or a hollow core, have created new opportunities in diverse areas of science and technology. Applications range from the generation of supercontinuum light to optical sensing, nonlinear telecom devices and the generation and delivery of extremely high optical powers.

This thesis concerns the modelling of such fibres with the finite element method, with the multiple purpose of: acquiring a clearer insight and understanding of the physical mechanisms the fibres are based on; designing optimum fibres for a range of applications; understanding experimentally observed phenomena; identifying fundamental limits and design rules.

Optical maps are proposed as a simple, yet effective way to understand the potential and limitations of hexagonally arranged index guiding fibres, and are used to design an optimised fibre for the generation of a broad and spectrally flat supercontinuum and to engineer tapered fibres with a high nonlinear figure of merit. More specific inverse design techniques are also applied to the optimisation of fibres with a larger number of free-parameters. With this approach, the dispersion of silica and compound glass fibres is optimised for applications in nonlinear telecoms devices.

Photonic bandgap fibres, allowing light guidance in a hollow core, are also extensively studied. The main issues preventing accurate simulations of the properties of fabricated fibres are identified and addressed. An ideal, accurate representation of a realistic fibre is then proposed and employed to obtain fundamental scaling rules and to study the interactions between air guided and surface guided modes. Anticrossings between these modes in slightly asymmetric structures are identified as the cause for the unusual polarisation effects experimentally observed in these fibres. And finally, guidelines for fabricating fibres with the widest possible operational bandwidth possible are developed and presented.

Contents

List of Figures

List of Tables

Acronyms

ASE	amplified spontaneous emission
BC	boundary condition
BFS	Brillouin frequency shift
BGB	Brillouin gain bandwidth
BGC	Brillouin gain coefficient
BGS	Brillouin gain spectrum
BOP	beginning of pull
BPM	beam propagation method
CL	confinement loss
CM	cladding mode
CW	continuous wave
DOF	degree of freedom
DOS	density of states
DWDM	dense wavelength division multiplexing
EOM	electro-optic modulator
EOP	end of pull
FBG	fibre Bragg grating
FDM	Fourier decomposition method
FEM	finite element method
FM	fundamental mode
FOM	figure of merit
FSM	fundamental space filling mode
FWHM	full width half maximum
FWM	four wave mixing
GA	genetic algorithm
HF	holey fibre
HNL	highly nonlinear
HOM	higher order mode
IG	index guiding
MM	multipole method
MOF	microstructured optical fibre
OFM	orthogonal functions method

PBG	photonic bandgap
PBGF	photonic bandgap fibre
PCF	photonic crystal fibre
PDE	partial differential equation
PDL	polarisation-dependent loss
PMD	polarisation mode dispersion
PML	perfectly matched layer
PWE	plane wave expansion method
SBS	stimulated Brillouin scattering
SC	supercontinuum
SEM	scanning electron micrograph
SEST	structured element stacking technique
SIF	step-index fibre
SM	surface mode
SMT	source-model technique
TE	transverse electric
TEM	transverse electric and magnetic
TM	transverse magnetic
ZDW	zero dispersion wavelength

DECLARATION OF AUTHORSHIP

I, Francesco Poletti declare that the thesis entitled *Direct and inverse design of microstructured optical fibres* and the work presented in the thesis are both my own, and have been generated by me as the result of my own original research. I confirm that:

- this work was done wholly while in candidature for a research degree at this University;
- where I have consulted the published work of others, this is always clearly attributed;
- where I have quoted from the works of others, the source is always given. With the exception of such quotations, this thesis is entirely my own work;
- I have acknowledged all sources of help;
- where the thesis is based on work done by myself jointly with others, I have made clear exactly what was done by others and what I have contributed myself;
- parts of this work have been published in the journal articles and conference proceedings reported in the List of Publications at the end of the thesis.

Francesco Poletti

February 2007

Acknowledgements

Although exciting, the last few years have certainly not been free of challanges and unforeseen difficulties – the change of supervisor and the fire being only the tip of the iceberg. Throughout all of these problems I have always found help, encouragement and comfort from a number of dedicated and enthusiastic people without whom I couldn't have made it, and that I would like here to thank profusely.

First and foremost I would like to thank my supervisor, Prof. David Richardson, for welcoming me into his stimulating group and giving me the opportunity to be involved in so many exciting projects. Dave has always advised me wisely and given me endless support and encouragement throughout this period; I am profoundly grateful for all the valuable time he dedicated to my supervision. A warm thanks also goes to Prof. Tanya Monro for suggesting a PhD project which was tailored to my expectations and skills, and for her contagious enthusiasm and passion for science. It has been a pleasure and a privilege to work with both of them. Many thanks also to Dr. Neil Broderick for useful discussions on theoretical aspects (as well as on the Tour de France!), for his computer support, which has often made up for my Linux incompetence, and for reading this thesis.

I am also thankful to Dr. Vittoria Finazzi, who introduced me to the 'magic' of modelling microstructured fibres, who taught me the first 'Matlab for dummies' lessons and who shared with me the frustrations of countless computer crashes and failed simulations. Dr. Marco Petrovich has also played an important role in this work: thanks to him and a good dose of his 'realistic pessimism' I never got too carried away from what my simulations seemed to suggest. Furthermore, his remarkable fabrication skills have produced many of the fibres analysed in this thesis and I have learned a great deal from his vast knowledge of experimental issues.

Thanks to Vincent Tse, Julie Leong and Dr. Xian Feng for many fruitful discussions and for the fabrication of several fibres that permitted me to keep in contact with the 'real' world. My warmest thanks also go to Dr. Joanne (Baggett) Flanagan who has been an invaluable source of help whenever it was needed, as well as a source of artistic inspiration in the realisation of posters and presentations. I would also like to thank Dr.

Peter Horak for his excellent guidance on the RGB work and for not letting me feel too isolated amongst so many experimentalists (!). I am grateful to Kazunori Mukasa, who has been my principal "employer" for most of the very enjoyable time we had during his permanence at the ORC, and to Symeon, Jonathan, Periklis, Adriaan, Rodrigo, John and Pascal for many fruitful discussions and for sharing the passion for what we were doing.

Last but not least, many friends should be thanked for taking part in numerous football matches, essential in washing out the bad-day-problems and in giving me the necessary fitness to reach this point. Rob, Chris, Rafiq, Paulo, Costa, Ciccio, Marty are only some of them: thanks to you all!

Without football I could have (perhaps!) survived, but I certainly could not have done it without the love and support of so many friends in Southampton, London and Reggio Emilia. To Francesca, Erica, Jacob, Katia, Gilberto, Elena, Riki, Betta, Simo-Maria-Save, Gianlu e Fabio a big, big thank you.

I am also deeply grateful to my parents, for their love and for a lot more than written words can tell. They had the worst job of all in supporting me through the phone – and they succeeded in it brilliantly!

Thanks to my grandma and to Lucia for reminding me that a few things are even more important than microstructured optical fibres!!!

Finally, and words are not enough for this, I would like to thank my wife Erika for jumping on that red car a few years ago and starting this adventure in the UK with me. Without her onboard, the ship would have surely sunken many times...

Part I

Introduction

Chapter 1

Background

1.1 Introduction to microstructured fibres

1.1.1 Historical perspective

The idea of guiding light through total internal reflection dates back to the late nineteenth century, when spectacular luminous fountains celebrated the technological progress in many Universal Exhibitions across the globe [15]. Glass was too opaque at that time to be thought at as a transmission medium, and the first successful demonstrations of light guidance and imaging in an unclad glass fibre had to wait until the late 1920s. It was only nearly 30 years later though, that the idea of introducing a dielectric cladding layer with a smaller refractive index allowed significant improvements to the achievable optical properties, renewing the interest in the field of optical fibres and starting the quest for purer and more transparent glasses. In 1966 Charles Kao, a scientist at STL, suggested that the fundamental limit on glass transparency was below 20 dB/km, which would be practical for optical communications [16], and only a few years later Schultz, Keck and Maurer at Corning invented a chemical vapour deposition process that allowed the fabrication of a single mode fibre with 16 dB/km attenuation at 633 nm [17]. By the end of the 1970s, further improvements in the fabrication technology resulted in the reduction of the optical loss to the remarkably low value of nearly 0.2 dB/km at 1550 nm [18]. Since then, conventional optical fibres, together with the invention of solid state lasers and optical amplifiers, have revolutionised telecommunications and have become the physical layer on which the internet revolution was based. Besides that crucial application, optical fibres have also become vital components in many other technologies, from sensing and medical imaging to high power applications, including laser welding and machining and active devices such as fibre lasers and amplifiers.

In recent years, a novel type of optical fibre, known as microstructured optical fibre (MOF) has enlivened this well-established field, exhibiting a wide range of novel optical properties impossible to achieve using conventional technology. In contrast to conventional fibres, in which the combination of glasses with different refractive indices is required, MOFs can be made entirely from one type of glass and light guidance is achieved by introducing microscopic air holes that run along the entire fibre length.

The first reported microstructured fibre is shown in Figure 1.1 and was fabricated in the early 1970s at Bell labs by Kaiser *et al.* [1]. The fibre consisted of a small-diameter rod supported by a thin, polished plate in the centre of a larger-diameter protective tube, all made from fused silica. Although it presented quite promising losses, of the order of 3 dB/km at 1.1 μm, the nearly contemporary improvements in doped-core all-solid fibre fabrication techniques captured the attention of the research community, due to an easier fabrication process, enhanced mechanical robustness and potentially lower losses: as a result MOFs were temporarily set aside.

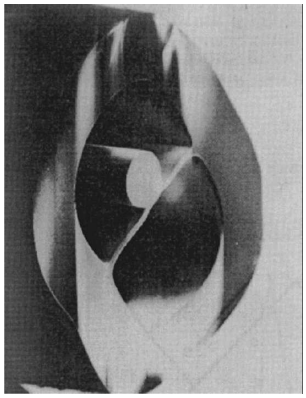

FIGURE 1.1: Single material microstructured fibre fabricated at Bell Labs in 1974 [1].

It was only nearly 20 years later that the MOF idea was brought back to the attention of the scientific community thanks to a breakthrough by Philip Russell and coworkers [2, 19]. Their idea was to combine the single material microstructured design with the emerging new area of *photonic bandgap materials*, also known as *photonic crystals*.

These had been proposed for the first time and almost independently in 1987, by Yablonovitch [20] and John [21], who suggested that in dielectric structures, periodic on a length scale comparable to the wavelength of light, spectacular phenomena of fully destructive interference may occur, preventing spontaneous light emission or light propagation at certain wavelengths, in analogy to the bandgaps familiar in solid state physics.

These pioneering studies in the area, and the large number of papers that followed, certainly inspired Birks and coworkers, who proposed, in 1995, to exploit a 2D photonic bandgap for out-of-plane propagation in order to confine light in a defect and guide it along the third direction. They suggested that a microstructured fibre with a suitable

periodic arrangement of holes running along its length could be used to trap light in the core [19].

The first working example of such a MOF, shown in Figure 1.2(a), came only one year later and was fabricated at the University of Southampton by Knight *et al.* [2]. The missing central hole defined a solid fibre core where light was 'trapped'.

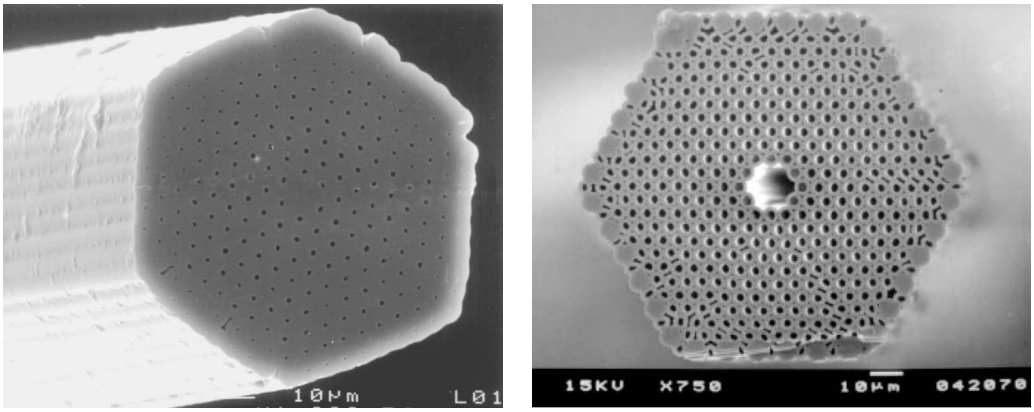

(a) (b)

FIGURE 1.2: (a) First ever reported single mode microstructured silica fibre [2]; (b) first single mode air-guiding fibre [3].

The fibre was soon discovered to guide light not by means of a photonic bandgap effect, for which the air holes were too small, but rather by exploiting a new guidance mechanism. This relied on the reduced average refractive index of the cladding, and was denoted *modified total internal reflection*. Subsequent studies on similar fibres revealed a number of unusual and useful optical properties, discussed in more detail in Section 1.2, which fuelled an immediate interest in the field. Initially considered as a sub-branch of the photonic crystal field, this new class of fibres soon developed as a field in its own right, as can be seen from the explosive growth in the number of journal publications per year regarding microstructured optical fibres, shown in Figure 1.3.

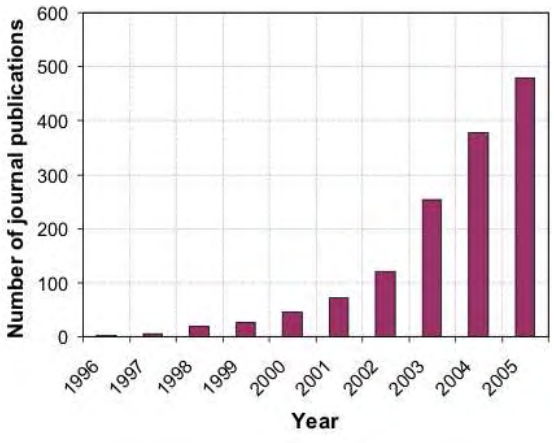

FIGURE 1.3: Number of journal publications per year related to microstructured, photonic crystal, holey or photonic bandgap fibres. Source: ISI Web of Science.

Since these pioneering works in the late 1990s, several new applications of MOFs have been proposed, as a result of the combined effort of many excellent theoretical and experimental works. Not too long after the fibre in Figure 1.2(a), the same group reported observation of the first single mode light guidance by the photonic bandgap effect in a 5 cm long MOF with a honeycomb cladding [22]. The fibre was fabricated according to a theoretical design devised by Bjarklev's group [23]. The lattice had been chosen because it allowed out-of-plane bandgaps even for the limited air-filling fractions compatible with the initial fabrication technology; the defect that allowed light confinement was an additional hole in the centre of the honeycomb pattern. Although the result was a milestone in the MOF history and an important proof of concept of the feasibility of *photonic bandgap fibres* (PBGFs), these initial fibres did not present a bandgap that allowed light propagation in air. Their fundamental mode was localised in the solid core region and presented a typical doughnut-like shape. This gave a poor overlap with a Gaussian mode as generated by most laser sources, and thus the advantages of this technology were not immediately evident.

A much greater scientific and technological impact resulted from the next improvement, achieved through an increase in air-filling fraction and by using a triangular hole arrangement: photonic bandgap (PBG) guidance was now possible also for propagation constants around the vacuum wavenumber. By realising such a cladding structure, with the omission of 7 central capillaries to form the core defect, Cregan *et al.* demonstrated the first single mode photonic bandgap guidance in air [3], shown in Figure 1.2(b). This opened up a multitude of potential new applications, from ultrahigh-power transmission to the laser guiding of small particles, to gas and biological sensing applications, which will be covered in more detail in Section 1.3.

From this moment on, the two fields of *photonic bandgap guiding* (PBG) fibres and *index guiding* (IG) fibres (used to refer to those fibres guiding by the modified total internal reflection mechanism) emerged. Although both share the same fabrication process (and most of the fabrication issues), each has its own applications and specific theoretical and numerical tools. This separation is reflected in the present thesis, where Part II focuses on the modelling of index guiding fibres, while Part III is entirely devoted to the study of PBGFs.

For both fibre types one of the first challenges was of course that of lowering the losses, which were initially of the order of several tens or hundreds of dB/m. In the space of less than 10 years these have been now reduced to values not too dissimilar to those of conventional fibres: the current record for an IG fibre is 0.28 dB/km [24], while the loss in an air-guiding PBGF with 19 missing capillaries core was measured to around 1.2 dB/km at 1620 nm [25]. At the same time, a large amount of fundamental and applied research was conducted in order to explore the achievable optical properties of these new fibres and to optimise the fibres for novel emerging applications. The large refractive index contrast in the microstructured area and the wavelength size features of

the air holes allow a larger control over the achievable group velocity dispersion, form birefringence and optical nonlinearity than is achievable in conventional fibres. A partial review of the recent progress in this area will be presented in Section 1.2 and Section 1.3, while a more detailed literature review and my personal contribution in specific areas will be presented in Part II and III of this thesis.

Pure undoped silica glass was the material of choice for the first MOFs, due its extremely low absorption in the near IR-wavelengths, relatively low cost, and due to the existence of established techniques for manipulating and processing the material. However there are a range of applications for which silica is not the best host, such as those requiring extremely high nonlinearities or mid-IR transmission. For these applications other glasses may present more suitable properties, and microstructured, index guiding fibres made of chalcogenide [26], lead oxide [27], tellurite [28] and bismuth oxide [29] glasses have all now been realised. The concept of microstructured, single material fibre has also led to interest in applications in the fibre-to-the-home (FTTH), low cost, short distance data transmission area. Here polymethyl methacrylate (PMMA) polymer microstructured fibres have recently shown interesting potential, both in the index guiding [30, 31] and in the hollow core, photonic bandgap guiding [32] form.

Further improvements to the microstructured concept were made by substituting air with a second, thermally, chemically and mechanically compatible glass, providing at the same time a large refractive index contrast. With this method, and a suitable choice of glasses, a highly nonlinear IG [33] and a PBG [34] fibre which did not suffer from structural deformation during the drawing process were realised. Moreover it was shown that, in order to open an out-of-plane bandgap for PBG guidance, a large index contrast was not even strictly required [35], and all-solid PBG fibres with a refractive index step of only nearly 1% were demonstrated by using higher refractive index, Ge-doped rods [36, 37].

In conclusion to this brief overview of the principal milestones in the short and yet significant history of MOFs, mention is due to a different type of hollow core fibre which has been developed in parallel to the PBGFs studied in this thesis, and which has currently assumed an important technological role in the transmission of high power CO_2 mid-IR laser radiation: the *Bragg* or *Omniguide fibre*. The possibility of using Bragg reflection in a cylindrical fibre to obtain lossless confined propagation, in a core with a lower refractive index than that of the cladding medium, was initially studied by Yeh, Yariv *et al.* in the late 1970s [38, 39]. As for the microstructured fibre though, a few decades had to pass before people could appreciate the full scientific and commercial exploitation of the original idea. Building on those solid theoretical foundations, a group at the MIT first demonstrated, in the late 1990s, that a periodic stack of alternating dielectric and metallic layers can provide omnidirectional reflection (i.e. reflection at all angles of incidence) with low losses [40]. Successively they realised the first hollow core fibre, by rolling an omnidirectional mirror (hence the name *Omniguide* fibre) composed

of alternating layers of a high refractive index glass and low refractive index polymer [41]. An alternative solution, based on a single material (silica) and exploiting circularly arranged air holes to generate the low index ring, was also recently proposed [42]. Despite the fact that the fibre possesses a very large bandgap, spanning more than an octave, the maximum available bandwidth for the air guided mode is severely limited by the presence of a very large number of modes, index guided at the intersection between the silica rings and interacting with the air guided mode.

Finally, in order to avoid confusion, a note must be added on the often controversial nomenclature of MOFs. Originally, since these fibres were made with a periodic arrangement of air-channels in the cross-section, for obvious reasons they were referred to as *photonic crystal fibres* (PCFs). In large part of the literature this name is still used to refer to all types of fibres with wavelength-sized transverse features. However, since it was soon recognised that even a non-periodic arrangement could lead to light guidance [43], the more general name *microstructured optical fibre* (MOFs) will be preferred throughout the thesis. This should help avoiding the widespread misconception that PCFs are fully synonymous with *photonic bandgap fibres* (PBGFs). In fact, PBG fibres constitute one subclass of microstructured optical fibres and high-index solid-core fibres, for which we will use the name *holey fibres* (HFs), constitute another.

1.1.2 Guidance mechanisms

In contrast to conventional fibres, relying uniquely on total internal reflection as a guidance mechanism, MOFs can confine light in the core through a number of physically different mechanisms, which can be selected by appropriately combining a homogeneous or a microstructured material to form the core and the cladding. A very general and intuitive way of representing all these possible mechanisms is to employ propagation diagrams, such as those in Figure 1.4.

If you consider a plane wave travelling along the z-direction in a homogeneous material, with wave-vector k_z (often called propagation constant and represented by the symbol β, within the fibre optics community), the dispersion relation between its wave number k and propagation constant β will be linear: $k = \omega/c = \beta/n$, where n is the material refractive index. This relation, plotted on a (β, k) diagram is called the *radiation line* for that specific material. Any other plane wave propagating along a direction different from z will have $\beta < nk$. No propagating wave can exist for $\beta > nk$, where light is evanescent. This permits us to identify a region of permissible guidance to the left of the material radiation line.

In the case of a conventional fibre, where two homogeneous materials with different refractive indices are present in the core (n_{co}) and in the cladding (n_{cl}), propagation can be represented as in Figure 1.4(a): the most relevant region for waveguiding applications

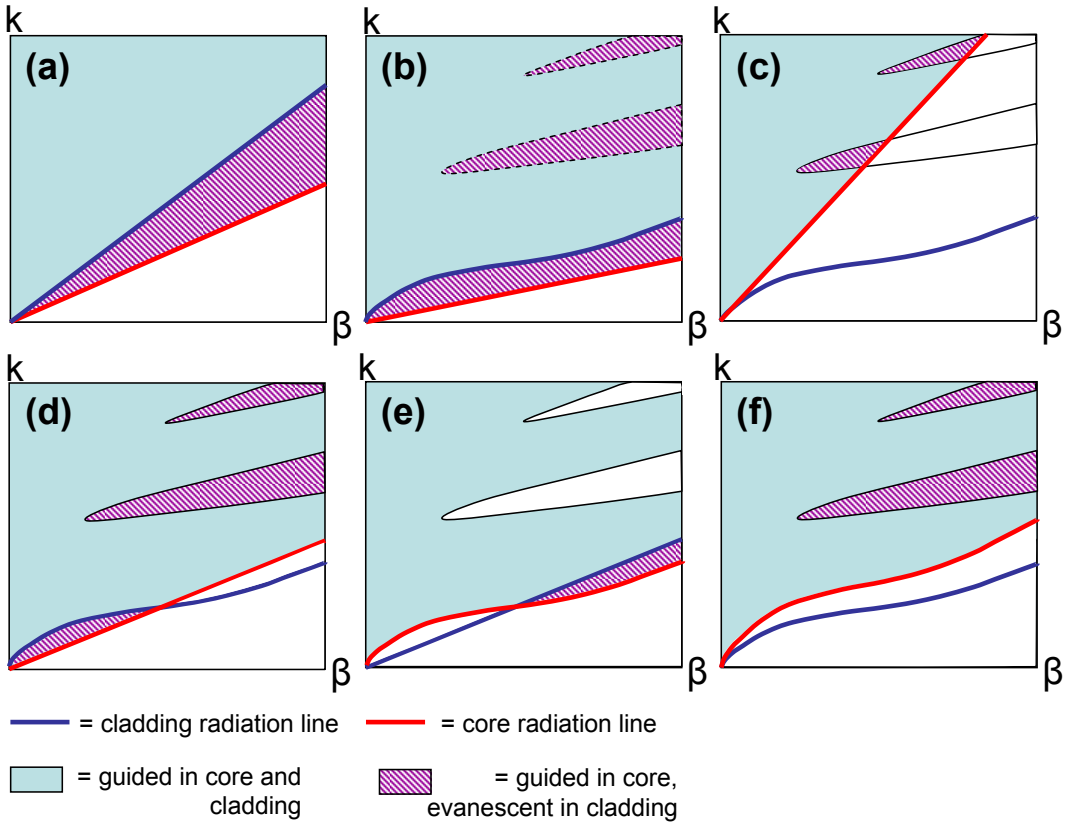

FIGURE 1.4: Propagation diagrams illustrating various waveguiding mechanisms achievable by combining homogeneous (straight radiation line) and microstructured (curved radiation line) cores and claddings in longitudinally invariant structures. (a) conventional step-index fibre; (b) MOF with homogeneous, high refractive index core (bandgaps are possible if the cladding is periodic); (c) MOF with low refractive index core and high index, periodically arranged cladding (guidance in the core is possible through photonic bandgaps or ARROW guidance); (d) MOF with core refractive index intermediate between the two materials forming the cladding (short wavelength cut off is possible for the index guided mode); (e) MOF with microstructured core and homogeneous, intermediate refractive index cladding (long wavelength cut off is possible); (f). MOF with microstructured core and cladding.

is between core and cladding radiation lines, for $n_{cl} < \beta/k < n_{co}$, where light can be guided in the core, but it is *evanescent* in the cladding. Here a discrete set of *bound modes* can exist, which are guided unattenuated in an idealised fibre with non-absorbing materials. The region to the left of the cladding radiation line represents the condition $0 < \beta/k < n_{cl}$, where guided modes are 'under cut-off' and solutions are generally referred to as *radiation modes* or *leaky modes* [44]. Finally, no electromagnetic radiation can propagate to the right of the core radiation line, for $\beta/k > n_{co}$.

The introduction of air holes in the cladding will cause, in general, the mode's dispersion to follow a nonlinear trend, as will be shown in Section 1.2.2. However the main guidance region will still remain between core and cladding radiation lines, as in Figure 1.4(b). If the cladding is periodic though, photonic bandgaps may also appear,

resulting in additional regions of core-only guidance, as shown by the dotted regions in Figure 1.4(b) [45].

A similar mechanism can happen in a low refractive index core, as shown in Figure 1.4(c), if the unit cell of the 2D periodic microstructured cladding is suitable to open a bandgap for out-of-plane light propagation (see Section 1.3). Periodicity is not even strictly needed for guidance in a low refractive index core, if the cladding is formed by high refractive index rods. In fact, guidance in these fibres is generally explained through the so called *Antiresonant Reflecting Optical Waveguiding* – ARROW – mechanism and relies on the existence of wavelength bands in which light is antiresonant with guided modes in the rods and therefore can be localised in a low index core with low resulting tunneling losses.

Other possibilities, which so far have received less attention, require a microstructured cladding [core] to be combined with a third material with an intermediate refractive index with respect to those forming the microstructure. For example down-doped silica or many types of liquids can be used. These concepts are shown in Figure 1.4(d) [Figure 1.4(e)] and would be characterised by a short [long] wavelength cut off even for the fundamental guided mode. A demonstration of the first mechanism was presented in Ref. [46].

Finally, a microstructured core and cladding can be combined, as in the case of the earlier honeycomb fibres [22]. Index guidance, photonic bandgap guidance or both can be achieved, depending on the average refractive index of the core and cladding, and on the cladding periodicity and arrangement (Figure 1.4(f)).

The numerical work presented in this thesis will be focused on the index guidance and photonic bandgap guidance mechanisms shown in Figure 1.4(b) and (c).

1.1.3 Higher refractive index glasses

As previously mentioned, although synthetic fused silica is an excellent material for many purposes and is still unsurpassed for low loss transmission in the near-IR, a range of applications exist for which it is not the best possible host. In particular it presents a relatively low intrinsic nonlinearity and its losses rise to extremely high levels above nearly 2 μm, due to the fundamental vibrational absorption of the glass network (multiphonon absorption). Both limitations can be overcome by moving to nonsilica glasses. These glasses are described as soft or compound, in reference to the fact that they have significantly lower melting temperatures than silica and are often composed of a number of chemical components. Glasses containing heavy metals and/or with a low bond strength generally exhibit a lower phonon energy, and their resulting multiphonon edge is shifted to longer wavelengths [5]. Therefore, glasses such as tellurites or chalcogenides are extremely promising for mid-IR transmissions.

Moving to glasses with a higher refractive index than silica, also allows access to material nonlinearities that are one or two orders of magnitude larger than silica's. Some examples are shown in Table 1.1. For example, Schott lead silicate glass SF57 has a refractive index of 1.78 at 1550 nm, and is ∼20 times more nonlinear than pure silica, while the chalcogenide glass As_2S_3 has a refractive index of ∼2.4 at 1550 nm and has a nonlinearity nearly 100 times grater than silica.

Glass type	Main component	n	$n_2 \times 10^{20}$ (m^2/W)
silica	SiO_2	1.44	2.2
lead silicate (SF57)	PbO-SiO_2	1.78	41
tellurite	ZnO-TeO_2	2.03	51
bismuth oxide	Bi_2O_3	2.2	82
chalcogenide	As_2S_3	2.44	200
	Ga_2S_3-La_2S_3	2.41	216

TABLE 1.1: Optical properties of some classes of optical glasses at 1550 nm.

High refractive index glasses are made of atoms with a larger atomic number (and therefore weight) than Si. The enhanced nonlinearity of high refractive index glasses is due to the increased nonlinear third order electronic polarisation of the bound electrons, typical of heavier atoms. When electromagnetic radiation propagates in a material, the field interacts with the charged electrons and results in a displacement of the electrons relative to the much heavier nucleus (electronic polarisation). The refractive index of the material is a measure of this electronic displacement or polarisation and it increases with the size of the atoms involved. For small field intensities the medium response is generally approximately linear, but for large enough intensities the nonlinear contributions, resulting in an anharmonic motion of the bound electrons, can no longer be neglected. The effect of the electronic displacement increases with the size of the atoms due to an increased distance from the nucleus to the bound electrons; as a result the nonlinear response of glasses formed by heavier atoms is also generally larger.

The electronic polarisation can be expressed as a function of the incident electric field by introducing the susceptibility coefficients $\chi^{(i)}$, where i defines the order, and each coefficient is a tensor of rank $i+1$ [47]. The linear susceptibility $\chi^{(1)}$ represents the dominant contribution and is related to the refractive index n via $n = 1 + \frac{1}{2}\Re e\left\{\chi^{(1)}\right\}$. The third-order susceptibility $\chi^{(3)}$ is the lowest-order term accounting for nonlinear effects in centro-symmetric amorphous glasses, and is related to the nonlinear coefficient n_2 via $n_2 = \frac{8}{3n}\Re e\left\{\chi^{(3)}\right\}$. The empirically derived Miller's rule [48] reveals that the relation between the linear and nonlinear electronic polarisation follows approximately $\chi^{(3)} \propto \left[\chi^{(1)}\right]^4$, as shown by the solid line in Figure 1.5(a). On the same graph, the squares indicate the values of linear and third-order optical susceptibilities correspondent to the some of the glasses in Table 1.1, showing a good fit to Miller's rule. An alternative representation is shown in Figure 1.5(b) and it directly relates the measured refractive

index n to the nonlinear coefficient n_2 for different glass families. The fitted line shows an almost linear relation between the two (on a logarithmic plot).

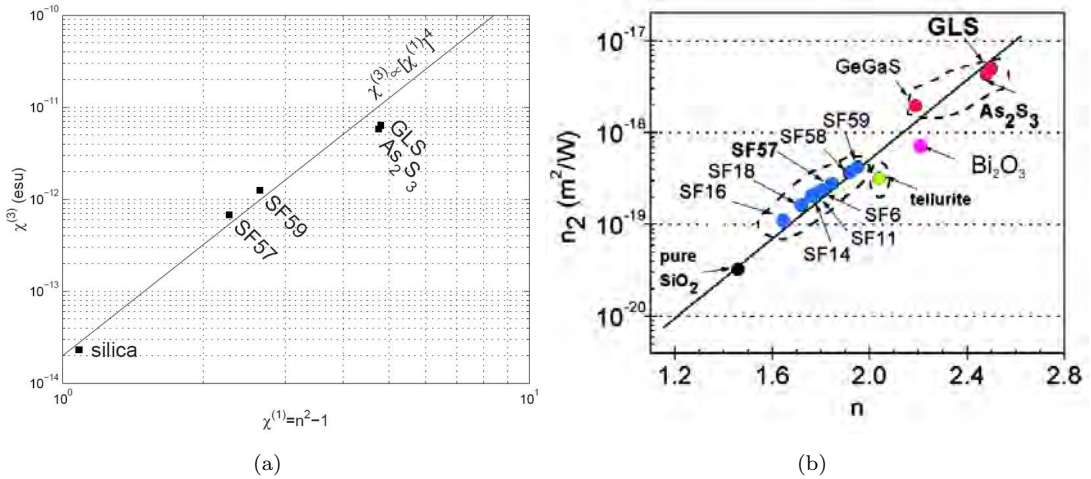

(a) (b)

FIGURE 1.5: (a) Relation between linear and third-order optical susceptibilities for some of the glasses considered in Table 1.1 (After [4]); (b) Relation between refractive index n and nonlinear coefficient n_2 for various optical glasses, including pure silica, lead silicate (Schott SF, in blue), tellurite (green), bismuth (pink) and chalcogenide (red) glasses (After [5]).

Although these glasses have been known for a long time, their application to the realisation of optical waveguides has always been difficult, because of the need to find a pair of thermally, chemically and mechanically compatible glasses with different refractive index in order to enable total internal reflection. The advent of MOFs though has allowed the realisation of fibres made using a single material, stimulating research into these alternative glasses and the exploration of new fabrication techniques. Extrusion of the glass preform has demonstrated to be one of the preferred techniques for MOF fabrication [29, 49, 50], but other approaches such as ultrasonic drilling [5], capillary stacking [51] and die cast processes [52, 53] have also been reported.

Besides the nonlinearity and transparency of the glass, for many applications *material dispersion* is also extremely important. The material dispersion, as will be shown in more detail in Section 1.2.2, gives an indication of the group velocity difference between two pulses travelling at slightly different wavelengths inside the material. Nonlinear effects can be enhanced in regions of nearly-zero dispersion, where pulse spreading and walk-off between pulses at different wavelengths are reduced. Figure 1.6 shows the material dispersion of some of the glasses mentioned above. Pure silica presents a zero-dispersion wavelength (ZDW) at around 1.28 μm, which is the shortest amongst all glasses useable for fibre fabrication. Above the ZDW the material dispersion is anomalous (D $>$ 0), allowing for example soliton propagation to occur, and below the ZDW the material dispersion is normal (D $<$ 0). All glasses follow a similar qualitative trend, even though the ZDW of higher-index glasses is shifted to longer wavelengths. Depending on the requirement of the specific application of the fibre, it is possible to modify the dispersion of

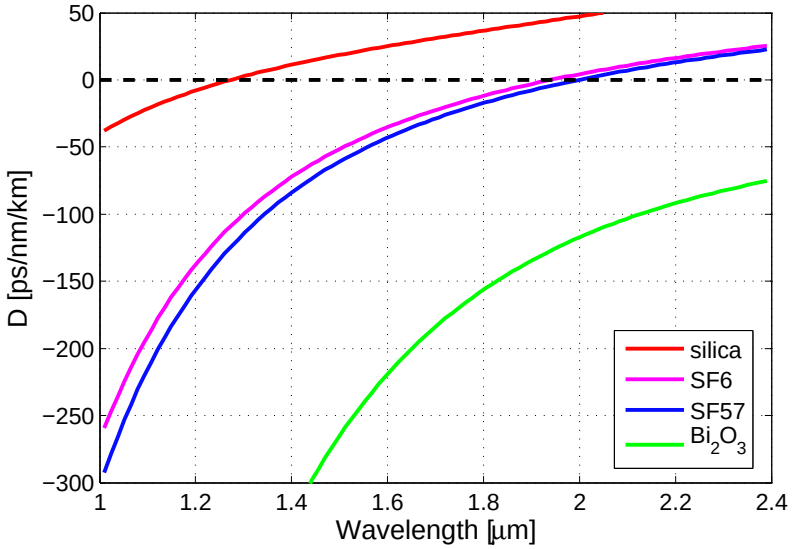

FIGURE 1.6: Material dispersion curves for silica [6], Schott lead silicate SF6 and SF57 [7], and bismuth oxide glass (see Section 3.4.4).

the material by employing a suitable waveguide, as will be shown briefly in Section 1.2.2 and in more detail for a number of the studies reported in Chapter 3 and 4.

1.1.4 Fabrication technique

MOF structures are currently fabricated in many laboratories around the world using a variety of different techniques. The first stage always requires the fabrication of a *preform*, a macroscopic version of the planned microstructure, which is then scaled down by using a conventional fibre drawing tower. As was already mentioned, there are many ways to produce a preform, even though the most widely used technique for silica MOFs involves *stacking* of circular capillaries.

For these fibres, typically, meter-length capillaries with an outer diameter of ∼1 mm are drawn from a starting tube of high-purity synthetic silica with an external diameter of tens of mm. The ratio between inner and outer diameter of the starting capillary, which typically lies in the range from 0.2 up to beyond 0.9, largely determines the relative hole size ratio (d/Λ, where d is the hole diameter and Λ is the hole-to-hole spacing) in the drawn fibre. The precise control of capillary dimensions and a high uniformity in the diameter of the capillaries are essential for structuring regularly arranged air holes within the preform.

The capillaries are stacked horizontally in such a way to form the desired crystalline arrangement, before being inserted into a jacketing tube. Packing rods are used to ensure the mechanical stability of the structure and the whole assembly is then mounted in a preform feed unit for drawing down to fibre. The top end of the capillaries is often sealed in order to create a self-pressurisation that counterbalances the effect of surface

tension and therefore prevents the collapse of the holes. Controlled use of pressure, vacuum and drawing temperature allows some limited control over the final structural parameters, and can be employed in order to achieve many different uniform structures from the same preform or, conversely, to obtain a deliberately tapered fibre, as will be shown in Section 3.4.1. Most of the fibres analysed in this thesis are fabricated using this stacking approach, even though extruded and drilled fibres are also considered.

Extrusion offers an alternative route to making the MOF's preform from bulk glass and it permits formation of structures that are not readily made by stacking. While not suitable for silica, as no die material has been identified that can withstand the $\sim 2000\,^{\circ}\mathrm{C}$ processing temperatures without contaminating the glass, extrusion is the preferred technique for making MOFs from compound silica glasses, tellurites, chalcogenides, and polymers–materials that melt at lower temperatures. A lead-silicate fibre combining the best advantages of stacking and extrusion will be designed, fabricated and analysed in Section 4.2. Finally, a novel approach to produce a preform with only 3 large holes by employing ultrasonic drilling is presented in Section 5.2 and the resulting fabricated fibre is extensively studied.

1.2 Index guiding fibres: an overview

In this section we consider the class of index guiding MOFs, first introduced by Knight *et al.* [2] and often referred to as *holey fibres* or *photonic crystal fibres*. Since the first reported HF shown in Figure 1.2(a), fibres with a large variety of hole shapes and arrangements have been presented in order to achieve a host of different functionalities. However the most typical cross section of a holey fibre, fabricated by using the widely employed procedure of *stack and draw* [54], has a hexagonal structure with equal sized holes, as shown in Figure 1.7.

The two parameters defining its structure are the hole diameter d and the hole-to-hole spacing Λ. The omission of one central air hole within the regular array of holes is usually used to define the solid fibre core (even if the central defect may be also formed by the omission of two [55], three [56], seven [57] or even more air holes). The air holes in the cladding act to lower the average refractive index of this region and light can be guided in the solid core via a modified form of total internal reflection, since ($\mathrm{n}_{core} \equiv \mathrm{n}_{silica}$) $> \mathrm{n}_{clad}$. The effective cladding index of the fibre, n_{clad}, is defined as the effective modal index of the lowest-order cladding mode. To good approximation this is similar to the fundamental mode of an infinitely periodic structure with the same d and Λ, which is referred to as the fundamental space filling mode (FSM), hence $\mathrm{n}_{clad} \simeq \mathrm{n}_{\mathrm{FSM}}$. Since the FSM becomes more confined to the silica region as the wavelength decreases, the effective cladding index increases towards shorter wavelengths, until $\mathrm{n}_{\mathrm{FSM}} \simeq \mathrm{n}_{silica}$ for $\lambda \ll \Lambda$. As λ becomes comparable to, or larger than, Λ though, a portion of the field

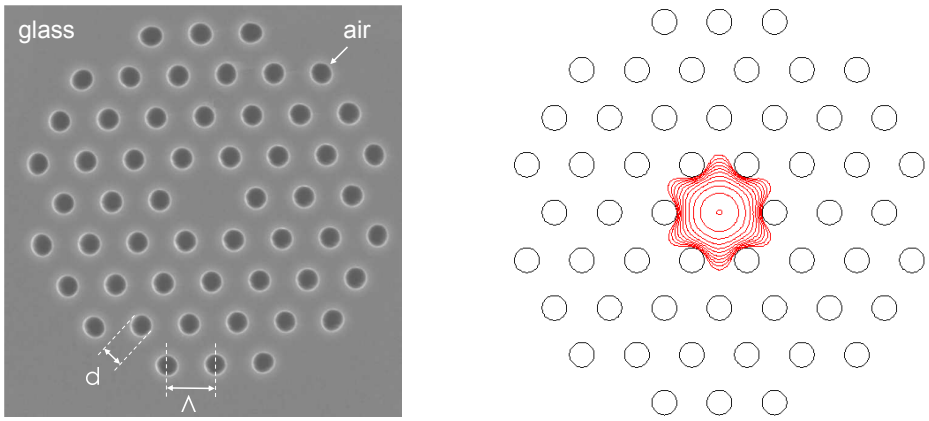

(a) (b)

FIGURE 1.7: (a) Scanning Electron Micrograph (SEM) of a typical holey fibre composed by a periodic triangular arrangement of air holes in a glass matrix; (b) simulated fundamental guided mode of the same fibre (2 dB contours).

will reside in the air region and the n_{FSM} will become some weighted average of n_{silica} and $n_{air} = 1$:

$$\lim_{\lambda \ll \Lambda} n_{\mathrm{FSM}} = n_{silica} \ , \qquad \lim_{\lambda \gg \Lambda} n_{\mathrm{FSM}} = f \times n_{air} + (1 - f) \times n_{silica} = \bar{n} \tag{1.1}$$

where f is the percentage of air in the structure, also known as its *air-filling fraction*.

It is this unusual and strong wavelength dependence of the refractive index of the cladding structure that is responsible for many of the novel properties of holey fibres. For example it leads to a short wavelength bend loss edge, which is the main limiting factor in the maximum achievable mode area in large core fibres. Perhaps most importantly, it also allows a holey fibre to guide a single mode at all wavelengths, a phenomenon known as *endlessly single mode guidance* [58].

1.2.1 Endlessly single mode guidance

The presence of air holes in the region surrounding the solid core imposes a wavelength dependence on the fundamental optical mode, guided in the core, that is similar to that of the cladding modes. This leads to a chromatic dispersion which is generally far from linear and, as we will see, can be drastically modified by the air hole characteristics. Above all, in certain structures, it can prevent the guidance of all higher-order modes, irrespective of the wavelength of propagation, thus enabling endlessly single mode guidance.

This surprising phenomenon was first reported by Birks *et al.* [58] and can be explained in direct analogy with a conventional, step-index fibre. In a step-index fibre the number

of supported modes is function of the V-parameter:

$$V = \frac{2\pi}{\lambda} a \sqrt{n_{\text{core}}^2 - n_{\text{clad}}^2} = \frac{2\pi}{\lambda} aNA = \frac{2\pi}{\lambda} a \sin\theta = k_\perp a \tag{1.2}$$

where a is the core radius, *NA* is the numerical aperture of the fibre, θ is the divergence angle and $k_\perp = k \sin\theta$ is the free-space transverse wave number. A step-index fibre is single mode if V remains below the first zero of the Bessel function J_0 (i.e. V < 2.405). Since n_{clad} is independent of wavelength, the V-parameter, and hence the number of modes, increases towards shorter wavelengths and the fibre becomes multi-moded below a certain *cut-off wavelength*.

In contrast, in a holey fibre the wavelength dependence of the cladding acts to lower the *NA* towards short wavelengths, thus balancing out the explicit wavelength dependence of the V-parameter. This results in a finite value of V, even in the limit $\lambda \to 0$; as a consequence, if the fibre's structural parameters are chosen suitably, the fibre can remain endlessly single mode [58]. Following Birks *et al.* several studies have analysed the cutoff properties of HFs, and a long debate followed on the most appropriate definition of the V-parameter and on the value of V that marks the second-order cutoff [59, 60].

A possible elegant solution was proposed by Mortensen *et al.*, who defined the V-parameter of a HF in the following way [61]

$$V_{\text{HF}} = k_\perp \Lambda = \frac{2\pi}{\lambda} \Lambda \sqrt{n_{\text{eff}}^2 - n_{\text{FSM}}^2} \tag{1.3}$$

and suggested that the fibre's single central defect could support a high-order mode only when the effective transverse wavelength $\lambda_\perp = 2\pi/k_\perp$ would fit into the defect region, i.e. $\lambda_\perp \leq 2\Lambda$. From this idea the conclusion that a HF can remain endlessly single moded as long as $V_{\text{HF}} = 2\pi\Lambda/\lambda_\perp \leq \pi$ easily follows.

Accurate multipole calculations of Maxwell's equations were employed to numerically confirm this result; and eventually they helped to deduce the expression for the single-mode – multimode boundary of silica hexagonally-arranged fibres:

$$\lambda/\Lambda \simeq \alpha(d/\Lambda - 0.406)^\gamma. \tag{1.4}$$

Here $\alpha = 2.80$ and $\gamma = 0.89$ are empirically derived fitting coefficients [62].

The singlemode – multimode phase diagram obtained was confirmed by experimental measurements on a number of HFs [63] and will be further explored in Section 3.2. In essence Equation 1.4 indicates that a fibre with $d/\Lambda < 0.406$ is endlessly single mode for all possible values of Λ; however, fibres with small Λ (of the order of λ) can also be single moded for much larger values of d/Λ.

1.2.2 Chromatic dispersion properties

Besides determining the number of supported modes, the hole size d and the hole-to-hole spacing Λ can also strongly influence the fibre's overall chromatic dispersion. It has been already mentioned how the dispersion of any guided mode in a HF is far from linear, due to the wavelength dependence of the effective index. The deviation from linear dispersion is often quantified, within the fibre community, by expanding the propagation constant $\beta(\omega) = n_{\text{eff}}(\omega) \cdot \omega/c$ in a Taylor series and by considering its coefficients $\beta_j = \partial^j \beta / \partial \omega^j$. The first derivative β_1 is inversely proportional to the group velocity ($\beta_1 = 1/v_g$), while β_2 is a measure of the variation of the group velocity with frequency, i.e. of the group velocity dispersion. Since it has become common use to work with wavelengths rather than frequencies, the group velocity dispersion is often quantified by the *group dispersion parameter* D [6]

$$D = \frac{\partial \beta_1}{\partial \lambda} = \frac{\partial}{\partial \lambda} \frac{1}{v_g} = -\frac{\lambda}{c} \frac{d^2 n_{\text{eff}}}{d\lambda^2}, \tag{1.5}$$

whose values are given in units of ps/nm/km.

The dispersion parameter D is central to both linear transmission of optical pulses and to nonlinear propagation. In optical data transmission the information bits are represented by pulses, whose envelope travels at the group velocity. If D = 0, all the frequency components of the pulse travel at the same speed, and the pulse maintains its shape; for D $\neq$ 0 however, the pulse will spread in time and, if the dispersion is not compensated for, the pulse may start overlapping with neighbouring pulses creating inter-symbol interference and ultimately loss of information. In nonlinear optics a low or zero dispersion may be preferable because a high intensity in the middle of the pulse can be maintained over longer distances if the pulse does not spread. Also, in order to enhance nonlinear interactions involving multiple channels, such as in parametric processes, a zero dispersion over the wavelength range of interest is very desirable. This would allow the nonlinearly interacting pulses to travel at the same (group) velocity, hence maximising the interaction length over which the nonlinear process takes place. For these applications, the *dispersion slope* $DS = dD/d\lambda$, which indicates how the dispersion changes with wavelength, also generally needs to be taken into account.

The total chromatic dispersion comprises two separate contributions: the intrinsic *material dispersion*, caused by the wavelength dependent interaction between light and matter (see Section 1.1.3), and the *waveguide dispersion*, which is strongly dependent on the fibre structure. In contrast to conventional fibre technology, which allows only a limited amount of waveguide dispersion to be introduced, the large refractive index contrast in HFs allows for a much greater control over the achievable D. For example the curves shown in Figure 1.8 represent the total chromatic dispersion of a HF for various values of d/Λ and a value of pitch $\Lambda = 2$ μm comparable to the wavelength. The curves provide a clear indication of the large amount of waveguide dispersion that can

be introduced by HFs (the dispersion of pure silica is plotted for reference as a dashed black line).

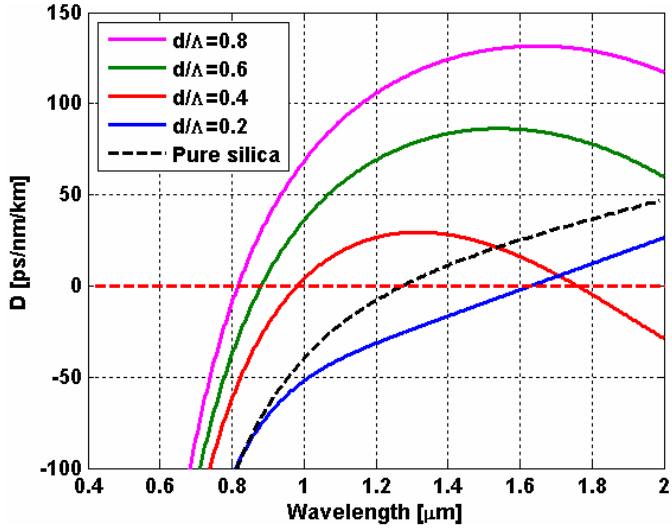

FIGURE 1.8: Dispersion curves (material + dispersion contributions) for a HF with pitch $\Lambda = 2$ μm and hole diameter d.

It can also be appreciated that by enlarging the hole size and thus increasing the amount of waveguide dispersion the zero dispersion wavelength can be pushed down to the visible range of the spectrum [64]. This can enable efficient Kerr nonlinear processes to take place at previously inaccessible wavelengths. Furthermore, the anomalous dispersion region, essential for soliton transmission, can also be greatly extended. This has enabled, for example, the generation of supercontinuum light spanning more than an octave from the visible to the near-IR [65] and the realisation of soliton transmission and compression experiments at the convenient operating wavelength of bulk lasers such as Nd:YAG and Ti:Sapphire [66], or of Yb-doped fibre lasers [67].

Alternatively, by using large air holes and subwavelength core size it is possible to achieve a very large normal dispersion at 1550 nm, allowing use of such fibres for dispersion compensation applications [68, 69]. Also, by carefully choosing d and Λ it is possible to achieve a small and flat dispersion over several hundred nanometers in the near IR [70]. The realisation of nonlinear fibres with such properties [71, 72] is potentially extremely promising for broadband nonlinear applications and this topic will be further analysed in Chapter 4.

Figure 1.9 shows how spectral regions with small and flat dispersion can be obtained, by carefully controlling the structural parameters of the fibre. Figure 1.9(a) shows three silica HFs designs presenting a flat total dispersion centred in the visible (532 nm), around 1.06 μm and at telecom wavelengths. Figure 1.9(b) shows 5 HF designs made of SF57 glass, presenting a flat dispersion at 1, 2, 3, 4 and 5 μm. Both figures have been obtained using an inverse design technique, the Downhill Simplex method, that will be presented in Section 4.2.1, and the results are shown here in order to

illustrate the typical dispersion behaviour of small core, dispersion flattened HFs. At wavelengths close to or below the zero dispersion wavelength (ZDW) of the material, the fibre dispersion is concave and typically two ZDWs appear. These have been found to improve the spectral flatness obtained during supercontinuum generation (see Ref. [73] and Section 3.3 in this thesis). At wavelengths above the material ZDW the dispersion profile is typically convex. Flat spectral regions spanning hundreds of nm can be realised (see the blue curve in Figure 1.9(a)) and even fibres with three ZDWs can be obtained, offering potentially novel nonlinear phase matching effects, although these remain to be studied in detail.

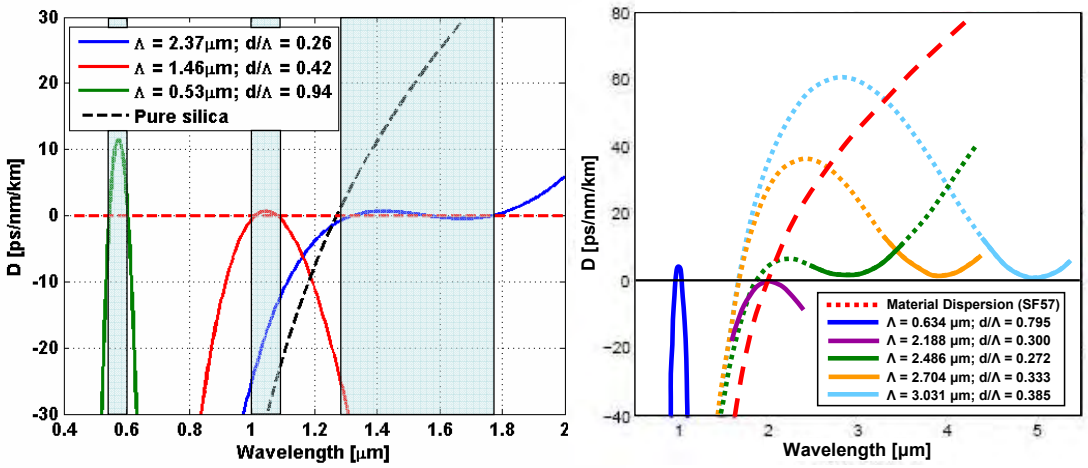

(a) (b)

FIGURE 1.9: Example of dispersion flattened fibres: (a) silica HFs with optimised flat dispersion profile at 532, 1060 and 1550 nm; (b) SF57 HFs with flat dispersion at 1, 2, 3, 4 and 5 μm.

Many of the studies reported in Part II of this thesis have been conducted with the aim of controlling the dispersion in HFs and to design nonlinear fibres with a specific dispersion profile, with the help of optical maps and inverse design techniques. Therefore a more detailed literature review on recent progresses in the previously discussed areas will be reported in Chapter 3, 4 and 5.

1.2.3 Polarisation properties

After having analysed the modal dispersion of MOFs, which ultimately depends on their propagation constant – or the eigenvalue of the Maxwell's eigenproblem (see Section 2.2) – we now address the polarisation properties of HFs, which are related to the eigenmodes of the problem. All the modes of a HF must reflect the rotational symmetry of the underlying dielectric structure, which in the case of the most common hexagonally arranged HFs is a 6-fold symmetry. This can be appreciated, for example, in the mode shown in Figure 1.7(b). In terms of polarisation, the modes of hexagonally arranged

HFs are organised in multiplets of degenerate or almost-degenerate modes, arranged approximately as those of a rotationally invariant step-index fibre [74]. In analogy to the fundamental modes of a conventional fibre, the first two HE_{11}-like modes of a HF form a polarisation doublet with orthogonal, linearly polarised states. The next four higher order modes form a multiplet, similar to the LP_{11} mode, which is formed by a TE_{01}-like and a TM_{01}-like non degenerate mode and by two HE_{21} twice-degenerate modes (see for example Figure 2.4).

The first full-vector numerical studies observed a small difference in the effective index of the two modes with the highest β, and erroneously predicted that ideal HFs with hexagonal symmetry would exhibit form birefringence [75]. This form birefringence has been subsequently proved false by Steel *et al.* [76], who retrieved a group theory study for uniform waveguides, conducted nearly 25 years before by McIsaac [8, 77]. According to this study, the modes of any waveguide with rotational symmetry of order $n > 2$ either exhibit the full waveguide symmetry and are non-degenerate or occur in degenerate pairs that support this symmetry only in combination. Thus a mode with a preferred direction, such as the HE_{11}-like of an HF, must belong to a pair of degenerate modes.

Moreover, by studying the properties of the irreducible representations of symmetry groups, additional information about the properties of the supported modes can be obtained. For example, in the hexagonally arranged lattice of HFs, which has a 6-fold rotational symmetry with one reflection plane and therefore belongs to the C_{6v} symmetry class, there are 8 distinct mode classes: 4 of them are non-degenerate and the remaining 4 share a 2-fold degeneracy in pairs. For a given mode class, a minimum waveguide sector can be also assigned; this is the smallest sector sufficient to determine all the modes in the class by applying the appropriate boundary condition (either perfectly magnetic of perfectly electric conductor) at either edge of the sector. For a C_{6v} symmetry the non-degenerate mode classes can be defined on a $\pi/6$ sector, while a $\pi/2$ sector is required for the degenerate modes such as the fundamental ones (see Figure 1.10). The use of a numerical method, such as the finite element method, which allows the restriction of the computational domain to these minimum sectors and the imposition of appropriate boundary conditions can allow a significant reduction in the computational time, as will be mentioned in Section 2.4.4.

Besides providing a useful framework for exploiting symmetries in electromagnetic simulations, this theory also elegantly proves that the nearly linearly polarised fundamental modes in an ideal C_{6v} structure must be degenerate, and that any deviation from that must be attributed to numerical errors: only the intentional or unintentional breaking of the symmetry can lead to birefringence.

The design flexibility of HFs indeed permits large values of birefringence to be achieved, by fabricating a largely asymmetric core with alterations of the geometry, size or position of the cladding holes, and by exploiting the large refractive index contrast between glass

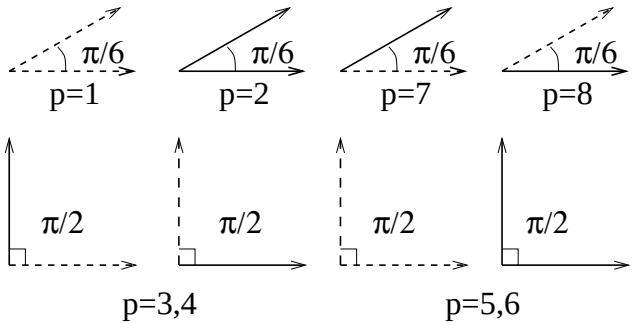

FIGURE 1.10: Minimum sectors for waveguides with C_{6v} symmetry. Mode classes $p = 1, 2, 7, 8$ are non degenerate; $p = 3, 4$ and $p = 5, 6$ are two-fold degenerate. Solid lines indicate Dirichelet boundary conditions for the electric field (perfect electric conductor); dashed lines indicate Neumann boundary conditions (perfect magnetic conductor). The class numbering, p, is after McIsaac [8].

and air. Fibres with high birefringence are valuable because light polarised parallel to one of the birefringence axis maintains its state of polarisation in spite of stresses, bends and other perturbations that might occur along the fibre length. The small core-cladding index difference in conventional fibres usually limits the achievable birefringence to beatlengths no shorter than a few mm at $\lambda = 1550$ nm. In contrast, the large index contrast achievable in HF permits very large values of form birefringence to be achieved. For example, by adopting smaller holes along one preferential axis, a HF with a beat length as short as 0.4 mm was fabricated, an order of magnitude smaller than is typical for conventional polarisation-maintaining fibres [78]. Since that first study by the University of Bath, several other designs have been proposed, employing, for example, a two-rod core [55] or 4 larger holes within the first ring surrounding the core [79].

Within the studies reported in this thesis, the polarisation properties of MOFs will be examined only with regards to air guiding photonic bandgap fibres, where for the first time the remarkable sensitivity of the surface modes to asymmetric variations in the glass ring surrounding the core is observed (Section 7.2).

1.2.4 Effective area control

The structural flexibility enabled by current holey fibre's fabrication techniques allows the possibility of scaling the pitch Λ to dimensions ranging from the sub-wavelength to several times the wavelength, and to achieve air-filling fractions from a few percent to more than 90%. This enables fibres with very different modal extensions, and therefore nonlinear properties, to be realised. The common way to quantify the spatial extension of the guided mode is to introduce an *effective area*, which is a fundamental quantity in the context of nonlinear phenomena. In the derivation of the nonlinear Schrödinger equation for the electric field $\boldsymbol{E}(\boldsymbol{r})$, a nonlinear coefficient γ is derived. This quantifies the strength of the nonlinear effects and depends on both material and waveguide

properties [6]:

$$\gamma = \frac{2\pi}{\lambda}\frac{n_2}{A_{\text{eff}}}. \tag{1.6}$$

Here n_2 is the material-related nonlinear coefficient and A_{eff} is the effective area, which depends on the geometric parameters and is defined as

$$A_{\text{eff}} = \frac{\left(\iint_{-\infty}^{\infty} |F(x,y)|^2\, dxdy\right)^2}{\iint_{-\infty}^{\infty} |F(x,y)|^4\, dxdy} \tag{1.7}$$

with $F(x,y)$ the modal field distribution and x and y the transverse coordinates.

Conventional single mode, step-index fibres for telecoms applications present $A_{\text{eff}} \simeq 80\ \mu\text{m}^2$, which corresponds to $\gamma \simeq 1\ \text{W}^{-1}\text{km}^{-1}$. Smaller values of A_{eff} are useful in nonlinearity-based devices, where a strong light confinement enhances the nonlinear interactions, while a larger mode area is attractive in high power applications where it helps minimise the nonlinear effects and increase the maximum power level that can be tolerated without incurring damage. By changing the dopant profile and concentration it is possible to realise conventional single mode fibres with A_{eff} ranging from $\sim 10\ \mu\text{m}^2$ [80] to $\sim 400\ \mu\text{m}^2$ [81].

The advent of HF technology has allowed improvements in both areas of highly nonlinear and large mode area fibres. Small core, large air-filling fraction HFs have permitted A_{eff} of a few μm^2 to be realised, almost matching the minimum theoretical value for a given material [82]. For example, by using a cross section design that allows for an extremely small core, suspended on three, nanometre-thin struts (similar to the design studied in Section 5.2) and employing a highly nonlinear glass (SF57), the current record in terms of the highest fibre nonlinearity was obtained at around 1860 $\text{W}^{-1}\text{km}^{-1}$ [50]. This is nearly two orders of magnitude larger than the maximum achievable with conventional fibres and it confirms that in the high nonlinearity regime the large index contrast and the possibility to employ a single, highly nonlinear glass are undoubtedly attractive advantages for MOFs.

The derivation of Equation 1.6 and 1.7 assumes that the nonlinear refractive index n_2 does not change significantly in the transverse plane. This is typically a good assumption for all-solid conventional fibres. However, in the case of microstructured air-glass fibres, n_2 presents order of magnitude variations between the air and the glass regions (n_2 of air is $\sim 3 \times 10^{-23}\ \text{m}^2\text{W}^{-1}$, three orders of magnitude smaller than silica). Generally it is energetically most favourable for the mode to localise itself in the high index regions and thus only a minority of the field resides in air. For $\lambda \ll \Lambda$, essentially all power is localised in silica and Equation 1.6 and 1.7 provide a reliable estimate of the fibre's nonlinear performance. However, for λ comparable to or larger than Λ or in the case of the air-guiding PBGFs discussed in Section 1.3, a large percentage of the optical

power can be localised in air. This requires the air's lower n_2 to be appropriately be taken into account. Alternative definitions of A_{eff} have been proposed in order to solve this issue [82, 83]; however, in order to correctly estimate the nonlinear parameter γ, these definitions produce a much larger and unphysical value of A_{eff}, a parameter usually associated with the spatial extension of the mode. In order to avoid this and to maintain the physical meaning of the effective area, in this thesis the approach suggested by Heinberger *et al.* will be preferred. This redefines n_2 as [84]:

$$\overline{n_2} = \frac{\iint_{-\infty}^{\infty} n_2(x,y)|F(x,y)|^4\,dxdy}{\iint_{-\infty}^{\infty} |F(x,y)|^4\,dxdy} \tag{1.8}$$

and maintains the nonlinear coefficient definition as $\gamma = 2\pi\overline{n_2}/(\lambda A_{eff})$ and the definition of A_{eff} as the one reported in Equation 1.7.

At the other end of the nonlinearity range, i.e. for small nonlinearity, large mode area fibres, HFs may still present some advantage over conventional fibres, but this is far less evident. Many studies have indicated that, while MOFs can have dramatically different performances across broad wavelength ranges [85], fair comparisons at specific wavelengths show modest differences with conventional fibres in the trade-off between effective area and bending losses [86]. MOFs are generally advantaged in applications requiring single modedness over a large operational bandwidth, but for operations at a single wavelength, or where a moderately multimode output is tolerated, the debate about which is the best technology for high power delivery and high power lasers applications is still ongoing.

Large mode areas would typically require a small effective index step. This can be achieved in a HF by employing claddings with very small holes and large hole separation, allowing a small decrease in the average refractive index. The largest A_{eff} achievable for a single mode HF with a standard design (see Figure 1.7) and a reasonable bend loss is around 600 μm^2 at 1550 nm, corresponding to $\Lambda = 23$ μm and $d/\Lambda = 0.5$ [87]. This can be increased to 1400 μm^2 by employing just one ring of large holes ($d/\Lambda = 0.7$) around a very large core [88]. This fibre operates in an effectively single mode regime due to higher confinement and bending losses associated with higher-order modes, which can 'leak' through the large gaps between the holes. A more detailed analysis of this fibre however demonstrated that its effective area under bend radii tighter than 10 cm would be reduced by more than 50% and designs employing a graded index core, less susceptible to this problems were advocated [89]. Even larger modal dimensions have been achieved with a conventional HF design with a 7-rod core and an additional outer cladding of large holes. This presented an A_{eff} of 2000 μm^2 and was successfully employed to realise an HF-based ytterbium-doped laser [57]. The bend loss issue is eliminated, in this fibre, by employing a rod-like design, resulting in a quasi-solid state configuration, with the obvious disadvantage of reduced packaging capabilities.

1.2.5 Leaky modes and confinement loss

Several mechanisms influence the overall loss of an optical fibre, such as intrinsic material and impurity related absorptions, Rayleigh scattering, multiphonon absorption and vibrational absorption of the hydroxyl group OH^-. In addition to these, in single material HFs there is a further mechanism, often referred to as *tunneling loss* or *confinement loss*. This arises from the fact that the holey area extends for a finite region around the core, beyond which lies an external solid cladding, or *jacket*, with the same refractive index as the core. The cladding cannot completely isolate the core from the external jacket and we can imagine some amount of light leaking out from the core, thus generating radiative losses. Since confinement losses are unavoidable in a practical MOF, its modes must decay while propagating; physically they cannot be described as guided modes and they are generally referred to as *leaky modes* (or, more appropriately, *tunneling leaky modes*), in analogy with the bound modes of a conventional fibre below cutoff [44].

Mathematically the propagation constant β of leaky modes is complex ($\beta = \Re e(\beta) + j\Im m(\beta)$), where the imaginary part identifies the rate at which guided power of the leaky mode is radiated. The power loss at a position z along the fibre axis is given by $\mathrm{P(z)} = \mathrm{P(0)}e^{-2\Im m(\beta)z}$, where P(0) is the initial modal power at z = 0. Therefore confinement losses (CL, in dB/m) are related to the imaginary part of the propagation constant β through

$$CL = 8.686 \times \Im m(\beta). \tag{1.9}$$

Although most of the current theoretical studies on MOFs treat those leaky modes as bound modes with an additional imaginary part of the propagation constant, this is not a mathematically correct approach. First of all the transverse profile of a leaky mode of an infinitely long waveguide is fundamentally different. It can be shown that it resembles a bound mode, until the radial position $\bar{\rho}$ (in MOFs determined by the end of the holey cladding) where radiation originates. From here outward the mode presents an exponentially increasing dependence on the radius ρ, which of course renders the modal field distributions non square-integrable. As a consequence leaky modes are not orthogonal in the usual sense and their completeness is not self-evident. Orthogonality condition can be restored only by integrating the transverse fields in the complex plane [44]. Furthermore, since there is no natural ordering in the complex plane, one can no longer use the simple relation $n_{cl} < \beta/k_0 < n_{co}$ to distinguish between guided and radiated modes and this may complicate the task of finding and ordering the modes.

In this thesis though, we will not deal with those mathematical issues and will adopt a more pragmatic and engineering approach. We will assume that the "most confined" leaky modes of a fibre with a finite cladding, which are the only ones that one is likely to observe in practice, are identical to the guided modes of a fibre with the same parameters

but infinite cladding, apart from a small imaginary part. These modes would satisfy $n_{cl} < \Re e(\beta)/k_0 < n_{co}$, where $n_{cl} = n_{\mathrm{FSM}}$.

It is also worth noting that in general, having $n_{cl} < \Re e(\beta)/k_0 < n_{co}$ does not guarantee that the imaginary part of β is small. However, in the case of a step-index fibre with infinite cladding, the fundamental mode is the one with the largest β, hence with the fastest decaying evanescent tail in the cladding. In close analogy, for a MOF with finite cladding, we would expect the confinement losses of the fundamental mode to be the smallest, so that its propagation constant would have both the smallest $\Im m(\beta)$ and the largest $\Re e(\beta)$. To locate the fundamental mode of a MOF it is therefore a good idea to start looking for values of β with the smallest imaginary part and with a real part in the vicinity of $n_{co}k_0$. Moreover, since for these modes generally $\Im m(\beta) \ll \Re e(\beta)$, we will retain the orthogonality and normalisation formulae used for bound modes and ignore the exponential increase of the mode shape for $\rho \to \infty$.

As one may expect, by increasing the number of rings of air holes that surround the solid core, and thereby increasing the physical separation between the solid core and the external environment, the confinement loss is reduced [90]. Therefore, although it is important to be able to estimate the CL of a fibre in order to introduce a sufficiently thick holey region around the core, CL are generally not the most serious issue in the design of a MOF, except in those limited cases where an impractically large number of holes would be required (see Section 3.2). Other sources of losses, and in particular scattering losses at the air-glass interfaces (see Section 1.3.2.2), represent the fundamental limiting factor in the lowest achievable loss in a MOF.

1.3 Photonic bandgap and 2D photonic bandgap fibres

1.3.1 The photonic bandgap

The idea of photonic crystals, or materials which exhibit a photonic bandgap, originated in 1987 from works in the field of strong localisation of light [21] and in the inhibition of spontaneous emission [20]. It was subsequently shown that in periodic arrangements of dielectrics, the propagation of light can be totally suppressed at certain wavelengths, regardless of propagation direction and polarisation. This inhibition results from the periodicity of the dielectric arrangement, and is quite fundamental in origin: in the frequency range where no propagation is possible (the so-called *photonic bandgap*), the density of possible states for light vanishes, so that even spontaneous emission becomes impossible.

The simplest device employing the concept of a photonic bandgap is a multilayer reflector, or Bragg mirror, consisting of a periodic stack of two alternating dielectric layers. Light propagating in a direction normal to the layers undergoes successive reflections and transmissions at the interface with each layer. With an appropriate choice of layer thickness and refractive index the device can behave as a reflector: waves reflected at each interface can add in phase, while transmitted waves can be out of phase, hence cancelling each other out. In such a device, light belonging to a certain wavelength range and incident with an almost normal angle can be totally reflected. One way to analyse the optical properties of a similar structure, whose stack extends infinitely, is by applying the Bloch theorem, that is so very well known from solid state physics. Since the structure possesses translational symmetry, the Bloch theorem says that solutions to the propagation equation in the stack can be expressed in the form of Bloch waves. Therefore two wave vectors differing by a vector of the reciprocal lattice associated with the periodic stack are physically the same: this allows us to consider the dispersion diagram only in the first Brillouin zone. At the edges of the Brillouin zone, two solutions exist having the same wave vector but different frequencies, and in between those frequencies no solutions for propagating waves exist at all. The frequency gap where no solutions exist is called a photonic bandgap [91].

Photonic crystals with two or three dimensional periodicity can be seen as a generalisation of Bragg mirrors, where the bandgap occurs for all directions of propagation either in the plane of periodicity or in the full space, respectively. If a defect is introduced in the infinite lattice, localised defect states for isolated frequencies within the bandgap can emerge, similar to bound states associated with defects in semiconductors, and light can be confined in the vicinity of the defect. One may imagine drilling a hole through a three dimensional photonic crystal and injecting light in the hole: as a result, the light will be reflected at the hole boundary and it will propagate through the hole, in a similar way to light propagation in a conventional fibre. Starting from this idea, Birks *et al.*

realised that in order to guide light along a linear defect, a full three dimensional periodicity of the bandgap material was not even needed, and simpler structures, periodic only in the transverse plane, could work as well [19]. The resulting fibre was initially denoted *photonic crystal fibre*, or *photonic bandgap fibre* in order to make more explicit the reference to the guidance mechanism these fibres relied on.

1.3.2 Photonic bandgap fibres

The most unusual feature of photonic bandgap fibres (PBGFs) is that, by using a PBG in the cladding, reflection is guaranteed for some frequency regardless of the refractive index of the material inside the defect. A defect in a PBG material can therefore confine and guide light in a low refractive index medium, such as vacuum, gas or liquid.

Two possible cladding periodicities exist that can confine light inside a longitudinally extending central defect: a one dimensional, radial periodicity and a two dimensional periodic arrangement of features, parallel to the defect. The former type is employed by the so-called Bragg fibres [38, 39], and requires quite large refractive index contrasts between the layers forming the omnidirectional reflecting stack [40, 41]. In this thesis the attention will be posed on the latter type of fibres, whose cladding consists of a two dimensionally periodic array of air holes. Figure 1.11 shows a typical cross section and the fundamental air-guided mode of one of these fibres.

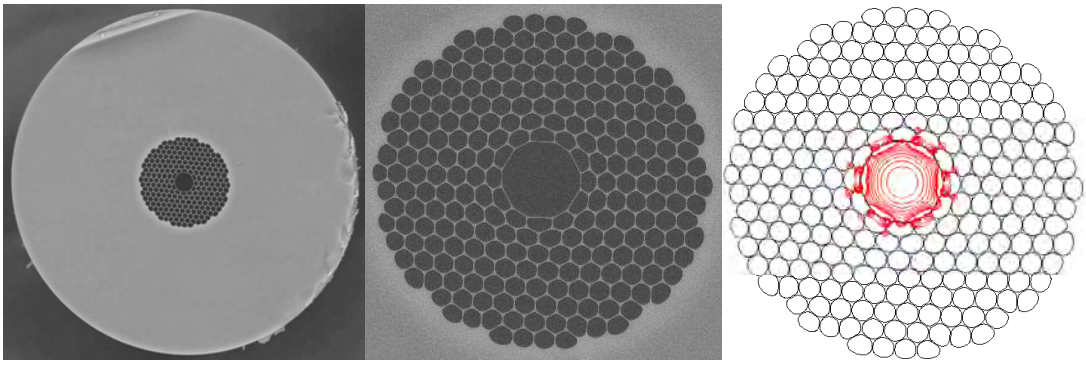

(a) (b) (c)

FIGURE 1.11: (a) SEM cross-section a typical two dimensional PBGF; (b) detail of the holey region; (c) simulated fundamental guided mode of the same fibre (2 dB contours).

Light propagation through air in a hollow fibre eliminates or greatly reduces the problems of nonlinearities, surface damage, and, when free-space coupling is used, end-reflections. This has permitted the demonstration of various novel applications, that are not possible with conventional fibres. For example, high energy (0.37 mJ) nanosecond pulses were delivered in single mode at 1 μm, demonstrating a 25 times improvement in the damage threshold as compared to solid core silica fibres, and showing potential for precision micromachining applications [92]. Ultra-high peak power femtosecond soliton transmission

has also been demonstrated at both 1550 nm (with up to 5.5 MW peak power, [93]) and 800 nm (with pulse energies around 120 nJ, [94]). The generation of short duration pulses with a high energy is also targeted through the soliton compression experiments in anomalously dispersive PBGFs. Compressions of more than a factor two have been reported for pulses with megawatt peak power [95]. PBGFs are also currently under intensive examination for all-fibre, high power chirped pulse amplification schemes, where their reduced nonlinearity allows the recompression of pulses with energies that would destroy conventional solid-core fibres. Demonstrations of the scheme at 1060 nm [96] and 1550 nm [97–99] have been presented. The long interaction length between a highly focussed optical field and a gas diffused into the fibre has been exploited to demonstrate low threshold nonlinear effects in gases [100] and guidance of small particles inside the hollow core by exploiting the light's radiation pressure [101]. Finally, compact gas-filled cells created by splicing one or both ends of a PBGF to conventional fibres [102] have been proposed as wavelength references for the active locking of a laser frequency [103] and for gas sensing applications [104].

1.3.2.1 Band diagrams and density of states

The properties of the out-of-plane bandgaps [105] that allow light confinement in PBGFs are quite different from those obtained when the component of the wavevector parallel to the periodic stack is equal to zero [106, 107]. Examples of the latter case are the in-plane propagation in a 2D photonic crystal or the fibre Bragg grating. In both cases the period of the lattice Λ must be of the order of half the wavelength, requiring submicrometre features for operation in the visible or near-IR. In contrast, for out-of-plane propagation the requirement is typically relaxed: in the most common configuration, the propagation constant β[1] is several times larger than the wave number in the transverse plane $k_\perp = \sqrt{n^2 k_0^2 - \beta^2}$. As a result the bandgap can operate on shorter wavelengths than in the analogous in-plane version, and a more practical Λ of several μm can be employed to create a PBG at visible or telecom wavelengths.

An additional advantage of the out-of-plane propagation is that a lower refractive index contrast is needed to open a bandgap. For a silica matrix with a triangular lattice of circular holes there is no complete photonic bandgap in the transverse propagation plane, due to an insufficient index contrast between the two regions [108]. For $\beta \neq 0$ however, a large contrast in transverse rather than absolute wave vectors is needed, and this can be made arbitrarily large, even if the contrast between the refractive indices itself is small [35]. This has allowed the use of pure silica to fabricate hollow core, air-guiding PBGFs, such as the one shown in Figure 1.11 and analysed theoretically for the first time by Broeng *et al.* [109].

[1] Although in practice also the modes of PBGFs are leaky (Section 1.2.5) and therefore their propagation constant β is complex, for simplicity in this section we will neglect this aspect and refer to β instead of, most appropriately, to $\Re e(\beta)$.

The existence of an out-of-plane bandgap for a silica-air structure is clearly shown by the band diagram in Figure 1.12, where for a periodic cladding similar to those achievable in practice [110] and for $\beta\Lambda = 15$ (note that, in comparison, Bragg gratings operate at a much smaller $\beta\Lambda = \pi$) a gap of no allowable frequencies appears around $k\Lambda = 15$. The specific value of $\beta\Lambda$ in this example was chosen to demonstrate that a bandgap can exist for an effective index $n_{eff} = \beta/k$ around the index of air (=1). This is the main requirement for modal confinement in air.

In analogy to the electronic density of states, we can also introduce a photonic density of states (PDOS, or simply DOS), $\rho(\omega, \beta)$, defined as the number of electromagnetic states existing in the frequency interval between ω and $\delta\omega$ and for a propagation constant between β and $\delta\beta$:

$$\rho(\omega, \beta) = \sum_m \int_{1BZ} \delta[\omega_m(\boldsymbol{k}_\perp, \beta) - \omega]\, d\boldsymbol{k}_\perp \tag{1.10}$$

Here m indexes the cladding eigenmodes with eigenvalues ω_m, $\delta[\omega]$ is the Dirac delta function and the integral is calculated for the transverse wave vector $\boldsymbol{k}_\perp$ scanning over the irreducible Brillouin zone. The DOS plot shown in Figure 1.12 for $\beta\Lambda = 15$ clearly confirms the indication that electromagnetic states can be completely inhibited for certain wavelength ranges.

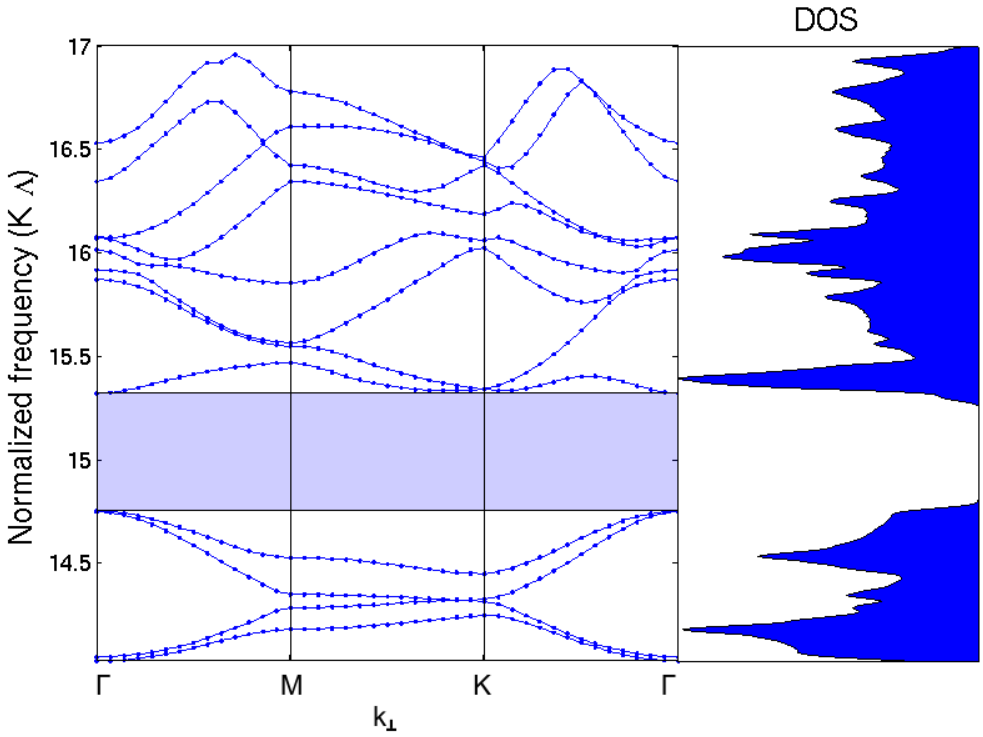

FIGURE 1.12: Band diagrams showing the normalised frequency $k\Lambda$ versus $\boldsymbol{k}_\perp$ calculated along the contour of the irreducible Brillouin zone and for $\beta\Lambda = 15$. The periodic dielectric structure consists of hexagonal holes with rounded corners and it is shown in the inset of Figure 1.13. The filled curve on the right shows the corresponding density of states (DOS). From both images a bandgap around the air index ($\beta/k = 1$) is visible.

In general the position and width of the bandgaps depend on the propagation constant β, and Figure 1.13 shows the results of changing β. The green patched areas represents bandgaps, where light propagation in the cladding is prohibited, and the dashed black line represents the air-line. As can be seen, several complete bandgaps exist for the studied lattice, and some of them are crossed by the air line.

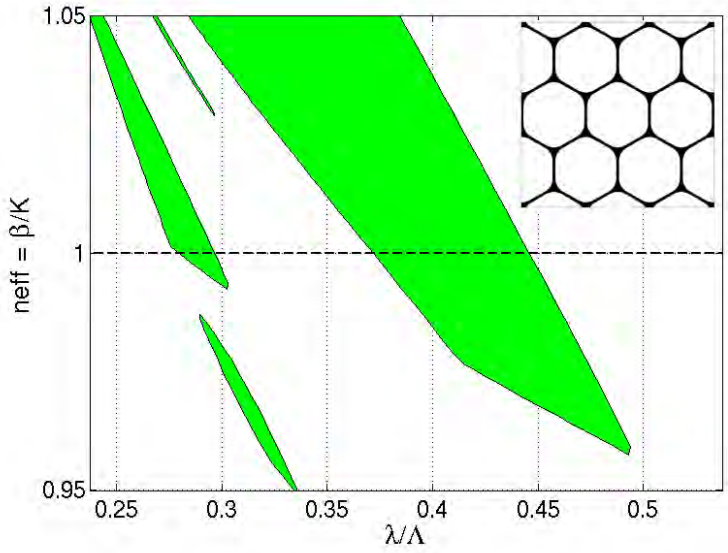

FIGURE 1.13: Plot of $n_{eff} = \beta/k$ versus λ/Λ for the realistic air-silica cladding shown in the inset and presenting d/Λ=0.96 and hexagons with rounded holes. The patched green regions indicate the bandgaps and the dashed line shows the air-line.

If a defect suitable to sustain one or mode modes is introduced, the structure can guide in air. Cregan *et al.* suggested, by employing a modification of a method often used in quantum electrodynamics to determine the density of modes [111], that the number of guided modes in the fibre is approximately given by:

$$N_{PBGF} = \frac{\rho^2(\beta_H^2 - \beta_L^2)}{4} \tag{1.11}$$

where β_H and β_L are the upper and lower edges of the PBG at a given λ and ρ is the core radius [3]. By employing typical values for a PBGF, it can be shown that a defect having nearly the size of Λ is insufficiently large to guide a mode. For a 7-cell defect however, not only a degenerate pair of fundamental modes, but also a group of additional 4 higher order modes, can be guided [109]. The defect modes will, to first approximation, follow the air-line, and their bandgap edges will thus be roughly given by the intersection of the air-line with the bandgap edges of the cladding shown in Figure 1.13.

The dependence of the central wavelength and of the edges of the bandgap as a function of the air-filling fraction f has been studied by Mortensen *et al.* [110], who showed that by increasing f the centre of the bandgap shifts towards shorter wavelengths, and at the same time the relative bandwidth increases (almost exponentially with f^2).

1.3.2.2 Confinement and scattering losses

As we have seen in Section 1.2.5, the modes of any fibre with a high refractive index in the outer jacket are leaky, and therefore characterised by a complex propagation constant. Modes of a hollow core PBGF are no exception and their confinement loss (CL) can be calculated by using suitable numerical methods (see Section 2.3). The CL of an air-guided mode is typically lower near the centre of the bandgap, and it exponentially increases for wavelengths approaching the bandgap edges, as shown in Figure 1.14.

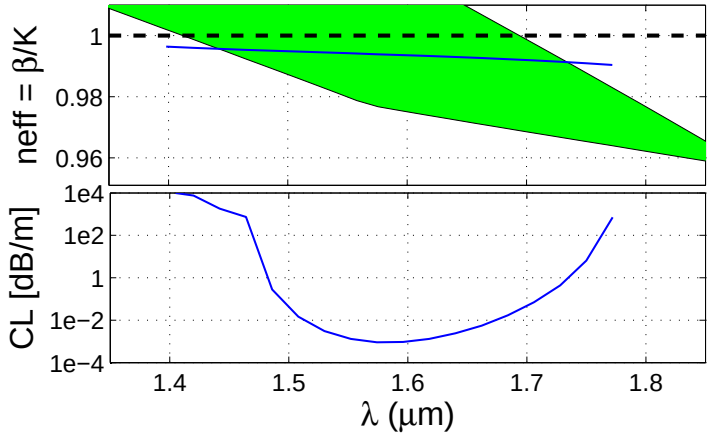

FIGURE 1.14: (Top) Bandgap edges for the infinitely periodic structure shown in the inset of Figure 1.13 and (blue line) effective index of the fundamental air guided modes; (bottom) Confinement loss for a 7 ring fibre.

Since the mode propagates in air, which has negligible absorption and suffers from much lower scattering than a solid material, it may not be unreasonable to imagine that confinement loss may represent the main source of losses in these fibres. However, generally the photonic crystal can have a high reflectivity even with only a relatively small number of periods, or ring of holes, around the defect. By including a sufficient (and reasonable from a fabrication point-of-view) number of air holes, the CL can be reduced to negligible levels, as was first shown in Ref. [112]. The same paper also demonstrates that CLs can be further suppressed by increasing the air-filling fraction in the cladding.

Another physical phenomenon however that can not be suppressed, and represents the fundamental limitation in the lowest achievable loss for an air-guiding PBGF, is the surface scattering at the air-glass interfaces [113]. Such scattering arises from the inherent roughness of the interfaces, caused by thermally excited surface capillary waves (SCW) which become frozen-in during the fibre draw at the glass transition temperature. This roughness-forming process has a thermodynamic origin and cannot by substantially reduced by technological improvements. The remarkable work by Roberts *et al.* has demonstrated that the loss in currently fabricated PBGFs is already limited by surface scattering. The typical rms roughness of only 0.1 μm achieved in currently fabricated

silica fibres and caused by SCW is enough to scatter light from the air-guided mode to a continuum of other lossier cladding modes, thus ultimately limiting the minimum achievable loss in these fibres to an (estimated) value of ∼0.2 dB/km at 1620 nm and ∼0.13 dB/km at 1900 nm. A dependence of the loss on the cube of the central wavelength of the bandgap has been predicted and experimentally verified [113]. Note that the same loss mechanism also represents the main loss contribution in small-core index guiding fibres at long enough wavelengths [113].

Apart from glass processing techniques aiming at increasing the surface tension, which we will not be concerned with in this thesis, a possible way to reduce scattering losses at the interfaces is by reducing the amount of field at the glass-air interfaces. In order to quantify the overlap between the electromagnetic mode and the perimeter of the holes where the scattering occurs, it is useful to introduce the following F-factor [25]:

$$F = \left(\frac{\epsilon_0}{\mu_0}\right)^{1/2} \frac{\oint_{hole\ perimeters} |\boldsymbol{E}|^2 dl}{\int_{full\ cross-section} (\boldsymbol{E} \times \boldsymbol{H}^* \cdot \hat{\boldsymbol{z}})\, dA}. \tag{1.12}$$

The F-factor is proportional to the fraction of scattered power, and designs of a fibre cross section that would allow a reduction of F would be highly desirable. Exploiting an antiresonant phenomenon in the glass ring surrounding the central defect has been suggested as one possibility to reduce F [114]; alternative practical core designs will be presented in Chapter 7.

1.3.2.3 Air modes and surface modes

As discussed in the previous sections, the introduction of a suitable defect inside the periodic crystal can allow the propagation of a guided mode inside the bandgap. For a typical silica-air PBGF with a core formed by the omission of 7-cells, the fundamental air guided mode concentrates around 95% of its power inside the central air region and presents an overlap with a Gaussian beam of in excess of 90% (see Figure 1.15(b) and Refs [94, 115]), facilitating an efficient coupling with step-index fibres.

At the same time though, the termination of the periodic cladding around the central defect may introduce modes that are localised at the surface between core and cladding, often referred to as *surface modes* (SM, [91]). The existence of surface waves bounded between two semi-infinite systems is frequently observed in physics. For example the ripple phenomenon in water is a surface wave guided by the interface between air and water. In the case of PBGFs, the surface modes are modes confined in the silica ring surrounding the core and exponentially decaying in any direction away from the surface. Examples of SM are shown in Figure 1.15(c) and (d).

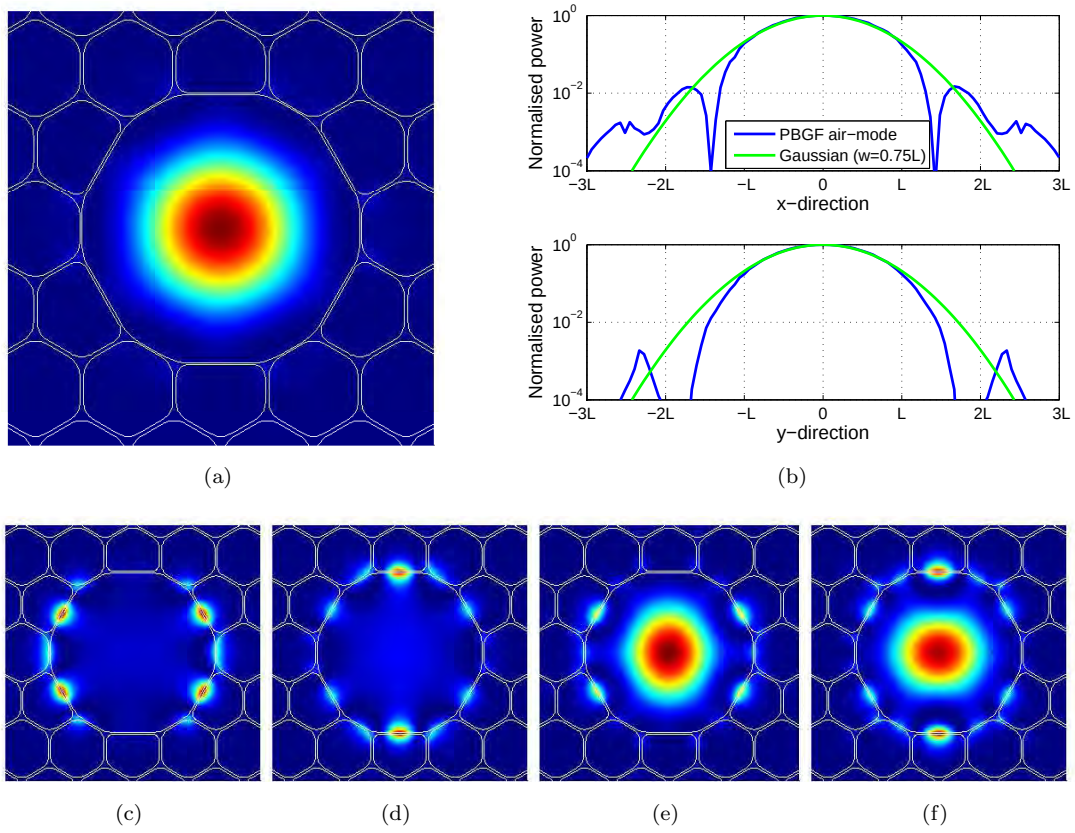

FIGURE 1.15: Examples of Poynting vector plots for modes allowed inside the photonic bandgap: (a) fundamental air-mode; (c), (d) surface modes; (e), (f) hybrid 'supermodes' existing around the anticrossing region between (a)-(c) and (a)-(d) respectively. The plots in (b) show a comparison between the normalised power of the fundamental air-mode and that of a gaussian function with $1/e$ width equal to 0.75 times the hole-to-hole distance L.

The existence of surface modes can be explained using perturbation theory. According to perturbation theory, the periodic dielectric cladding can be considered as a system of interacting index guiding waveguides. These waveguides are identical to each other, except for those near the surface. The interaction strength between neighbouring waveguides depends on their separation, due to the overlap of the evanescent field distributions. When the separation is infinite, there is no interaction and the waveguides can be considered as independent of each other. The eigenvalues of the system thus fall into two groups: one is an infinitely degenerate state corresponding to the identical waveguides in the photonic crystal; the other is composed of non-degenerate states corresponding to the waveguides near the surface. As the waveguides are brought together, the interaction between them causes the eigenvalues to split. In doing so they fully occupy the allowed energy band for the semi-infinite periodic structure. As a result, the non-degenerate levels corresponding to the waveguides near the surface will be 'expelled' from the allowed energy band. The only place where these states can be accommodated is within the forbidden bandgap. Their field distribution is localised near the surface, with exponentially decaying tails from both sides of the surface [91].

Since the surface modes are tightly confined to very small silica regions, their dispersion is rather steep compared to air-core modes. Having two different classes of modes with steep and flat slopes very often leads to hybridisation and avoided crossing of the modes. In other words the eigenmodes of the system become 'supermodes' or linear combinations of the individual core and surface modes, two examples of which are shown in Figure 1.15(d) and (e). A more detailed analysis of these avoided crossings, including symmetry and polarisation considerations, will be presented in Chapter 7. Here it will suffice to say that in the close proximity of these avoided crossings additional loss mechanisms arise, due to energy coupling between air-guided modes, surface modes and lossy cladding modes [13, 112, 116]. These modal interactions result in Lorentzian-like peaks in the fibre transmission spectrum, which in certain circumstances can severely limit the fibre's transmission bandwidth [117, 118]. A number of studies have been therefore recently devoted to the problem of minimising the impact of surface modes by fabricating an appropriate termination of the photonic crystal [119–121]. In Section 7.3 we will study how realistic air silica PBGFs can be realised in a regime where the fundamental core mode is robustly free of anticrossings with surface modes at all frequencies within the bandgap.

1.4 Conclusion and outline of the thesis

The aim of this introductory chapter was to provide the reader with an overview of the potential of microstructured optical fibres to produce optical properties unreachable with conventional fibres, to exploit novel physical effects and to permit entirely new applications. At the beginning of this project, nearly 7 years after the first fabricated MOF, a wide variety of fibres had been already fabricated and characterised at the ORC, as well as in a few other research facilities worldwide, employing different glasses and fabrication techniques. An example of some of these structures is shown in Figure 1.16.

In order to improve our understanding of these fibres and to design novel fibres for specific applications, adequate modelling tools are also required. The modelling of these fibres however was still a demanding task and a rather unexplored field at that time. This motivated the development and application of novel simulation methods for the study of MOFs, which represents the underlying theme of this research project. As will be further discussed in Chapter 2, analytical models can not be applied to the modelling of MOFs, and numerical models have to be specifically formulated or adapted from other applications. A number of numerical models were already available at the beginning of this project, and the first task was therefore to review the various methods and assess their efficiency, accuracy and suitability to simulate a broad range of ideal and real fibres. The outcome of this work, reported in Chapter 2, suggested the finite element method (FEM) as one of the most complete, versatile and efficient methods. Rather

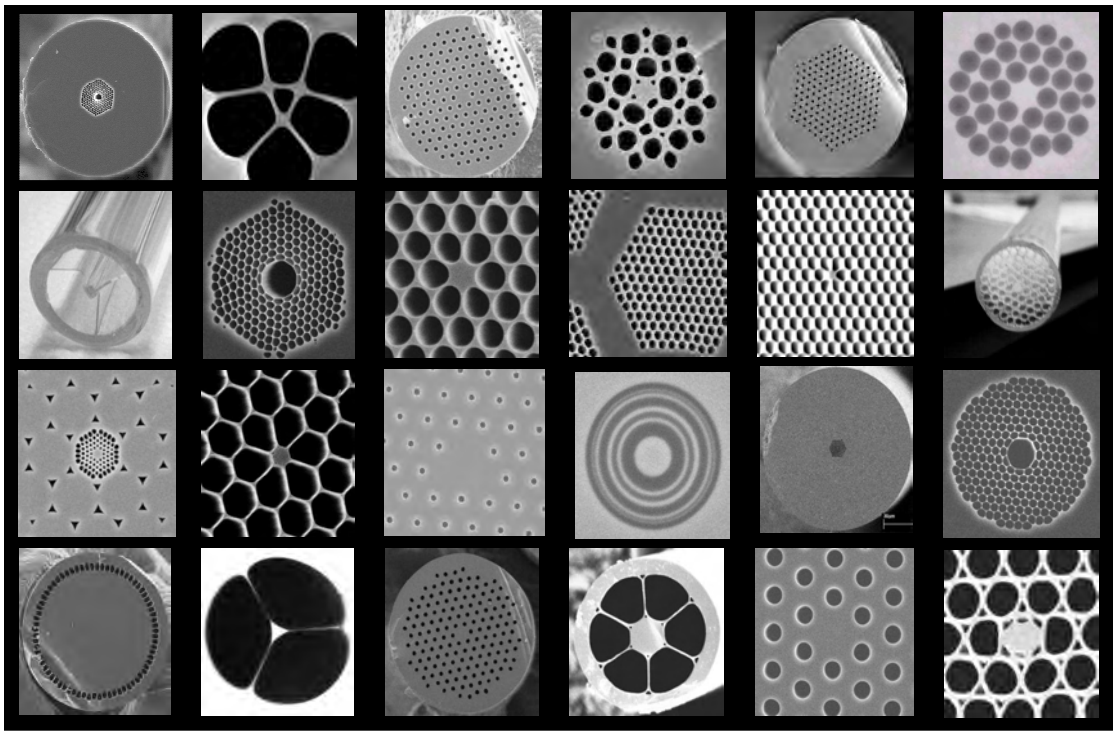

FIGURE 1.16: Some examples of the wide variety of MOFs and preforms fabricated at the ORC in recent years by employing various glasses and fabrication techniques.

than implementing the FEM ourselves, it was decided to adapt a general commercial FEM package for the specific needs of MOF modelling. A number of scripts were therefore implemented, allowing us to design a range of new fibres and to complement the experimental characterisation of fabricated fibres in several different projects, as will be reported in the following chapters. Scripts and specific methods for studying both index guiding and photonic bandgap guiding fibres have been developed. In addition, another requisite of the project was to develop inverse design techniques that would help in the search for the best microstructure to provide one or more target optical properties. The outcome of this work is presented in Chapter 3 and 4.

An outline of the main content in each chapter of this thesis is reported in the following. In Chapter 2 an introduction on the electromagnetic modelling of MOFs is presented. This contains an overview of the specific issues to be faced, of the various modelling tools currently available to study MOFs, and of the particular numerical method – the finite element method – that will be employed throughout this work, for which some details of our implementation and an accuracy test will also be presented.

The following three chapters included in Part II of this thesis, Chapter 3, 4 and 5, are devoted to the study of index guiding fibres. Chapter 3 and 4 explore different inverse design methods finalised at finding the structure which possesses some desired optical properties, while Chapter 5 presents additional modelling work carried out to support various experimental results.

In particular, Chapter 3 introduces two dimensional optical property maps, which visually overlap the contour plots of many optical properties of hexagonally arranged HFs, and shows the wide applicability of such maps to many HF design problems. Three different studies are reported: (i) the examination of the applicability of HFs as telecoms transmission media; (ii) the optimisation of the chromatic dispersion of silica HFs for the generation of supercontinuum light at wavelengths around 1 μm; (iii) the design of fibre tapers in a number of different glasses allowing simultaneous reduction of the stimulated Brillouin scattering and control of the overall dispersion properties.

In Chapter 4 the inverse design is taken one step further, to allow the optimisation of fibres with a larger number of free-parameters. Although the inverse methods implemented are quite general and suitable for a large variety of fibre optimisations, two specific applications are presented. First the simplex method is employed to obtain dispersion flattened, highly nonlinear lead silicate fibres for application at telecoms wavelengths; then a genetic algorithm is applied to the inverse design of dispersion flattened silica fibres with a large number of free-parameters. The tolerance to fabrication inaccuracies for the resulting optimum structures is also analysed.

Chapter 5 contains two additional numerical studies of index guiding MOFs, where the simulations have been used to support experimental measurements and to enhance our understanding of the fibres and of the physical phenomena under observation. A fabricated suspended-core HF is studied in order to explore its potential for applications within evanescent field sensing, as well as a polarisation maintaining highly nonlinear fibre. The efficient generation of light in the visible range of the spectrum is then tackled by both optimising a fibre for the generation of a supercontinuum around those wavelengths and through the exploitation of red and blue sidebands, generated through a Four Wave Mixing (FWM) process when a green light is pumped into the cladding of a particular MOF.

The following two chapters which form Part III of this thesis, Chapter 6 and 7, deal with the modelling of photonic bandgap fibres. Chapter 6 proposes a structural model to represent accurately the cross section of fabricated hollow core PBGFs and it applies the model to the study of the typical properties of these fibres, their dependence on the material properties and to obtain general scaling rules. The chapter also includes a study of real (i.e. unsymmetric) fibres from the simulation of their cross-section, as obtained from scanning electron micrograph (SEM) images. This study is made possible by the unique capability of the FEM to describe accurately structural details over a length scale ranging over three orders of magnitude. The necessity of using high resolution scanning electron micrographs is advocated and the influence of the gold coating layer employed in the SEM acquisition is also discussed.

Finally, Chapter 7 is devoted to the study of the surface modes in PBGFs and presents two separate analyses. The first one observes how these modes are extremely dependent

upon the shape of the glass core boundary, and it shows how small asymmetric variations in this boundary can lead to the high birefringence and polarisation dependent loss experimentally observed at some wavelength within the bandgap. The second study tackles the problem of maximising the operational bandwidth of realistic PBGFs by eliminating anticrossings with surface modes. For a particular thickness of the core boundary, a regime is found for which the fibres are surface mode-free. This finding is then confirmed by experimental measurements.

NOTE: The work reported in this thesis has been deeply affected by the fire which, on 30 October 2005, destroyed the ORC clean rooms and a number of offices, including the author's. Besides the loss of all codes and simulation results produced in the period between December 2004 and the fire, this event has negatively affected most of the experimental projects I was collaborating with. As a result, some of the works presented here could not be completed as originally intended. This is the case, for example, of the works reported in Section 3.3 and Section 4.2, which required the fabrication of silica fibres (which was only recently resumed) and of soft glass fibres (which has not yet been resumed). In all cases however, the theoretical or numerical part representing my contribution to the project, has been either recovered or completely regenerated, and it is thus presented in a consistent form. Please note that a limited number of images reported in the thesis have been recovered from previously generated bitmaps, and therefore they present a lower resolution.

Chapter 2

Modelling microstructured optical fibres

2.1 Introduction

After the general introduction to the history, main properties and applications of microstructured optical fibres presented in the previous chapter, this chapter provides the background information necessary to understand the modelling work conducted in this thesis. The chapter starts with an overview of the differential mathematical problem that needs to be solved in order to study light propagation in a MOF; then the principal simulation methods so far developed for the study of MOFs will be presented. The choice of the finite element method (FEM) as the preferred method for the studies in this thesis is then supported. A final section is then devoted to the introduction of the FEM, to the presentation of the implementation used throughout the thesis and to an analysis of the accuracy achievable with the method.

2.2 The Maxwell's eigenproblem

Like all macroscopic electromagnetic phenomena, the propagation of light in a MOF can be described by the well-known Maxwell's equations. In the case of a *mixed dielectric medium*, where no free charges or currents are present in the entire domain, the four equations can be written in a differential form and according to the International System of units (SI) notation as:

$$\nabla \times \boldsymbol{E}(\boldsymbol{r},t) = -\frac{\partial \boldsymbol{B}(\boldsymbol{r},t)}{\partial t} \tag{2.1a}$$

$$\nabla \times \boldsymbol{H}(\boldsymbol{r},t) = \frac{\partial \boldsymbol{D}(\boldsymbol{r},t)}{\partial t} \tag{2.1b}$$

$$\nabla \cdot \boldsymbol{B}(\boldsymbol{r},t) = 0 \tag{2.1c}$$

$$\nabla \cdot \boldsymbol{D}(\boldsymbol{r},t) = 0 \tag{2.1d}$$

where $\boldsymbol{E}(\boldsymbol{r},t)$ and $\boldsymbol{H}(\boldsymbol{r},t)$ are respectively the vectorial electric and magnetic fields, $\boldsymbol{D}(\boldsymbol{r},t)$ and $\boldsymbol{B}(\boldsymbol{r},t)$ the electric displacement and magnetic induction fields. All of these fields are functions of both space and time.

Most of the cases of interest for this research are represented by *isotropic materials*, and it is often a good approximation to assume propagation in the *linear regime*. Therefore the constitutive relations relating $\boldsymbol{E}$ to $\boldsymbol{D}$ and $\boldsymbol{H}$ to $\boldsymbol{B}$ can be simplified from a more general tensorial, non-linear form, to a much simpler scalar and linear version:

$$\boldsymbol{D}(\boldsymbol{r},t) = \varepsilon(\boldsymbol{r})\boldsymbol{E}(\boldsymbol{r},t) \tag{2.2a}$$

$$\boldsymbol{B}(\boldsymbol{r},t) = \mu\boldsymbol{H}(\boldsymbol{r},t). \tag{2.2b}$$

where $\varepsilon(\boldsymbol{r})$ is the electric permittivity and μ is the magnetic permeability. For most of the dielectric materials of interest, μ can be assumed to be a constant, equal to its free-space value, $\mu = \mu_0$. The electric permittivity ε is generally a function of frequency (ω), and its complex spatial dependence is one of the main difficulties to address when modelling MOFs. The imaginary part of ε accounts for material-related losses (absorption), but in the case of *low-loss dielectrics* such as silica in the near infrared part of the spectrum, ε can be assumed to be purely real.

The constitutive relations (2.2) allow equations (2.1) to be expressed as a function of only two unknowns, $\boldsymbol{E}$ and $\boldsymbol{H}$. These can generally have a complicated frequency dependence, but the linearity of Equation 2.1 permits the application of Fourier analysis. This means that any general solution can be expressed as a combination of *harmonic modes*, each calculated at a specific optical frequency. This allows the temporal dependence to be removed from the original problem, by solving the problem one frequency at a time. Introducing the complex representative vectors $\boldsymbol{\mathcal{E}}$ and $\boldsymbol{\mathcal{H}}$ via

$$\begin{aligned} \boldsymbol{H}(\boldsymbol{r},t) &= \mathrm{Re}\{\boldsymbol{\mathcal{H}}(\boldsymbol{r})e^{j\omega t}\} \\ \boldsymbol{E}(\boldsymbol{r},t) &= \mathrm{Re}\{\boldsymbol{\mathcal{E}}(\boldsymbol{r})e^{j\omega t}\} \end{aligned} \tag{2.3}$$

and by the substitution of Equation 2.3 into (2.1), the following system is obtained:

$$\nabla \times \boldsymbol{\mathcal{E}}(\boldsymbol{r}) = -j\omega\mu\boldsymbol{\mathcal{H}}(\boldsymbol{r}) \tag{2.4a}$$

$$\nabla \times \boldsymbol{\mathcal{H}}(\boldsymbol{r}) = j\omega\varepsilon(\boldsymbol{r},\omega)\boldsymbol{\mathcal{E}}(\boldsymbol{r}) \tag{2.4b}$$

$$\nabla \cdot \boldsymbol{\mathcal{H}}(\boldsymbol{r}) = 0 \tag{2.4c}$$

$$\nabla \cdot (\varepsilon(\boldsymbol{r},\omega)\boldsymbol{\mathcal{E}}(\boldsymbol{r})) = 0. \tag{2.4d}$$

The first two curl equations can be decoupled to obtain an equation in only one unknown, for example $\boldsymbol{\mathcal{H}}$:

$$\nabla \times \left(\frac{1}{\varepsilon(\boldsymbol{r},\omega)} \nabla \times \boldsymbol{\mathcal{H}}(\boldsymbol{r}) \right) = \omega^2 \mu \boldsymbol{\mathcal{H}}(\boldsymbol{r}). \tag{2.5}$$

This is the master equation, which, in addition to the divergence equation (2.4c), completely determines $\boldsymbol{\mathcal{H}}(\boldsymbol{r})$ for any given spatial distribution of $\varepsilon(\boldsymbol{r},\omega)$.

In the case of interest of z-invariant structures, we can seek solutions of Equation 2.5 in the form

$$\boldsymbol{\mathcal{H}}(x,y,z) = \hat{\boldsymbol{\mathcal{H}}}(x,y)e^{-j\beta z} \tag{2.6}$$

where β is the propagation constant along z. By substituting Equation 2.6 into (2.5) an *eigenvalue problem* is obtained, where the harmonic mode $\hat{\boldsymbol{\mathcal{H}}}(x,y)$ is the eigenvector associated with the eigenvalue β. As we have already seen in Section 1.2.5, the propagation constant of the leaky modes typical of MOFs is generally a complex number, where the imaginary part accounts for the confinement loss of the mode as it propagates along the fibre. Amongst the various possible loss contributions, such as Rayleigh scattering, micro-scattering at the interfaces and confinement loss, the latter can have a dominant role in the case of MOFs. For a complete fibre design it is therefore quite important to employ simulation methods that are able to calculate the confinement loss, as will be discussed in the next Section.

In the case of a *homogeneous medium* ($\varepsilon(\boldsymbol{r},\omega) = \varepsilon(\omega)$) Equation 2.5 reduces to the well-known scalar Helmholtz equation, which can be solved analytically in either cartesian or cylindrical coordinates. If the geometry of the problem is such that boundary conditions can also be applied in a closed form at the interfaces between different homogeneous zones, the problem can have a full analytical solution. This is the case, for example, of conventional step-index fibres [44] or of Bragg fibres [38]. In the case of MOFs however, expressing the boundary conditions in an analytical form is usually impossible, due to the complexity of the spatial refractive index profile. Furthermore, the high index contrast of MOFs, typically two order of magnitude greater than in conventional fibres, prevents us from employing the approximations that lead, for example, to the definitions of LP modes of conventional fibres. Analytical solutions therefore cannot be formulated for MOFs, and numerical methods must be applied in order to solve Equation 2.5, and to calculate eigenvalues, eigenvectors and finally the optical properties of the structure.

The next section will provide an overview of the principal numerical methods developed so far for the solution of the eigenproblem (2.5).

2.3 Numerical methods

A significant amount of work has been conducted in recent years in order to formulate numerical methods for the simulation of MOFs. As mentioned in Section 2.2, one of the main difficulties in the analysis of MOFs lies in the two-dimensional spatial complexity of the refractive index profile. This has generally precluded the use of analytical methods from traditional fibre theory, and has either required the adaptation of already existing numerical methods, or stimulated the formulation of new methods. Examples of the first case are the Multipole Method or the Finite Element Method, while the Plane Wave Expansion technique and the Fourier decomposition method with adjustable boundary conditions belong to the second class. Most of the methods outlined below can be applied to the study of both index-guiding and photonic bandgap fibres; their different approaches and limitations will be analysed in detail in the following.

2.3.1 Effective index method

The first work trying to obtain an insight into the operation of a MOF was conducted by Birks *et al.* and later became referred to as the *effective index method* [58]. Although it is not a numerical method, it deserves a brief mention in this section because it can provide a good approximation of the main properties of a restricted range of index guiding fibres, without the need for numerical computations. The idea of the method is to substitute the holey cladding with an equivalent homogeneous material presenting a wavelength-dependent *effective* cladding index. This is defined as the refractive index of the fundamental space filling mode (see Section 1.2.1). In this way, guidance in a MOF can be understood as a modified form of total internal reflection and the V-number of a MOF can be defined, in analogy with that of conventional fibres. Although this simple model is unable to predict accurately many of the properties of a MOF, it is sufficient to demonstrate the endlessly single-mode guidance experimentally observed. An elegant improvement of the V-number definition was later presented by Mortensen *et al.* [56]: using this they demonstrated that any triangular-lattice fibre is single mode for $V < \pi$. Several interesting papers followed, from the same Danish group, presenting a parametrisation of many fibre properties in terms of this V-number definition, such as mode field radius and effective area [122] and macrobending losses [123]. By using a similar approach, a slightly different V-number definition and the support of finite element method simulations, Saitoh and Koshiba also presented simple empirical relations for the dependence of V and n_{eff} on the structural parameters d and Λ [124]. Through these

relations, and by employing well known formulae for conventional fibres, properties such as group velocity dispersion, mode field diameter and splice loss can be estimated [125].

All of these approximate methods however are valid for a restricted class of fibres (e.g. those with a triangular lattice of circular air holes) and/or cannot accurately predict properties such as dispersion, birefringence or confinement loss. Full numerical methods, able to solve Equation 2.5, which account for the complex spatial transverse profile of the fibre, are therefore necessary to overcome these limitations. Generally these methods initially tackled the much simpler solution of the scalar Helmoltz equation, but with time they developed into a full vectorial formulation. As a general rule, scalar methods can be employed for low-NA fibres, where the fundamental mode is almost TEM and one of the transverse field components is substantially bigger than the others. For triangular lattice fibres an upper limit of $d/\Lambda = 0.35$ was suggested [126]. Larger air-filling fractions than this would require vectorial solutions.

2.3.2 Plane wave expansion method

One of the first numerical methods formulated to study MOFs relied on periodic boundary conditions and was based on plane wave decomposition [127, 128]. The method, usually referred to as the *Plane Wave Expansion Method* (PWE), decomposes both refractive index profile and eigenmodes into some truncation of an orthogonal basis of wave functions, thus transforming the problem (2.5) into the linear matrix eigenproblem $[A]\{\phi\} = \lambda\{\phi\}$. The periodicity of the basis functions imposes the application of periodic boundary conditions, and a *supercell* with a periodically repeated defect must be considered in order to account for the presence of the central core. The accuracy of the approximation increases with the size of the supercell, as adjacent defects become progressively more and more uncoupled. As compared to most of the following methods, the choice of the plane wave basis can be rather inefficient in representing the guided, localised modes, and a very large number of plane waves may be required. However, if combined with the use of an efficient Fast Fourier transform algorithm, iterative eigensolvers and appropriate pre-conditioners, this method can still prove to be an efficient and attractive solution. The freely available version developed by Johnson and Joannopoulos at MIT [129] is currently used by a large number of research groups around the world to simulate both index guiding and photonic bandgap fibres. One of the main disadvantages of this particular implementation though, is that the propagation constant β is required as an input, and the eigenvalue returned from the solver is the frequency ω. Therefore it is not possible to include the material dispersion ($\varepsilon = \varepsilon(\omega)$) directly into the numerical calculation. An alternative implementation reformulating the method for the solution of an eigenproblem for the propagation constant has been recently presented [130, 131].

2.3.3 Orthogonal function method

A fundamental improvement to the computational efficiency of the PWE algorithm was achieved by the introduction of two basis sets of orthogonal functions. The method, later called the *Orthogonal* or *Localised Function Method* (OFM) employs at the same time periodic basis functions (plane waves) to describe the refractive index in the cladding, and localised (Hermite-Gaussian) functions to better describe the localised nature of both the core defect and the confined core modes. Both scalar [126, 132] and full vector [133, 134] approaches have been presented and they have been extensively used in early numerical studies of HFs.

Both the PWE and the OFM can accurately model several fibre properties, such as group velocity dispersion and effective area, but they cannot estimate the modal confinement loss (CL) associated with propagation in a transversely finite structure. In fact, due to the implicit periodic boundary conditions assumed, the resulting solutions are bound modes and their propagation constant is purely real. Initial measurements on the losses of the first MOFs however suggested that the fibre's CL may represent the main contribution to the overall loss; as a result numerical methods which would allow an accurate estimate of the CL were subsequently developed.

2.3.4 Fourier decomposition with adjustable boundary conditions

One of the first methods specifically conceived to target the design issues of MOFs and able to calculate their confinement loss was the *Fourier decomposition method with adjustable boundary conditions* (ABC-FDM). The scalar version was proposed in Ref. [135] and the full vector version followed shortly after [136]. The Maxwell equations are reduced to an eigenvalue equation for the transverse magnetic field, so that the mode effective index appears in the eigenvalue. The MOF structure is enclosed in a circular computational domain. Outside the computational domain fields are expanded using modified Bessel functions of the second kind, that result in evanescent fields for bound modes and outward radiating fields for leaky modes (see Section 1.2.5). This expansion depends on the effective index only. Inside the domain, the fields are expanded using a set of complete basis functions, chosen to be a modified azimuthal and radial Fourier series for improved computational efficiency. The Fourier series is modified by two adjustable parameters that allow any boundary condition to be satisfied. After setting an initial guess for the value of the effective index, the external field is determined and it provides the boundary conditions for the internal field. A mode solver can then find the internal field that satisfies these boundary conditions and generate an improved estimate of the effective index. The process can be iterated using the new effective index value until the required solution accuracy is reached. The Maxwell eigenvalue equation contains several inner products. Inner products that depend on basis functions only can

be readily solved (and pre-tabulated) since they contain simple trigonometric functions. Inner products that depend on the structure can be done analytically if the holes are in the shape of annular sectors; otherwise they can be done numerically, although this is likely to affect the computational efficiency.

In addition to these novel methods, specifically designed for the study of MOFs, further works have targeted the modification of general methods for the study of electromagnetic phenomena, to the specific field of propagation in MOFs. This is the case, for example, of the *Beam Propagation Method* (BPM), of the *Multipole Method* (MM), of the *Source-model technique* (SMT) and of the *Finite Element Method* (FEM).

2.3.5 Beam propagation method

BPM is one of the most widely used propagation techniques for modelling integrated and fibre optic photonic devices. In its standard formulation an initial field profile is propagated step by step in the longitudinally invariant direction of the structure by using either a split-step Fourier method or a finite-difference approach. Usually a paraxial approximation is employed in order to reduce the order of the differential equations involved, even though the paraxiality restriction can be relaxed through the use of extensions that have been referred to as *wide-angle BPM*. Since the BPM is a propagative method, it is not designed to calculate the modes of a structure; however it can be adapted to provide a mode-solving capability by either using a *Correlation method* [137] or by the so-called *Imaginary-distance method* [138]. The Correlation method obtains the eigenvalues of the structure by Fourier-transforming a correlation function between the input field and the propagated field. In the Imaginary-distance method the fundamental mode is obtained by propagating an initial input mode along an imaginary distance axis. When z is substituted by jz, the propagative term $e^{j\beta z}$ becomes a gain term $e^{\beta z}$. Therefore, since the fundamental mode is characterised by the largest propagation constant, its contribution will have the highest growth rate and will dominate all other modes after a certain distance. Higher order modes can be obtained by using an orthogonalisation procedure to subtract contributions from lower order modes, while performing the propagation. Modal losses can be calculated by observing the attenuation on propagation, but the propagation distance required increases as the loss decreases, which makes it very inefficient for studying low-loss fibres. Both scalar and vector versions of the algorithm are available [139] and fibres of any geometry can be modelled.

2.3.6 Multipole method

More recently the Multipole Method (MM) has been also adapted to deal with MOF modelling [9, 140]. The multipole method is a multiple scattering technique, that regards

every inclusion or hole in the fibre cross section as a light scatterer.

The circular air-holes or cylinders are finite in number and can have an arbitrary diameter and a refractive-index different from that of the uniform material in which they are all embedded. The arrangement of cylinders and their host medium is enclosed within a circular jacket of arbitrary refractive-index. Complex refractive indices can be set in any subdomain of the MOF structure, thus allowing for material gain or absorption to be considered. The jacket surrounding the arrangement of cylinders has been introduced for a number of reasons. For the method to be mathematically rigorous, the fields of bound modes should be zero at infinity in order to ensure the square integrability of the fields on the transverse plane, and this is enforced by the jacket. Alternatively, using a complex refractive index for the jacket allows the confinement loss of the leaky mode to be estimated.

At the boundary of each inclusion two different fields can be distinguished, the first is transmitted through the boundary from beyond it, the second is reflected from the boundary itself and comes from all the other inclusions. Therefore, even though no actual sources or sinks of fields are present, the boundary of each inclusion in the microstructured optical fibre is effectively a source of radiating fields. The problem is to find a relation between all these fields that effectively results from multiple reflections at the boundaries of each inclusion (scatterer). The essential idea of the multipole method, is to define a field identity that relates the field incident on each inclusion to the fields scattered from all the other inclusions; this identity is named the *Rayleigh Identity* after Lord Rayleigh who proposed it for the first time. In summary, the method uses two different kinds of field expansions to represent the electromagnetic field. The first kind (local expansion) uses decompositions based on cylindrical harmonic functions localised in each of the circular holes; it is valid just outside each inclusion and expresses the field components that are incident on the inclusions and scattered away by the inclusions. The second kind of field expansion is valid throughout the different parts of the structure (i.e. inside the inclusions, outside the jacket and throughout the host uniform material). This second expansion (global expansion) is equal to the sum of all the field components scattered away by all the inclusions. At the boundary of each inclusion, the electromagnetic field must satisfy boundary conditions given by the Maxwell's equations. A relation between the coefficients of expansions defined on the opposite side of a boundary can therefore be found. The combination of local and global expansions finally results in a homogeneous system of algebraic equations. The system can be expressed in the form of a homogeneous matrix equation, $\boldsymbol{\mathcal{M}}\mathcal{B} = 0$, whose nontrivial solutions correspond to nonzero fields that exist without any exterior source of energy, in other words, propagating modes. The problem of finding the propagating modes is therefore reduced to finding the zeros of the determinant of the complex matrix $\boldsymbol{\mathcal{M}}$, as a function of the complex effective index $\mathrm{n_{eff}}$.

The method allows an accurate estimate of the confinement loss of leaky modes and, in contrast to any other numerical method, correctly predicts the fundamental mode degeneracy. The MM is generally quite efficient and its modelling accurate, in the sense that no approximation is introduced other than a truncation in the number of basis functions used for the field expansion. It has previously been successfully applied to two classes of microstructured optical fibres, both index-guiding HFs [90] and photonic bandgap fibres [141], to study their confinement loss, dispersive properties and modal cut-offs. The circularity of the inclusions however is central to the analytical formulation of the MM by White *et al.* [9] and it effectively reduces the range of structures that can be studied with it.

2.3.7 Source-model technique

The Source-model technique (SMT) is another general method for the solution of scattering problems. The mode field patterns in a propagation problem can be seen as nontrivial solutions to a scattering problems with vanishing excitations. Such solutions can exist if there is a transverse resonance, which can be found be seeking the singularities of a carefully constructed impedance matrix. An advantage of the SMT over the MM is that it can deal with structures of arbitrary cross-section. The method has been applied to the analysis of strictly bound modes in MOFs surrounded by an air jacket [142] and it has later been extended to the study of leaky modes in Ref. [143].

In the SMT, the electromagnetic field is approximated by a superposition of fields generated by fictitious electric and magnetic current filaments. These are suitably placed near the media interfaces of the fibre, on curves conformal to the boundary between the two media. A point-matching procedure is subsequently used to enforce the continuity conditions across the interfaces, leading to a homogeneous matrix equation. Nontrivial solutions to this equation yield the mode field patterns and propagation constants.

When the SMT is applied to problems of dielectric cylinders (intended here as inclusions of any possible transversal shape) immersed in a dielectric of a different refractive index, two sets of *fictitious elementary sources* are used to approximate the fields everywhere. One set is placed outside the cylinder, and the field it generates is used to approximate the field inside the cylinder; the other set is placed inside the cylinder, and the field it generates is used to approximate the field outside the cylinder. The elementary sources making up each set are placed in a homogeneous medium with the proper parameters; i.e. the sources placed outside the cylinder radiate in a homogeneous medium with the same parameters as the cylinder's medium, and the sources placed inside the cylinder radiate in a homogeneous medium with the same parameters as the medium surrounding the cylinder.

In general, the fields propagating in a homogeneous part of a cylindrical waveguide (cross section independent of z) can be expressed as a superposition of transverse-electric (TE) and transverse magnetic (TM) fields. The elementary sources used to simulate the TM part of the field are electric current filaments; the ones used to simulate the TE part of the field are magnetic current filaments. Both sets of sources run parallel to the waveguide.

The complex amplitudes of the sources are then adjusted for the continuity conditions at a set of *testing points*, uniformly distributed on the cylinder surface. Thus expressed, the fields automatically satisfy Maxwell's equations exactly and the continuity conditions approximately, the accuracy of the approximation increasing with the number of sources and testing points. The result is a homogeneous matrix equation, $[Z]\vec{I} = \vec{0}$, whose nontrivial solutions are employed to derive the dispersion curve and the mode field patterns. Here $[Z]$ is the impedance matrix and the source amplitude vector $\vec{I}$ is composed of a vertical concatenation of the amplitudes of all the sources. For a given frequency ω, the singularities of [Z] are to be found for values of β corresponding to guided modes.

2.3.8 Finite element method

The FEM is a very general technique for obtaining approximate solutions to those boundary-value problems of mathematical physics which are described by partial differential equations (PDEs). It originated from the needs for solving complex elasticity and structural analysis problems in civil and aeronautical engineering in the early 1950s and has since been generalised into a branch of applied mathematics for numerical modelling in a wide variety of engineering disciplines, including electromagnetism. In particular, it was recently applied to the study of MOFs in either a Beam Propagation Formulation [138], or in a mode solving formulation (see, for example Refs. [59, 144, 145]).

More details on the method itself will be presented in Section 2.4. Here it will just suffice to mention that the FEM operates by discretising the domain into a *mesh* of smaller, polygonal subdomains and by solving the original PDEs on each subdomain. Instead of approximating the PDEs as in the finite difference method, the FEM approximates their solutions. The decomposition in locally defined polynomials is conducted in such a way that the final fields are exact solutions of the Maxwell's equation on a finite number of points (in the most simple implementation located at the vertices of the mesh) and interpolated everywhere else. In order to improve the accuracy it is therefore sufficient to increase the mesh density. Denser meshes can be used only in structural regions – such as the core of a MOF – where the solutions change more rapidly, while lower-density meshes can be used elsewhere, to improve the computational efficiency. Absorbing boundary conditions can also be used to restrict the computational window. These are techniques well known for solving open region scattering and radiation problems. They introduce

an artificial absorbing boundary, which minimises back reflections for incoming waves of any possible wavelength and incidence angle. Furthermore the complex permittivity used in their definition allows confinement losses to be estimated.

2.3.9 Comparison and conclusion

In conclusion, a considerable number of numerical methods are currently available for the modelling of MOFs. At the beginning of this project, a comparison between the methods previously illustrated was conducted, with the aim of determining the most efficient and versatile numerical method to be used, in prevalence, during the course of my PhD for tackling the simulation of different MOFs. Accuracy of the method was, of course, one of the first prerequisites, while its efficiency was also rather important, in view of its application in inverse simulations (see Chapter 4). In addition, the following requirements were also identified as highly desirable for a versatile, multi-purpose method:

- *Full vector formulation*, in order to allow the study of fibres with arbitrary air-filling fractions and refractive index contrast;
- Direct inclusion of the wavelength dependence of the refractive index for more accurate dispersion calculations;
- Capacity to calculate *confinement losses*, which can have a profound relevance in the design of MOFs (see Section 1.2.5);
- Capacity to simulate *fibres with arbitrary cross section*, in order to model the properties of fabricated fibres from their SEM images and support or complement measurement results;
- *Symmetry exploitation*, in order to take advantage of any possible structural symmetry of the fibre to reduce the computational demand.

The main properties of the previously described methods are reported for comparison in Table 2.1:

As can be appreciated, all the methods analysed present a full vector formulation. The material dispersion cannot be included in the widely employed PWE implementation of Johnson *et al.* [129], although a modification of the method itself can be formulated to this aim [130, 131]. All other methods presents either an eigenvalue formulation, in which β is the eigenvalue and $\varepsilon(\omega)$ can be provided as an input, or a homogeneous matrix equation where, again, the solution – from which β can be derived – is found as a function of $\varepsilon(\omega)$.

	PWE	OFM	ABC-FDM	BPM	MM	SMT	FEM
Fully vectorial	√	√	√	√	√	√	√
Material disp.	× (√)	√	√	√	√	√	√
CL calculation	×	×	√	∼ √	√	√	√
Arbitrary cross-section	√	√	×[a]	√	×[b]	√	√
Symmetry exploitation	×	partial	partial	×	×	√	√
Ref.	[129]([131])	[134]	[136]	[146]	[9]	[143]	[144]

Limited to: [a] annular inclusions, [b] circular inclusions.

TABLE 2.1: Comparison between the principal numerical methods for the study of MOFs.

As was already mentioned, the CL can be evaluated by most methods except for the PWE and the OFM; the BPM can be rather inefficient for low-CL fibres.

All methods are generally suitable for the simulation of an arbitrary cross-section, with the exception of the ABC-FDM and the MM. These are limited, in their original formulation, to structures with annular or circular inclusions, respectively, even though the authors indicate that both techniques could be extended to include arbitrary inclusions. This can be done by combining the general features of the methods with numerical integrations of the overlap integrals for the ABC-FDM or with a more general code (e.g. FEM) solving for the scattering matrix of a single inclusion, in the case of the MM.

Finally, the FEM and the SMT are the only methods allowing the full exploitation of potential structural symmetries to reduce the physical computational domain. PEW, BPM and MM always require the full transverse structure to be simulated. A partial advantage can be gained from symmetries for the other two methods: in the OFM only even terms in the field expansion can be retained for symmetric structures. In the ABC-FDM the presence of radial symmetries are likely to allow for a reduction in the number of terms in the azimuthal Fourier decomposition.

In order to assess the accuracy of a particular method in solving for the fundamental or higher-order modes of MOFs, many comparisons among the various methods have been presented (see for example [136, 143]). A particularly interesting and rigourous comparison between four of the previous methods was recently reported by researchers of a consortium of Universities working within the framework of the European Science Foundation COST P11 [147]. Full vector PWE, OFM, FEM and SMT were applied to the study of the same fabricated birefringent HF from an SEM image of its cross-section. A convergence test on the accuracy of the effective index of the LP_{01}^{x} mode, indicated a convergence of n_{eff} to the sixth stable decimal digit for FEM and SMT, while

PWE and OFM were only stable up to the fourth/fifth digit. The residual differences in the value of n_{eff} between all these methods were lower than 4×10^{-4}. Moreover, since these discrepancies have a systematic character, they are further suppressed in the calculation of birefringence. A variation of between 0.1 and 1% was finally observed between the simulated values of GVD at 1550 nm. From the values reported, FEM and SMT, beside converging to a better precision, also seems generally quicker, even though a fair comparison of the computational time required was not entirely possible due to the use of machines with different CPUs.

From all of these considerations, the FEM and the SMT emerge as the most versatile and accurate methods for studying a vast range of MOFs. The SMT however was only proposed very recently, and it was not available at the beginning of this project, when the FEM was reputed to be the only method possessing all the desired requirements. For this reason the FEM was chosen as the preferred method to be developed and employed throughout the project.

Almost all the simulations reported in this thesis have been conducted with the FEM, for which we employed a commercial package, COMSOL MULTIPHYSICS™[1]. The next section will present an overview of the method, the details of its implementation for the study of out-of-plane electromagnetic propagation and the specific adaptations that were required in order to study MOFs.

2.4 Finite Element Method

2.4.1 Introduction

The FEM is a numerical method used to approximate an arbitrary boundary-value differential problem with a problem that has a finite number of unknown parameters and it is therefore solvable with standard methods from linear algebra. In this section a general overview of the method will be presented, followed by some comments on its application to the solution of electromagnetic propagation problems. Then issues specific to the chosen COMSOL MULTIPHYSICS™ implementation will be presented; the chapter will be closed by some convergence tests for the accuracy of the implemented method.

2.4.2 General overview

The FEM begins by casting the differential problem into an equivalent integral problem, which is more easily solvable with numeric techniques. In order to do this it employs

[1] www.comsol.com

a classical method for solving boundary-value problems: either the *Rayleigh-Ritz variational method* or the *Galerkin's method* of *weighted residuals*.

For example, suppose you want to solve the boundary-value problem defined by the inhomogeneous partial differential equation:

$$\mathcal{L}\phi = f \tag{2.7}$$

defined on a domain Ω and completed by some boundary conditions on the boundary Γ that encloses the domain. In Equation 2.7, $\mathcal{L}$ is a differential operator, f is the forcing function (typical for example of scattering or excitation problems where sources are present) and ϕ is the unknown solution. In the Rayleigh-Ritz method the solution of Equation 2.7 is sought by minimising the functional associated with the differential equation. In the Galerkin's method (GM), which leads to the same solution provided that $\mathcal{L}$ is self-adjoint [148], the solution is obtained by minimising an appropriately defined residual of the differential equation.

The GM works in the following way: assume that $\tilde{\phi}$ is an approximate solution of (2.7) which can be expanded as

$$\tilde{\phi} = \sum_{j=1}^{N} c_j v_j = \{c\}^T \{v\} \tag{2.8}$$

where the v_j are chosen expansion functions defined over the entire domain, c_j are the constant coefficients to be determined and $\{\cdot\}$ is a column vector. The substitution of $\tilde{\phi}$ for ϕ in (2.7) would result in a non-zero *residual*:

$$r = \mathcal{L}\tilde{\phi} - f \neq 0. \tag{2.9}$$

The solution of (2.7) can therefore be approximated by the search of $\tilde{\phi}$ which minimises r in Ω, in some mathematical sense. The problem at this point is that r is a continuous function of the entire infinite space ($r = r(\boldsymbol{r})$, $\boldsymbol{r} \in \Omega$); it is therefore a common approach to minimise instead a weighted integral of r, calculated over the entire domain Ω. Weighted residual methods define a number of those weighted residuals R_i, upon which the following condition is enforced:

$$R_i = \int_\Omega w_i r \, d\Omega = 0 \qquad i = 1, 2, 3, \ldots \tag{2.10}$$

where w_i are chosen weighting functions. In the particular case of the Galerkin method, the weighting functions are selected to be exactly the functions used in the expansion of the approximate solution, i.e. $w_i = v_i$ for $i = 1, 2, 3, \ldots, N$. Therefore Equation 2.10 becomes:

$$R_i = \sum_{j=1}^{N} c_j \int_\Omega v_i \mathcal{L} v_j \, d\Omega - \int_\Omega v_i f \, d\Omega = 0 \qquad i = 1, 2, 3, \ldots, N. \tag{2.11}$$

This can be written as the matrix equation

$$[S]\{c\} = \{b\} \tag{2.12}$$

where $\{c\}$ is the vector of the unknown coefficients, $[S]$ is an $N \times N$ matrix with elements

$$S_{ij} = \int_\Omega v_i \mathcal{L} v_j \, d\Omega \tag{2.13}$$

and the column vector $\{b\}$ is composed by

$$b_i = \int_\Omega v_i f \, d\Omega. \tag{2.14}$$

So far we have simply transformed the original differential problem (2.7) with an infinite number of degrees of freedom (DOFs) into a linear system of integral equations with a finite number of DOFs. Nothing so far has been said about the expansion or *interpolating* functions v_j. Generally the selection of a complete set of v_j, defined over the entire domain and in such a way they can satisfy the boundary conditions, can be extremely difficult, if not impossible. To alleviate this difficulty, in the FEM, the domain Ω is divided into smaller subdomains or *finite elements* which, in the case of two-dimensional problems usually assume the shape of triangles and for three-dimensional problems that of tetrahedrons. The interpolating functions are then defined only locally, over each subdomain (*local shape functions*), in such a way that they are identically zero outside it. Since the subdomains are small, the local functions do not need to vary in a complicated manner to approximate $\phi(\boldsymbol{r})$ accurately: such trial functions are usually much simpler than the globally-defined functions used in other methods.

Without entering into the details of the method (for which the reader is pointed to the book by Jin [148]) here we will just add a few considerations:

- In the simpler FEM formulations, based on *nodal elements*, the local shape functions are chosen as simple polynomials. For example in 2D these take the form of $N_i(x, y) = ax + by + c$ for a linear case or $N_i(x, y) = ax^2 + by^2 + cxy + dx + ey + f$ for the quadratic case. For each triangle a number of 3 and 6 nodal points – or DOFs – respectively is therefore required. Increasing the order of the polynomial improves the overall accuracy at the expense of the computational time;
- By employing locally defined functions N_i the integral in (2.13) can be expressed as a sum of many integrals, each of which operates only on a single subdomain Ω_e:

$$S_{ij} = \sum_e \int_{\Omega_e} N_i \mathcal{L} N_j \, d\Omega_e. \tag{2.15}$$

  Each integral will now comprise the product of local shape functions and/or their derivatives, depending on the specific form of the differential operator $\mathcal{L}$. By a

careful choice of the N_i, each integral can be solved analytically, transformed into a sum of rational functions and stored for a subsequent quick evaluation. The elements of $[S]$ can therefore be easily obtained by the combination or *assembly* of the local integrals. Before the system of equations is ready to be solved the boundary conditions can be also simply imposed, directly on the elements of the matrix;

- The initial differential problem has been thus transformed into the linear algebraic system (2.12), where the size of $[S]$ is DOF×DOF. With DOF typically on the order of 100,000 or more, it is easy to understand why the FEM requires the largest amount of memory amongst the various numerical methods, as was observed in the comparison in Ref. [147];

- In current computers however, memory is generally not the limiting factor. Moreover, from the choice of employing local functions which are zero outside the subdomain where they are defined, all the elements S_{ij} for which i and j belong to different subdomains are identically zero. The matrix $[S]$ is therefore *sparse* – or mainly composed by zero elements – and numerical procedures optimised for solving Equation 2.12 for sparse matrices can be exploited, reducing considerably the time and memory requirements;

- Recent FEM formulations can employ more complicated shape functions, either based on *vector* or *edge elements* or on a combination of (hybrid) edge and nodal elements [149]. The latter is the formulation that will be employed throughout this thesis. Although the specific form of the local integrals is more complicated, the general FEM procedure highlighted above remains unaltered. These vector elements provide at least two advantages over conventional nodal implementations: they allow the elimination of *spurious solutions* (see [148] for more details) and automatically enforce the field continuity at the interface between media with different permittivity (see the next Section).

2.4.3 Application to electromagnetic propagation

In the previous Section a brief and general introduction to the FEM has been presented. Here it will be shown how the method can be applied to the study of the electromagnetic propagation in a microstructured fibre.

In Section 2.2 the curl-curl equation (2.5) for the three components of the magnetic field was derived from Maxwell's equations. This, or a similar formulation for only the two transverse components, is the master equation which is generally solved by all numerical methods described in Section 2.3. The magnetic field is chosen because in nonmagnetic media it is continuous everywhere, and continuity conditions at the interfaces need not to be included (in contrast to formulations solving for the electric field). This restriction

however does not apply for the FEM based on edge elements: here one can in principle employ also the electric field $\boldsymbol{\mathcal{E}}$ as a working variable. From the system (2.4) the following curl-curl equation can be obtained:

$$\nabla \times \nabla \times \boldsymbol{\mathcal{E}} = \omega^2 \mu \varepsilon \boldsymbol{\mathcal{E}} \quad \text{in} \quad \Omega \tag{2.16}$$

which, together with the boundary conditions

$$\hat{n} \times \boldsymbol{\mathcal{E}} = 0 \quad \text{in} \quad \Gamma_{\text{el}} \tag{2.17}$$

$$\hat{n} \times (\nabla \times \boldsymbol{\mathcal{E}}) = 0 \quad \text{in} \quad \Gamma_{\text{mag}} \tag{2.18}$$

form the boundary-value problem to be solved. Equation 2.17 represents general Dirichelet boundary conditions while Equation 2.18 represents Neumann conditions. By splitting the field into transverse and longitudinal components and introducing the typical z-dependence of longitudinally-invariant structures, so that

$$\boldsymbol{\mathcal{E}}(x, y, z) = [\boldsymbol{E}_\perp(x, y) + \hat{\boldsymbol{z}} E_z(x, y)] \cdot e^{-j\beta z} \tag{2.19}$$

Equation 2.16 can be recast into an eigenvalue form for the propagation constant β:

$$\begin{bmatrix} \nabla_\perp \times \nabla_\perp \times - k_0^2 n^2(\boldsymbol{r}) & 0 \\ 0 & 0 \end{bmatrix} \begin{bmatrix} \boldsymbol{E}_\perp \\ E_z \end{bmatrix} = -\beta^2 \begin{bmatrix} 1 & \nabla_\perp \\ \nabla_\perp & \nabla^2 + k_0^2 n^2(\boldsymbol{r}) \end{bmatrix} \begin{bmatrix} \boldsymbol{E}_\perp \\ E_z \end{bmatrix} \tag{2.20}$$

where $k_0 = \omega/c = \omega/\sqrt{\varepsilon_0 \mu_0}$, $\mu = \mu_0 \mu_r = \mu_0$ and $\varepsilon(\boldsymbol{r}) = \varepsilon_0 \varepsilon_r(\boldsymbol{r}) = \varepsilon_0 n^2(\boldsymbol{r})$.

By employing Galerkin's method and the finite element decomposition discussed in the previous Section, this can be transformed into the following generalised eigenvalue equation for sparse matrices and for the eigenvalue $\lambda = -\beta^2$:

$$[A]\{\phi\} = \lambda [B]\{\phi\} \tag{2.21}$$

The majority of the eigensolvers that can be applied to the solution of this equation are restricted to finding *extremal* eigenvalues. However in the study of MOFs, and in particular of hollow-core PBGFs, the solutions of interest often correspond to *interior* eigenvalues. Ideally, one would like to compute, for example, only the defect modes in the band gap, without the waste of computation and memory in finding all the modes above them.

A shift-and-invert matrix transformation can be used to enable the access to a desired portion of the spectrum of eigenvalues. If $(\{\phi\}, \lambda)$ is an eigenpair for ([A],[B]) and $\sigma \neq \lambda$, then (2.21) is equivalent to

$$[C]\{\phi\} = ([A] - \sigma[B])^{-1}[B]\{\phi\} = \frac{1}{\lambda - \sigma}\{\phi\}. \tag{2.22}$$

Finding the eigenvalues closest to the shift σ is equivalent to computing the largest eigenvalues of the matrix $[C] = ([A] - \sigma[B])^{-1}[B]$. The eigenvectors of the transformed system are identical to those of the original one.

Among the most widely employed solvers for this eigenproblem is the *implicitly restarted Arnoldi method* implemented in ARPACK[2]. To locate the largest eigenvalues of $[C]$ the ARPACK routines must perform several matrix-vector multiplications $[C]\{\phi\}$ for arbitrary vectors $\{\phi\}$, and therefore require the results of $([A] - \sigma[B])^{-1}[B]\{\phi\}$. This can be obtained from the solution of the linear system

$$([A] - \sigma[B])\{\psi\} = [B]\{\phi\} \tag{2.23}$$

for the vector $\{\psi\}$, given $\{\phi\}$.

Many methods are available to solve the system, but they can all be categorised into two groups: *direct* and *iterative* methods. The direct methods are usually based on Gaussian elimination and theoretically yield an exact solution to the system. In contrast, iterative methods start with an initial guess and then minimise the residual error through iterations. Usually they produce an approximate solution with a prescribed accuracy.

In conclusion, we have seen how the original boundary value problem can be reduced to the solution of a number of linear systems: Equation 2.23 allows the determination of the interior eigenvalues and eigenvectors of (2.21) through the use of ARPACK routines and of Equation 2.22. The next Section will discuss some implementation details of the FEM employed in this thesis.

2.4.4 Implementation

In order to focus on the application of the numerical simulations, rather than on the implementation of the solver itself, it was decided, at the beginning of the project, to opt for a commercially available implementation of the FEM. This allowed us to rely on external competence for the continuous update of the libraries of numerical subroutines and for the incorporation of the latest development in terms of solver algorithms, which would otherwise require the dedication of a large amount of time.

After a number of comparative tests on accuracy and computational time with alternative numerical solvers which were available at the ORC (Multipole Method, Orthogonal Function Method, Beam Propagation Method and Plane Wave Expansion Method), it was concluded that COMSOL MULTIPHYSICS™ would provide an excellent solution, combining the advantages of the FEM (see Section 2.3) with a flexible and versatile platform.

[2] `http://www.caam.rice.edu/software/ARPACK/`

COMSOL MULTIPHYSICS™ is a commercial implementation of the FEM, allowing the application of the method to a vast range of engineering problems, including acoustics, fluid dynamics, structural mechanics and electromagnetic problems. The software contains many physical models of interest (including the full vectorial Equation 2.5 or 2.16) and presents an integrated CAD for structural design, a mesh generator, an internal matrix assembler, various state-of-the-art numerical solvers for sparse matrices and several postprocessing features.

Despite all these characteristics, though, COMSOL MULTIPHYSICS™ is a general tool, not optimised for simulating electromagnetic propagation in MOFs. Its CAD interface, for example, can be useful and intuitive to use in certain circumstances, but it certainly is not adequate for frequent structural changes such as those required by an inverse design procedure. Besides the CAD however, the software also presents a `Matlab` scripting interface which allows full control of the various modelling phases. Therefore, a number of `Matlab` scripts allowing the automatic definition of the structure, the imposition of physical and boundary parameters, meshing and simulation of a vast range of MOFs have been developed, implemented and used throughout the project.

The principal steps to simulate the optical behaviour of a MOF are discussed in the following and are illustrated in Figure 2.1, by means of a simple example concerning a 5 ring index guiding holey fibre. Note that symmetry considerations allow the use of a $\pi/2$ minimum sector for the study of the fundamental mode (see Section 1.2.3).

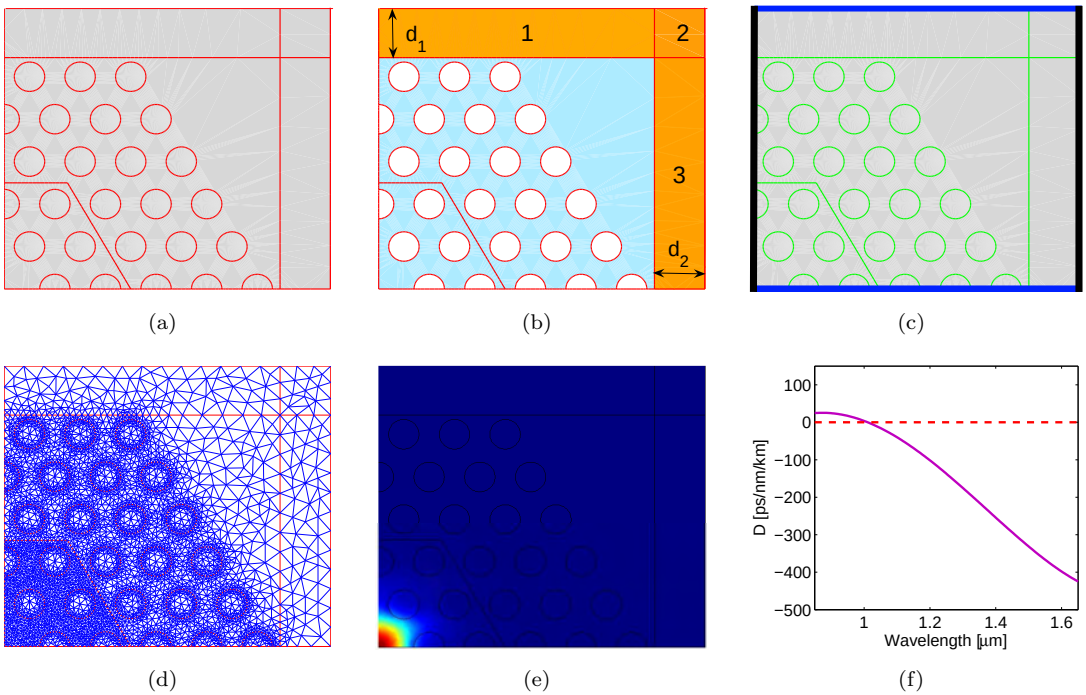

(a) (b) (c)

(d) (e) (f)

FIGURE 2.1: Example of an FEM simulation: (a) structural design; (b) subdomain definition; (c) setting of the boundary conditions; (d) mesh generation; (e) post-plotting; (f) calculation of the dispersion curve.

1. **Geometrical definition.** The first step is to define the transverse structure of the fibre. Depending on the fibre's symmetry, a smaller sector may be considered ($\pi/2$ in this example), reducing the calculation domain without loosing any information. For some studies however, such as those analysing many higher order modes, studying the full structure may be more convenient. In both cases the script automatically draws the inclusions with the required shape (here circular, with the same diameter d), and positions them on the desired lattice (here triangular, with constant pitch Λ). Note that, for the fibre in the example, the core is represented by a missing hole in the middle (shown in the bottom left corner). Alternatively, the contour of the cross section of a real fibre can be extracted from an SEM image; then it can be interpolated with splines and used as the structure to simulate. The boundaries of the Perfectly Matching Layers (PML), used to avoid reflections from the outer boundaries and emulate an infinite structure with a finite domain, also need to be drawn at this stage. Depending on the formulation, either square [as in Figure 2.1(a)] or circular shapes can be employed.

2. **Subdomain setting.** Next, the physical properties of the material in each subdomain need to be set. The white holes in Figure 2.1(b) indicate the air region (refractive index equal to 1), while the cyan region corresponds to glass, whose refractive index can be set as function of frequency using the Sellmeier equation [6]:

$$n^2(\omega) = 1 + \sum_{j=1}^{m} \frac{B_j\,\omega_j^2}{\omega_j^2 - \omega^2} \tag{2.24}$$

where the m resonant frequencies ω_j and the strength of their resonances B_j depend on the glass.

The external, orange layers are the *Perfectly Matched Layers* (PMLs) introduced to limit the computational domain. PMLs are absorbing layers, specifically designed to introduce no reflections for any angle of incidence, polarisation or frequency of the incoming electromagnetic radiation, and are therefore perfectly suited to surround the simulation area. Their original concept was introduced by Berenger in 1994 [150], even though in that first definition they required the local modification of Maxwell's equations. Shortly after, Sacks *et al.* demonstrated that the same absorbing and reflectionless behaviour could be achieved without modifying Maxwell's equations, provided that the material was appropriately defined as anisotropic and complex [151]. This approach was much more easily implemented into standard numerical methods and immediately gained much popularity.

Here the formulation for square PMLs surrounding the $\pi/2$ sector of Figure 2.1(b) is presented. A similar formulation for the layers surrounding the full cross-section can be found in Ref. [152], while alternative definitions for circular and spherical PMLs are presented in Ref. [153, 154].

According to Sacks, the PMLs are defined as anisotropic materials, whose permittivity and permeability diagonal tensors are [151]:

$$[\varepsilon] = \varepsilon_0 n^2 [\Lambda] \quad \text{and} \quad [\mu] = \mu_0 [\Lambda] \tag{2.25}$$

with

$$\Lambda = \begin{bmatrix} s_y/s_x & 0 & 0 \\ 0 & s_x/s_y & 0 \\ 0 & 0 & s_x s_y \end{bmatrix} \tag{2.26}$$

where ε_0 and μ_0 are the permittivity and permeability of free space, n is the refractive index of the adjacent region and the PML parameters s_x and s_y are defined in Table 2.2 for region 1, 2 and 3 [see Figure 2.1(b)].

PML parameter	PML region 1	2	3
s_x	1	s_2	s_2
s_y	s_1	s_1	1

TABLE 2.2: PML parameters

Here s_i (i = 1,2) must be a complex number, the real part of which attenuates potential evanescent waves, while the imaginary part is effective in damping the propagating waves. In many studies (including the present one) the imaginary part is modelled by a polynomially increasing profile, so that

$$s_i = b + j a_{max} \left(\frac{\rho}{d_i} \right)^{\alpha} \qquad i = 1, 2 \tag{2.27}$$

where ρ is the distance from the beginning of the PML, d_i is the PML width in the horizontal or vertical direction, b, a_{max} and α are PML free-parameters. After a number of tests and according to a frequent convention in preceding studies it was decided to fix a parabolic profile ($\alpha = 2$) with $b = 1$ for all simulations. A number of convergence tests on the best value of a_{max} were also conducted; these are reported in Section 2.4.5.

3. **Boundary setting.** The physical properties of all boundaries of the simulation domain then have to be set. The boundary condition (BC) at an edge outside the PML is generally irrelevant, as the field at that point has been attenuated to a negligible level. Therefore the BCs for a full-structure simulation can be set arbitrarily. In contrast, if a smaller minimum sector is employed, the particular BC applied at the boundaries without PMLs allows one to distinguish between the various mode classes sharing the same sector (Section 1.2.3). For example, since the fundamental degenerate modes of hexagonal HFs belong to classes $p = 3$ and 4 of the original McIsaac's definition [8], they can be distinguished by imposing,

at the bottom and left sides of the $\pi/2$ domain, either a perfectly electric – perfectly magnetic (PE-PM) boundary condition or a (PM-PE) boundary condition, respectively. PE and PM boundary conditions are indicated in blue and black in Figure 2.1(c). A different combination of BCs may be needed in order to study higher order modes that belong to a different symmetry class. However note that, on the $\pi/2$ sector which is compatible with the definition of square PMLs, each combination of BCs allows two symmetry classes to be studied at the same time, as reported in Table 2.3.

BC	p
(PE-PM)	4 and 8
(PM-PE)	3 and 7
(PE-PE)	6 and 2
(PM-PM)	5 and 1

TABLE 2.3: Mode classes that can be studied on a $\pi/2$ sector by applying given BCs to the (bottom, right) edge.

Internal boundaries between subdomains (in green in Figure 2.1(c)) need, in COMSOL MULTIPHYSICS™, to be assigned the 'internal boundary' condition, which guarantees the continuity of both Displacement and Magnetic fields at the interfaces. The scripts implemented automatically assign the desired BC to all the triangles lying at edges of the structure.

4. **Meshing.** Several mesh parameters can be adjusted, ultimately determining both accuracy of the solution and calculation time. As a general rule, a large number of triangles need to be positioned both around curved boundaries, in order to accurately define their shape, and where high accuracy is needed (e.g. where the field is more concentrated or where it changes more rapidly). An example is provided in Figure 2.1(d) where an inner hexagonal zone has been defined around the core with the only purpose of allowing a denser mesh. Generally a mesh convergence test is required in order to ensure that the structure has been properly meshed, and to minimise the related numerical errors (see Section 2.4.5).

5. **Solving.** As was mentioned in the previous section, ARPACK is the solver used by COMSOL MULTIPHYSICS™ for all eigenvalue problems. A choice of linear solvers is however available, enabling both direct and iterative approaches to be selected. All solvers have been tested on a number of simulations, and in conclusion the direct solver UMFPACK[3] was found to be the one generally providing the fastest solution. UMFPACK is a set of routines for solving unsymmetric sparse linear systems, in the form $[A]\{x\} = \{b\}$, using the Unsymmetric Multifrontal method.

[3] `http://www.cise.ufl.edu/research/sparse/umfpack/`

Once the solvers have been chosen, various parameters need to be defined. Among the most important are the guess for the eigenvalue (σ) and the number of eigenvalues to be calculated around this value. This is a critical choice, often requiring some knowledge of the structure to be simulated.

The scripts implemented during this project, are generally able to select automatically the desired mode of the structure, among the numerous solutions calculated. This can be done by exploiting symmetries and BCs, together with several possible additional criteria. For index guiding fibres, for example, the confinement loss is a good criterion for selecting the fundamental mode (for which it is generally the lowest); for hollow-core photonic bandgap fibres, a better indication is generally provided by the percentage of power in the core. Other rules can be set in order to recognise, without the need for manual intervention, cladding modes or surface modes.

6. **Postprocessing.** Once the eigenvalues and eigenvectors have been calculated, several postprocessing functions are available, for example for plotting or integrating the eigensolution on specific edges or subdomains, directly from the values it assumes on the FEM mesh. Figure 2.1(e) shows, for example, intensity levels of the Poynting vector of the fundamental mode of the fibre. At this stage it is possible to calculate the principal properties of the desired mode such as effective area, confinement loss, percentage of field in a given domain, etc. (see Section 1.2).

   As already observed, the main advantage of the scripting approach employed, as opposed to the manual use of the CAD, is that loops can be implemented easily. This can be used, for example, in order to scan the behaviour of the structure at different wavelengths and obtain dispersion curves (Figure 2.1(f)), or to perform convergence tests for the mesh or PML parameters, as will be reported in the next section.

2.4.5 Accuracy

In order to validate the method, a number of convergence tests were run for the main free-parameters of the algorithm: the size of the finite element mesh and the PML parameters. As was mentioned in the previous Section, it is generally a widespread practice to fix $\alpha = 2$ and $b = 1$ in the PMLs (see for example Ref. [152]). Therefore the parameters whose convergence will be analysed in the following are the maximum value of the imaginary part of s_i, a_{max}, and the size of the finite element mesh.

The general practice to validate a numerical method would be to test its results against a known analytical result. However as has been previously observed, no analytical results are available for MOFs; furthermore comparisons with the analytical solution of, for example, a step index fibre would be inadequate for testing the imaginary part

of the propagation constant. It has become a common practice therefore, to validate a numerical code by comparison with the results obtained with the method which is recognised as the most accurate for MOF modelling: the multipole method. The most employed 'benchmark' for such comparisons is typically the fibre with a single ring of 6 equally spaced holes studied at $\lambda = 1.45$ μm by White *et al.* [9] and presenting $\Lambda = 6.75$ μm and $d = 5$ μm. The silica refractive index is assumed to be $n = 1.45$.

Figure 2.2 compares the effective index calculated by the MM (n_{eff}= $1.445395345 + j\,3.150 \times 10^{-8}$) with the results obtained with the FEM for increasing values of a_{max}. A $\pi/2$ sector with BCs for the $p = 4$ mode, and a mesh of 28328 triangles (56907 DOFs), denser in the core, have been used for the FEM. The real part of n_{eff} is almost unaffected

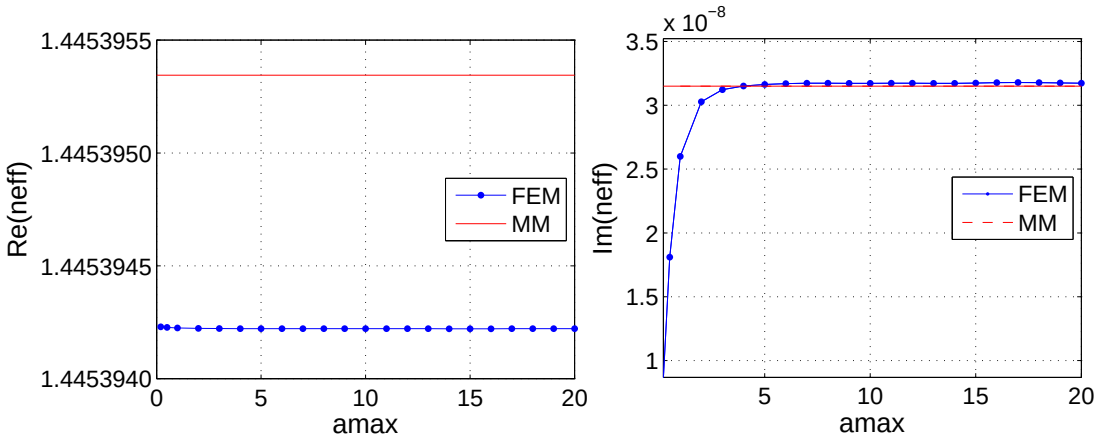

FIGURE 2.2: Effective index dependence on a_{max} for the fundamental mode of the fibre studied in [9], calculated with the FEM (blue); the MM result is shown in red for comparison.

by the change of α, while a good convergence of $\Im m(n_{eff})$ is observed for α larger than 5. A value of $\alpha = 10$ will be therefore employed for all future simulations.

The n_{eff} convergence as a function of mesh density is shown in Figure 2.3 for the same fibre and with $\alpha = 10$. Both $\Re e(n_{eff})$ and $\Im m(n_{eff})$ are affected by an increase in the number of points, but for a number of triangles greater than ~40000 they both seem to have converged to a stable value. For this converged value the difference in the real part of n_{eff} between the two methods lies in the 6^{th} significant digit ($\sim 1 \times 10^{-6}$), while the error in the imaginary part is around 1×10^{-10}, corresponding to a variation of less than 1% in the calculated confinement loss.

Finally, for an additional confirmation of the good agreement between the two methods, a comparison between the first ten modes of the fibre (see Figure 2.4), calculated with the FEM and with the MM is shown in Table 2.4. Note that, while the MM is able to correctly predict the modal degeneracy, due to the use of local cylindrical coordinates centred about each hole, in the FEM a small false birefringence is observed for the modes in class $p = 3, 4$ and $p = 5, 6$. This 'numerical birefringence' is intrinsic in the FEM procedure, where the generated meshes do not reflect the symmetries in the structure;

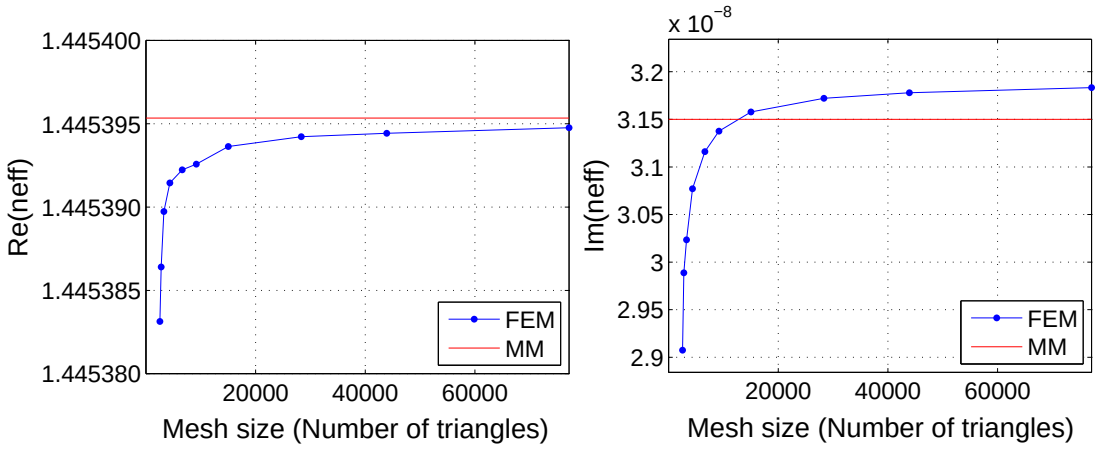

FIGURE 2.3: Effective index dependence on the mesh size for the fundamental mode of the fibre studied in [9], calculated with the FEM (blue); the MM result is shown in red for comparison.

FEM		Class	MM		Class
$\Re e(n_{eff})$	$\Im m(n_{eff})$	p	$\Re e(n_{eff})$	$\Im m(n_{eff})$	p
1.44539443	3.172×10^{-8}	4	1.445395345	3.150×10^{-8}	3,4
1.44539422	3.181×10^{-8}	3			
1.43857915	5.352×10^{-7}	2	1.438585801	4.986×10^{-7}	2
1.43844140	9.666×10^{-7}	6	1.438445842	9.929×10^{-7}	5,6
1.43844094	9.659×10^{-7}	5			
1.43836265	1.400×10^{-6}	1	1.438366726	1.374×10^{-6}	1
1.43038897	2.135×10^{-5}	8	1.430175	2.220×10^{-5}	8
1.42994844	1.577×10^{-5}	4	1.4299694	1.577×10^{-5}	3,4
1.42994834	1.578×10^{-5}	3			
1.42925107	8.796×10^{-6}	7	1.429255296	9.337×10^{-6}	7

TABLE 2.4: n_{eff} of the first 10 modes of the fibre in Ref. [9]: comparison between FEM and MM.

however for the mesh considered here (28328 elements) it is already as small as 1 to 5×10^{-7}, and it can be further reduced by increasing the mesh size [144].

An agreement in excess of 1×10^{-5} is generally observed for $\Re e(n_{eff})$ for all solutions other than for the seventh eigenvalue, for which it is considerably larger. By analysing the results of a similar comparison between SMT and MM [143] though, a similar discrepancy for the same eigenvalue emerges. In this case the result of the SMT ($\Re e(n_{eff})$= 1.430408204) is much closer to the FEM result; this seems to suggest a possible unintentional error in the determination of the eigenvalue for the MM method. The order of magnitude of $\Im m(n_{eff})$ agrees in all cases, and the errors in its significant digits are in the order of a few percent. The level of accuracy found for our implementation of the FEM is therefore in line with that of other numerical methods. For all the studies reported in this thesis it is well above the accuracy that can be obtained in practice when modelling fabricated fibres.

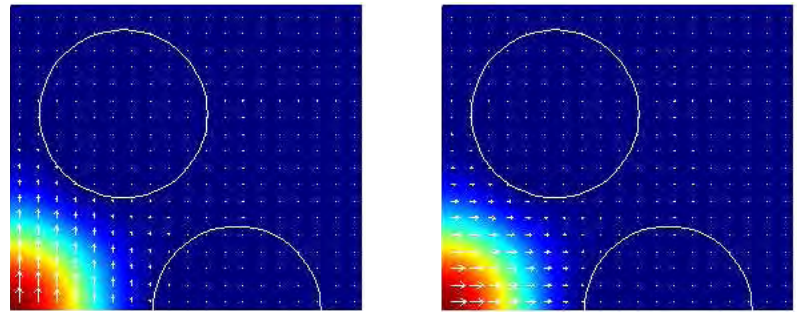

(a) $p = 4$

(b) $p = 3$

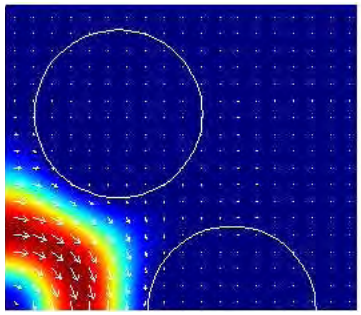

(c) $p = 2$

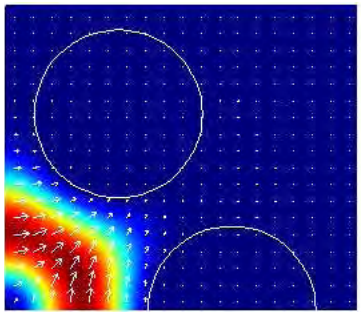

(d) $p = 6$

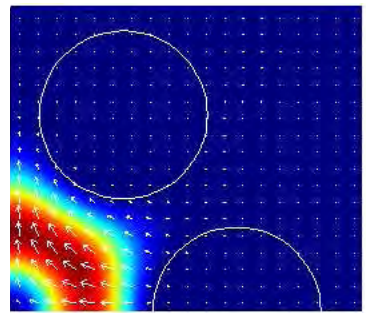

(e) $p = 5$

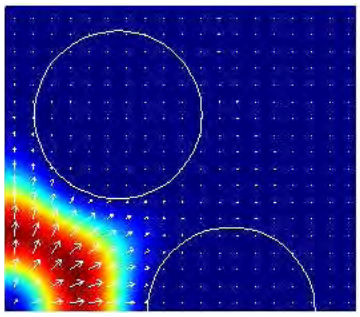

(f) $p = 1$

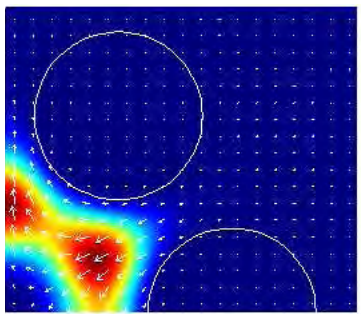

(g) $p = 8$

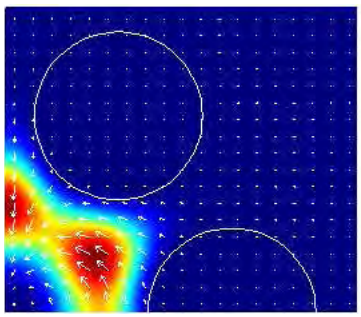

(h) $p = 4$

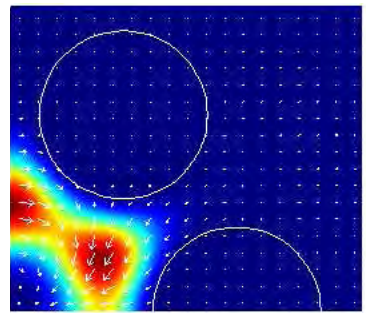

(i) $p = 3$

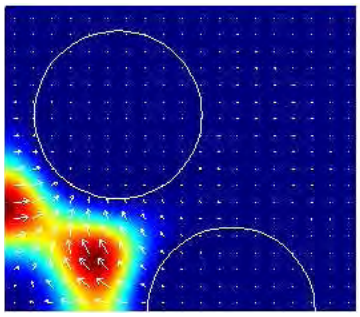

(j) $p = 7$

FIGURE 2.4: Poynting vector and vector plots of the transverse electric field of the first 10 modes of the fibre studied in [9]. The n_{eff} of the modes is show in Table 2.4.

2.5 Conclusion

In this chapter the general theoretical framework of equations that need to be solved in order to study electromagnetic propagation in MOFs have been introduced. The main issues in the MOF modelling have been presented, together with the principal numerical solvers that have been proposed so far. The FEM has emerged as one of the most complete methods for the efficient and accurate modelling of a vast range of MOFs. Therefore a dedicated effort was made, during this thesis, to adapt a standard FEM package to the harmonic analysis of high frequency electromagnetic waves for the study of both index guiding and photonic bandgap guiding fibres. Some details on the typical procedure employed to model a fibre with COMSOL MULTIPHYSICS™ have been presented, and the scripting approach developed was introduced. The number and variety of studies that were undertaken and successfully completed during this thesis using the FEM, and the accuracy of the results, verified by comparisons with the MM and with experiments, have convinced other researchers at the ORC to adopt the FEM, which has now become the preferred tool for the design of MOFs. The efficiency of the method, which allows simulations that required days of computation time with the OFM to take place in minutes or at most hours, has also permitted the implementation of proper inverse design techniques, which will be extensively reported in Chapter 4.

The next two parts of this thesis will report on the results obtained from the application of the FEM to the study of index guiding fibres (Part II) and photonic bandgap guiding fibres (Part III).

Part II

Index Guiding Fibres

Chapter 3

Fibre design using optical property maps

3.1 Introduction

The large refractive index contrast between glass and air in a microstructured optical fibre and the vast choice of possible fibre designs allow for a broad range of optical properties to be achieved. Being able to condense the achievable values of a given property or set of properties onto a single map for all the possible structural parameters would provide the fibre designer with an invaluable tool in the design of new fibres. A very useful way to condense the achievable range of variation of many optical properties on a single plot is to overlap the contour maps of each property. This visual method, although very powerful, can only be applied when the number of design parameters is limited to 2 or at most 3, each one to be plotted on one axis of a bidimensional rectangular or triangular map. Only two free-parameters are present in hexagonally stacked holey fibres (HFs) with equal hole size, where the pitch Λ and the hole size d are sufficient to completely describe the fibres, and therefore these fibres are perfectly suited to be studied by means of optical maps.

This mapping technique has already been successfully applied to analyse the bend loss properties of large mode area fibres [155]. In this chapter the technique is extended to the study of additional optical properties of HFs, such as dispersion, dispersion slope and effective index, and it is applied to a range of very practical design problems. The chapter is organised in the following way: in Section 3.2 the optical maps are employed to study whether HFs have the potential to replace conventional fibres in telecom applications; Section 3.3 shows how an optical map can be used to inverse-design a fibre optimised for supercontinuum generation around a wavelength of 1 μm; while in Section 3.4 three maps are presented, representing the main properties of HFs made with different glasses,

and they are employed to design tapered paths allowing a potential reduction of the undesired stimulated Brillouin scattering.

3.2 Fibres for telecom applications

Since their first introduction by Knight *et al.* in 1996 [2], holey fibres (HFs) have created a lot of interest in the telecommunication field. These new fibres possessed unique optical properties such as endlessly single mode guidance [58], and appeared to enable the achievement of dispersion and mode field diameters not otherwise possible in conventional step index fibres (SIFs) [64]. Moreover, and probably most importantly, due to their single material composition, they hold promise for even lower attenuation losses than conventional germanium-doped SIFs. For this reason, most of the initial studies were focused on the reduction of the attenuation loss. Thanks to inputs from many research groups around the world and to some pioneering work from telecom companies such as the Nippon Telegraph & Telephone Corporation (NTT), the fabrication technology was dramatically improved and, in the space of only 4 years, losses were reduced by nearly 3 orders of magnitude, from 0.24 dB/m [156] to the current record of 0.28 dB/km [24]. This extraordinary improvement was mainly made possible by the use of high purity silica glasses made from the vapour phase axial deposition (VAD) technique [157], by the introduction of polishing processes to reduce the internal hole roughness, by the reduction of OH contamination, and by the careful use of designs that minimised the confinement loss. After the initial excitement though, it became clear that a loss reduction beyond the level of conventional fibres would not be so easily achieved, due to an additional intrinsic loss contribution caused by scattering at the air-silica interfaces [158].

Once the losses were reduced to a level at least comparable to conventional fibres, and the capability of reproducibly drawing long fibre lengths, in excess of 100 km, was demonstrated [159], the research focus shifted to the control of other optical properties, essential for dense wavelength division multiplexing (DWDM) data transmission: the fibre dispersion, dispersion slope and nonlinearity. An obvious advantage possessed by HFs over SIFs was their endlessly single mode guidance, which might open up wider transmission bandwidths [160]; however, in terms of attenuation, the conventional technology still had the lead. The next question to answer was therefore whether the HFs could compete with SIFs or outperform them in terms of dispersion and effective area characteristics, and if that could be achieved in all application areas, or at at least in a few, specific ones.

One of the first low-loss HFs ever reported (HF1, [161]) presented a dispersion of 76 ps/nm/km and an effective area of $\sim$17 μm^2 at 1550 nm. For a comparison the Corning SMF-28, a workhorse amongst SIFs and still one of the most employed fibres for telecoms

transmission, presents D = 17 ps/nm/km and $A_{eff} \simeq 80$ μm^2, thus outperforming HF1 both in terms of its linear and nonlinear performance. Subsequent low-loss HFs presented improvements in both aspects, even though they could still not compete with SIFs: HF2 [160] and HF3 [159] presented a dispersion of 36 and 33 ps/nm/km, and an effective area of 38 and 50 μm^2 respectively. Almost at the same time another fibre (HF4, [162]), reported by Nielsen *et al.*, eventually showed that, with a careful choice of the fabrication parameters, some properties of standard SIFs could even be improved: despite a quite large dispersion, 27 ps/nm/km, and a loss of 0.48 dB/km the fibre had an effective area of 130 μm^2.

All these fibres have been fabricated through hexagonal stacking and therefore can ultimately be described by using only 2 parameters, the hole-to-hole distance Λ and the relative hole size d/Λ. This suggested to us the possibility of mapping the optical properties of this family of fibres as a function of only these two free parameters. By overlapping contour plots relating to different optical properties, a very concise optical property map can be obtained, presenting a visual and very effective way of summarising the range of achievable optical properties and highlighting structural areas of technological interest.

An example of such a map is presented in Figure 3.1, showing the A_{eff} contour plots for an HF with Λ between 1 and 10 μm and d/Λ between 0.2 and 0.8. Fibres in this range present effective areas between <10 μm^2 (too highly nonlinear for multichannel data transmission) and >200 μm^2 (for which the bending loss starts to become an issue) and thus cover, almost entirely, the parameter-space relevant to telecom applications. A few relevant dispersion contours are also shown with red lines (circle markers), while the dispersion slope contours are shown in green (with triangular markers). The boundary line separating the single mode (SM) from the multimode (MM) regime, according to Ref. [62], is shown in orange[1]. The fabricated low-loss fibres previously mentioned (HF1, HF2, HF3 and HF4) are also shown on the map, and their main properties are reported in Table 3.1, together with the reference SMF-28 fibre and with additional holey fibres which will be discussed in the following.

The map was calculated for 8-ring HFs on a grid of 13 equally spaced d/Λ-points and 23 Λ-points, unequally spaced and denser in the 1-4 μm region, where both D and D_{slope} present the steepest behaviour. Due to the relatively smooth behaviour of the functions plotted, this grid size and the 2D spline interpolation between the discrete calculated values guarantee that the accuracy of each point on the map is equal to or better than the fabrication tolerances of these fibres.

The map allows a few conclusions to be drawn:

[1]Single modality is rather essential to eliminate intermodal dispersion in multichannel telecoms transmission. For hexagonally stacked HFs the cut-off condition after which the first higher-order mode effectively vanishes is reported in Equation 1.4

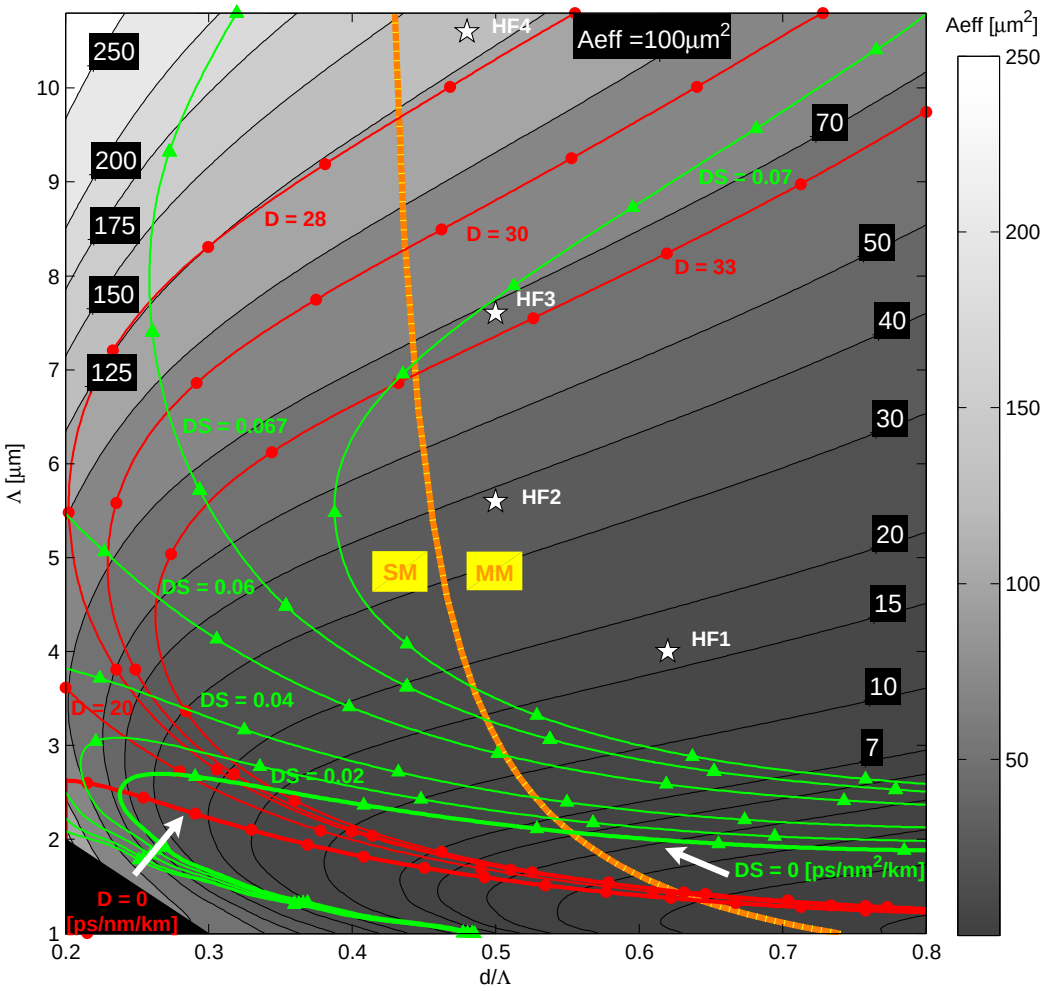

FIGURE 3.1: Optical property map for silica HFs at 1550 nm. The background grayscale contours represent A_{eff} variations; D contours are shown in red with circle markers; D_{slope} contours are in green with triangular markers; the fabricated fibres (HF1, HF2, HF3 and HF4) are shown with white star markers. The orange line shows the separation between single mode (SM) and multimode (MM) regime.

- Zero or negative dispersion and/or dispersion slope are only possible for Λ below 3 μm. In this region, other than in the case of very small holes, the A_{eff} tends to be too small for telecom applications, where nonlinear effects that distort the pulses need to be minimised. For larger structures both D and D_{slope} are positive;

- The material dispersion of silica is 21.9 ps/nm/km at 1550 nm; this is obtained for larger values of the pitch Λ than reported in the map, when the waveguide dispersion contribution becomes negligible. For pitches between ∼3.5 and 10 μm the waveguide dispersion contribution *adds* to the material dispersion (as opposed to what happens for SIFs). Therefore a larger value of dispersion than for SIFs has generally to be expected;

- The material dispersion slope of silica and the dispersion slope of the SMF-28 at 1550 nm are 0.065 and 0.06 ps/nm^2/km respectively; similar or slightly larger

values are generally achieved with large Λ fibres, but smaller values can also be obtained in selected regions of the map;

- A structure with zero dispersion and dispersion slope exists for Λ ~2.5 μm and $d/\Lambda \sim 0.24$. Its small A_{eff} however makes it rather unsuitable for telecom applications, and such a fibre will be discussed in more detail in Section 4.3 within the context of nonlinear fibres;

- The validity of the SM/MM line is mainly theoretical (marking the cutoff line of the first higher order mode). In practice the fabricated fibres HF2, HF3 and HF4, despite clearly lying in a theoretical MM regime, have all been practically found to be effectively single mode. An explanation of this may lie in the presence of scattering loss at the core boundary interface, which suppresses the weakly guided higher order modes more than it does to the fundamental modes.

Most importantly, the map shows that there are only two zones where hexagonally stacked HFs may provide improvements over the conventional technology, or at the very least can compete with it: the first one is for large pitches ($\Lambda \sim$ 8-10 μm) and d/Λ around 0.3-0.5, while the second one is in the region around $\Lambda = 3$ μm and $d/\Lambda \sim$ 0.2-0.22.

The first interesting area leads to fibres similar to HF4, with D ~ 26 - 30 ps/nm/km and A_{eff} between 80 and 120 μm^2. These fibres could ideally replace conventional fibres in metropolitan DWDM applications: their larger A_{eff} (i.e. smaller nonlinearities) would allow an increased power per channel to be launched into the fibre, hence allowing longer spans to be covered, while the higher fibre dispersion could be compensated at the receiver with a minimum additional penalty. The main factor limiting in practice the maximum effective area that can be achieved with these fibres is the presence of bend losses. A substantial amount of research has been carried out, aiming at understanding and modelling bend losses in HFs (for a good overview, see for example the PhD thesis of Dr. Joanne Baggett [155]). In order to evaluate the practical limitations that bend losses impose on the maximum A_{eff} of HFs, we employ the empirical model presented by Nielsen et al. [123], which together with previous works from the same group [122, 163] allows the calculation of A_{eff}, V-parameter and bend loss from the knowledge of the fibre's structural parameters. Although no standard exists at the moment on the bend loss requirement for telecom fibres, a common assumption is to require a bend loss lower than 10 dB/m when the fibre is wrapped around a mandrel with a 1 cm radius. By using the previously mentioned model for a bend radius of 1 cm, the map in Figure 3.2 is obtained. Here the blue line represents the bend loss limit of 10 dB/m and the green area highlights the parameter-space satisfying the bend loss condition. It can be appreciated how single-modality and bend loss requirement set an upper limit to the maximum achievable A_{eff} to around 100-130 μm^2. This is not very different from what can be achieved with SIFs under the same bend loss limitation, and is a further demonstration that bend losses for a fixed A_{eff} can be very similar for HFs and SIFs [86].

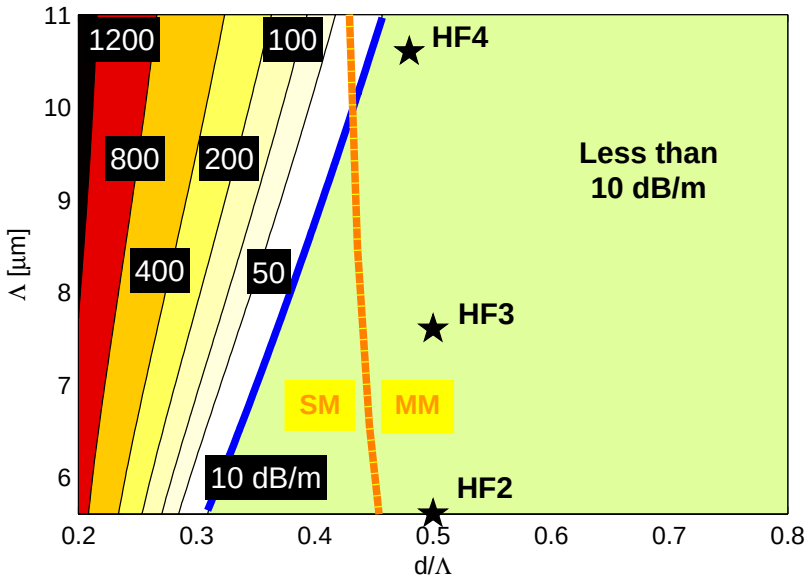

FIGURE 3.2: Attenuation loss at 1550 nm in dB/m for a fibre wrapped around a mandrel of 1 cm radius. Note the reduced Λ range, imposed by the invalidity of the model when used for small A_{eff}.

In the second zone identified on the map, we can obtain fibres that could compete with, and in some respect outperform, conventional non-zero dispersion shifted fibres (NZ-DSF), currently largely employed in long-haul and ultra long-haul DWDM transmission. In this region a trade-off must be sought between modest dispersion and low dispersion slope for the desired value of A_{eff}. Dispersion has to be sufficiently hight to reduce the detrimental effect of inter-channel Four Wave Mixing, while a low slope guarantees a similar dispersion over a broad wavelength range. As an example of such a fibre type, we proposed HF5 [164], with $\Lambda = 3.1$ μm and $d/\Lambda = 0.2$ (see Figure 3.3), whose properties can be found in Table 3.1 together with a reference, state-of-the-art NZ-DSF. This HF would clearly present an interesting advantage: its low dispersion slope and its endlessly single modedness would allow for a useable bandwidth of nearly 400 nm, almost twice that of conventional NZ-DSF [164]. The main issue with HF5, though, is the confinement loss: its very small holes and relatively small pitch would require a large number of full hole rings in order to reduce the confinement loss to an acceptable level. Although the issue is not a fundamental one and fibres with as many as 20 rings of holes have been fabricated [165], this could pose practical fabrication and cost issues for such a fibre. In Figure 3.3 the minimum number of hole rings required to reduce the confinement loss to below 0.1 dB/km (i.e. a value comparable to or less than other intrinsic sources of loss) is shown for all fibres in the parameter space under investigation.

It is evident from the figure how the design of HF1, HF2, HF3 and HF4 benefits from the relatively large hole size, requiring only 4 full rings of holes (60 holes in total). From this point of view the previously identified region with large A_{eff} is also quite favourable, as only 4 to 6 rings of holes would be required. In contrast as many as 15

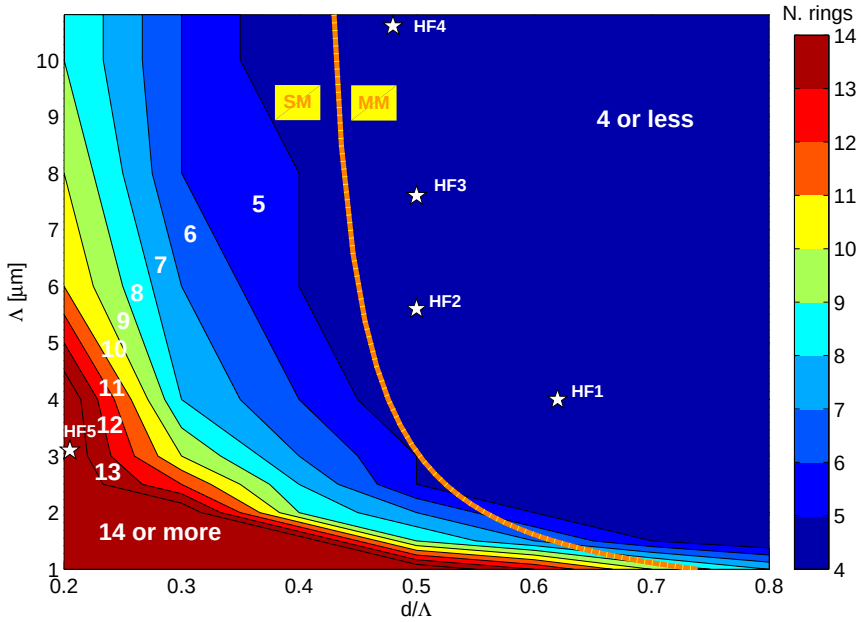

FIGURE 3.3: Number of hole rings required to obtain a confinement loss ≤ 0.1 dB/km at 1550 nm

rings of holes would be needed for HF5 or similar designs, if equal sized holes were to be used. In order to exploit the dispersion and effective area properties of this region of the map without such a difficult and costly fabrication process, though, alternative designs employing larger holes in the outer rings, can be devised. This has the disadvantage of introducing higher order modes in the structure, even if Matsui *et al.* have demonstrated that through a careful design, a fibre with 3 small and 5 large holes (HF6, see Table 3.1) could essentially behave as a single mode fibre and yet still retain similar characteristics to the fibres in the region around HF5 [166].

	Λ [μm]	**d/Λ**	**A_{eff}** [μm^2]	**D** [ps/nm/km]	**D_{slope}** [ps/nm^2/km]	N. rings	Loss [dB/km]	Ref.
SMF-28	-	-	**80**	**17**	**0.06**	-	**0.18**	
NZ-DSF	-	-	**70.6**	**12.3**	**0.061**	-	**0.179**	[164]
HF1	4	0.62	17	**76**	0.076	5	**0.77**	[161]
HF2	5.6	0.5	38	**36**	0.072	4	**0.55**	[160]
HF3	7.6	0.5	**50**	**33**	0.07	4	**0.3**	[159]
HF4	10.6	0.49	**130**	**27.2**	**0.06**	3.5	**0.48**	[162]
HF5	3.1	0.2	72.6	11.5	0.025	15	-	[164]
HF6	2.4	0.28	>100	5	∼0	3	-	[166]
	5.92	0.59				5		
HF7	2.8	0.29	100	6.3	∼0	1	-	[167]
		0.4				9		
		0.31				1		

TABLE 3.1: HF for telecoms applications: comparison of optical properties. Values in bold have been measured while the remaining are simulation results.

In conclusion, the detailed map calculated in this section has shown that hexagonally stacked HFs with equal holes can span a wide range of optical properties, and these fibres may provide some advantages over conventional fibres in at least two different areas. Trade offs between dispersion properties, effective area or fabrication complexity must however be considered. Equal holes and a hexagonal arrangement are generally preferable in order to simplify the fabrication procedure, but they are not the only possible solution. By considering holes with different sizes within the same fibre it is possible to tailor the fibre's linear and nonlinear properties even further, as will be shown in Section 4.3. An example of this strategy, applied to an HF for telecom applications is presented in Ref. [167] (HF7), where a triangular instead of hexagonal core fibre with 3 different hole sizes and a total of 11 rings of holes has been shown to present very desirable optical properties, providing advantages over a conventional SIF in all areas. The reproducible and cost effective fabrication of such a fibre however still remains an open challenge.

3.3 Silica fibres for supercontinuum generation at 1.06 μm

This section presents a different application for the optical property maps. Here a map is calculated and used in order to design a silica HF, with flat dispersion at 1.06 μm, optimised for supercontinuum (SC) generation. Besides providing the target value and some indication on its tolerance to fabrication inaccuracies, modelling with the FEM code is also used to characterise several fabricated fibres both by using an ideal model and a simulation of the true fibre cross section. The dispersion curves obtained from these simulations are then used, in combination with experimental data and simulations of the nonlinear Schrödinger equation preformed by my colleagues, in order to better understand the underlying mechanisms leading to the SC generation. Finally a fibre design to achieve an even flatter dispersion profile at 1.06 μm is proposed.

Supercontinuum generation in holey fibres (HFs) is an established technique for producing broadband light sources [65, 168]. This has revolutionised the field of frequency metrology and has opened up a host of new and significant applications in areas such as medical imaging, telecommunications and sensing. Previously, bulky and expensive Ti:Sapphire-based femtosecond pump sources operating at wavelengths around 780 nm were used for investigations of SC generation and, therefore, most HFs are designed for use at this pump wavelength. However, there is rapidly growing interest in the development of more practical pump lasers to facilitate more widespread deployment of SC technology [169]. High average power excitation of HFs can be realised by employing Yb-doped fibre lasers operating near 1.06 μm, which offer high optical efficiencies and the capability to generate pulses with durations ranging from <100 fs through to the CW regime. Moreover, the holey fibre can be spliced directly to the laser output to make a robust fully-integrated fibre-based SC source. There is thus a great demand for HFs with optimised dispersion profiles for SC generation in the vicinity of this wavelength.

A requirement for the generation of broadband continua is small (but positive) group-velocity dispersion (GVD) at the pump wavelength. From earlier work it is clear that, in addition to reducing dispersive spreading of the input pulse, propagation near the zero-dispersion wavelength (ZDW) allows phase matching and group-velocity matching of four-wave mixing processes. The propagation of intense femtosecond pulses near the ZDW of an ordinary single-mode fibre leads therefore to the generation of new spectral frequencies through a combination of self-phase modulation, soliton formation, Raman soliton self-frequency shifting and parametric processes within the fibre. Recent studies have shown that pumping in the anomalous region and controlling the position of the two zero-dispersion wavelengths relative to the pump wavelength can be used to tailor the extent of the spectral broadening, as well as the detailed spectral shape of the SC radiation [73, 170, 171].

3.3.1 Fibre design

The main optical properties of silica hexagonally stacked HFs at 1.06 μm are calculated for various fabrication parameters, and are shown in the map in Figure 3.4 for d/Λ between 0.2 and 0.8 and Λ between 1 and 3 μm. For clarity, only a few relevant contour lines for dispersion (D) and dispersion slope (DS) are shown: the zero level and one contour on each side of it in order to provide a visual idea of the fabrication tolerances. The fibre design of interest, with zero DS and slightly anomalous dispersion at 1.06 μm, is immediately recognisable from such a representation. The intersection between the D = 0 ps/nm/km and DS = 0 ps/nm^2/km curves provides the starting point, from which one has to deviate slightly towards larger d/Λ and along the DS = 0 contour in order to obtain the desired structure.

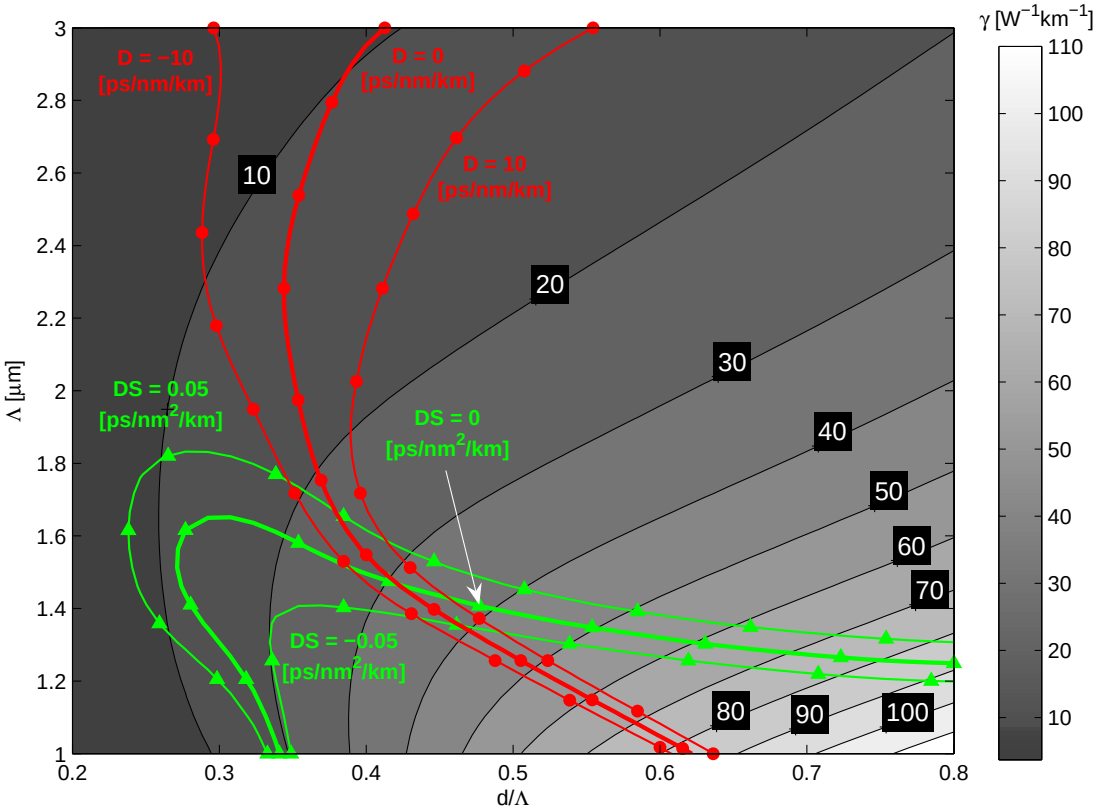

FIGURE 3.4: Silica HF: optical property map at 1.06 μm, calculated for 5-ring HFs on a 8 × 5 grid. The background grayscale contours represent the nonlinear parameter γ; D contours are shown in red with circle markers; D_{slope} contours are in green with triangular markers.

The optimum design is found for Λ = 1.5 μm and d/Λ = 0.4136. It corresponds to an endlessly single mode fibre with predicted effective area of 4.4 μm^2 (γ= 29.4 W^{-1}km^{-1}), DS = 0 ps/nm^2/km, D = 1 ps/nm/km and it presents an anomalous dispersion region nearly 90 nm wide with the two zero dispersion wavelengths equally spaced about the intended pump wavelength of 1.06 μm. A confinement loss of 0.25 dB/m and 0.015 dB/m was found for 5 and 6 rings of holes respectively; while with 7 rings it decreased

to 8×10^{-4} dB/m, well below all other sources of loss for the practical fibre. In order to provide the fibre fabricators with useful information about the degree of accuracy required to maintain useful optical properties, the two plots in Figure 3.5(a) and Figure 3.5(b) have been calculated. They represent the effect of imprecisions of the order of $\pm 1, 2, 5$ and 10% on both the pitch Λ and the relative hole size d/Λ. It can be seen how larger pitches or larger holes tend to enlarge the anomalous dispersion region (hence shifting apart the two ZDWs), while slightly smaller pitches or holes than the target values would produce an all-normal dispersion fibre. Fibres with structural parameters a few percent larger than the target should still possess interesting characteristics for SC generation.

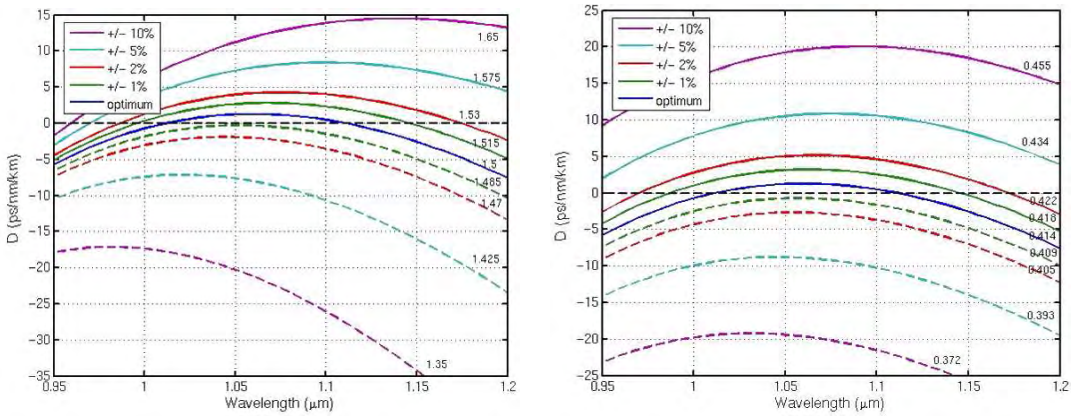

(a) Resultant dispersion as Λ is changed from its optimum value of 1.5 μm ($d/\Lambda = 0.4136$)

(b) Resultant dispersion as d/Λ is changed from its optimum value of 0.4136 ($\Lambda = 1.5$ μm)

FIGURE 3.5: Tolerance analysis for the target fibre for SC generation at 1.06 μm.

3.3.2 Dispersion calculation

The information extracted from Figure 3.5 can be usefully employed to study the effect of the two ZDWs on the overall SC spectrum. For this purpose, a set of fibres with 7 rings of holes and structural parameters close to the target value was fabricated, and experimentally characterised with a mode-locked Nd:glass pump laser operating at 1.06 μm by my colleague M. L. V. Tse. An SEM image of the cross section of one of these is shown in Figure 3.6(a).

In order to estimate the dispersion of each fibre, two different approaches have been followed: in the first approach an ideal model of a hexagonally structured HF was used, while in the second the actual fibre's cross section as determined from SEM images was simulated. The main issue with the ideal model was the acquisition of the information about structural parameters and the choice of the most appropriate model. Since the fibre presented small but significant variations between the holes belonging to different rings, a model with equally sized and spaced holes was believed to be insufficiently accurate. Therefore each hole size and hole-to-hole distance were measured using an

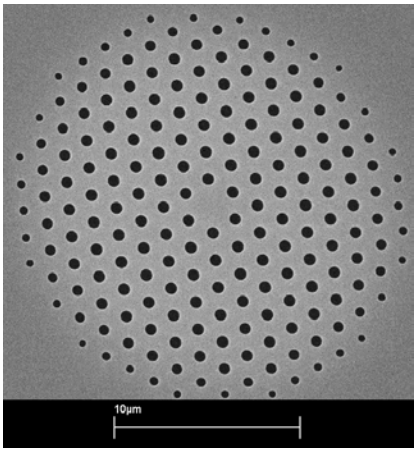

(a) SEM of a typical fibre cross section.

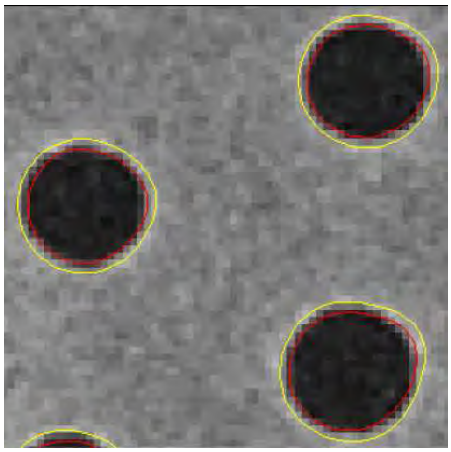

(b) Detail of the holes. Red and yellow curves show the hole contours used for the simulations (1 pixel difference).

FIGURE 3.6: Fabricated fibre.

image processing tool, and for each ring average values of Λ and d/Λ were obtained. These values were then used to create an averaged structure to be used for dispersion calculations. Although this model accounts reasonably well for the main features in the fibre, it does not take into account the small variation of each hole from its optimum position.

The second method consisted in simulating the structure directly obtained from the SEM image of the fibre. In this case, position and size of each hole can be accounted for more accurately, and also properties depending on the overall asymmetry such as the fibre birefringence can be estimated. However, also in this case the issue of the exact determination of each hole size remains. To clarify this point, an example is reported in Figure 3.6(b) where the curves in red represent the best hole contour recognition, while the yellow curves have been obtained by enlarging the red domain by just one pixel all around the perimeter. Figure 3.7 shows the dispersion curve calculated with the averaged-ideal model and those corresponding to both polarisations of the red and yellow contours obtained from the original SEM image.

It is worth noting that the fibre considered in the example presents as many as 168 holes, and therefore the pixel resolution for each hole is quite low: even a difference of just one pixel in the contour recognition produces significant changes in the fibre's dispersion. This clearly shows that for accurate dispersion predictions SEMs with improved resolution would be required. This issue will be further discussed in Section 6.3 for the case of photonic bandgap fibres. The results from the average model are somehow intermediate between the two SEM calculations, which proves the validity of the model. Similar simulations were conducted for the whole range of fabricated fibres. Through experimental observations of the generated SC it was then possible to observe a good agreement with the upper curves in Figure 3.7. This can be explained by considering that the additional

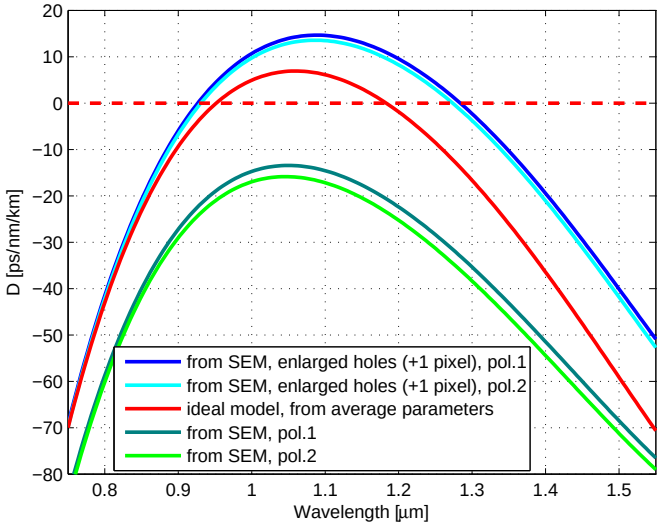

FIGURE 3.7: Calculated dispersion.

conducting gold coating layer applied to the fibre end for SEM imaging purposes reduces the apparent hole size, which in reality is actually slightly larger than it appears in the picture (seeSection 6.3).

An exhaustive numerical and experimental study on the set of fibres with different ZDWs has been conducted by my colleagues M. L. V. Tse and Dr. P. Horak, and the detailed report of this work can be found in Ref. [172]. Here the main conclusions of the study are reported, for completeness. It was found that the different behaviour of supercontinuum generation in fibres with narrow and broad anomalous dispersion regions can be understood by the following considerations. The fibres with broad anomalous dispersion, such as Fibre A in Figure 3.8, exhibit comparably large dispersion at the pump wavelength of 1.06 μm. The dispersion length $L_D = T_0^2/|\beta_2|$ (where T_0 is the input pulse duration and β_2 is proportional to D, see Ref. [6]) is thus short enough that dispersion effects play a significant role in the pulse dynamics within the first 1 m length of the fibres. Fundamental solitons are then formed and subsequently shifted to longer wavelengths by soliton self frequency shifting. This process is strongly dependent upon the specific pump characteristics. Simultaneously, the large dispersion and the large wavelength difference between the frequency components generated by FWM lead to spatial walk-off within 1 cm of propagation. This effect strongly suppresses the FWM gain and therefore higher pump powers are required in order to observe a very large SC spectrum. For fibres such as Fibre E in Figure 3.8, which exhibit a narrow anomalous dispersion region, on the other hand, the dispersion at the pump wavelength is small. Therefore, nonlinear effects dominate over dispersion effects and no solitons can be formed within the first 1 m of fibre. Moreover, spatial walk-off between the FWM components occurs only after a few cm of propagation and therefore the FWM gain is much larger in this fibre and the sudden increase in SC bandwidth occurs at lower pump powers. The overall spectrum, which is much flatter than for broad anomalous

dispersion fibres, is primarily determined by the fibre characteristics, and as a result is essentially largely independent on the specific characteristics of the pump laser itself [73].

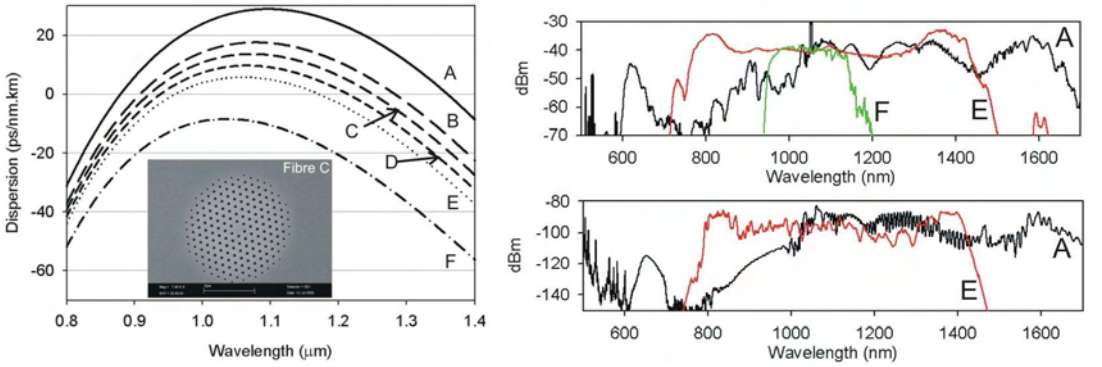

(a) (b)

FIGURE 3.8: (a) Simulated dispersion of the set of fabricated fibres; (b) measured (top) and simulated (bottom) SC spectra for fibres A, E and F. Both images are courtesy of M. L. V. Tse.

3.3.3 Improved design

From the discussion in the last section, the benefits in terms of spectral flatness and the relative independence of the source characteristics for fibres with small anomalous dispersion are quite evident. On the other hand, it is also important to be able to achieve as broad as possible a SC spectrum, as this is directly related to the separation between the two ZDWs. For all these reasons a fibre design producing a small anomalous dispersion over as flat a region as possible, centred around the pump wavelength, would be highly desirable.

Several fibre designs have been explored with this target in mind. The best solution was found in the case of the triangular core fibre which follows the idea by Hansen *et al.* [173] previously applied to a fibre operating at wavelengths around 1.55 μm, and is shown in Figure 3.9(a): three of the six holes within the inner ring are smaller in size. The structural values of the best design, found by using an inverse design method such as the one described in Section 4.2, are: $\Lambda = 1.15$ μm; $d/\Lambda = 0.637$ for the larger holes and $d/\Lambda = 0.264$ for the smaller holes. Due to the smaller pitch, Λ, and larger relative hole size (producing a very high γ around 44 $\mathrm{W^{-1}km^{-1}}$), it was estimated that 4 rings of holes would be enough to limit the confinement loss to negligible values for this design. The dispersion characteristic of the fibre, compared to the uniform-hole fibre design, is shown in Figure 3.9(b) and allows a nearly 20% increase in the separation of the two ZDWs, for the same maximum dispersion of 1 ps/nm/km.

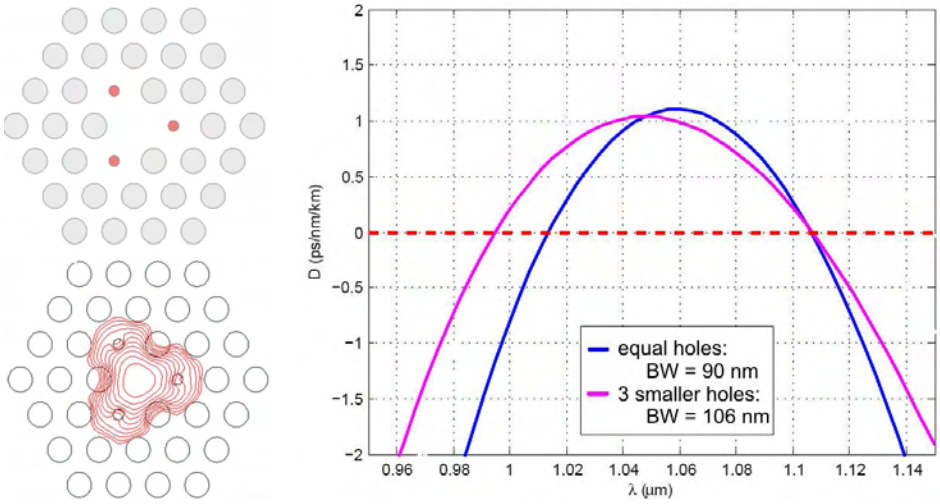

(a) Target structure with $\Lambda = 1.15$ μm, $d/\Lambda = 0.637$ and $d_{small}/\Lambda = 0.264$ (top); field profile (bottom).

(b) Dispersion comparison: uniform-hole vs. improved design.

FIGURE 3.9: Improved fibre design for SC generation at 1.06 μm.

Tolerances on the size of the small holes were also calculated. Although a very tight match of the target parameters was found to be necessary (of the order of ±1-3%) in order to preserve the required dispersion behaviour, a first attempt at fabricating the fibre, shown in Figure 3.10, was conducted. Unfortunately the fibre was destroyed in the ORC fire (30/10/2005) before any characterisation was possible, and new plans for its fabrication have not yet been made.

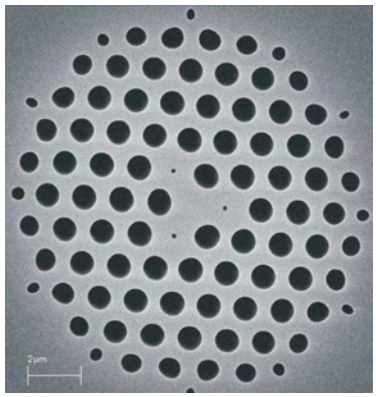

FIGURE 3.10: First fabrication attempt of the dispersion flattened improved fibre (SEM courtesy of M. L. V. Tse).

3.4 Nonlinear fibres with high SBS threshold

In this section several optical property maps for different glasses will be shown, with the aim of proposing tapering strategies to be applied to the fabrication of nonlinear fibres with optimum optical properties and suppressed stimulated Brillouin scattering.

Chapter 1 demonstrated how HFs can exhibit a variety of unusual optical properties that cannot be accessed using conventional optical fibre technology. Arguably, one of the most exciting possibilities is the potential to fabricate fibres with large values of Kerr nonlinearity per unit length and tailored dispersion characteristics, as required for applications such as optical switching, parametric amplification and FWM-based wavelength conversion. Whilst the Kerr nonlinearity and dispersion characteristics of a fibre are the primary issues for many optical signal processing applications, for others, particularly those employing narrow linewidth optical signals, the stimulated Brillouin scattering (SBS) properties of the fibre are also of great concern.

SBS in an optical fibre results from a nonlinear interaction between the pump signal and a backward propagating Stokes wave, mediated by an acoustic wave [6]. The Stokes wave, downshifted in frequency by a structure and material dependent Brillouin Frequency Shift (BFS, ∼11 GHz for pure silica conventional fibres at 1550 nm) can deplete most of the pump signal, once the SBS threshold is reached. The reader is referred to Appendix A for additional information on the SBS process in an optical fibre.

Due to its generally low threshold, parasitic SBS can adversely affect the performance of many Kerr-based devices, limiting the maximum powers that can be effectively used. The development of techniques that allow the relative strengths of these (often competitive) nonlinear processes within the fibre to be controlled is thus extremely important. Various SBS suppression methods have been proposed, including dithering of the laser linewidth [174] or concatenation of fibres with different BFS [175]. Another possibility for controlling the effective strength of the Brillouin effect is to change the fibre structural parameters along its length in order to vary the local Brillouin linewidth down the fibre. This has the effect of broadening the effective Brillouin linewidth of the fibre as a whole, thereby reducing the overall effective gain coefficient and increasing the SBS threshold. This has been shown to work well in conventional fibres, where SBS suppression factors in excess of 7 dB have previously been reported by longitudinally varying the dopant concentrations [176]. Broadening of the Brillouin linewidth (by a factor of 7 or so) due to a structural variation along the fibre length has also previously been reported in the case of a highly nonlinear silica HF [177]. However, in this work there was no attempt to correlate the observed line broadening with the structural variation along the fibre, nor any attempt to establish how modification of the structure affected the other linear/nonlinear properties of the fibre. This is a key issue if such fibres are to be used and optimised for nonlinear device applications.

In this section the results of systematic measurements of the Brillouin frequency shift (BFS) in a tapered, small core silica HF as a function of its structural parameters will be presented. The study confirms that BFS of a HF scales linearly to first order with respect to the effective index (n_{eff}), as would be expected from a simple consideration of the SBS process. Since the HF technology allows for a far greater range of n_{eff} values than conventional doped fibre technology, due to the large index contrast between glass and air, it offers great scope for significant Brillouin line broadening control. However, the other linear and nonlinear characteristics of a HF are also highly sensitive to the fibre structure. In order to design the most efficient fibre for a given nonlinear application and to understand the levels of sensitivity involved in its fabrication, a set of optical property maps for hexagonally stacked HFs made of different glasses have been calculated. The results of this study are presented in the case of 3 particularly interesting glasses: silicates, lead oxide (SF57) and bismuth oxide glasses. For each case multiple bi-dimensional contour plots are presented, all showing, at the same time, the variation of n_{eff}, dispersion (D), dispersion slope (D_{slope}) and nonlinear coefficient (γ) over the range of Λ and d/Λ that defines small core, high nonlinearity HFs. In each case several longitudinal structural modulation strategies, designed to control the dispersion variation along the fibre, are presented.

3.4.1 A tapered nonlinear HF

A 40 m long, small-core, hexagonally-stacked, silica HF was fabricated with a deliberate longitudinal structural variation along its length, obtained by making a step-change to the fibre draw speed during the drawing process. The fibre, which will be denoted as HF1, had a germanosilicate core, extracted from a typical single mode optical fibre preform (NA = 0.12). This length of fibre was then cut up into 2 m sections, and both the hole-to-hole spacing (Λ) and the relative hole diameter (d/Λ) were measured from SEM images of the samples. The BFS associated with each sample was then measured by my colleagues K. Furusawa and Z. Yusoff [178] using the pump-probe technique proposed by Nikles *et al.* [179]. The variation in structural parameters along the fibre length and an SEM image of a typical section are shown in Figure 3.11(a) and Figure 3.11(b) respectively. In Figure 3.11(c) the measured BFS and the simulated n_{eff} along the fibre are plotted, where the n_{eff} values were calculated with the FEM solver by considering a perfect structure with the parameters plotted in Figure 3.11(a).

A direct correlation is observed between simulated effective index and measured BFS (or ν_B), in excellent agreement with the simple formula [6]:

$$\nu_B(z) = \frac{2n_{\text{eff}}(z) \cdot v_A}{\lambda} \tag{3.1}$$

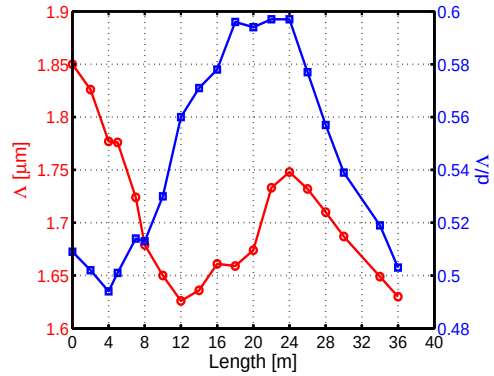

(a) Structural parameters

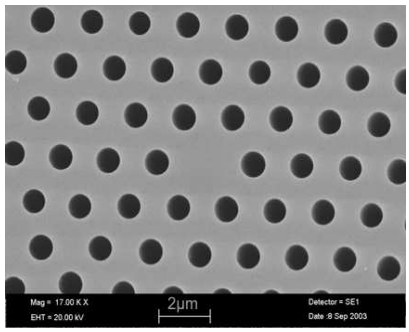

(b) Typical SEM (courtesy of K. Furusawa)

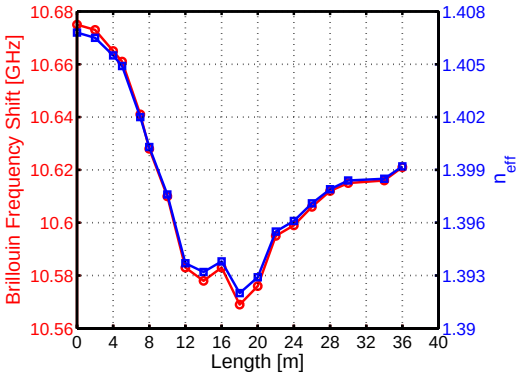

(c) Measured BFS and simulated n_{eff}

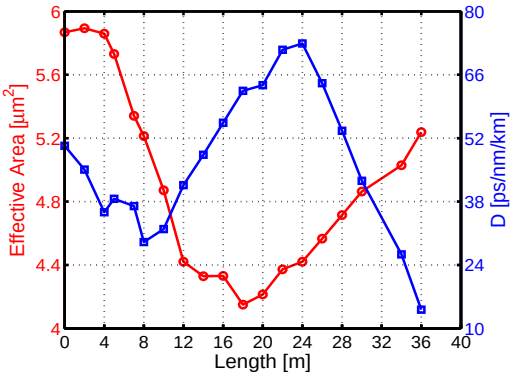

(d) Simulated D and effective area (A_{eff})

FIGURE 3.11: Measured and simulated parameters of the fabricated, tapered HF1.

where v_A is the acoustic velocity within the fibre, $n_{eff}(z)$ the effective modal index, and λ the vacuum wavelength of the pump lightwave. From our data $v_A = 5880$ m/s, in good agreement with previously reported values for germanium doped silica.

The effective index of the fibre at 1.55 μm is seen to vary between 1.407 and 1.392 over its length, resulting in an SBS shift variation of ∼3 linewidths (∼105 MHz), and an anticipated increase in SBS threshold by a factor of 2.2. Figure 3.11(d) shows how the fibre dispersion varies strongly along the length of the pull, ranging from 50 ps/nm/km at the beginning of the pull (BOP) to 80 ps/nm/km near its centre, before dropping to 10 ps/nm/km at the end of pull (EOP). The dispersion slope varies between -0.1 and -0.2 ps/nm/km^2 and the effective area decreases by ∼30%, from 5.9 to 4.2 μm^2. The increased Brillouin threshold is thus seen to be accompanied by very significant variations in key fibre properties for this particular structural modulation profile. Whilst these results highlight the sensitivities involved, this fibre was not designed a priori with SBS threshold reduction in mind, and the key issue addressed in the remaining part of this section is whether we can envisage modulation profiles for which substantial increases in SBS threshold can be achieved without associated large changes in the fibre dispersion properties. A regime of a particular technological interest is for zero (or very low) values

of dispersion in a certain wavelength range, which would reduce the walk-off between pulses with different wavelengths and allow efficient nonlinear processes to take place over a substantial length. This regime is targeted in the following subsections.

As a final note, the reader should be aware that if the microstructuring itself results in more complex acousto-optic interactions in certain regions of the fibre design space, as is likely e.g. through interactions with additional higher-order acoustic modes (see for example the excellent work by Dainese *et al.* [180]), then this would broaden further both the effective local and overall Brillouin linewidths. Hence the FOMs presented in this section should be considered as likely lower bounds on the improvements that can be expected.

3.4.2 Silica fibres

Silica fibres are analysed first because, despite their relatively low material nonlinearity coefficients, they still offer the most mature fabrication method (capillary stacking), and hence represent a useful benchmark for other glasses and fabrication approaches. In order to study the most appropriate tapering profiles for obtaining, at the same time, a large SBS suppression and good control of the fibre dispersion properties, the optical property map shown in Figure 3.12 has been calculated for hexagonally stacked silica fibres at 1550 nm. The map, scanning d/Λ between 0.35 and 0.8 and Λ between 1 and 2 μm, was obtained by calculating the most relevant optical properties for an 8 ring hexagonally stacked HF, on a 17 x 13 point grid. The results were then interpolated using a 2D spline function to obtain a smooth figure.

As can be seen, an n_{eff} variation in the range 1.42 to 1.31 is obtainable in this parameter space – corresponding to a $\sim$7% variation in effective BFS across the plot. Note that the ratio of Brillouin spectral gain width to BFS is typically 3.5×10^{-3} for fused silica. Each n_{eff} contour (0.01) is thus seen to correspond to a shift of $\sim$2 Brillouin linewidths. Superposed on the plot in Figure 3.12, and labelled as HF1, is the longitudinal structural variation of the fabricated fibre mentioned in Section 3.4.1. Note that the n_{eff} contour density is highest in the small core, large air fill fraction region and thus substantial linewidth broadening and increased Brillouin thresholds should be achievable in this region. All the proposed fibres will therefore lie in this design-space, although care is also paid in order to guarantee their single modedness.

We propose two possible approaches to increase the SBS threshold while controlling the fibre dispersion. According to the first strategy the dispersion is kept constant by controllably modulating the fibre structure along the D = 0 ps/nm/km contour (obviously this can be done for any other dispersion value, or other fibre property contour that one is interested in). The second approach tends to keep d/Λ constant while scaling

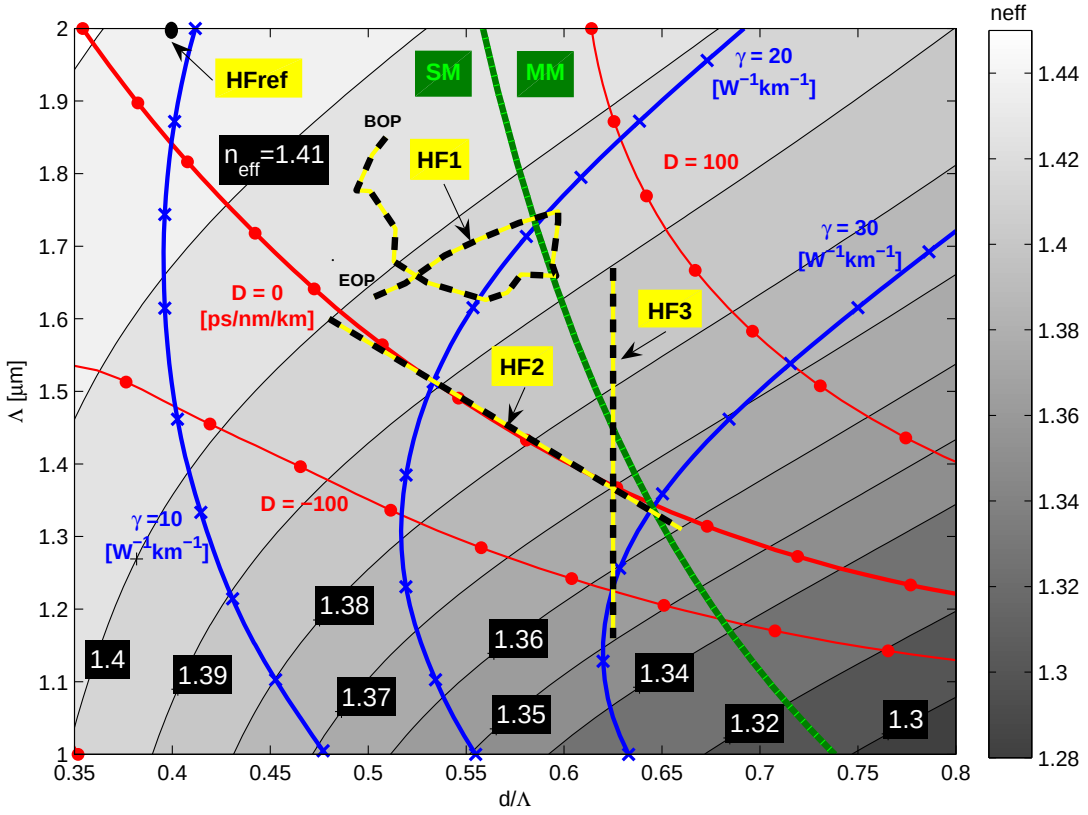

(a) Optical property map for nonlinear silica HFs at 1550 nm. The background grayscale contours represent n_{eff} variations; D contours are shown in red with circle markers; γ contours are in blue with cross markers; the fabricated (HFres and HF1) and proposed (HF2 and HF3) fibres are shown in dashed black and yellow. The green line also shows the separation between single mode (SM) and multimode (MM) regime.

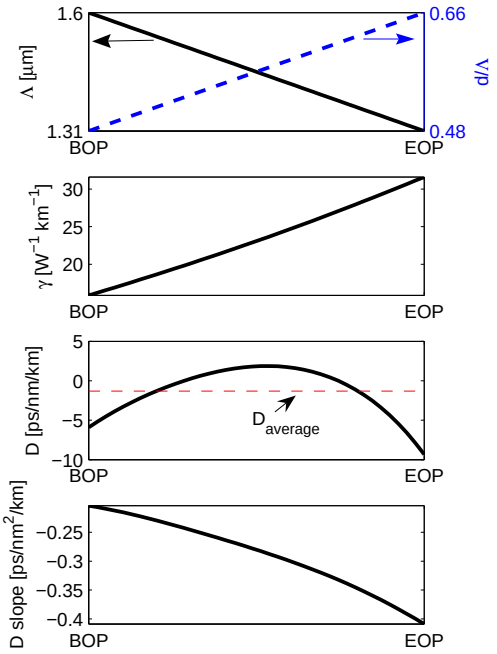

(b) Simulated properties of HF2

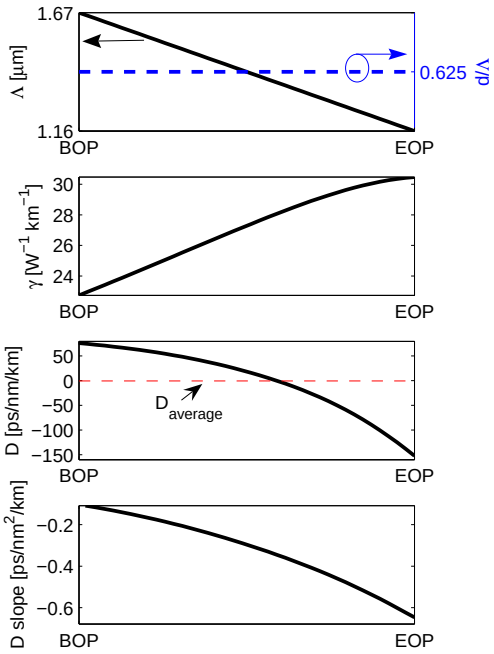

(c) Simulated properties of HF3

FIGURE 3.12: Nonlinear Silica HFs at 1550 nm

the structure, in such a way as to obtain a low total average dispersion and a tapered fibre with less demanding fabrication issues.

An example of the first strategy is the fibre which is denoted as HF2: a linear tapered trajectory between BOP (d/Λ, Λ) coordinates of (0.48, 1.6 μm) and EOP coordinates of (0.66, 1.31 μm), which closely follows the zero dispersion contour line and provides a Δn_{eff}= 0.04. Its structural and main optical properties are shown in Figure 3.12(b). An example of the second modulation type is the fibre following the trajectory labelled HF3, with a BOP of (0.625, 1.67 μm) and EOP of (0.625, 1.16 μm), which would still have an n_{eff} variation as large as 0.04 and hence provide a similar threshold increase as for HF2 [Figure 3.12(c)], yet with clear advantages in terms of ease of fabrication. It is worth noting that in the case of HF2 one could try to follow exactly the D = 0 contour, although such a careful control of the structural parameters is still probably difficult to achieve with the current fabrication technology. I have here chosen to show linear paths instead, as this also permits me to highlight the dispersion sensitivity in the design space of interest.

Assuming that the fibre has a Brillouin gain spectrum with a Lorentzian profile $g_B(\nu,z)$, centred at $\nu_B(z,)$ at each point z along its length, we can calculate an effective gain coefficient as (see Appendix A):

$$G(\nu) = \int_0^L g_B(\nu, z) \cdot e^{-\alpha z} dz \tag{3.2}$$

where α is the fibre loss and L its length [176]. With this definition, the SBS threshold is ultimately inversely proportional to the maximum value of the effective gain $G(\nu_{max})$,

$$P_{th} \cong 21 \frac{K A_{\text{eff}}}{G(\nu_{max})} \tag{3.3}$$

where K is a polarisation factor and A_{eff} is the effective area. Conversely, for a uniform fibre the SBS threshold is simply

$$P_{th} \cong 21 \frac{K A_{\text{eff}}}{g_{B0} L_{\text{eff}}}, \tag{3.4}$$

where g_{B0} is the Brillouin gain coefficient and L_{eff} is the effective interaction length given by $L_{\text{eff}} = [1 - e^{-\alpha L}]/\alpha$. Therefore the SBS threshold increase, P_{inc}, resulting from longitudinal structural non-uniformities can be numerically calculated as

$$P_{inc} = 10 \log_{10} \left[\frac{g_{B0} L_{\text{eff}}}{G(\nu_{max})} \right]. \tag{3.5}$$

In order to estimate the Brillouin properties of any tapered structure on the map, Brillouin measurements of a uniform fibre are needed as a reference. From its measured BFS

and simulated n_{eff} it is possible to obtain v_A through Equation 3.1, and thus the BFS of any other point on the map; the nonlinear index n_2, attenuation, Brillouin gain coefficient and the FWHM of the gain spectrum of the measured, uniform fibre are needed in order to estimate the other properties of the tapered fibres. With this aim a uniform fibre with $\Lambda = 2$ μm and $d/\Lambda = 0.4$ (HFref) was fabricated and characterised [178]. Its main optical and acousto-optical properties are summarised in Table 3.2.

Table 3.3 shows the Brillouin properties of the measured and proposed fibres, together with those of a conventional, state-of-the-art, highly nonlinear dispersion shifted fibre (HNL-DSF) for comparison. The table includes the values of BFS, the FWHM of the effective gain spectrum and the maximum value of the effective gain coefficient normalised to the effective length, $G(\nu_{max})/L_{eff}$. Note that in the case of uniform fibres this simply reduces to the Brillouin gain coefficient g_{B0}. Besides these, the table also reports the value of a Kerr-to-Brillouin figure of merit (FOM), recently introduced in order to take the fibre's SBS limitation into account when comparing the Kerr performance of highly nonlinear fibres [181]. According to this definition,

$$FOM = \gamma Ł_{eff} P_{th} \cong \frac{42\pi}{\lambda} \frac{n_2 L_{eff}}{G(\nu_{max})} \tag{3.6}$$

where γ is the fibre nonlinearity and P_{th} is the SBS threshold. This FOM hence represents the maximum nonlinear phase shift available from the nonlinear fibre, for light sources of a bandwidth much smaller than the Brillouin linewidth.

The optical performances of HF2 at 1550 nm have been calculated assuming a reasonable attenuation of 0.1 dB/m, a tapering length corresponding to the effective length of 43.4 m, and an intrinsic Brillouin gain bandwidth of 43 MHz. The large difference in effective index, between 1.4 and 1.36, would result in an overall linewidth FWHM of 280 MHz (∼6.5 times enhancement) and a corresponding increase in SBS threshold of ∼4.2 times (6.2 dB). HF2 would have an average nonlinear coefficient of 23 $W^{-1}km^{-1}$ and a low dispersion at all points along its length (see Table 3.2 and Table 3.3). Please note that a linear change in the structural parameters along the length has been assumed for the calculations and that the tapering length is only relevant if losses are taken into account: a length independent Brillouin performance would be achieved if losses were to be ignored.

	$\mathbf{n_{eff}}$	**D** [ps/nm/km]	$\mathbf{D_{slope}}$ [ps/nm^2/km]	$\mathbf{n_2}$ [m^2/W]	γ [$W^{-1}km^{-1}$]
HNL-DSF	N.A.	**1.7**	N.A.	$\mathbf{4.2 \times 10^{-20}}$	**15.5**
HFref	1.4178	20.6	-0.07	$\mathbf{2.16 \times 10^{-20}}$	9.5
HF2	1.4 → 1.36	-1.3	-0.2 → -0.4	”	16 → 31
HF3	1.39 → 1.35	-0.4	0.1 → -0.6	”	23 → 30

TABLE 3.2: Comparison of optical properties for silica fibres (L = L_{eff}= 43.4 m).

	BFS [GHz]	**BGB FWHM** [MHz]	$\mathbf{G(\nu_{max})/L_{eff}}$ [m/W]	$\mathbf{P_{inc}}$ [dB]	**FOM**
HNL-DSF	**9.48**	**20.6**	$\mathbf{7.19 \times 10^{-12}}$	-	0.5
HFref	**10.925**	**43**	$\mathbf{0.898 \times 10^{-11}}$	-	0.20
HF2	10.79 → 10.48	280	2.15×10^{-12}	6.2	0.85
HF3	10.71 → 10.40	280	2.15×10^{-12}	6.2	0.85

TABLE 3.3: Comparison of acousto-optical properties for silica fibres (L = 43.4 m). Values in bold have been measured; those remaining have been estimated or simulated.

The practical realisation of this fibre may however prove challenging, since it requires accurate control and variation of two fibre parameters: in this regard fibre HF3 may be considered advantageous. Its trajectory has been chosen in order to provide nearly-zero overall dispersion, averaged between the two extremes of +70 and -150 ps/nm/km, and at the same time a high average γ of 27 $W^{-1}km^{-1}$. Its Brillouin characteristics would be similar to HF2. Both the proposed fibres HF2 and HF3 lie in a region of the structural design plane where the dispersion slope is between -0.1 and -0.6 ps/nm/km^2. Furthermore, as can be seen from the map in Figure 3.12, particular care has been taken to assure that they both lie in a region of effectively single modedness[2].

A similar design approach could be employed to target fibres with smaller dispersion slope, even if the nonlinearity would need to be traded off, or a larger and constant γ. Alternatively, in order to minimise the extent of structural variation necessary, other trajectories, which are at all points in a direction normal to the n_{eff} contours, can be envisaged. It is to be appreciated that the techniques and strategies outlined so far are applicable to a far broader range of fibre structures and operating wavelengths. Also the type of glass chosen can have a profound impact on the final Kerr and Brillouin properties of the fibre and possible additional advantages for Kerr based device applications, involving narrow bandwidth signals, can be envisaged by the use of compound glass HFs. For this reason, in the following, a similar analysis of tapering trajectories through the use of optical maps is presented for two of the most promising compound glasses available for HF fabrication: a lead silicate glass (SF57) and a bismuth oxide glass with high Bi concentration.

[2]As it was pointed out in Section 3.2 the line separating SM and MM fibres describes the theoretical cut off point of the second mode; fibres lying in a region slightly to its right however have been found to behave essentially as single mode, as the second mode is still, in practice, much lossier than the fundamental one.

3.4.3 SF57 fibres

Lead-silicate glasses, such as the Schott SF57 considered here, are very promising materials for highly nonlinear fibres, due to a suitable combination of optical and mechanical properties. The fabrication technology for compound glass HFs has improved greatly in recent years and fibres with many holes and complex geometries can now be fabricated [52, 182], as will be also discussed in Section 4.2. Also for this glass optical property maps have been calculated and tapering trajectories will be proposed to enhance the SBS threshold while controlling the overall dispersion. The map in Figure 3.14 was calculated for 8 ring HFs and is here presented for d/Λ between 0.4 and 0.8 and Λ between 1 and 2 μm. In this structural space n_{eff} varies between 1.6 and 1.73, corresponding to a variation of $\sim$8% in effective BFS across the plot. The D = 0 ps/nm/km contour line can be obtained with smaller pitches as compared to the silica case. This can be explained by considering that the material dispersion of SF57 at 1550 nm has a larger absolute value than silica (around -51 ps/nm/km), and thus a larger amount of waveguide dispersion (hence a smaller pitch for the same d/Λ) is needed in order to compensate for it.

In order to obtain some reference values of the Brillouin properties of this glass - to the best of my knowledge never reported in the literature before - a 2 m length of the nonlinear fibre, which will be described in detail in Section 4.2, has been characterised using the pump-probe technique [179]. Briefly, the selected fibre was fabricated using a Structured Element Stacking Technique (hence the acronym *SEST* with which it will be referred to), it had a core diameter of $\sim$3.5 μm and an n_{eff}, estimated from a simulation based on its SEM cross-section, of 1.778. Its SEM image and the measured Brillouin gain are shown in Figure 3.13, while its measured and simulated properties are shown in Table 3.4 and Table 3.5.

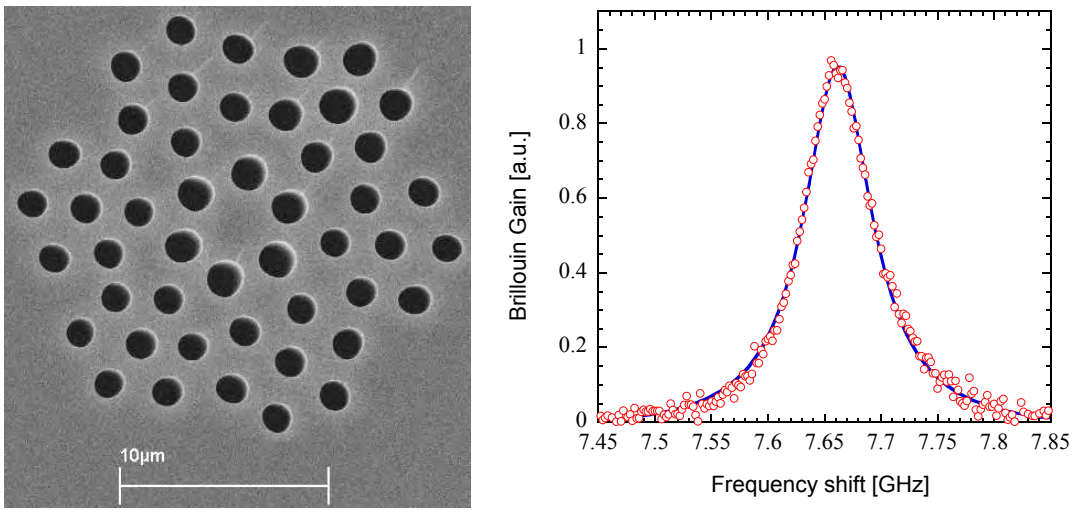

(a) SEM image (courtesy of J.Y.Y.Leong) (b) Measured Brillouin gain (data courtesy of H. Ono)

FIGURE 3.13: Measured SF57 SEST fibre for reference purposes.

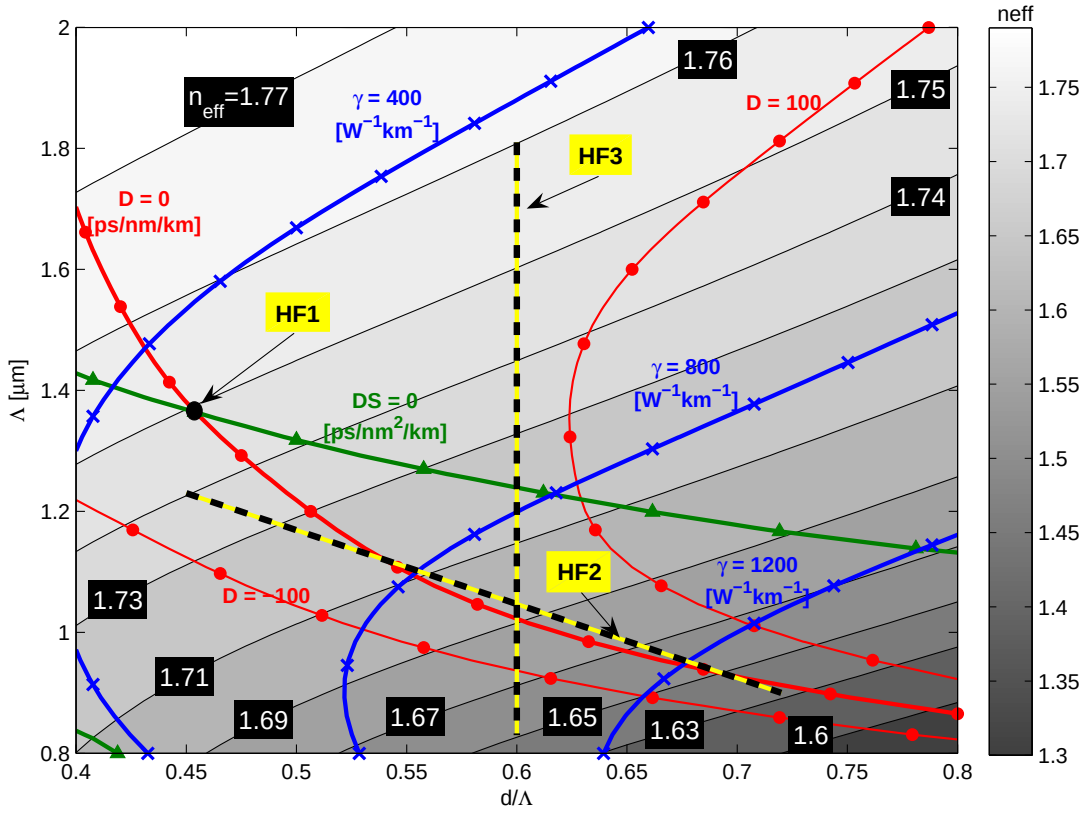

(a) Optical property map for nonlinear SF57 HFs at 1550 nm. The background grayscale contours represent n_{eff} variations; D contours are shown in red with circle markers; D_{slope} contours are in green with triangular markers; γ contours are in blue with cross markers; the proposed HF2 and HF3 fibres are shown in dashed black and yellow.

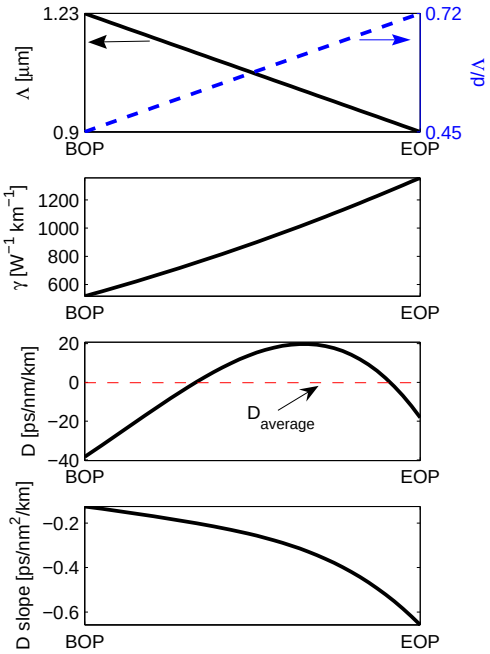

(b) Simulated properties of HF2

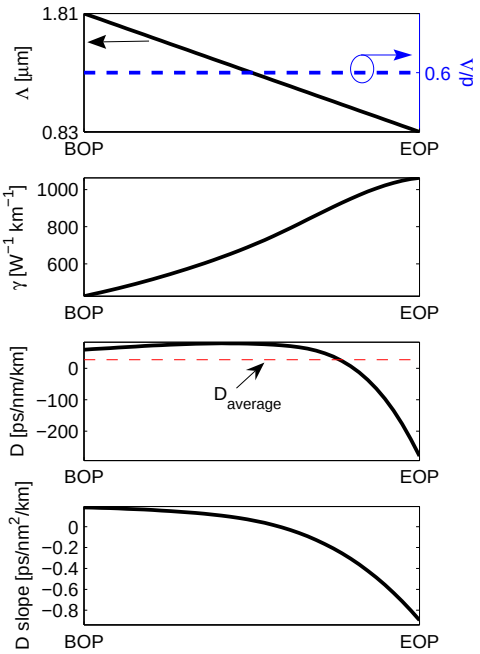

(c) Simulated properties of HF3

FIGURE 3.14: Nonlinear SF57 HFs at 1550 nm

Despite presenting a nonlinear index coefficient nearly 20 times as large as silica, SF57 has a Brillouin gain coefficient only ∼3 times as large, thus providing obvious advantages in terms of FOM. These excellent Kerr-Brillouin properties could be enhanced by the fabrication of a uniform fibre with D = 0 ps/nm/km and D_{slope} = 0 ps/nm^2/km at 1550 nm. The structural parameters of such a fibre (HF1) are easily found on the optical map and correspond to (d/Λ, Λ) = (0.45, 1.36 μm). Its large γ of 468 W^{-1}km^{-1} and FOM of 1.16 would make this an interesting fibre to fabricate for nonlinear CW or quasi CW applications. Note that, in contrast, fibres with a ZDW shorter than around 2 μm would not be possible with conventional all-solid designs.

In order to further increase the SBS suppression and improve the FOM, tapered fibres can also be realised. Following the approach adopted for silica HFs, 2 fibres are proposed: HF2 is a linearly tapered fibre along the D = 0 ps/nm/km contour line, while HF3 is a tapered fibre at constant d/Λ, with small average dispersion. Their main properties, shown in Figure 3.12(b) and Figure 3.12(c) and in Table 3.4 and Table 3.5 have been calculated by employing the measured properties of the SEST fibre, by assuming an attenuation of 1 dB/m and for a tapering length of 4.3 m (corresponding to the maximum nonlinear effective length). Both fibres present a small average dispersion, a large average γ around 800 W^{-1}km^{-1} and the same Δn_{eff} of 0.11 which gives them similar Brillouin properties. The effective gain FWHM is enlarged up to 434 MHz and the SBS threshold is increased by 5.8 dB, generating a FOM as large as 4.4.

	$\mathbf{n_{eff}}$	**D** [ps/nm/km]	$\mathbf{D_{slope}}$ [ps/nm^2/km]	$\mathbf{n_2}$ [m^2/W]	γ [W^{-1}km^{-1}]
SEST	1.778	22	0.2	$\mathbf{4.1 \times 10^{-19}}$	249
HF1	1.75	0	0	”	468
HF2	1.74 → 1.63	∼0	-0.15 → -0.65	”	510 → 1330
HF3	1.76 → 1.65	27	0.2 → -0.9	”	430 → 1060

TABLE 3.4: Comparison of optical properties for SF57 fibres (L = L_{eff}= 4.3 m).

	BFS [GHz]	**BGB FWHM** [MHz]	$\mathbf{G(\nu_{max})/L_{eff}}$ [m/W]	$\mathbf{P_{inc}}$ [dB]	**FOM**
SEST	**7.66**	**74**	$\mathbf{3 \times 10^{-11}}$	-	1.16
HF1	7.54	74	3×10^{-11}	-	1.16
HF2	7.50 → 7.02	434	7.85×10^{-12}	5.8	4.4
HF3	7.58 → 7.11	434	7.85×10^{-12}	5.8	4.4

TABLE 3.5: Comparison of acousto-optical properties for SF57 fibres (L = 4.3 m). Values in bold have been measured; those remaining have been estimated or simulated.

3.4.4 Bismuth fibres

It has recently been demonstrated that solid core step-index fibres (SC-SIFs), fabricated using two different types of bismuth-based glass, can provide a very high FOM due to the extremely high Kerr nonlinearity coefficient and the relatively low Brillouin gain coefficient of the core glass [181]. The large normal material dispersion of the glass at 1.55 μm (-260 ps/nm/km), however, can only be partially compensated by the waveguide dispersion of SC-SIFs, and this is likely to limit the ultimate performance and use of these fibres. The HF structure, on the other hand, can provide a large enough value of waveguide dispersion to compensate for tthe material dispersion and may be the basis for more efficient nonlinear optical devices. Bismuth oxide holey fibres with three holes and a suspended-core structure have already been fabricated using an extrusion procedure by Ebendorff *et al.* [29], while Nagashima *et al.* recently presented a 6-hole fibre made from a drilled preform [183]. A further evolution in the fabrication technology is therefore quite likely to allow, in the near future, the production of fibres with an increased number of rings of hexagonally arranged holes.

In this study the design of hexagonally arranged HFs, made from the Bi_2O_3-based glass previously developed as the core material for SC-SIFs, is investigated. The key optical properties of this particular glass, with a very large bismuth concentration (65.5 mol%) are presented in Refs. [10, 181]. Its absorption coefficient and refractive index are also shown in Figure 3.15.

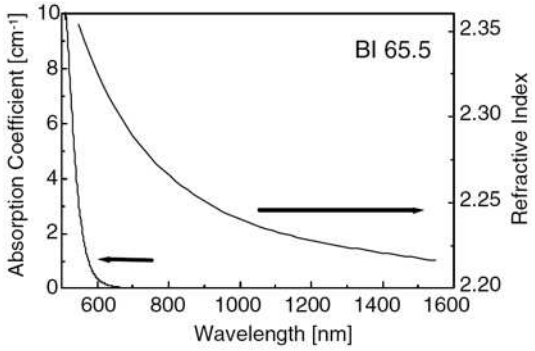

FIGURE 3.15: Wavelength dependance of refractive index and absorption coefficient. After Hasegawa *et al.* [10]

From the figure we derived an analytical expression for the refractive index of the glass, to be used in the simulations, by fitting the digitised refractive index profile to a polynomial equation. Amongst the several possible models for fitting the refractive index variation with λ, we found that the polynomial expansion based on a Laurent series devised by Schott Glasswerke [7] and shown in Equation 3.7 provided accurate interpolated results:

$$n(\lambda) + 1 = A_0 + A_1\lambda^2 + \frac{A_2}{\lambda^2} + \frac{A_3}{\lambda^4} + \frac{A_4}{\lambda^6} + \frac{A_5}{\lambda^8}. \tag{3.7}$$

The resulting coefficients are shown in Table 3.6:

Coefficient	**Best fit**
A_0	4.8270881
A_1	3.9929852×10^{-3}
A_2	1.7852359×10^{-1}
A_3	9.3099043×10^{-3}
A_4	-7.977633×10^{-5}
A_5	1.7116618×10^{-4}

TABLE 3.6: Best fit coefficients.

The material dispersion information was then used to calculate an optical map, shown in Figure 3.17, between d/Λ of 0.6 and 0.8 and Λ of 0.5 and 1.5 μm. Note that the D = 0 ps/nm/km curve is found for even smaller Λ than for SF57 HFs. It was also found that all the fibres within this parameter space are single mode and 4-5 rings of holes are sufficient to obtain a confinement loss that is negligible with respect to the bulk glass loss.

An HF design that should provide a similarly large FOM as the solid step-index version, but with zero dispersion and zero dispersion slope at 1.55 μm is first presented. Then two tapered fibres following the guidelines of the silica and SF57 examples will be proposed.

The fibre indicated on the map as HF1, with $(d/\Lambda, \Lambda) = (0.674, 0.823\ \mu\text{m})$, presents both zero dispersion and zero dispersion slope at 1550 nm and its effective area is 0.89 μm^2 ($\sim$3 times smaller than the SC-SIF version). The associated increase in nonlinearity (γ) would be accompanied, in the worst case, by a corresponding decrease in SBS threshold. As a result, we would expect the HF and SC-SI versions to have a similarly high FOM ($\sim$1). The simulated dispersion of this optimum fibre and the contour plots of the fundamental modes of both the SC-SIF and HF1 are shown in Figure 3.16.

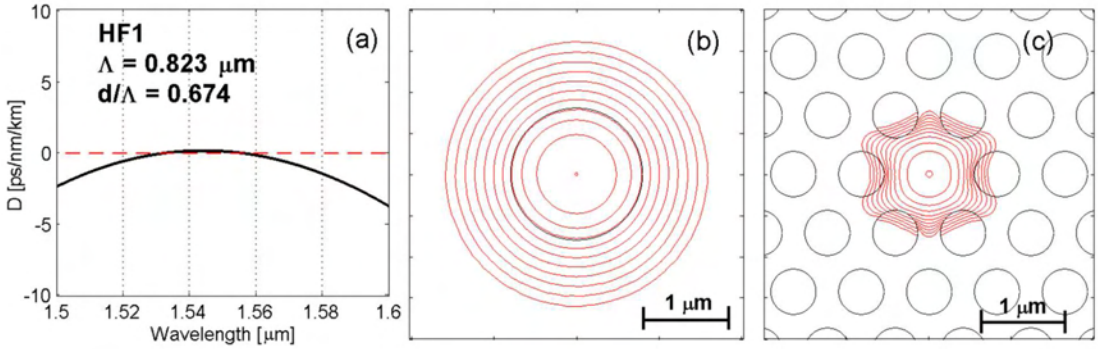

FIGURE 3.16: (a) simulated dispersion of HF1; 2 dB contour plot of the SC-SIF (b) and HF1 (c) at 1550 nm.

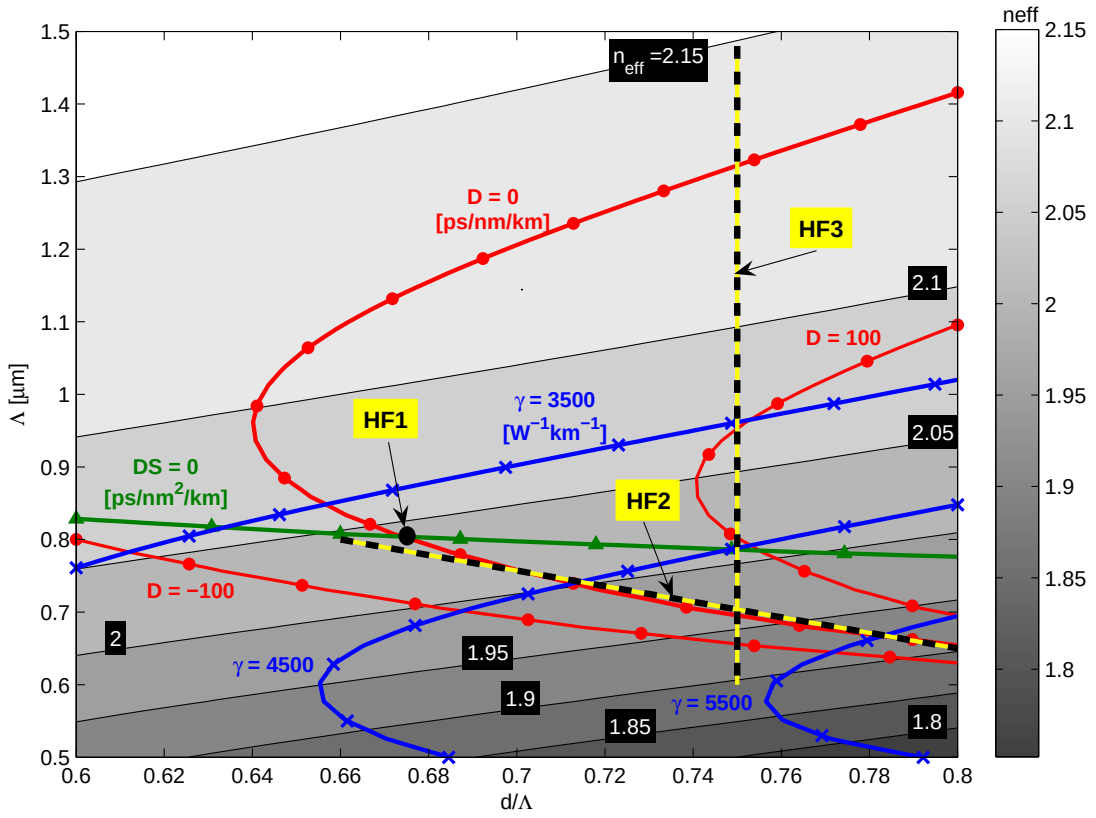

(a) Optical property map for nonlinear bismuth HFs at 1550 nm. The background grayscale contours represent n_{eff} variations; D contours are shown in red with circle markers; D_{slope} contours are in green with triangular markers; γ contours are in blue with cross markers; the proposed HF2 and HF3 fibres are shown in dashed black and yellow.

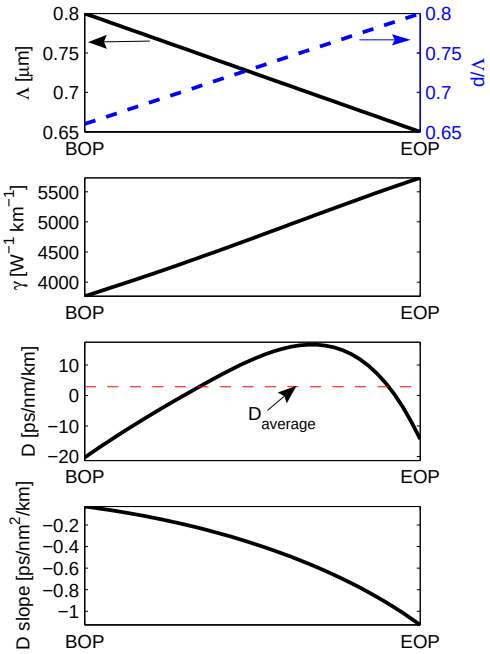

(b) Simulated properties of HF2

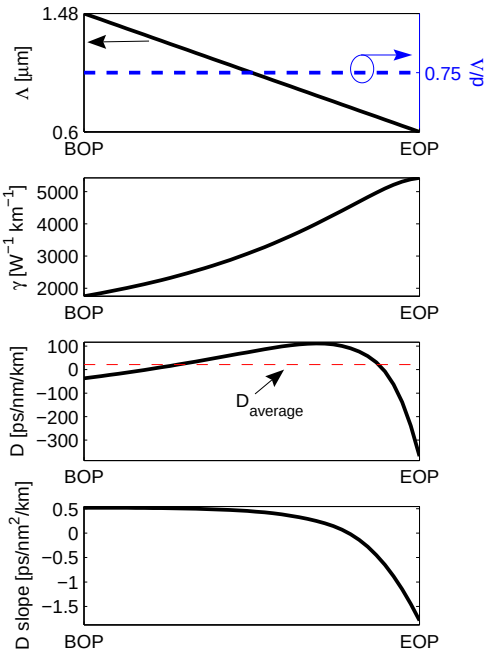

(c) Simulated properties of HF3

FIGURE 3.17: Nonlinear Bi_2O_3 HFs at 1550 nm

As already done for silica and SF57, longitudinal structural tapering trajectories designed to suppress the SBS, while controlling the average value of dispersion, are presented. This study shows that a tapered fibre (HF2), in which both d/Λ and Λ scale linearly from an initial (d/Λ, Λ) dimension of (0.65, 0.8 μm) to a final value of (0.8, 0.65 μm), would closely follow the zero dispersion contour line and have at the same time a large n_{eff} and associated variation in BFS. Its main structural and optical parameters are shown in Figure 3.17(b). Note that in theory dispersion variation could be avoided altogether using a trajectory that follows the D = 0 ps/nm/km contour.

The procedure explained in Section 3.4.2 is employed to establish the effect of the tapering on the fibre's Brillouin properties. In this case, the reference Brillouin properties are those measured for the SC-SIF [181], with the assumption that they do not change significantly in the case of a HF made with the same material as the core of the SC-SIF. These values are reported in Table 3.7 and Table 3.8.

	$\mathbf{n_{eff}}$	**D** [ps/nm/km]	$\mathbf{D_{slope}}$ [ps/nm^2/km]	$\mathbf{n_2}$ [m^2/W]	γ [W^{-1}km^{-1}]
SC-SIF	2.17	**-260**	0.46	$\mathbf{8.17 \times 10^{-19}}$	**1100**
HF1	2.043	0	0	”	3850
HF2	2.05 → 1.9	3	0 → -1.1	”	3700 → 5700
HF3	2.15 → 1.9	21	0.5 → -1.8	”	1750 → 5400

TABLE 3.7: Comparison of optical properties for Bi_2O_3 fibres (L = L_{eff}= 4.3 m).

	BFS [GHz]	**BGB FWHM** [MHz]	$\mathbf{G(\nu_{max})/L_{eff}}$ [m/W]	$\mathbf{P_{inc}}$ [dB]	**FOM**
SC-SIF	**8.81**	**32**	$\mathbf{6.43 \times 10^{-11}}$	-	1.03
HF1	8.29	32	”	-	1.03
HF2	8.32 → 7.71	527	6.75×10^{-12}	9.8	9.8
HF3	8.73 → 7.71	848	4.26×10^{-12}	11.8	15.5

TABLE 3.8: Comparison of acousto-optical properties for Bi_2O_3 fibres (L = 4.3 m). Values in bold have been measured; those remaining have been estimated or simulated.

If we assume, in the first instance, that the detailed lineshape is not grossly affected by the microstructure, then we can use the measured BFS and Lorentzian Brillouin Gain Bandwidth (BGB) of 8.81 GHz and 32 MHz of the SC-SIF fibre to estimate the effective line shape and peak gain coefficient of HF2. By further assuming that through careful fabrication it will be possible to achieve similar losses for HF1 and HF2, as already obtained for SC-SIFs (∼1 dB/m), we estimate that HF2, tapered over a length of 4.3 m, equal to its maximum L_{eff}, would have a Brillouin Gain FWHM of 527 MHz (i.e. a 16.5 times linewidth enlargement). This would provide a Brillouin threshold increase of 9.8 dB, and an increase of ∼9.8 in the FOM with respect to a uniform fibre. An even larger FOM could be achieved by the fibre HF3, tapered at a constant d/Λ = 0.75 between Λ = 1.5 and 0.65 μm. This fibre would present an effective BGB of

848 MHz, an average γ of 3400 $W^{-1}km^{-1}$ and an average dispersion of 21 ps/nm/km, and would be of interest for low latency, increased-bandwidth, SBS based slow-light generation [184]. A comparison of the main properties of the SC-SIF, HF1, HF2 and HF3 is shown in Table 3.7 and Table 3.8.

3.4.5 Conclusion

In conclusion, in this section I have demonstrated that HF technology provides great scope for managing the Brillouin lineshape (and effective Brillouin threshold) for high nonlinearity fibres due to the high index contrast between glass and air, allowing one to control the effective strength of Kerr and Brillouin nonlinearities through longitudinal manipulation of the structural parameters of the fibre. It has also been shown that the dispersive and effective area properties of HFs are also a very strong function of the fibre structure and that attention needs to be paid to how any structural modulation applied to increase the SBS threshold impacts the variation of these parameters. Modulation strategies helping to manage the extent of dispersion variation within nonlinear fibres have therefore been proposed through the use of optical property maps. The performances of three glasses currently employed in the fabrication of microstructured fibres have been compared. Although the arbitrary choice of the tapering paths does not allow a fair comparison to be made, and also the very broad Brillouin gain measured for the reference SF57 fibre was probably due to inhomogeneities along the fibre and would thus compromise the glass SBS performance, a few considerations can be made. Tapered silica HFs can in theory have advantages over the state-of-the-art untapered conventional HNL-DSF. Both SF57 and Bi_2O_3 glasses present advantages (for nonlinear narrow linewidth applications) over silica: the 20 and 30 times (respectively) Kerr nonlinearity improvement is associated with a much smaller Brillouin gain coefficient improvement. Furthermore they also present a larger achievable ratio $\Delta n_{eff}/n_{eff}$, which ultimately determines the effective gain bandwidth width, and hence the SBS reduction factor. There are of course significant differences between the two compound glasses considered, but I do not believe that the type of analysis carried out in this section allows yet a clear conclusion to be drawn about the best glass for these types of applications.

It is finally to be appreciated that the techniques and strategies outlined here are applicable to a far broader range of fibre structures, operating wavelengths and indeed glass materials than I have presented here.

3.5 Conclusion

The studies presented in this chapter highlighted the versatility of the optical maps for the study and design of hexagonally stacked HFs. The maps have been used to acquire a more fundamental understanding of the applicability of HFs in the telecoms area, to obtain a simple design of a fibre with suitable dispersion characteristics for SC generation, and for the more complex design of tapered fibres that allow the simultaneous optimisation of many optical properties. Most importantly perhaps, this chapter has demonstrated that the optical mapping approach can provide a significant contribution to a vast range of design problems. For example, they can be employed to devise tapering trajectories that would allow, at the same time, a reduction in the effective area and in the dispersion, can would be extremely useful in soliton compression experiments [185]. Furthermore the applicability of these maps is not restricted to hexagonally stacked holey fibres: they could be applied, for example, also to the design and optimisation of one dimensional index guiding [186] or photonic bandgap [187] fibres, where the periodic spacing between the rings and the index difference between the two materials could be identified as free-parameters.

Chapter 4

Fibre design using inverse techniques

4.1 Introduction

In Chapter 3 it was demonstrated how some fibre design problems can be efficiently solved by using a graphical mapping approach. This is however a rather demanding method, requiring a fine grid of points to be calculated, and it is a viable solution only if the number of parameters to optimise is small. In HF design many features of the fibre cross-section can be parameterised, and the number of free-parameters can potentially be almost unlimited. Although test and trial approaches based on simplified analytic assumptions can be effective for simple structures with a small number of free-parameters [70, 71] such approaches become impractical as the number of free design parameters is increased, e.g. by introducing a different hole size for each ring of holes. Moreover, the manual optimisation of one parameter at a time can produce sub-optimum answers. For this reason the application of proper inverse design techniques, allowing the optimisation of more complex designs, will be presented in this chapter.

The two sections in the chapter will show, through real fibre design examples, the application of two different inverse design methods to the optimisation of the dispersion of nonlinear holey fibres (HFs). Section 4.2 will introduce the *downhill simplex method* and apply it to the design of dispersion flat, lead silicate, structured element stacked fibres. In Section 4.3 a *genetic algorithm* will be employed to design dispersion optimised silica HFs with many free-parameters.

4.2 Dispersion optimisation of SF57 HFs with the simplex method

In Section 3.4 it was shown how the high effective nonlinearities per unit length (γ) in soft glass HFs offer the potential for significant improvement in the miniaturisation of compact nonlinear optics devices at low powers. Initial fibre fabrication efforts in these glasses have therefore focused on maximising the value of γ, by producing fibres with a small core, supported by three fine struts. By making these struts sufficiently thin and long, the waveguide properties of these structures become very similar to those of a circular solid core fibre surrounded by an air-cladding. Using this method, effective nonlinearities approaching the maximum theoretical values possible have now been achieved for several materials, including both lead silicate glass (Schott SF57) [50] and bismuth oxide glass [29]. These nearly-suspended-core HFs offer very large nonlinearities but allow for only relatively limited dispersion control. In the case of the lead silicate glass which will be considered in this section, for example, values of nonlinearity as high as 1860 $W^{-1}km^{-1}$ have been achieved, but the fibre's zero dispersion wavelength (ZDW) was around 900 nm and its dispersion at 1550 nm was greater than 200 ps/nm/km. It has been already mentioned how the control of the dispersion is a critical issue for the majority of nonlinear device applications, and therefore fibre designs that allow a trade-off in nonlinearity for improved dispersion control (whilst maintaining single mode operation) are of great technological interest. Generally, these designs require more complex arrangements of air holes than a simple air-suspended core, and improvements in both fabrication and design techniques are thus needed.

The studies reported in Chapter 3 have shown that a design approach based on optical property maps can be employed in a number of different design tasks, including inverse optimisations. This approach however requires a large number of structures to be simulated in order to obtain well resolved maps, and can only be effectively applied when the number of free-parameters is one or two. In this section an alternative inverse design technique, the *Downhill Simplex* method, will be applied to the search for the best HF structure providing the required dispersion characteristics. The target fibre will be, in this case, a HF made by SF57 glass, with D $\sim$ 0 ps/nm/km and D_{slope}= 0 $ps/nm^2/km$ at 1550 nm; optimisations will be carried out in the case of structures with two and three free-parameters.

4.2.1 The Downhill Simplex method

The Downhill Simplex method (also called Nelder-Mead method, after its original authors [188]) is one of the simplest multidimensional optimisation methods, arguably providing, of all algorithms, the most functionality for the least amount of code. In optimisation problems where the analytical calculation of partial derivatives with respect

to the design parameters is impossible, as in the current problem (where the function being searched is obtained from numerical calculations), the simplex method can provide an efficient solution. The Nelder-Mead algorithm evaluates the multidimensional function to be optimised in a constellation of points, randomly chosen at the beginning of the process, and uses a recurrent algorithm, based on a few simple rules, to find the point at which the function is maximised or minimised.

A simplex is a geometrical figure that has one more vertex than dimensions: a triangle in 2D, a tetrahedron in 3D, etc. The algorithm starts by choosing an initial simplex (for example by adding D unit vectors to the starting point chosen by the user) and evaluating the function being searched at the D+1 vertices of the simplex. Then, at each step an iterative procedure attempts to improve the vertex with the highest value of the function (assuming the goal is minimisation; for maximisation the vertex with the smallest value is updated). The possible moves are summarised in Figure 4.1.

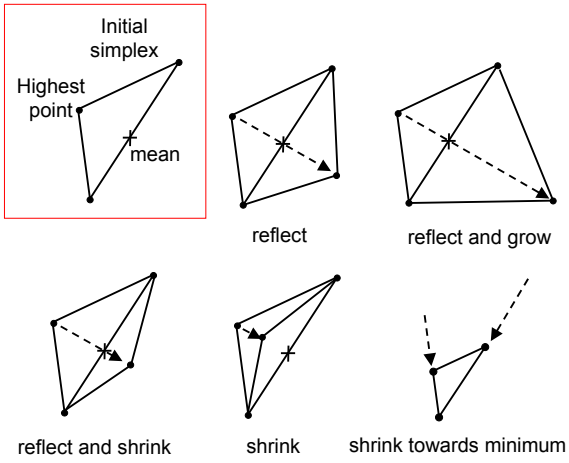

FIGURE 4.1: Downhill Simplex method in 2D: update moves.

The first step is to calculate the centre of the face of the simplex defined by all of the other vertices other than the one we are going to improve (from here on we will assume we want to minimise a function). Since the other vertices have a better function value, it is a reasonable guess that they give a good direction to move into. Therefore the next step is to reflect the point across the face (`reflect`). If the function calculated in the new vertex has improved, the move is clearly a good one. Therefore it's worth checking to see if it is even better to double the size of the step (`reflect and grow`). If growing like this gives a better function value than just reflecting we keep the move, otherwise we go back to the point found by reflecting alone. If growing succeeds it's possible to try moving the point further still in the same direction, but this isn't normally done because it would result in long and asymmetric simplex shapes. For the simplex to be most effective, its size in each direction should be similar; therefore after growing it is better to go back and improve the new worse point. If the point obtained after reflection is still the worst point, it means we probably overshot the minimum of the function. Therefore, instead

of reflecting and growing we can try to `reflect and shrink`. If this results in a better point we keep the move and update the new worse point; if it still results in a worse point we can try just to `shrink`. If after shrinking we still haven't found a point providing an improvement we can come to the conclusion that the moves we are making are too big to find the minimum, so we shrink all the vertices towards the best one (`shrink towards the minimum`).

This set of simple rules automatically shrinks and enlarges the simplex to find the most advantageous length scale for searching in each direction; the only required inputs are the definition of the function to maximise or minimise, a starting point and a stopping criterion. A possible drawback of the algorithm, in it's simplest form, is that it easily gets caught in a local minimum. This behaviour can be overcome by forcing the search to sometimes make moves that are not locally the best choice. For example this can be done by adding a *momentum* to the search, and forcing a fraction of the previous move to be added to the new update move calculated by the algorithm. Of course including a momentum does not guarantee that local minima will be avoided: this depends on the amount of momentum, on the initial condition and on the shape of the function. Moreover adding a momentum will generally slow down the search, in the case of simpler functions.

Local minima were indeed found in the optimisations reported in this section. However, due to the small number of free-parameters considered (2 or 3 only), the implementation of the additional momentum was not considered to be necessary, and the local minima were avoided simply by starting each optimisation from a number of different initial conditions. As will be presented in Section 4.3, when an additional number of free-parameters is taken into account, thus increasing the complexity of the function to optimise and presumably the number of local minima, a different optimisation strategy based on a *Genetic Algorithm* will be applied.

For the studies reported in this section, the simplex method has been integrated with our FEM modal solver. A target objective function, to be minimised by the simplex method, is defined, and its value is evaluated with the FEM solver for each new structure. The objective function is defined as:

$$Obj = w|D - D_t| + (1 - w)|D_{slope} - D_{slope_t}| \tag{4.1}$$

where D_t and D_{slope_t} are the target values of dispersion and dispersion slope, respectively, while w is a weight coefficient chosen in such a way as to balance out the relative contribution of the two terms in the right hand side of the equation, and typically between 0.01 and 0.001. Keeping in mind the fibre fabrication tolerances, the algorithm was set to stop once the solution converged to within 1% of the optimum value of Λ and d/Λ.

4.2.2 Optimum fibre designs

The optical property map calculated for the SF57 glass and shown in Figure 3.14 easily allows one to predict that a hexagonally stacked fibre (denoted as HF1 on the map) with $\Lambda = 1.36$ μm and $d/\Lambda = 0.45$ would satisfy the dispersion requirements of zero dispersion and dispersion slope at 1550 nm, with γ as large as 468 $\mathrm{W^{-1}km^{-1}}$. This fibre is used as a reference in order to check the convergence of the inverse design method. In this case, the free-parameters to optimise are Λ and d/Λ, while D_t and D_{slope_t} are both set to zero. The inverse simulation was found to converge to the same structural parameters of HF1 in between 20 and 70 optimisation steps , depending on the chosen starting point. Note, as a comparison, that in order to obtain a map such as the one in Figure 3.14, more than 100 calculations are generally required. An example of the evolution of *Obj* when two different initial conditions are chosen is shown in Figure 4.2(a), showing that the algorithm tends to converge with an exponential behaviour. In Figure 4.2(c) the results of similar optimisations are also reported, relating to the case of a hexagonally stacked fibre in which the interstitials between the stacked capillaries would not collapse during fabrication. This situation is likely to happen, for example, if vacuum is not applied during the fibre pull, and the resulting fibre structure, shown in Figure 4.2(b), is modelled by further assuming that the external circular shape with a radius of $\sim\Lambda/2$ is retained by each capillary. The optimum structures in this case, when $D_{slope_t} = 0$ and D_t is set to 1.5 and 5 ps/nm/km, require slightly larger holes and a smaller pitch than the structure without interstitials.

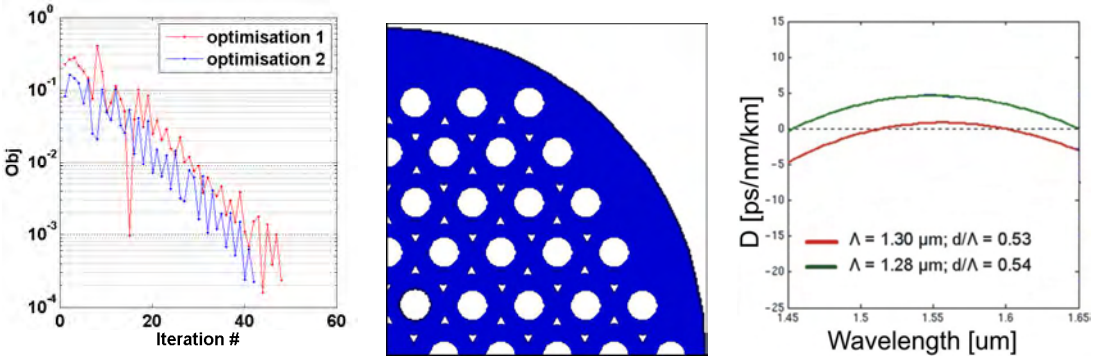

(a) (b) (c)

FIGURE 4.2: (a) Typical evolution of the parameter *Obj* (b) Structure with interstitials with (c) two optimisation results for $D_t = 1.5$ and $D_t = 5$ ps/nm/km.

While these examples confirmed a correct implementation of the algorithm, they also showed that values of the pitch smaller than 2 μm would be required in order to take advantage of the favourable dispersion properties of the fibre. Such a small scale can only be reached, in ordinary hexagonally stacked HFs, with a two-step drawing process, in which the cane, resulting from the first draw is subsequently inserted into a larger jacketing tube and then drawn again. This process is fairly standard now for small-core silica fibres, but it still presents technical issues in the case of soft glasses, where

the repeated heating steps required are more likely to induce crystallisation, and the accurate control of the final dimensions is more difficult.

Other fabrication procedures for soft glass HFs which may overcome these issues have been recently suggested by other research groups, and consist of either stacking rods of two different glasses and then etching one glass away [52] or of using a die-cast process whereby the alloy steel die is removed by using an acid solution [53]. Alternatively, a fabrication approach which has been referred to as the Structured Element Stacking Technique (SEST) and combines the best features of both extrusion and stacking, has been recently implemented at the ORC [182]. The SEST technique, whose fabrication scheme is shown in Figure 4.3, requires the extrusion of 3 separate types of elements: several 7-hole cladding elements, one 6-hole central element, and one jacketing tube. The structured preforms obtained from extrusion are drawn into canes with an outer diameter of ~ 600 μm and stacked into the extruded tube. At this point, the assembled preform can be drawn to the required size, allowing micron-sized pitches to be achieved, as required in order to control the overall fibre dispersion.

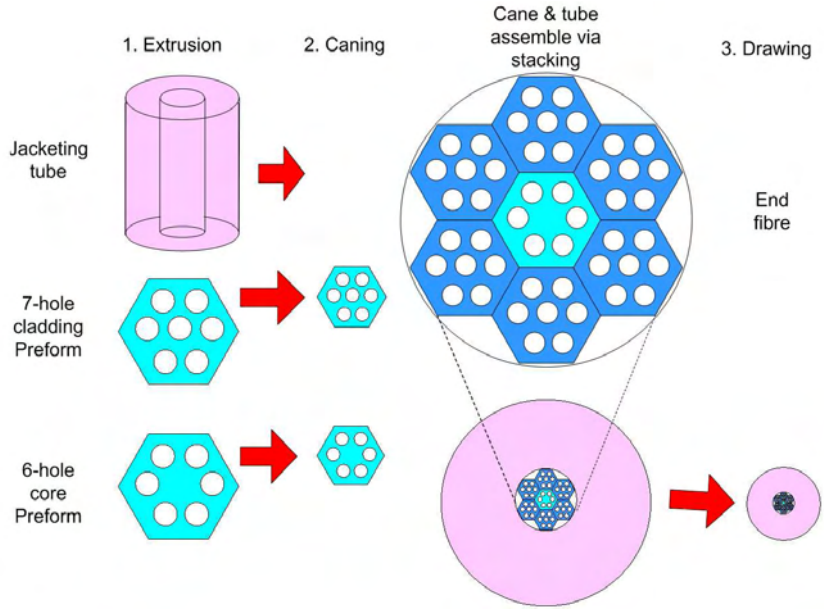

FIGURE 4.3: SEST technique, combining extrusion and stacking to fabricate soft glass fibres with complex profile and small dimensions.

The inverse design procedure already explained for the case of a hexagonally stacked fibre, has also been applied to the design of an optimum SEST fibre. The separation between the holes in each extruded structure, Λ, and the relative holes size, d/Λ, are considered as the only two free-parameters, as the distance between the most external holes and the boundary of each hexagonal element is assumed to be fixed to $\Lambda/2$. The target dispersion slope at 1550 nm (D_{slope_t}) was set to 0 ps/nm^2/km, while D_t was set to 2 ps/nm/km, in order to allow for a relatively broad region with small and anomalous dispersion. The best fibre, whose structure is shown in Figure 4.4(a) and whose dispersion and confinement loss are shown in Figure 4.4(b), was obtained for $\Lambda =$

1.36 μm and $d/\Lambda = 0.46$. Note that the control of the total dispersion characteristics is achieved at the expense of a reduced nonlinearity: γ is 526 $W^{-1}km^{-1}$, nearly 30% of the maximum achievable nonlinearity in this glass. The small scale of the structure and the limited number of holes produce a rather high confinement loss of ~20 dB/m at 1550 nm. This can be reduced to ~ 1 dB/km, well below the bulk loss of SF57 by adding a second ring of stacked elements. Note that, from a theoretical perspective, this fibre is expected to support higher order modes. However, the high confinement loss of these higher order modes (nearly 5 orders of magnitude worse than the fundamental mode) and the large difference in effective index between them and the fundamental mode, leave us confident to predict that this fibre design is likely to be effectively single mode, in practice.

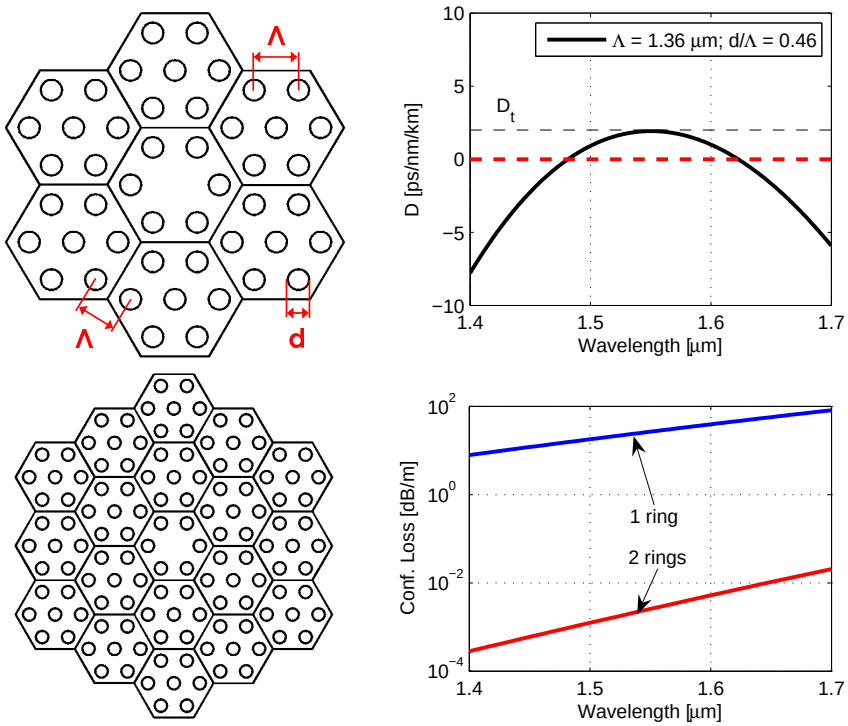

(a) SEST structure with 1 (top) and 2 (bottom) rings of stacked 7-holes elements

(b) Optimum structure: dispersion and CL

FIGURE 4.4: Optimum SEST structure.

Instead of adding a second ring of stacked elements, a different fibre design can be envisaged, requiring a more complex extruded element in the centre of the stack, but allowing for a better confinement loss to be achieved with only one ring of stacked elements. Its underlying concept is shown in Figure 4.5 where only one quarter of the structure is shown for symmetry reasons: an extruded element with 2 rings of air holes and whose Λ and d/Λ are designed to obtain the target dispersion characteristics is positioned in the centre of the fibre. This allows multiple 6-hole elements with much larger hole size to be stacked all around the central element, effectively improving the modal confinement. A geometrical consideration suggests that the pitch of the internal

(Λ_{int}) and external (Λ) elements are simply related by:

$$\Lambda_{int} = \frac{\sqrt{3}+1}{2\sqrt{3}+1}\Lambda \approx 0.68\Lambda, \tag{4.2}$$

hence the number of free-parameters for this structure can be reduced to 3: Λ, the diameter of the internal holes ($d1$) and the diameter of the external holes ($d2$).

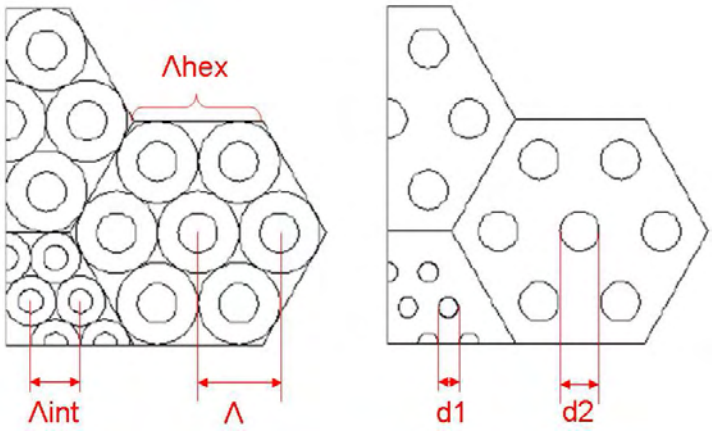

FIGURE 4.5: Improved SEST design: the final structure is shown on the right, while the additional circles in the left figure have been drawn to help visualising the geometrical relationship between Λ and Λ_{int}.

The Downhill Simplex method has been applied also to this improved SEST fibre. The optimum structure, shown in Figure 4.6(b), was found for $\Lambda = 2.29$ μm, $d1/\Lambda_{int} = 0.46$ and $d2/\Lambda = 0.64$. Its dispersion is shown by the red curve in Figure 4.6(a) together with the dispersion curves of all the other structures evaluated by the algorithm during the inverse search. Although the nonlinear parameter of this fibre is slightly smaller

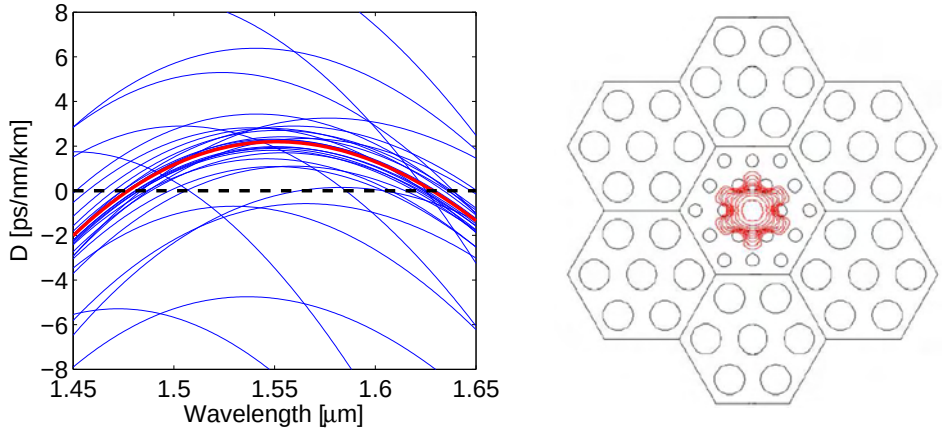

(a) (b)

FIGURE 4.6: (a) Dispersion curves of all the fibres evaluated during the inverse optimisation and, in red, the optimum solution; (b) best structure and 2 dB contour plot of its fundamental mode.

than for the ordinary SEST variant ($\gamma = 464$ W^{-1}km^{-1}), the confinement loss is rather small, even with only one ring of stacked elements (CL = 0.026 dB/m).

4.2.3 Analysis of fabricated fibres

The highly desirable optical properties of the optimum fibres obtained from the simplex optimisation encouraged the soft glass group at the ORC, and in particular my colleague J. Y. Y. Leong, to attempt fabricating the fibres. First the SEST fibre of Figure 4.4(a) was targeted. Several fibres, with slightly different structures and sizes, were produced and the best three were thoroughly analysed (HF1, HF2 and HF3, in the following). They had core sizes ranging between 2.4 and 4.5 μm, d/Λ of 0.48 in the outer region and 0.55 in the region surrounding the core. The scanning electron micrograph (SEM) of the cross-section of one of these, shown in Figure 4.7(a), was used to simulate the fibre's optical properties.

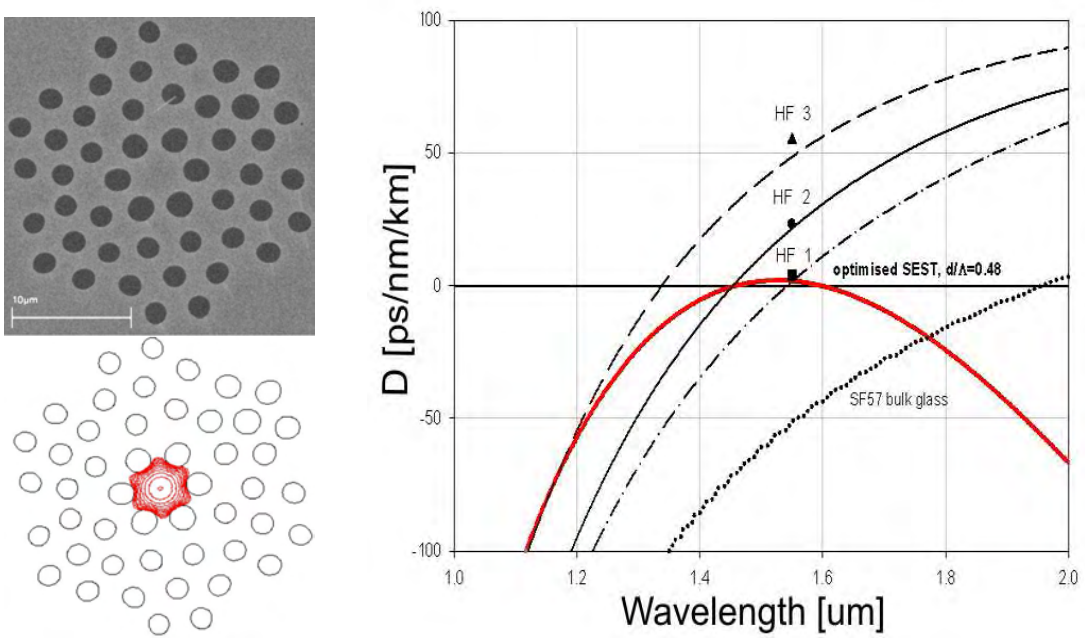

(a) Typical SEM (courtesy of J. Y. Y. Leong) (top) and simulated fundamental mode (2 dB contour plot, bottom)

(b) Simulated dispersion curves of the 3 fibres, compared to the measured values at 1550 nm (triangle, square and circle marker); in red is the dispersion of the optimum fibre.

FIGURE 4.7: Fabricated SEST fibres.

The simulated mode profile for all fibres exhibited the nearly hexagonal symmetry of the fibre core, in good agreement with the measured profile. The confinement loss of the fibres, estimated at a few dB/m, were only slightly smaller than the measured losses (between 3.2 and 4.3 dB/m), confirming that light leaking into the outer jacket is the main source of loss for these fibres and that an additional ring of holes is really required. The simulated nonlinear coefficients were 172, 246 and 414 W^{-1}km^{-1} for fibres HF1,

HF2 and HF3 respectively, in excellent agreement with the measured values of 170, 250 and 410 $W^{-1}km^{-1}$. Simulated and measured values agreed very well also for the group velocity dispersion, as can be seen in Figure 4.7(b). The noticeable structural differences between fabricated and target fibre did not allow the target dispersion to be achieved. Nevertheless fibre HF1 exhibited a ZDW near 1550 nm, with a $D_{slope}\sim$ 0.2 $ps/nm^2/km$, thus presenting a clear improvement over the suspended-core structures previously fabricated [50].

Finally, a few attempts were also conducted at the fabrication of the improved SEST fibre with two different hole sizes [Figure 4.6(b)]. An SEM of the cross-section of one of these attempts and its simulated mode profile and dispersion are shown in Figure 4.8. The holes in the central region partially collapsed during the fibre drawing and their final size, smaller than it was designed, did not allow the target dispersion to be achieved: at 1550 nm D was simulated at ∼-40 ps/nm/km. However the simulation confirmed that a small confinement loss of 0.03 dB/m can be achieved at 1550 nm by means of this design, with only one ring of stacked elements.

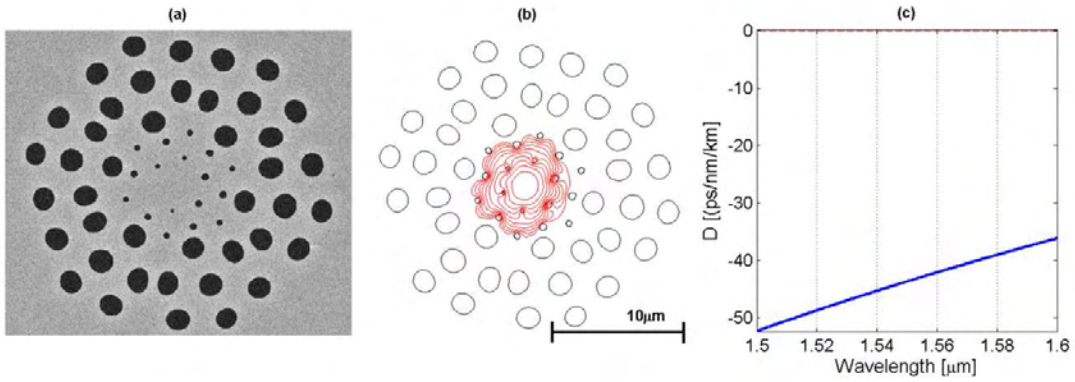

FIGURE 4.8: (a) SEM of the fabricated, improved SEST (courtesy of J. Y. Y. Leong); (b) simulated modal profile at 1.55 μm; (c) simulated dispersion.

The fibre was destroyed in the ORC fire (30/10/2005) before any characterisation of it was possible. Since then, the fabrication of soft glass fibres was stopped and this work has been put on hold. However, once our new facilities are available, we anticipate rapid progress in resuming the SEST fabrication approach, and ultimately realisation of our target structures.

4.3 Design of nonlinear, dispersion flattened silica HFs with a Genetic Algorithm

In this section the design of hexagonally stacked, small core silica HFs with a different hole size for each ring is considered, and a Genetic Algorithm (GA) is implemented in order to optimise the dispersion of such fibres. This section will present, after the background and the aims of the project, the results of the GA application. Some considerations about fabrication tolerances will be also presented.

Nonlinear fibre-based devices such as wavelength converters, parametric amplifiers, supercontinuum sources and switches are attractive candidates for application in future high-capacity, all-optical networks. In order to reduce the physical length and/or required operating powers, and to maximise the operating bandwidth of many such devices, it is generally desirable to use fibres with as high nonlinearity and low and flat a group velocity dispersion as is possible. As a result the development of dispersion-flattened, dispersion-shifted fibres with high nonlinearity has attracted considerable attention in recent years. Steady progress has been made and, by careful design and engineering of the refractive index profile, conventional doped fibre fabrication approaches have been used to produce fibres with dispersion slopes as low as 0.0002 ps/nm^2/km with nonlinear parameters of 10 W^{-1}km^{-1} [189] at wavelengths in the C-band. These figures represent the current state-of-the-art, in terms of trade-off between dispersion flatness and nonlinearity per unit length, for fibres with zero-dispersion wavelengths around 1550 nm. It is to be appreciated that fibres with higher nonlinearity can be produced, but only by compromising the dispersion slope.

On the other hand it has already been demonstrated, in a number of examples in the previous sections, how holey fibres (HFs) can produce high nonlinearities and, at the same time, unique dispersive properties. The large index contrast between silica and air allows for extremely tight optical confinement and a strongly wavelength dependent effective cladding index, providing the possibility to compensate for the material dispersion over an extremely broad wavelength range [70, 126]. So far nonlinear dispersion flattened HFs (NL-DFHFs) have been experimentally realised using triangular lattice cladding structures with constant diameter holes. For example, the fabrication of a fibre with 11 (and later 13) rings of uniform sized holes with $\Lambda \simeq 2.47$ μm and $d/\Lambda \simeq 0.23$ was reported in Refs. [71, 190], closely corresponding to structure with zero dispersion and zero dispersion slope identified in Section 3.2. Alternatively, a hybrid germanium doped triangular core with 12 rings of air holes ($\Lambda \sim 1.4$ μm and $d/\Lambda \sim 0.5$) was proposed [72]. The large number of ring layers is required in both instances to reduce the confinement losses to an acceptable level, and this adds complexity to the fabrication process. More recently, it has been shown in a number of theoretical papers that by increasing the size of the holes in the outer rings it should be possible to reduce the number of rings of air holes required [191–193]. These studies indicate that between 4 and 9 rings of holes can

be sufficient to reduce the confinement loss of dispersion flattened fibres to values close to the Rayleigh limit, without significantly compromising the dispersion flatness. Various dispersion flattened fibre designs offering nonlinear parameters in the range between 2 and 44 $W^{-1}km^{-1}$ have been proposed.

These theoretical papers have been primarily concerned with establishing designs that provide flat dispersion and low confinement loss and so far no consideration has been paid to the fabrication precision required in order to obtain the desired dispersion behaviour. However, it has been demonstrated both experimentally [71], and theoretically [145], that small deviations from the target design due to fabrication inaccuracies for even the simplest structures (i.e. a triangular lattice, with uniform hole size throughout the cladding), can lead to a significant deviation from the anticipated dispersion properties. Understanding the sensitivity of the dispersion parameters to fabrication errors for different structural designs is thus an important issue.

In this section the optimisation of some of the NL-DFHFs already presented in the literature is targeted. In order to approach inverse design problems with a large number of free-parameters, a technique, more robust to the presence of local minima than the simple Downhill Simplex method illustrated in Section 4.2, is required. A Genetic Algorithm was chosen for the task, implemented and successfully applied to the problem. Its effectiveness in solving the inverse problem is demonstrated, as compared to the time consuming test-and-trial approach used previously to design fibres with multiple degrees of freedom. Typical statistical errors in both hole dimension and hole positions for a range of recently fabricated fibres are then assessed to establish the current structural accuracy within holey fibres produced using the stack and draw technique. The sensitivity of the dispersion of such fibres to fabrication errors is also analysed, allowing us to deduce some general guidelines for obtaining the desired dispersion characteristics.

4.3.1 The Genetic Algorithm

The Genetic Algorithm (GA) is a general adaptive method which can be used for solving search and optimisation problems, and it is part of the broader family of the so called *evolutionary methods*. The aim of the algorithm is to reproduce in a mathematically encoded way the genetic evolutionary process of biological organisms where, generation after generation, a natural selection of the 'fittest' individuals is applied. Rather than concentrating on trying many changes around a single design, the GA works by using a large population to explore many options in parallel. Starting from a random initial population, through the definition of a problem-dependent *fitness function* for the evaluation of each individual, and by using stochastic laws, the algorithm gradually improves the population fitness. GAs are generally not guaranteed to find the optimum, even if they can be efficient in finding acceptably good solutions in an reasonable time. They were designed with the purpose of searching efficiently large and poorly understood spaces,

where a specialised technique was not available: this is one of the main reasons why this method was chosen to tackle the inverse problem of designing HFs with many degrees of freedom. GAs have already been successfully applied to some inverse electromagnetic problems, such as the design of fibre Bragg gratings [194] or the design of constant hole size, dispersion flat HFs with only two degrees of freedom [195].

The basic principles of the GA were first laid down by Holland [196] and are comprehensively described in Ref. [197]. A pseudo-code, illustrating how a GA works, is shown in Figure 4.9.

```
BEGIN /* genetic algorithm */
      generate initial population
      compute fitness of each individual
      WHILE NOT finished DO
      BEGIN /* produce new generation */
            FOR (population size / 2) DO
                  BEGIN /* reproductive cycle */
                  select two individuals from old generation for mating
                  /* biassed in favour of the fittest ones */
                  recombine the two individuals to give two offsprings
                  compute fitness of the two offsprings
                  insert offsprings in new generation
                  END
      IF population has converged THEN
            finished := TRUE
      END
END
```

FIGURE 4.9: Basic scheme of a GA, after Ref. [11]

The algorithm has a parallel structure, working on several solutions, or *individuals*, of a large population at the same time. Each individual of the population is represented by a *chromosome*, which carries all the information about the parameters (*genes*) to optimise. Chromosomes are encoded into strings of values (either binary or real) and their 'fitness' is evaluated. During this phase, one direct problem is solved for each individual (in our case multiple FEM simulations at different wavelengths of the structure encoded into the chromosome), and a fitness value is assigned, according to how close the solution of the direct problem comes to the desired objective function. Individuals, randomly generated at the beginning, are then chosen for reproduction with a probabilistic law, that is more rewarding for the fittest (*selection*). Afterwards, reproduction is applied to selected pairs of parents, according to one of several possible *crossover mechanisms*. During reproduction, a genetic random error or *mutation* may occur with a certain probability, with the effect of allowing a bigger solution space to be searched. Next generation offsprings are ultimately generated, and their fitness value calculated. According to a predetermined law, they are then reintroduced into the original population, replacing some of the initial, less fit parents. The same loop of stochastic laws is then applied to the new generation. Generation after generation the average genotype of the population

improves and tends to converge towards the optimum, provided of course that proper care is observed to avoid *premature convergence* towards a local minimum.

In contrast to the Simplex method, where only the starting point and stopping criterion had to be decided, a large number of reproduction, mutation and reinsertion rules must be chosen for the GA, depending on the problem to solve. The main functional blocks of the Genetic Algorithm used in this study were contained in a `Matlab` toolbox[1] which allows the choice of several crossover, selection, mutation and reinsertion functions. Adaptation of the algorithm to a new problem is not straightforward, and a good choice of parameters and functions can improve the algorithm's efficiency by orders of magnitude, as I empirically verified in the several tests I conducted. Due to the rather long time required by each direct simulation (of the order of a few minutes), particular care was devoted, at the beginning, to the choice of functions and individual parameters best suiting our specific optimisation.

In order to illustrate typical behaviour of the GA, the results of 6 consecutive runs of the same minimisation problem are shown in Figure 4.10(a)n. The objective value of the best solution is plotted at each generation in the 6 cases, showing the random nature of the algorithm. Despite starting from different random populations, the GA tends to draw each population towards the same element. In this particular example, a population with a small number of elements was chosen on purpose, in order to illustrate the phenomenon of *premature convergence*. Although the algorithm effectively improves the solution, after a few generations all the individuals in the population may have converged to the same genotype, not necessarily corresponding to the optimum (this is particularly evident in the case of Sim. 3 in the example). This behaviour can be minimised by increasing the population size, by carefully choosing the objective function and by tweaking some probability-related parameters in the algorithm, such as the mutation rate. In Figure 4.10(b) the objective value of the best solution for one particular run is shown, together with the average value of the whole population; this shows how, during the optimisation process, that the GA sometimes generates worse populations than at the previous iteration. This allows a deeper search of the whole parameter space, reducing the chance of converging towards a local minimum.

It is finally important to notice that the number of direct simulations needed by the GA algorithm is on average N·G, where N is the number of individuals and G is the average number of generations necessary before convergence, and thus depends on the fitness function and on several other GA parameters. With N generally between 30 and 1000 and G, empirically found from a few to several hundreds, the importance of optimising the efficiency of the direct problem is evident. Parallel computation within each generation is certainly an option, which has not been implemented for the studies

[1] Available under a GNU General Public Licence at `http://www.shef.ac.uk/acse/research/ecrg/gat.html`

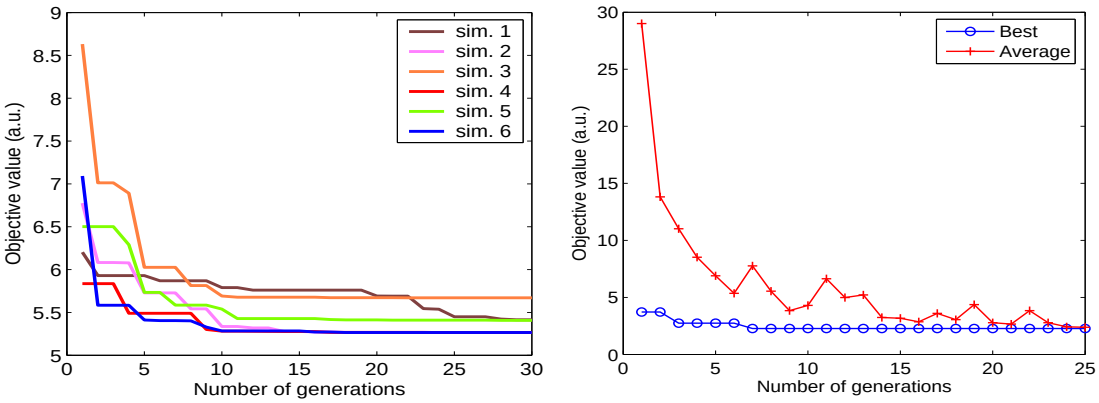

(a) (b)

FIGURE 4.10: Application of a GA to a minimisation problem. (a) Evolution of the fitness value for the best individual for 6 consecutive runs of the same optimisation problem. (b) Evolution of the best individual and of the average fitness of the total population.

in this section, but may be considered for future investigation, if sequential operation proves too inefficient.

4.3.2 Optimised fibres

The present study examines the class of fibres shown in Figure 4.11: F1 and F2 are a 4 and 5 ring structure respectively in which the size of the inner holes is scaled down in order to control the dispersion profile, while the outer holes are kept large to improve the confinement loss, as previously suggested by Saitoh *et al.* [191]. Fibre F3 is a 5 ring fibre where the holes within the three internal and two outermost rings are of the same size, thereby reducing the fabrication complexity whilst preserving a flat dispersion curve.

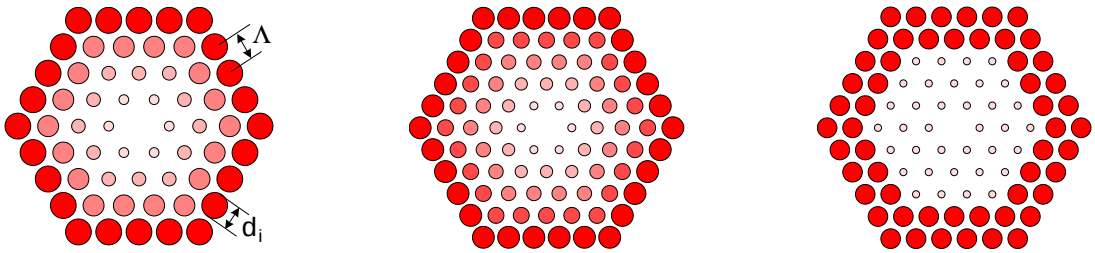

F1 F2 F3

FIGURE 4.11: Fibre structures to be optimised by the GA.

For most telecoms applications operation of the nonlinear device around 1550 nm is desirable, and this typically requires fibres with a dispersion magnitude and slope designed to be as small as is possible around that wavelength. It was therefore chosen to define a fitness function F, used to evaluate the 'quality' of a given structure and minimised by

the algorithm, as

$$F = \sum_{\lambda_i=1.5\mu m}^{1.6\mu m} |D(\lambda_i)| \tag{4.3}$$

where D is the dispersion parameter calculated at a wavelength λ_i, and the sum is performed over 5 (uniformly spaced) points in the wavelength range 1.5 - 1.6 μm. The free-parameters (or the 'genes' of the algorithm) are the pitch of the triangular lattice, Λ, and the diameter d_i of the holes in the i-th ring.

All the simulations were conducted on an initial population of 30 individuals, randomly chosen at the beginning of the computation. Convergence in the output fibre design specification was generally observed after 15 to 25 generations and took between 12 and 20 hours of computation time. Randomly controlled processes of selection, crossover and mutation were implemented between each generation [196].

The structural parameters of the best fibres of each type, obtained through GA simulations, are reported in Table 4.1. The worst-case effective area (A_{eff}) and confinement loss (CL) in the region of interest, hence those calculated at the longest wavelength of 1.6 μm, are also reported. Also included, for means of comparison, are the details of a fourth type of fibre, F4, which has equal sized holes throughout the structure. A GA optimisation was not required in order to optimise this design with only 2 free-parameters (Λ and d). By using the map in Figure 3.1 and a few further manual optimisations, an 11-ring design, close to that previously reported in Ref. [71], was obtained. The optimised dispersion curves for the 4 fibres are shown in Figure 4.12.

Fibre	**Λ** [μm]	**d_1/Λ**	**d_2/Λ**	**d_3/Λ**	**d_4/Λ**	**d_5/Λ**	**A_{eff}** [μm^2]	**CL** [dB/m]
F1	1.567	0.323	0.450	0.693	0.853	-	8.75	$3.8 \cdot 10^{-3}$
F2	1.516	0.317	0.484	0.571	0.632	0.667	8.3	$1.1 \cdot 10^{-4}$
F3	2.133	0.281	0.281	0.281	0.767	0.767	21.9	$1.6 \cdot 10^{-5}$
F4	2.406	0.251	0.251	0.251	0.251	0.251	38.7	$6.5 \cdot 10^{-1}$

TABLE 4.1: Structural parameters and optical properties of the best fibres obtained through the GA

A very flat dispersion behaviour with a dispersion parameter D between $\pm$ 0.1 ps/nm/km across the wavelength range of interest is found for all 4 fibre types. The dispersion slopes of all fibres are less than 3×10^{-3} ps/nm^2/km across the full 1.5 - 1.6 μm range considered, and remain below 1×10^{-3} ps/nm^2/km for more than 50 nm around the central wavelength. Refinement of the objective function in order to minimise the slope itself rather than the total magnitude of dispersion across a given wavelength range should permit even lower slopes about specific wavelengths in the C-band. As previously stated, a primary advantage of using the GA approach is that these structures were determined in a fully automated manner in a time of between 12 and 20 hours rather

than using the laborious manual test and trial approaches originally used to iterate to these general forms of structure.

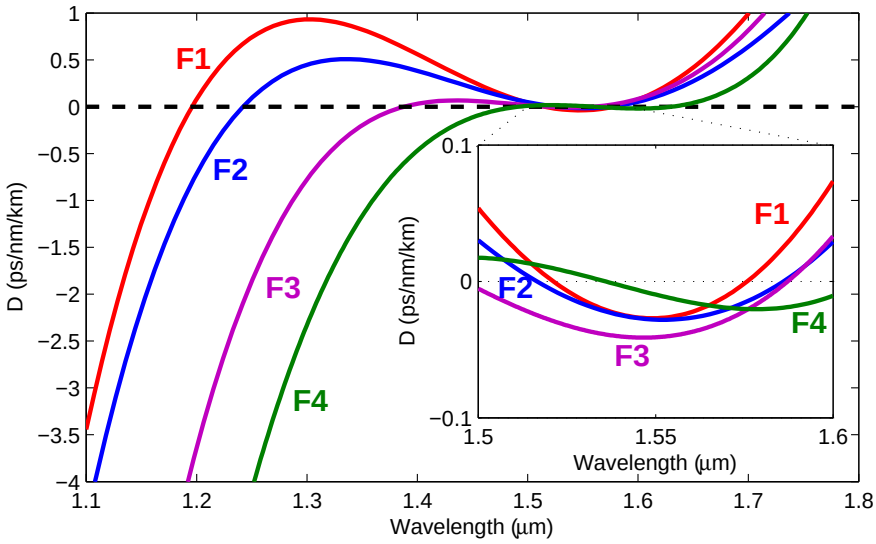

FIGURE 4.12: Solutions of the Genetic Algorithm for the 3 fibres in Figure 4.11. Plot F4 is the dispersion of an 11 rings structure with constant d/Λ for all the holes. The inset zooms on the wavelength range in which the fibres have been optimised

Despite a similar dispersive behaviour in the region of interest, evident differences can be seen in terms of A_{eff} and CL. Fibres F1 and F2 offer a higher nonlinear parameter γ whereas fibre F3 presents the best confinement loss. The simplest structure, fibre F4, despite showing the flattest behaviour, exhibits the worst characteristics in terms of both nonlinearity and confinement loss, and as can be seen in the map in Figure 3.2, an impractical number of more than 15 rings of holes would be required in order to reduce the confinement loss to a level similar to fibre F3. However we note that of all the fibres considered, only fibre F4 is rigorously single mode: fibres F1-F3 all theoretically present higher order modes that are localised between the innermost two rings of holes. However, the higher confinement loss of these modes and the large difference in effective index between them and the fundamental mode suggests that these fibres are likely to be effectively single mode in practice [193]. Note for completeness that, due to the larger mode mismatch, the splice loss to a conventional SIF is likely to be more significant for fibres F1 and F2 than for F3 and F4.

4.3.3 Practical fabrication considerations

Having demonstrated that fibres with exceptional flatness in a 100 nm range around 1550 nm can be theoretically realised using various different design approaches, the analysis went on to investigate how the inevitable imprecision introduced during the fabrication process affects the final dispersion profile. Before doing this, in order to inform our calculations, it was decided to establish the accuracy that we are currently

able to achieve in terms of hole size definition and positioning using the current stack and draw procedures. To do this Scanning Electron Micrographs (SEMs) of three fibres recently produced at the ORC were taken, and the hole diameter and shift from their target position on a hexagonal lattice for the 2 innermost rings of air holes was measured. These air holes have the largest influence on both the nonlinear and dispersive properties of the fibre. Two of the fibres were large mode area (LMA) HF designs and the third a small-core, high-nonlinearity (HNL) HF design. The results are summarised in Table 4.2 where, to measure the accuracy in hole size, the standard-deviation to the average diameter ratio is used, and the mean absolute off-centeredness over the average pitch (θ_{pos}) is taken as measure of precision in the hole position:

		Hole diameters				$\theta_{\mathbf{pos}}$	
Fibre	$\mathbf{\Lambda_{avg}}$ $[\mu m]$	$\mathbf{d_{avg}}$ $[\mu m]$	$\mathbf{d_{min}}$ $[\mu m]$	$\mathbf{d_{max}}$ $[\mu m]$	**st. dev. / $\mathbf{d_{avg}}$**	**Ring 1**	**Ring 2**
LMA-1	11.37	2.33	2.21	2.60	4%	2.4%	3.9%
LMA-2	7.65	3.79	3.65	4.09	3%	2.0%	2.6%
HNL-1	1.93	0.80	0.76	0.85	2%	2.2%	3.7%

TABLE 4.2: Fabrication tolerances for a range of structurally different fibres

It interesting to note that despite the large difference in terms of hole size and pitch between the two forms of fibre, the overall percentage discrepancies from the target values are all very similar. The hole size can be defined to a level of between 2 and 4% of the average value. The mean absolute distance between the holes and their optimum position in the triangular lattice was defined to a value of between 2 and 2.4% of Λ for the first ring of holes, increasing slightly to around 3-4% for the second ring.

In order to understand how this level of imprecision in fabrication manifests itself in terms of the overall dispersion behaviour, a set of simulations on all 4 fibre types was run, in which Λ and d/Λ were modified for each ring of holes by $\pm 1\%$, $\pm 2\%$, $\pm 5\%$ and $\pm 10\%$ from the optimum value. Note that this study serves to provide an upper bound on the severity of the fabrication imperfections, because in reality not all the holes are distorted from their optimum value or position in the same way, and some averaging effect is likely to occur. Results for fibre F2, presented in Figure 4.13, permit us to deduce the following general rules which are also valid for the other fibres studied:

- In the case of an already flat dispersion, an error in the pitch dimension mainly results in a shift towards a higher or lower value of the dispersion parameter. This can be used to achieve a slightly normal or anomalous flat dispersion from the same stacked preform or cane;
- The dimension of the first ring represents the main contribution to the overall dispersion slope, and particular care must be applied to try and match the optimum value, if a flat behaviour is required. Also it can be observed that an increase of

d_1 causes the dispersion parameter to decrease, the opposite behaviour is observed for all the other rings,. This has previously been observed in Ref. [192] and is further evidenced by the fact that HF for dispersion compensation needs a large air fill fraction for the first ring of holes.

- The overall contribution of the second ring to the total dispersion is still large, but it has less effect on the slope. An error in the dimension of the second ring of holes can be compensated through an overall scaling of the structure.
- The influence of the third ring of holes is more limited and, although not shown here, the contribution from the fourth and fifth rings is almost negligible. This suggests that for this fibre the holes in these rings can be designed with as large a d/Λ as desired to reduce the confinement losses.

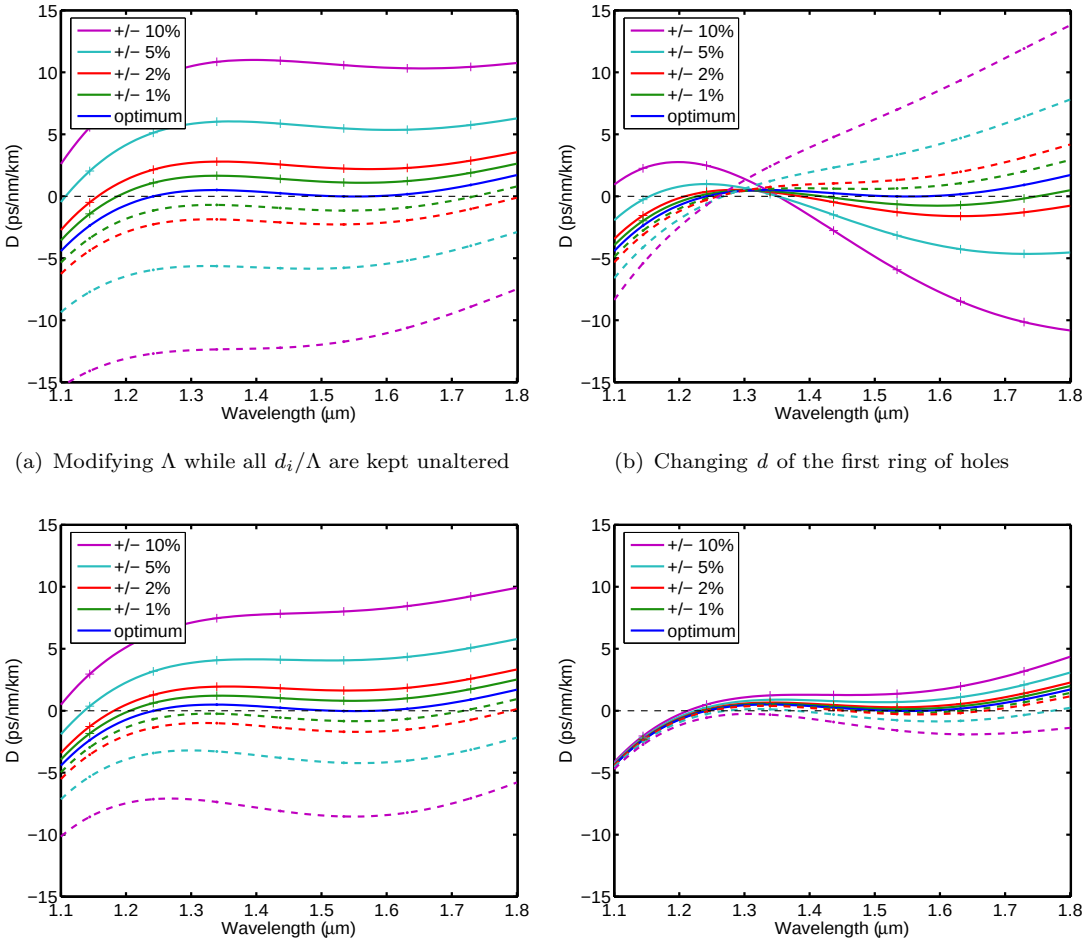

(a) Modifying Λ while all d_i/Λ are kept unaltered

(b) Changing d of the first ring of holes

(c) Changing d of the second ring of holes

(d) Changing d of the third ring of holes

FIGURE 4.13: Variation of the total dispersion profile as some structural parameters are changed for fibre F2. Dotted lines indicate a '-' variation, while continuous lines represent a '+' variation.

Figure 4.14 represents the effect of modifying the radius of an entire ring while the rest of the structure is unaltered. It is experimentally found that, while this occurrence is

very rare in the fabrication of fibres with equal hole sizes, it can easily happen during the pulling of fibres with different d/Λ per ring due to the different forces that each capillary is then subjected to, due to pressure and surface tension. Figure 4.14(a) shows that the detrimental effect of inaccuracy in the position of air holes in the first ring is even more severe than an inaccuracy in the hole size, and that off-centredness of the holes can cause significant modifications to the overall dispersion profile. Errors in the position of the second ring of holes also produces large undesirable effects. Effects within the third ring outwards are small and progressively less significant.

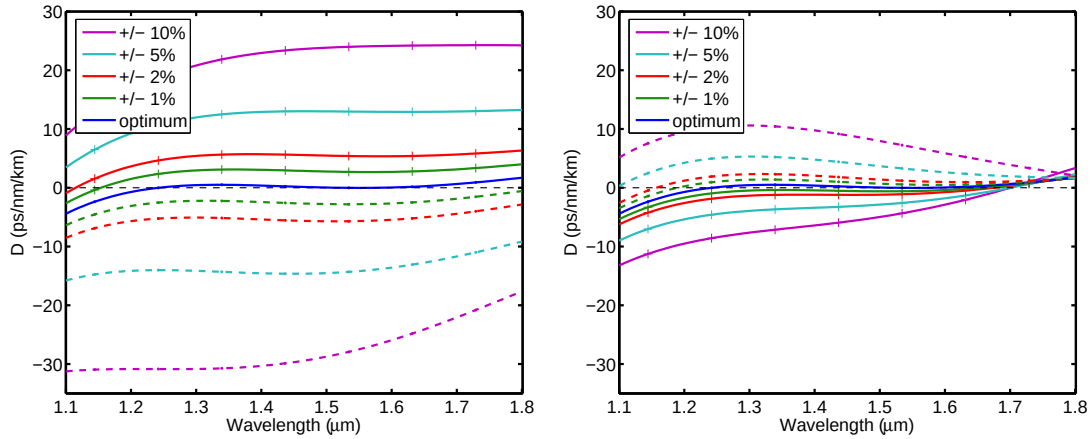

(a) Effect of moving the first ring of holes

(b) Effect of moving the second ring of holes

FIGURE 4.14: Variation of the total dispersion profile as all the holes in a ring are displaced from optimum position for fibre F2. Dotted lines indicate a '-' variation, while continuous lines represent a '+' variation.

A similar qualitative behaviour to that shown in Figure 4.13 and 4.14 for fibre F2 was also observed for the other fibre types, albeit with different magnitudes. To complete the analysis we present, in Figure 4.15, a sensitivity comparison between fibres F1-F4 to a change in d_1, which, as shown in Figure 4.13 is the most critical parameter as far as dispersion flatness is concerned. The average dispersion parameter $D_{average} = (D_{1.5\mu m} + D_{1.6\mu m})/2$ and the average dispersion slope $D_{slope} = (D_{1.6\mu m} - D_{1.5\mu m})/100nm$ are plotted for all the fibres as d_1 is either increased or decreased from its optimum calculated value. From both figures it is evident that structure F3 is generally the least sensitive to structural variations. Fibre F4 is also less sensitive to perturbations than fibres F1 and F2, other than for large positive errors which cause large negative dispersion shifts from the optimum. Fibres F1 and F2 exhibit similar behaviour, and are almost a factor of 2 more sensitive to fabrication errors than fibre F3. Their overall slope is also the most sensitive to imperfections of this type. Figure 4.15(b) also shows very clearly that in order to achieve the theoretically predicted ultra-low slopes of less than 10^{-3} ps/nm^2/km a precision of less than 1% has to be reached in the size of the first ring of holes with these types of NL-DFHF.

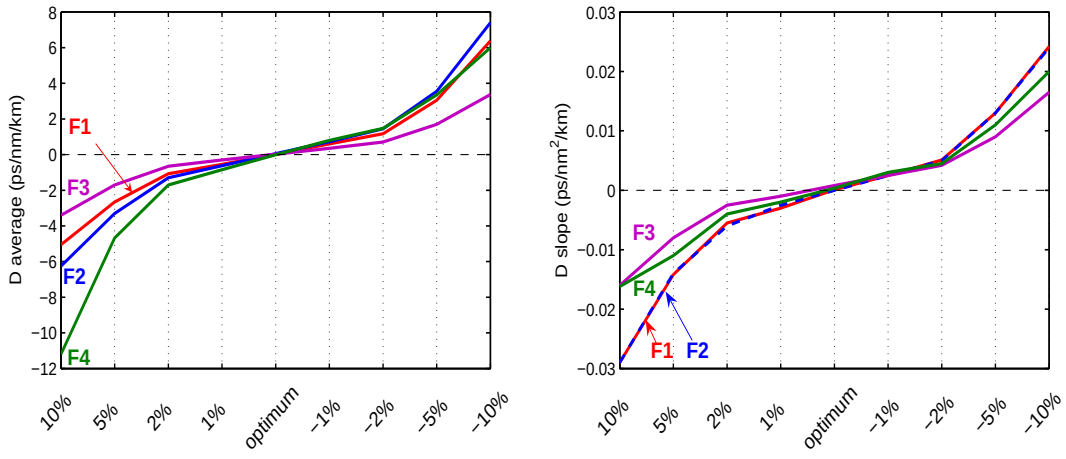

(a) (b)

FIGURE 4.15: Sensitivity of the 4 fibres to an error on the dimension of the first ring of air holes. (a) shows the average dispersion parameter and (b) the resulting dispersion slope in the interval 1.5 - 1.6 μm.

4.3.4 Discussion and conclusions

A GA has been applied, for the first time to the best of my knowledge, to the inverse design of HFs with a large number of free-parameters (up to 6) and for which the manual optimisation approach becomes unreliable and cumbersome.

The chosen design goal was a holey fibre with flat and nearly zero dispersion characteristics over a 100 nm range centred at 1.55 μm, and our approach has proved effective in finding various optimised solutions with D = 0 ± 0.1 ps/nm/km over the full wavelength range of interest. Despite possessing similar dispersion characteristics, the fibres analysed present different nonlinear parameters, ranging from 2.2 $W^{-1}km^{-1}$ for fibre F4 to 10.4 $W^{-1}km^{-1}$ for fibre F2. Fibre F3, representing a structural compromise between holes with the same size throughout the cladding and different hole sizes for each ring, offers an intermediate nonlinear parameter (γ= 3.9 $W^{-1}km^{-1}$). Similar values of dispersion slope and nonlinear parameter to those provided by the 4 NL-DFHF analysed here have also recently been achieved in conventional doped fibres [189] although it is to be appreciated that the fabrication tolerances are extremely demanding. However, it is well known that the higher index contrast of HF can lead to the realisation of fibres with a larger nonlinear parameter than is achievable with conventional fibres. Silica NL-DFHF with a nonlinear parameter as high as 44 $W^{-1}km^{-1}$ and slightly compromised slope have already been identified and simulated [192], and can be targeted more systematically in the future by extending the generic approach demonstrated in this section. Through the definition of different fitness functions, future work could also address the maximisation of the nonlinear parameter of NL-DFHF, or of their recently proposed figure-of-merit [29, 181]. Other useful design goals can also be targeted such

as flattened dispersion at wavelengths around 1 μm, or a dispersion characteristic with two specifically positioned zero-dispersion wavelengths (see Section 3.3).

Fabrication guidelines for the structures established in this section have also been proposed, indicating that the dimension of the first ring of holes is particularly important in controlling the dispersion flatness. It is also important to accurately define the pitch, the dimension of the holes in the second ring of holes, and the position of the first two rings of holes. During the work it was found that some geometries, like F3, beside presenting an easier fabrication target than fibres F1 and F2, are also nearly twice less sensitive to fabrication errors - albeit with reduced fibre nonlinearity. From the analysis presented, we can roughly estimate that an accuracy of order 1-2% will be required for most of the critical structural parameters in order to control the overall dispersion with reasonable accuracy. Measurements on some of our recently fabricated fibres indicate that such a level of accuracy is well within sight and should be achievable with realistic improvements in the preform fabrication and fibre drawing processes.

4.4 Conclusion

In this chapter two different, general methods for the optimisation of complex functions have been presented, implemented and applied to practical inverse designs. Using this approach nonlinear fibres with optimised dispersion characteristics have been designed and, in some cases, fabricated and characterised, showing a good agreement between simulated and measured values. Although the two methods presented are rather general and could have been used in conjunction with any of the other methods for the modal simulation of HFs (see Chapter 2), the efficiency of the method chosen for the solution of each direct problem – the FEM – allows these computationally intensive simulations to be carried out overnight, making this design approach suitable and appealing to a vast range of other design tasks. The combination of GA and FEM proposed in this chapter has been subsequently used, for example, by other groups to design broadband dispersion compensating fibres [198] or holey fibres optimised for gain-flattened discrete Raman amplifications [199].

Although these inverse approaches have quite a large applicability in the structural inverse design of fibres, they both require a parametrisation of the structures to be optimised. For example, in the previous examples the holes were assumed to be circular, and their radius was a free parameter. Since the parametrisation must be chosen a-priori, the existence of potentially better solutions cannot be excluded. Alternative methods able to modify the structure and topology of the fibre's cross section in a way free of any pre-fixed rules would represent a further improvement and are currently under examination. An example of such a method is the Level-Set method, which can be employed to move arbitrarily the interface between two media [200]. If this algorithm is

driven by the generalised gradient of the function to optimise, a very powerful topology optimisation method is constructed, as the work by Kao *et al.* [201] for the maximisation of photonic bandgaps for in-plane propagation demonstrates.

Chapter 5

Other fibre designs

5.1 Introduction

This section presents additional modelling work and fibre designs carried out during my PhD using the modal solver based on the finite element method. These studies have been conducted in collaboration with a number of colleagues, in order to complement and reinforce their fabrication and/or experimental work. Every time a comparison between a measured and simulated value was possible it showed a good agreement, indicating the reliability and accuracy of the implemented full-vector method, and also that simulation results can be employed to reliably design new fibres and to predict optical properties where actual measurements are not possible.

A particularly useful feature is the possibility of simulating an exact representation of a real, fabricated fibre, through the processing of an SEM image of its cross-section. This method is used, in the first part of the chapter, to study the performance of a fabricated suspended-core fibre and to foresee some of its possible applications.

In the second part of the chapter, my contribution to a larger project, aiming at the production of fibre sources for efficient white light generation, is presented. A fibre with a suitable core shape and dimension for optimised supercontinuum generation in the visible is designed. Some modelling is conducted in order to support experimental observations of parametric processes in the visible region of the spectrum, taking place in the cladding of microstructured fibres.

5.2 Modelling suspended-core holey fibres

In this work, FEM modelling is applied to studying an index guiding fibre, obtained from a drilled-preform, that can achieve, at the same time, a very high mode overlap with air and a very small mode field area. The fibre was fabricated and characterised at the ORC by my colleagues Dr. M. Petrovich and K. Mukasa [12, 202]; FEM modelling, based on high definition SEM images, was used to confirm the experimentally measured properties and to infer the behaviour of similar structures, scaled to different sizes. The study suggests possible applications for this fibre in evanescent-wave chemical sensing of gases and liquids, as a dispersion compensating fibre, or as a polarisation maintaining, highly nonlinear fibre.

The basic idea is shown in Figure 5.1: the hollow region is composed of just three holes, and the core is suspended on thin struts; we term this structure suspended core holey fibre (SC-HF). A similar structure has been obtained previously in soft glass using an extrusion technique [27, 29]. The simple structure of SC-HFs presents some key advantages over the triangular lattice-based structures examined in the previous chapters. Firstly, the fabrication of the preform is considerably less labour-intensive. Secondly, the core size can be chosen to be very small, in order to obtain the maximum fibre nonlinearity for a given glass, or even smaller than optimum in terms of nonlinearity, in order to increase the percentage of field in air. The holes can be made much larger than the core dimensions and, by allowing the struts to be sufficiently long and thin the confinement loss can be reduced to negligible levels.

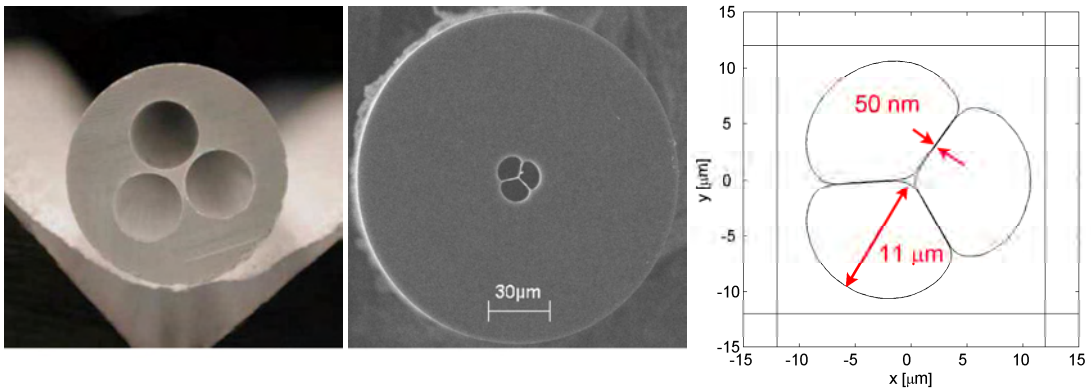

(a) (b) (c)

FIGURE 5.1: Suspended core holey fibre: (a) drilled preform and (b) SEM of the final drawn fibre [both images courtesy of Dr. M. Petrovich and K. Mukasa]. (c) shows the cross-section employed in the FEM simulations, obtained from a highly magnified SEM image and surrounded by PML layers.

5.2.1 Fibre fabrication, characterisation and modelling

High precision ultrasonic drilling was employed to fabricate the microstructured preform shown in Figure 5.1(a). The core and microstructured region were obtained from a single, very high purity silica rod, produced by Vapour Axial Deposition (VAD) [157]. After ultrasonic drilling, the bores were mechanically polished in order to reduce the surface roughness. Finally, the preform was dehydrated, using a standard technique, and fire polished. Then it was drawn into a fibre via a two-step process, during which the three holes were expanded to the required size. Several fibres, with different core dimensions, were fabricated. The one shown in Figure 5.1(c) and Figure 5.4(a) has 0.8 μm core diameter, the cladding holes measure $\sim$11 μm in the radial direction and the struts are approximately 8 μm long in their thinnest section, where they are only $\sim$50 nm thick. Despite such an extreme geometry, these fibres were found to have good mechanical properties and tolerance to bending; in addition they could be spliced to highly nonlinear (HNL) standard fibres with splicing losses that, although high ($\sim$10 dB), were found to be in accordance with the value expected from the mode-field diameter mismatch. We expect that, through the use of even smaller core HNL fibres or through properly designed tapered fibres, these losses can be considerably reduced.

The biggest challenge in the fabrication of HFs with subwavelength core dimension is to obtain a low transmission loss. There are three main loss mechanisms affecting small core HFs: confinement loss, which is due to the finite extent of the cladding region; absorption loss, induced by surface and bulk hydroxyl impurity; and scattering loss, due to surface roughness at the silica/air interfaces [113]. The fibre was designed and fabricated with a separation between the core and the outer silica jacket sufficient to obtain a negligible confinement loss at telecoms wavelengths. Therefore the latter two mechanisms were expected to be predominant. Loss measurements for two different fabricated samples, shown in Figure 5.2, indicated a transmission loss at 1.55 μm between 0.15-0.20 dB/m and showing only weak dependence on the wavelength, proportional to about $\lambda^{-1.1}$ (as opposed to the usual $\propto \lambda^{-4}$ dependence due to Rayleigh scattering). This is in good agreement with recent results by Roberts *et al.* [158], clearly indicating that the predominant loss mechanism is the surface roughness scattering due to frozen-in surface capillary waves.

The transmission properties of the SC-HF were modelled using our FEM-based mode solver. The calculations were based on the fibre profile shown in Figure 5.1(c), which was obtained from a high magnification digitised SEM image. This method allows a precise determination of the guided modes and their properties. These include effective mode area, percentage of power in air, confinement loss and group velocity dispersion. The wavelength dependence of these properties was studied, as well as their dependence on the core diameter, simply obtained by rescaling the whole structure. Figure 5.3 shows the modes (2 dB contour plots) calculated at 1.55 μm for four different core sizes (0.6,

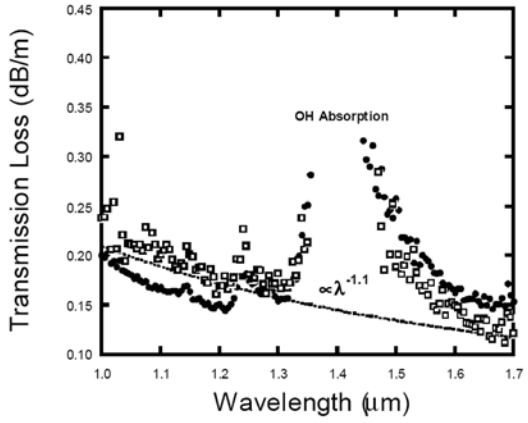

FIGURE 5.2: Loss spectra of two samples of SC-HF [courtesy of K. Mukasa].

0.8, 1 and 1.2 μm). It is obvious that the mode overlap with air increases with decreasing core size (d_{core}) over this range. The optical field distributions are not too dissimilar, but the mode becomes much less confined in the silica core in the smallest core size.

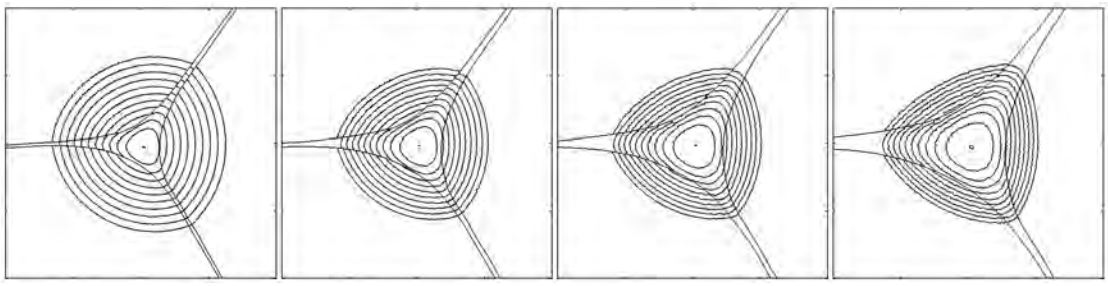

FIGURE 5.3: Simulated mode profiles at 1.55 μm (2 dB contour plots) of SC-HF structures with 0.6, 0.8, 1 and 1.2 μm diameters.

The wavelength dependence of the fraction of power in air, effective mode area and group velocity dispersion, calculated for different values of the core diameter, are shown in Figure 5.4.

Figure 5.4(b) very clearly shows the same trend as indicated by the mode profiles, i.e. the fraction of power in air increases with increasing λ and decreasing d_{core}. The calculations show that, for the fibre in Figure 5.4(a), nearly 34% of the power is transmitted in air at 1550 nm, and values in excess of 50% could be achieved with even smaller structures.

Figure 5.4(c) indicates that, for short enough wavelengths, the effective mode area decreases with decreasing d_{core}; however, when the wavelength becomes larger than about twice the core size, the trend reverses, a clear indication of the waveguide becoming less and less able to confine light in the core. The simulated A_{eff} for the fabricated SC-HF ($d_{core} = 0.8$) is 1.66 μm^2 at 1.55 μm. By using the approach detailed in Section 1.2.4 in order to estimate the nonlinear coefficient per unit length, this corresponds to a γ of 47.7 $W^{-1}km^{-1}$, which is in excellent agreement with the measured value of 49.7 $W^{-1}km^{-1}$.

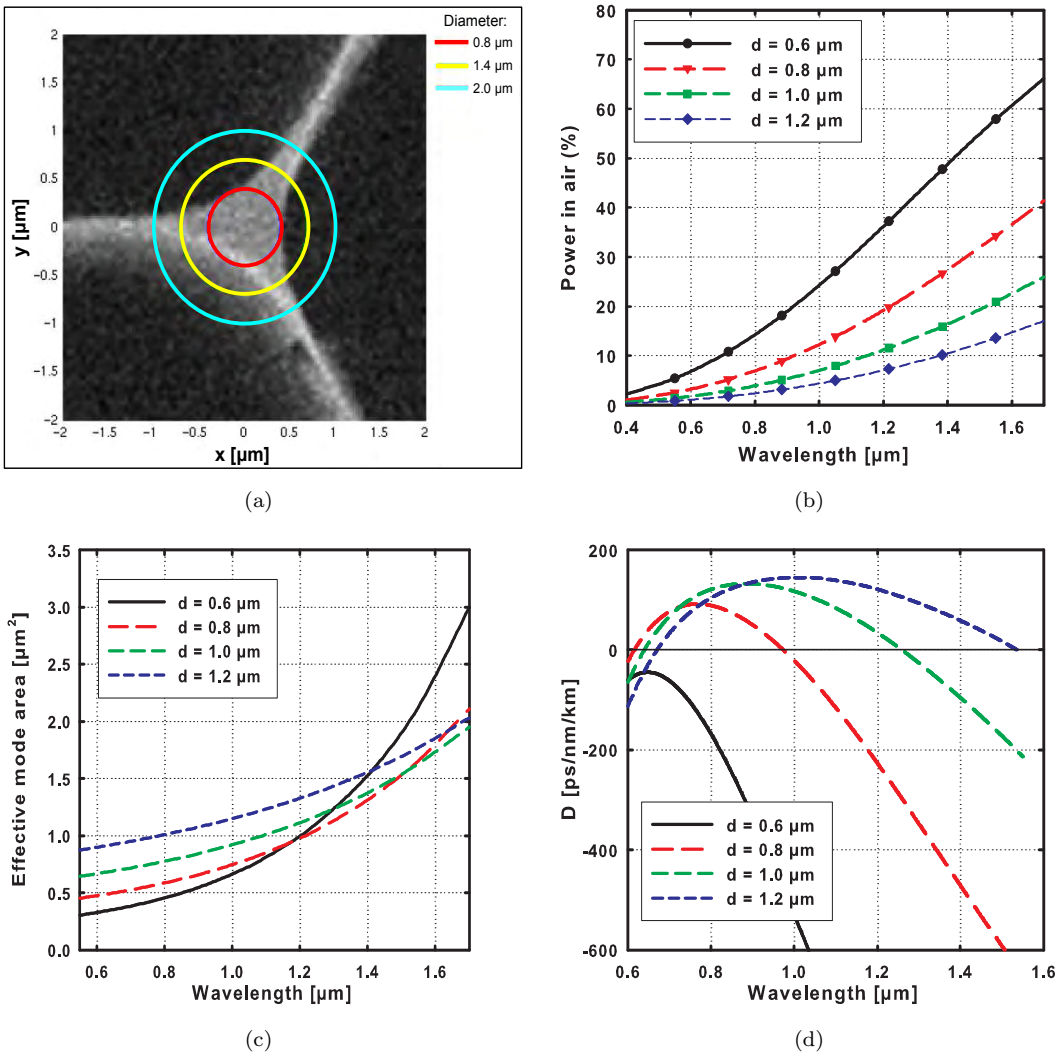

FIGURE 5.4: (a) SEM image of the core of a SC-HF. Simulated wavelength dependence of: (b) percentage of power in air, (c) A_{eff} and (d) group velocity dispersion for SC-HF structures with core diameters of 0.6, 0.8, 1 and 1.2 μm.

The simulated dispersion curves shown in Figure 5.4(d) illustrate the large amount of waveguide dispersion introduced by these fibres, as one should expect from their small dimensions and large index contrast. All of the smallest fibres present large and negative dispersion and dispersion slope at 1.55 μm; for $d_{core} = 0.8$ and 1.0 μm there are two zero dispersion wavelengths (ZDWs) between the visible and the near-infrared regions, while for $d_{core} = 0.6$ μm the dispersion is normal at all wavelengths considered. The two ZDWs of the larger structure ($d_{core} = 1.2$ μm) fall in the red and in the C-band, respectively. The measured dispersion of the fabricated fibre at 1.55 μm was -641 ps/nm/km, very close to the simulated value of -651 ps/nm/km.

Confinement loss calculations indicate that for all structures, except the smallest one,

this loss mechanism should be negligible (less than 10^{-6} dB/m) over the whole wavelength range 0.4 – 1.7 μm considered here. This seems to confirm our interpretation on the predominant loss mechanism previously reported. For $d_{core} = 0.6$ μm the confinement losses are negligible until about 1 μm, gradually increasing to about 0.05 and 2.6 dB/m at 1.55 and 1.7 μm respectively.

5.2.2 Device applications of SC-HF

The measured and simulated properties of SC-HFs, reported in the previous section, allow us to speculate on possible applications of this type of fibres.

The large mode overlap with air is a very attractive feature for sensing applications, where for example the concentration of pollutants in a gas can be determined by measuring the absorption that occurs as the evanescent light field propagates through the gas under test [203]. This can also be used for detection of trace chemicals or biomolecules; the long interaction lengths (hence high sensitivity) and small losses provided by these SC-HFs can offer a substantial improvement, as compared to systems based on bulk cells and unguided light beams. Moreover extremely small volumes ($\sim$ μl per meter length) are required to fill the holes, which is highly desirable when sampling hazardous substances or expensive preparations.

The first device reported using evanescent waves in an optical fibre for gas sensing employed a D-shaped fibre and had a very low sensitivity ($\sim$0.1%), as compared to sensing through an open path gas cell [204]. The advent of microstructured fibres opened up new opportunities for exploiting the much stronger evanescent fields that could be achieved. Early design studies by Monro *et al.* pointed out that careful design of the fibre geometry could afford reasonably high overlap between the guided light and the air holes [203, 205]. It was shown that the strength of the evanescent field in triangularly stacked HFs increases with the ratio λ/Λ, where λ is the wavelength and Λ the hole-to-hole distance. The simple rule of thumb $\lambda \geq 2.2\ \Lambda$ was suggested in order to identify structures with a large fraction of power in air, and it was shown that fibres with up to 30% of power in air at 1.55 μm are feasible if such a condition is satisfied. Hoo *et al.* [206, 207] have subsequently studied the sensor performance of commercially available highly nonlinear HFs and measured, at 1.53 μm, a maximum sensitivity coefficient of 12.6% as compared to a free-path gas cell[1]. While this represented a very substantial improvement compared to previous fibre-based evanescent sensors [204], it is still less than what is expected from theoretical predictions.

We have shown that the SC-HF design proposed in this section is theoretically capable of allowing $\sim$50% of the mode overlap with air, with small overall losses and a relatively simple fabrication procedure. The fibre with $d_{core} = 0.8$ μm was used in evanescent field

[1]The result refers to Crystal Fibre's HNL-HF: $\Lambda = 3.24$ μm, $d/\Lambda = 0.925$, see `www.crystal-fibre.com`

sensing experiments by my colleague A. van Brakel [12]. By comparing the absorption strength of the same line of acetylene (C_2H_2) measured in a standard free-path cell with the SC-HF results, an estimated relative sensitivity of 21.5% was obtained, corresponding to a percentage of power in the holes of ∼26%. This value, although smaller than that predicted by simulations, probably because of un-optimised launch conditions, is the highest mode overlap factor ever reported in an index-guiding HF, and is almost twice as high as the value previously reported by Hoo *et al.* [207], clearly showing the potential of SC-HFs for evanescent field sensing.

Moreover the fabrication technique that has been presented in this section allows the realisation of holes with a very large radius with respect to the core size, which is very advantageous in sensing schemes where a continuous flow of gas or liquid must be transported through the fibre. For streamlined flow of a liquid through a small tube, the volume rate of flow Φ is given by Poiseuille's formula:

$$\Phi = \frac{dV}{dt} = \frac{\pi |\Delta P| r^4}{8\eta L} \tag{5.1}$$

where V is the volume of the liquid, flowing in the time unit t, $|\Delta P|$ is the pressure difference between the two ends, η is the fluid viscosity, L is the total length of the tube and r is the internal radius of the tube. Since the flow rate $\Phi \propto r^4$, the advantage of a structure with large holes is evident.

The nonlinear and dispersive properties of the SC-HF can also be attractive for a number of applications. The very small core dimensions allow an effective nonlinearity approaching the maximum value ever reported for all-silica fibres of γ= 70 $W^{-1}km^{-1}$ [208]. Moreover, even slight asymmetries in the fibre structure produce, at such small d_{core}/λ ratios, quite a significant birefringence (measured in our fibres to be between 2 to 3×10^{-4} at 1550 nm), suggesting the potential use of those SC-HF as polarisation maintaining highly nonlinear fibres.

The large and normal dispersion achievable with $d_{core} < 1$ μm finally makes these fibres suitable for dispersion compensation in the C-band, while the high nonlinearity and the presence of two ZDWs around 1 μm for some designs can be used for flat and relatively source-independent supercontinuum generation (see Section 3.3).

5.3 Efficient generation of visible light

This section reports on two different solutions to the same challenging problem of exploiting HFs for the efficient generation of visible light. The FEM modal solver has been used, in the first instance, to design a suitable fibre for the generation of supercontinuum in the visible, while subsequently it has helped in interpreting the physical mechanism behind experimentally observed nonlinear phenomena in the propagation through the cladding of a microstructured fibre.

It has already been stressed many times in the previous chapters how HFs have now become a well established technology to provide tailorable dispersion profiles and within which to exploit specific nonlinear effects. A fibre suitable for efficient supercontinuum (SC) generation for 1.06 μm pumping was presented in Section 3.3. Supercontinuum generation in similar fibres has attracted a lot of interest in recent years due to its potential to produce white light sources [65, 209]. White light generation from a fibre can be implemented in a simple scheme and its main attraction resides in the remarkable spectral brightness achieved, compared to traditional white light sources [210]. A supercontinuum extending to the visible region can be produced in a HF from pulsed high-intensity bulk or fibre lasers, emitting in the near infrared. Although this technique is very simple, as it only involves a pump laser and a nonlinear fibre with suitable dispersion properties, it is relatively inefficient since generation of visible wavelengths is also accompanied by the transfer of a significant fraction of the pump power to longer wavelengths in the infrared. Two-pump schemes have also been demonstrated, but they also suffer from a similar low efficiency issue [211]. Improved efficiency can be obtained with a single pump beam, centrally located in the visible spectrum, to generate a supercontinuum restricted to the visible wavelengths. Besides the difficulty of obtaining powerful pump sources in the visible however, the fibre requirements are also more stringent in this case, because the technique requires a zero dispersion wavelength near the pump wavelength. Due to the difficulty in obtaining a ZDW in the centre of the visible spectrum, efficient SC in the visible has been reported so far only using alternative methods, such as using tapered conventional fibres [212, 213], cascaded HFs with decreasing ZDWs [214], or through the excitation of a higher order fibre mode [215]. The first part of this section is devoted to the study of a suitable, non-tapered and effectively single mode HF for this purpose.

Some applications such as laser projection displays, require very high spectral density at specific wavelengths in the visible. An alternative to supercontinuum generation is therefore to distribute the pump intensity between discrete wavelengths, so that the resulting spectral brightness is greatly enhanced. The generation of red, green, and blue radiation from a single, near-infrared source, combined with multiple frequency conversion steps using crystal based devices has been demonstrated at high power [216].

Despite its potential for power scaling, this technique involves a large number of components with complex optical arrangements. A simpler approach is to exploit the large nonlinearities of holey fibres and, in particular four-wave mixing (FWM), to produce specific, narrow wavelength, phase-matched bands. This study will be discussed in the last part of the chapter.

5.3.1 HF design for efficient supercontinuum generation in the visible

It is known that low and anomalous dispersion is key to an efficient SC broadening, as it enables the phase matching of the nonlinear processes broadening the spectrum to take place over a long fibre length. Optimising the fibre dispersion relaxes the need for high intensity pulses, allowing longer pulses to be used [217]. Efficient SC generation in the visible would therefore require one, or preferably two (see Section 3.3), ZDWs close to the pump, which in the following will be assumed to be at 532 nm (such as the one obtained by frequency doubling an Yb-doped fibre laser). Silica's material dispersion at 532 nm is however strongly normal ($\sim$-440 ps/nm/km) and a large amount of waveguide dispersion of opposite sign is necessary to obtain the required net-zero dispersion. One may wonder if any practical HF design exists, that is able to generate the desired dispersion characteristics. A literature search amongst fabricated fibres suggests that the shortest ZDW achieved so far in a HF is, to the best of my knowledge, 565 nm, obtained using a rather extreme cobweb design with a core diameter of $\sim$1 μm [64]. This section investigates whether (and how) this limit can be pushed to even shorter wavelengths.

It is well known from the literature that a fibre (or equivalently, a circular silica rod in air), tapered down to very small, wavelength-size diameters, can provide the required two ZDWs around 532 nm [212]. However, tapers are generally both short and fragile, and it would be desirable to obtain the same dispersion characteristics from a more structurally robust HF design. The study of the SC-HF in Section 5.2, on the other hand, seems to suggest that the shape of the core is fundamentally important to the maximum amount of waveguide dispersion obtainable: with a triangular and strongly concave core shape, it is not possible to achieve ZDWs shorter than $\sim$600 nm. All these considerations prompted us to conduct a detailed study on how the minimum ZDW achievable in a silica waveguide depends on the shape of the waveguide itself.

Please note that this study could have been presented, in a normalised and more general way, by ignoring the material dispersion and then simply analysing the maximum waveguide contribution to the overall dispersion. However I have chosen the present approach, related to a specific application of silica fibres, because it links well with the study illustrated at the end of the chapter, presenting an alternative solution to the same design problem.

The influence of the shape and dimension of a silica rod in air on the dispersion of waveguides with small cross-section is simulated for regular polygons with a circular, hexagonal, square and triangular shape. The core shape of two realistic HFs are also studied: a hexagonal core with rounded angles and six additional thin struts, closely representing the core of a fabricated *cobweb fibre* [such as the one in Figure 5.8(b)]; and the core of the SC-HF analysed in the previous section and obtained from an SEM image. Figure 5.5 shows the results. Note that, in the case of the fabricated fibres,

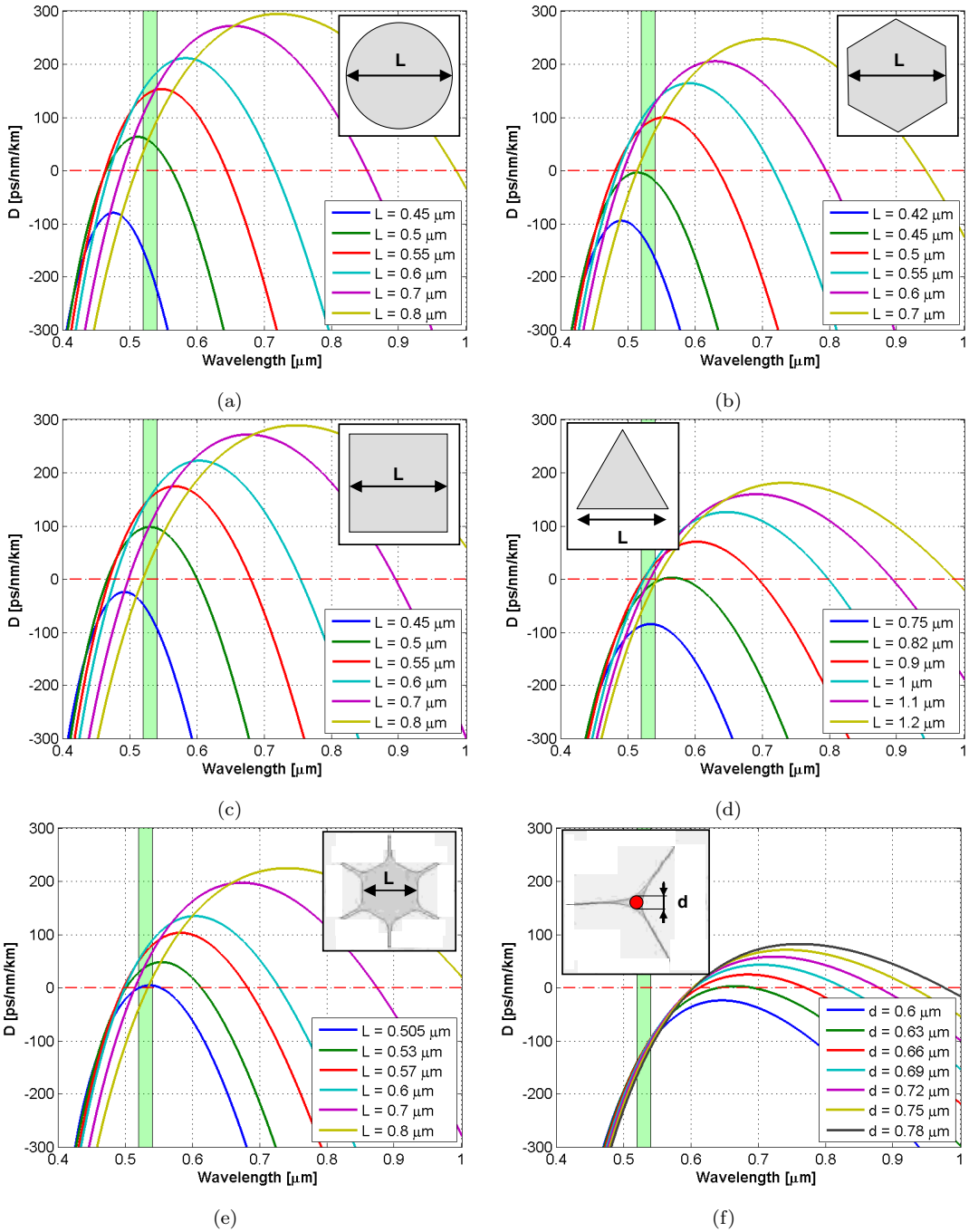

FIGURE 5.5: Dispersion curves for small-scale silica rods whose shape is: (a) circular, (b) hexagonal, (c) square (d) triangular and (e) hexagonal with struts. (f) shows the results for the core of the SC-HF analysed in Section 5.2.

neglecting the cladding is a reasonable approximation only in the wavelength region around the pump wavelength, where $\lambda/\Lambda \simeq 1$ and the field is highly localised in the core. For much longer wavelengths the field expands out of the core and the full fibre cross section should be analysed for accurate results.

Figure 5.5 shows that circular, hexagonal and square waveguides allow anomalous dispersion at the pump wavelength and at the same two ZDWs at shorter and longer wavelengths to be achieved, provided the appropriate waveguide dimension is chosen. It was previously shown in Section 3.3 how this dispersion profile is desirable in order to achieve a flat and relatively pump-independent supercontinuum. Conversely, the triangular shape is unable to achieve two ZDWs equally spaced around the pump, and only allows one ZDW close to 532 nm to be obtained. The plots in Figure 5.5 indicate an influence of the core shape on the achievable waveguide dispersion, and they suggest that, for application to the visible SC generation targeted in this study, the waveguide shape must be carefully chosen. This is further demonstrated by the analysis of the two realistic cores. The hexagonal core of a cobweb fibre with 6 very thin struts, only wide 5% of the core dimension, can still provide anomalous dispersion at the pump wavelength, as shown in Figure 5.6(e), even though the two ZDWs are shifted to longer wavelengths if compared to the perfect hexagonal case. In contrast, as already observed, the waveguide dispersion of a triangular SC-HF is insufficient to compensate for the material dispersion at 532 nm [Figure 5.6(f)].

All of these results are summarised in Figure 5.6, which shows the anomalous dispersion region achievable as a function of the area of the central rod and for the different core shapes analysed.

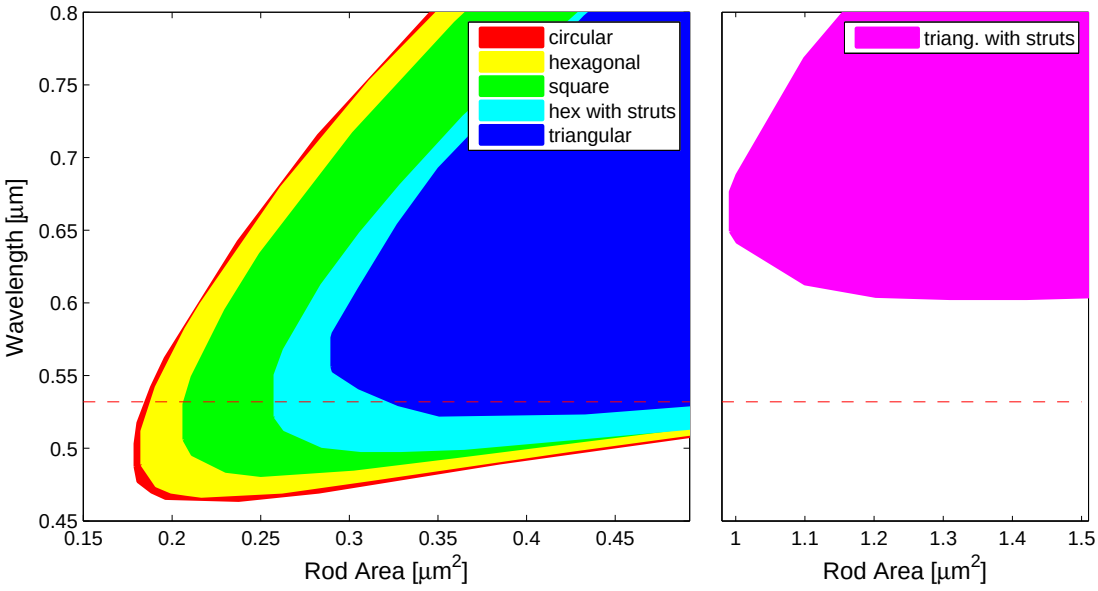

FIGURE 5.6: Anomalous dispersion region achievable as a function of the core size and shape. The dashed red line indicates the pump wavelength at 532 nm.

One important conclusion is that the circular shape allows, amongst all the shapes considered, the shortest theoretical ZDW to be achieved. The minimum wavelength for which an overall zero group velocity dispersion can be achieved in a silica rod is ∼0.46 μm, and it is achieved with circular waveguides of diameters around 0.55 μm. The remaining regular polygons provide an amount of waveguide dispersion which decreases with the number of symmetry axes. Furthermore, for a given symmetry (e.g. hexagonal or triangular), the maximum waveguide dispersion is decreased by the introduction of silica struts at the corners of the polygon, which increase the total concavity of the cross-section. All of these rules can be explained by considering that, for an optical mode concentrated in the core, the additional corners or struts extending out of it act like perturbations that reduce the cladding effective index. As a result the relative strength of the waveguide dispersion is also reduced.

To investigate further the influence of the struts on the achievable waveguide dispersion, a hexagonal core with 6 struts is simulated, and the strut thickness t is varied from 5% to 10% and 15% the core dimension L, as shown in Figure 5.7.

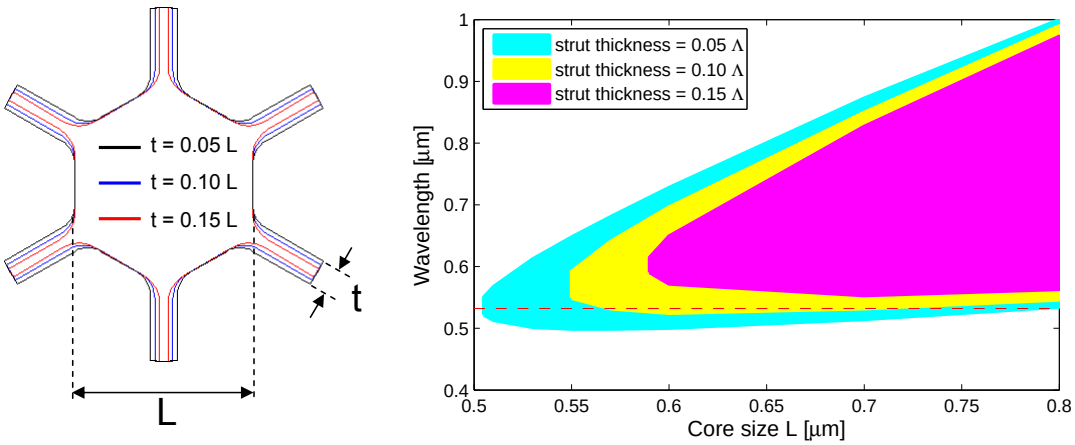

(a) (b)

FIGURE 5.7: Influence of the strut thickness on the overall dispersion: hexagonal core under analysis; (b) anomalous dispersion regions achievable.

The simulation results indicate that in order to achieve anomalous dispersion at 532 nm, care must be paid during fabrication in order to maintain the strut thickness to below 0.1 times L. Such thin struts may be difficult to achieve if the submicron core is obtained through tapering a larger core MOF, since some unavoidable hole collapse under the surface tension would tend to increase the strut thickness [212]. Although Leon-Saval *et al.* demonstrated SC generation in the visible, using 90 mm long MOFs tapered down to a core size of 500 and 700 nm [212], from the results in Figure 5.7 and from the SEM of their tapered cross section, one can conclude that their fibre's dispersion was probably far from optimum.

An improved control over the strut thickness can be, in principle, achieved during the fibre drawing, provided active pressurisation is used in order to control the holes expansion. Therefore, based on the previous results, a cobweb fibre with a structure similar to that of fibres already fabricated at the ORC [see for example Figure 5.8(a)] and with a dispersion profile allowing two ZDWs around the 532 nm pump has been designed. Its structure, fundamental mode and optical properties are shown in Figure 5.8(b) and Figure 5.8(c).

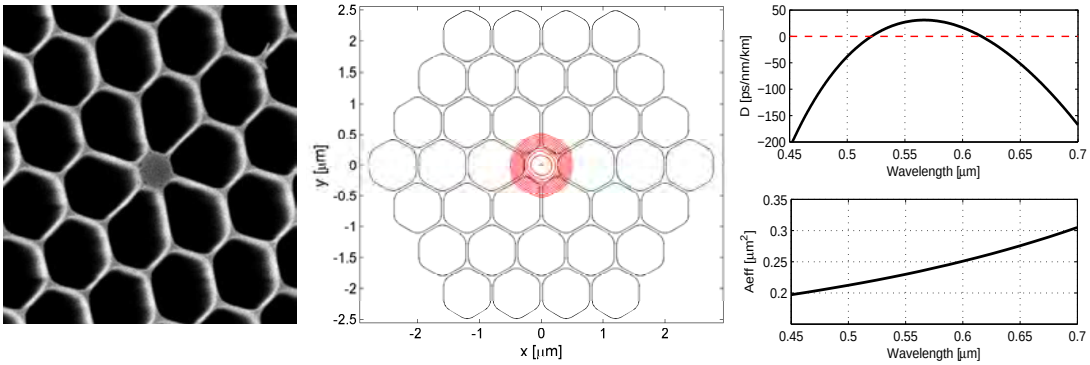

(a) (b) (c)

FIGURE 5.8: (a) Example of a fabricated cobweb fibre; (b) designed cobweb fibre for SC generation, with a core diameter of 0.55 μm (2 dB plot of the fundamental mode at $\lambda = 532$ nm, in red); (c) dispersion and effective area of the designed fibre.

Key to the achievement of the required dispersion properties are both the core diameter, which must be around 0.55 μm, and the air-filling fraction, which needs to be very large, corresponding to $d/\Lambda \sim 0.95$. At the short wavelengths targeted in this application the mode is extremely confined, and 3 rings of holes are sufficient to reduce confinement loss to less than 10^{-5} dB/m. The fibre is also strictly single mode in the whole wavelength range of interest.

5.3.2 Efficient white light generation in secondary cores of a photonic bandgap fibre

In this subsection, a second method to generate white light in a short length of microstructured fibre is described. The experimental realisation of it, led by P. Dupriez, employed sub-micrometre-scale secondary cores in the cladding of a photonic bandgap fibre (PBGF) as highly nonlinear waveguides; these were pumped by a green beam from a frequency doubled pulsed fibre laser. The resulting output beam contained discrete red, green, and blue (RGB) spectral lines, with equal frequency spacing between the green pump and the red and blue sidebands, characteristic of phase-matched FWM processes. FEM modelling was employed to identify the cause of this phase-matching. which turned out to be due to birefringent phase matching, resulting from the asymmetry of the secondary cores. Although all the FEM modelling presented here has been conducted by myself, I am profoundly grateful to Dr. P. Horak for his help and guidance in the analysis and interpretation of the results presented here.

5.3.2.1 Experimental setup

The experimental set-up is presented in Figure 5.9. The green pump laser is based on a fibre master-oscillator power amplifier (MOPA) source producing 80 ps pulses at 1060 nm, which is composed of four Yb-doped fibre amplifiers capable of amplifying the signal up to 200 W. These amplifiers are seeded by a gain-switched laser diode operating at repetition rates ranging from 32 MHz up to 1 GHz. The lowest frequency of 32 MHz is adopted to achieve maximum peak power with lowest average power. The collimated beam at 1060 nm passes through a half-wave plate to adjust its polarisation and is then focused into a 15 mm long LBO crystal to a spot diameter of 56 mm for optimal frequency doubling. The frequency doubled radiation at 530 nm is separated from the fundamental beam by a wavelength selective dielectric mirror. The green output beam then passes through a half wave plate to control the polarisation and is launched into the nonlinear cladding of a MOF, as described below. Although power scaling of this system up to 80 W average power in a nearly diffraction limited beam ($M^2 = 1.15$) is possible [10], in this experiment the output average power was restricted to 2 W, corresponding to a peak power of 780 W to avoid damaging the fibres.

5.3.2.2 Fibre design

The fibres considered in this study are photonic bandgap fibres (PBGFs) originally designed to achieve air-guidance in the hollow core around the following central wavelengths: 1070, 1210, 1550, 1800 and 2000 nm (fibres A, B, C, D, and E, respectively). The fibres were drawn from two different preforms: fibres A and B from one preform,

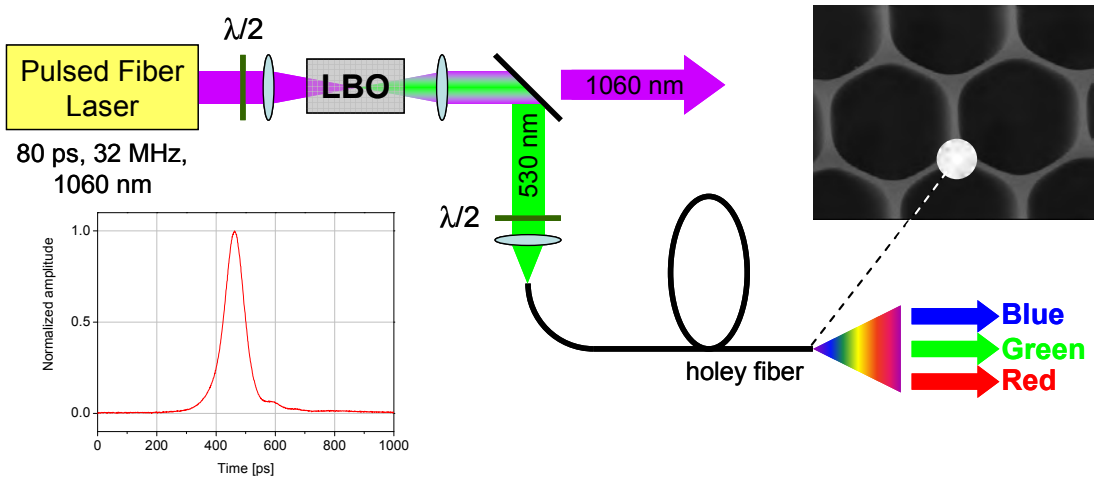

FIGURE 5.9: Experimental arrangement for the generation of RGB in a single secondary core of a holey fibre [courtesy of P. Dupriez]. LBO: Lithium Triborate (LiB_3O_5) crystal, $\lambda/2$: half-wave plates at appropriate wavelengths.

fibres C-E from the other. The geometry is similar in all cases and the fibres differ essentially only by the scale factor of the structure. For the work reported here, the fibres are not exploited for their air guiding properties but for the index guiding properties of the holey silica structure surrounding the hollow core. The fibre cladding is shown in Figure 5.10. It is formed by a periodic arrangement of air holes on a triangular lattice. Each hole can be accurately represented as a hexagon with rounded corners [110] and the entire structure is completely determined by three parameters: the hole-to-hole spacing Λ, the hole diameter d, and the radius of the circles used to round the corners r_c. Our fibres exhibit a relative hole size $d/\Lambda \sim 0.935$ and a $r_c/d = 0.25$, while the pitch Λ scales from 2.5 to 4.7 μm. In this study, we are interested in the light-guiding properties of the secondary cores in the cladding (indicated by the green circle in Figure 5.10), whose dimensions, measured by the radius of an inscribed circle, vary between ∼200 and ∼400 nm. This corresponds to a nonlinear parameter γ between 394 and 200 $W^{-1}km^{-1}$ for green light.

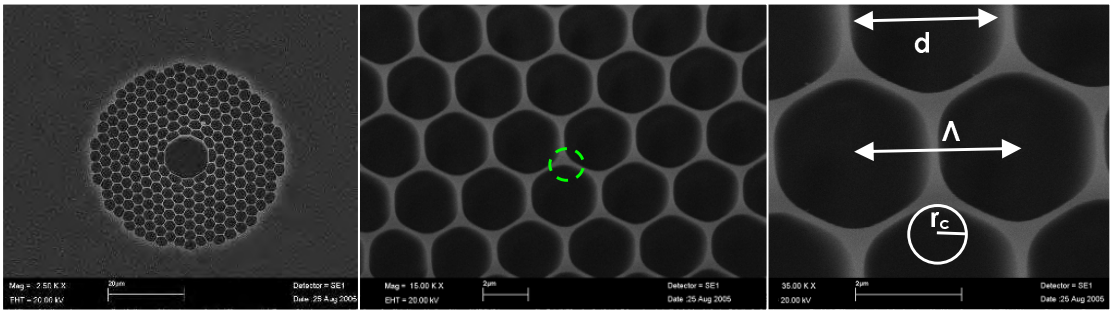

FIGURE 5.10: Typical SEM images of the fibres used for RGB generation.

5.3.2.3 Experimental results

The second-harmonic beam at 530 nm was carefully launched into a single secondary core in the cladding region of the different PBGFs using an objective lens. After propagation through 1 m in the holey fibre, the output beam and its spectrum were measured and analysed. The output power typically reached in excess of 300 mW for 2 W of pump power. Typical optical spectra, measured directly from the output of the different fibres, are presented in Figure 5.11. We observe distinct spectral sidebands appearing around the pump wavelength in the blue and red parts of the visible wavelength range. The separation between the generated frequencies and the pump frequency satisfies energy conservation, i.e. $2\omega_{green} - \omega_{red} - \omega_{blue} = 0$, which clearly points to a FWM process as the generating mechanism. The output spectra vary significantly among fibre samples as well as from core to core within the same fibre. For instance, fibre C could generate blue and red components separated by 100 nm to 300 nm depending on the launch conditions and the choice of excited core. Slight qualitative changes in the spectra of fibre E can be observed, in particular a broadening of the red sidebands. In order to improve our understanding of these features, we also plot in Figure 5.11 the dispersion of light propagating in individual secondary cores of fibres A-E, calculated for the idealised fibre structure as outlined in Section 5.3.2.4. We find that for all fibres the green pump is in the normal dispersion regime. However, for fibre E there exists a region of anomalous dispersion where soliton formation and subsequent Raman self-frequency shifting leads to broadening of the red sideband.

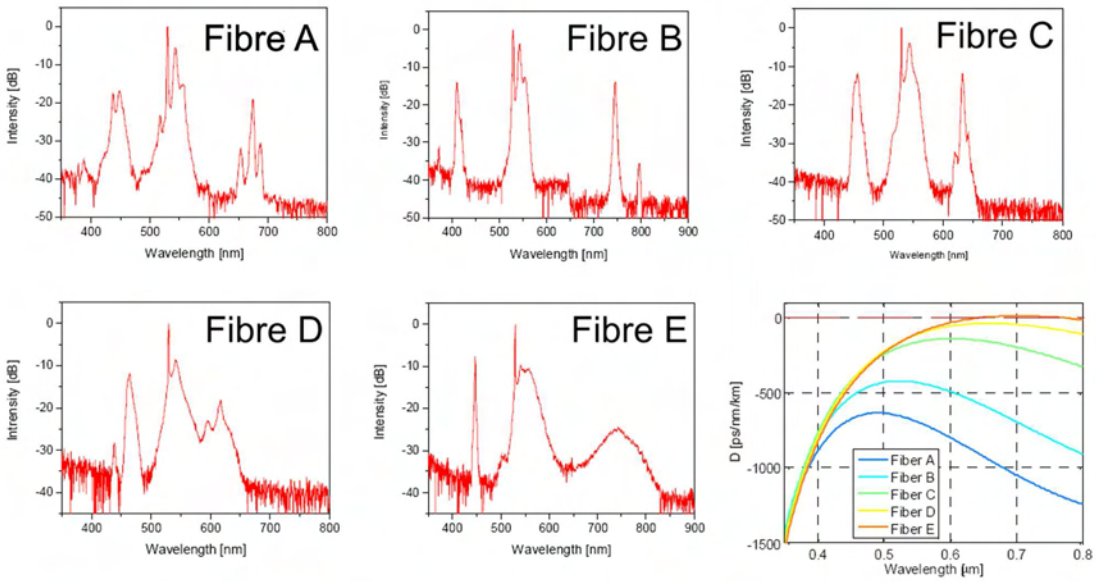

FIGURE 5.11: Normalised output spectra obtained from fibres A-E, and corresponding dispersion profiles calculated for a single secondary core as shown in Figure 5.10.

Figure 5.12 depicts the diffracted radiation emitted from fibre D. The use of red, green, and blue colour filters to image the individual colour mode at the fibre facet confirmed that all colours were generated in a single secondary core. A cut-back measurement with

fibre C revealed that the RGB generation takes place within the first 30 cm of the holey fibre. In fact, compared to the full length of 1 m, we observed a slight improvement in the FWM conversion efficiency at 30 cm, which we attribute to significant loss in the blue, resulting from surface scattering for the longer fibre. The maxima of the blue and red sidebands were less than 10 dB below the residual green pump. In this configuration, a total of 360 mW average output power was obtained with 47, 292 and 21 mW of blue, green, and red average power, respectively. In addition, a strong polarisation dependence of the FWM process was observed. The conversion efficiency to the sidebands was found to be highly dependent on the alignment of the input polarisation. In general, only one specific input polarisation state resulted in RGB generation. The output polarisation state of each spectral component was analysed and this showed that the red as well as the blue components were polarised orthogonally to the green pump beam.

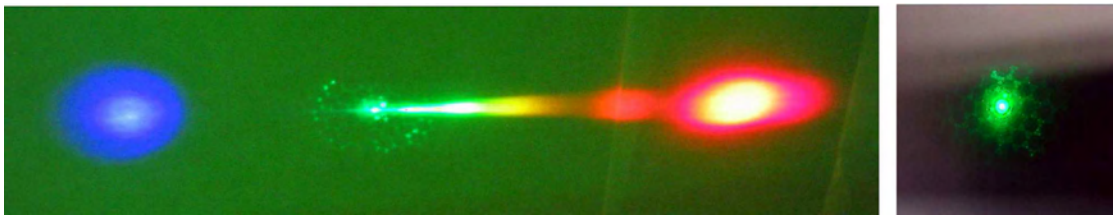

FIGURE 5.12: Left: Diffracted picture of the RGB components generated by fibre D. Right: The fibre output observed in the green and showing the location of the single excited core.

5.3.2.4 Modelling and interpretation

In order to interpret the experimental results and to understand the details of the underlying FWM process, it is important to identify the modes involved and to investigate the phase-matching conditions, which determine the exact wavelengths of the red and blue sidebands. To this end, we performed numerical simulations on the fibre cross-section using a our full vector FEM mode solver. A portion of the periodic cladding of our fibres, comprising either one or two silica cores and surrounded by air holes, was modelled with anisotropic perfectly-matched-layer (PML) boundary conditions matched to air. Propagation constants for the fundamental modes (FM) and for all higher order modes (HOMs) were evaluated at different wavelengths, and relevant phase-matching curves were calculated using the procedure described in Appendix B. We studied four different hypotheses, which could all in principle explain the measurements. We hypothesise that coupling occurs either (a) between FM and HOMs within a single secondary core; (b) between even and odd supermodes in a system of two identical, adjacent secondary cores; (c) between two modes centred in two adjacent secondary cores that are slightly different in geometry; or (d) between the two orthogonally polarised FMs within a single birefringent secondary core.

Because of the apparently large symmetry of the structures under investigation, we initially focused our attention on the idealised, perfectly symmetric, single-core structure shown in Figure 5.13(a). The structural parameters were chosen to match the average features of fibre C ($\Lambda = 3.66$ μm, $d/\Lambda = 0.935$, $r_c/d = 0.25$). Since such an ideal structure possesses a C_{3v} symmetry, its FMs are doubly degenerate [8], and phase-matching is only possible between a fundamental and a higher order mode. The propagation constant mismatch between a FM and any HOM is however too large to generate phase matching between the experimentally observed wavelength bands, and therefore this process cannot be responsible for RGB generation.

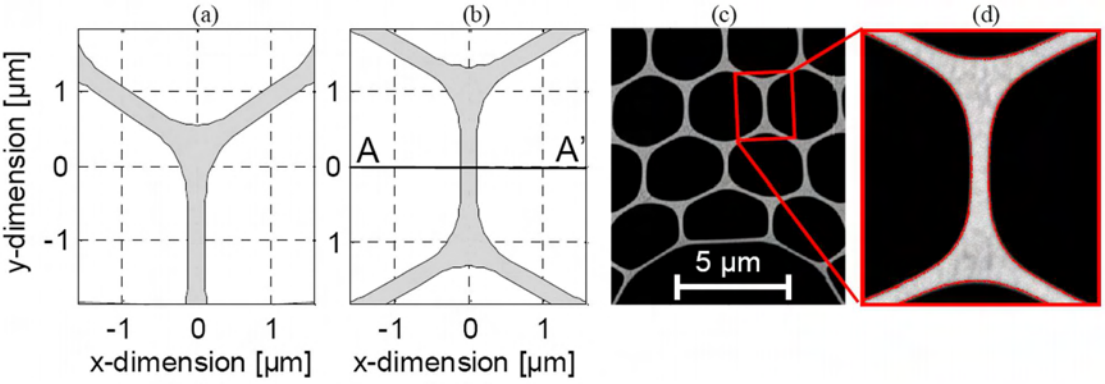

FIGURE 5.13: Idealised structure used in the simulations: (a) single-core and (b) double-core. In this example $\Lambda = 3.66$ μm, $d/\Lambda = 0.935$, $r_c/d = 0.25$. (c) High magnification SEM image of fibre C, and (d) detail of the simulated profile.

We then studied the possible interactions between multiple cores, focusing on the elementary cell consisting of two adjacent, separate cores, as shown in Figure 5.13(b). Such a structure possesses inversion symmetry with respect to the AA′ axis. Therefore, if the overlap between the modes guided in the two separate cores is not negligible, the structure supports either even or odd supermodes. Our calculations show that the splitting in propagation constant between even and odd fundamental supermodes is too small to explain the observed phase-matched peaks. On the other hand, good agreement of the measured sideband wavelengths with theory can be achieved by a number of specific even and odd higher order supermode pairs. However, a simple coupled-mode theory suggests that in this case light initially coupled into a single HOM would repeatedly couple into adjacent cores during the propagation and would eventually exit the fibre guided by multiple cores. This contradicts our experimental observation shown in Figure 5.12, according to which light at the fibre output was always confined to a single core.

Next, we investigated the effects of small structural fluctuations in a real fibre. Starting with a pair of secondary cores from a highly magnified SEM image of the cladding [Figure 5.13(c)] and through image thresholding and splining we obtained the contour shown in Figure 5.13(d), which was then meshed and used in the FEM simulation. The effective indices of the first 12 modes of such a structure and the mode fields and polarisations

of the two pairs of orthogonal FMs centred in each core are shown in Figure 5.14. The simulations show that, as a result of minor structural deformations, the difference in propagation constant between two modes centred on the different cores would produce phase-matched wavelengths approximately in the observed spectral positions. However, the overlap between modes propagating in the different cores is very small, with ∼10% of the intensity propagating outside the central core at 700 nm and much less than this in the green and blue, see Figure 5.14 (right). The nonlinear conversion efficiency by FWM would therefore be extremely small and in particular would be well below the efficiency of Raman conversion within the central cores, in contrast to the spectra shown in Figure 5.11.

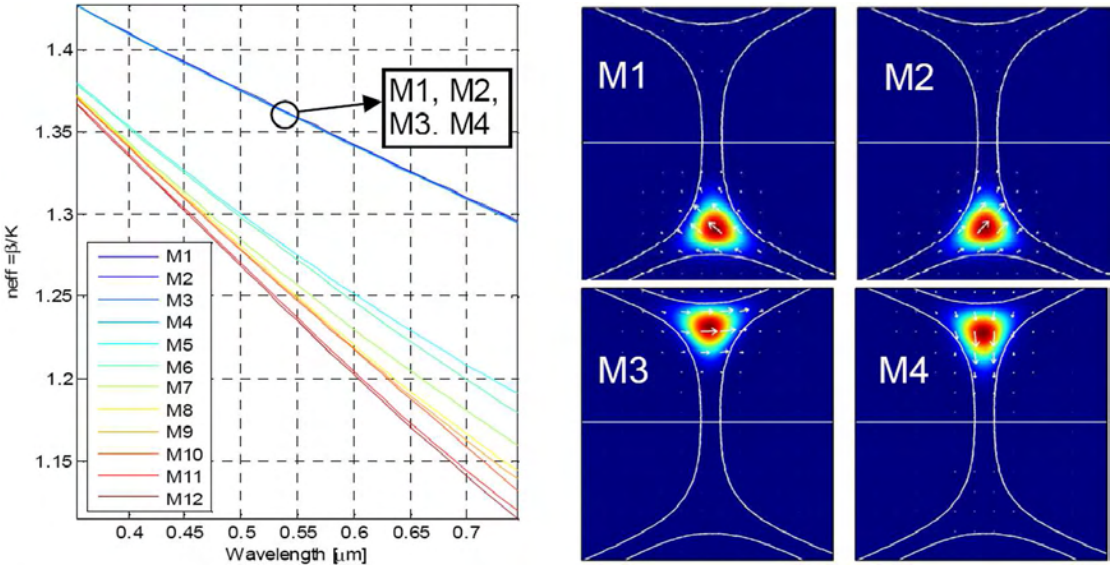

FIGURE 5.14: Simulation results for the structure in Figure 5.13(d): Effective indices of the first 12 modes (left); Mode intensity and polarisation distribution of the first 4 modes at 530 nm (right).

On the other hand, the simulations also show that each core exhibits a significant modal birefringence B, as large as 2.5×10^{-4} at 530 nm, where $B = |n_{eff_1} - n_{eff_2}|$, and n_{eff_1} and n_{eff_2} are the effective indices of the two orthogonal FMs. Phase matching can thus occur if the polarisation states of the signal and idler are orthogonal to that of the pump, which is in line with the experimentally observed polarisation dependence of RGB generation. The corresponding phase matching curves are shown in Figure 5.15. The phase-matched wavelengths agree well with the observed sidebands of Figure 5.11. Repeating the procedure for other cores, in the same and in other fibres, confirmed a value of modal birefringence in the green between 10^{-4} and 2×10^{-3}, with corresponding phase matching curves able to account for the range of sideband splittings observed in the experiment. Moreover, since all contributing modes are propagating within a single secondary core, their spatial overlap is close to 100% and we can expect efficient wavelength conversion. Because of the orthogonal polarisations of the pump and the sidebands required for birefringent phase matching in the normal dispersion regime, the

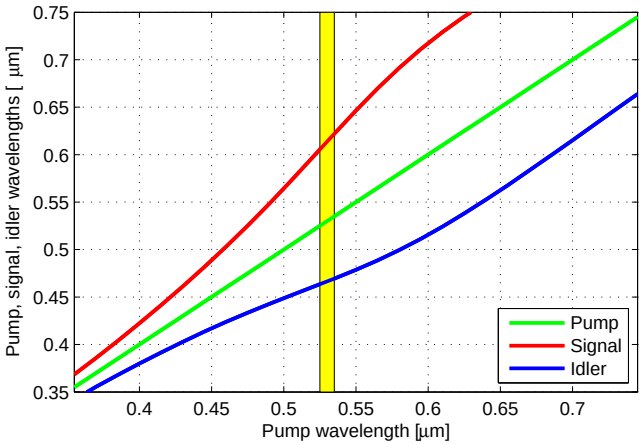

FIGURE 5.15: Phase matching curves for the modes of Figure 5.14: The pump is in mode M1, while signal and idler are in the orthogonally polarised mode M2.

nonlinear gain coefficient is reduced to 1/3 compared to the case of parallel polarisations. The peak gain for FWM processes is thus slightly below, but of the same order of magnitude as the peak Raman gain [6], in good agreement with the observed spectra where a Raman shifted peak of the pump is clearly visible and its maximum is comparable to or larger than the FWM sidebands. We thus interpret the mechanism leading to RGB generation in our fibre as a phase-matched FWM process between the polarisation modes of highly birefringent fibre cores. Note that this process has also been termed "polarisation modulation instability" in the literature [6] and has been observed in holey fibres [218, 219], but no such large splitting and high conversion efficiency has been reported in the visible region before.

In order to investigate the unexpectedly large value of birefringence obtained from simulations on the realistic fibre structure, we calculated the form birefringence resulting from deliberately deforming the ideal single core shown in Figure 5.13(a). The results of linear deformation along the x and y axes for fibres A, C and E are presented in Figure 5.16. As expected, the smallest structure (fibre A) exhibits the largest sensitivity to asymmetric structural variations. However, even for larger structures a scaling factor between 10 and 20% is sufficient to generate B $\sim 5\times10^{-4}$, which according to our model produces well spaced sidebands at ∼450 and ∼600 nm.

Note that this analysis is based on longitudinally uniform fibres. Overall, the required asymmetry of 10-20% seems compatible with the structure of our fibres [see e.g. Figure 5.13(c)], which, especially in the first few rings outside the core, exhibit small but significant deformation, due to expansion of the air core during the fibre drawing process.

To conclude the study, a remark on the conversion efficiency of the RGB generation reported here will be added. FWM can be a very efficient process with, in principle, up to 100% conversion of the pump power into the sidebands. In practice, however, the conversion efficiency is limited by several factors: (i) Because of the large spectral

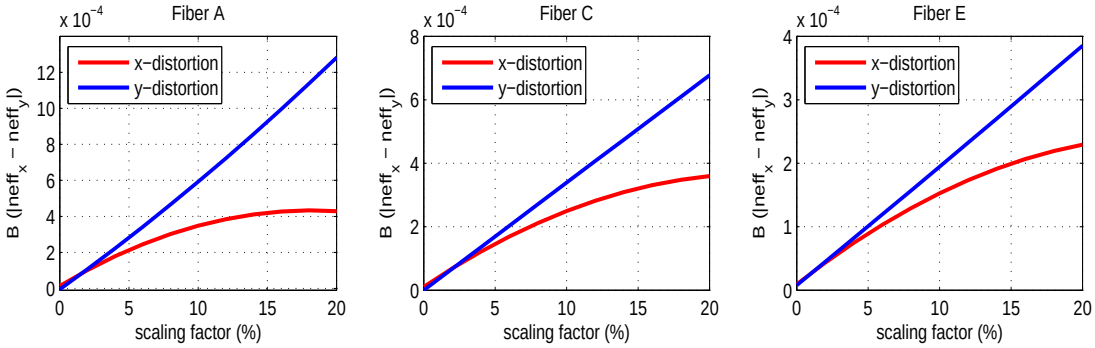

FIGURE 5.16: Simulated birefringence at 530 nm when a deformation (linear scaling) is applied along the x and y directions to a single core with structural parameters corresponding to 3 of the fibres under examination.

separation of the sidebands and the large group velocity dispersion in the visible regime, the short pump, signal, and idler pulses experience considerable walk-off. For example, two pulses at 460 nm and 625 nm, respectively, will be spatially separated by ∼14 mm after 1 m of propagation. The length of 80 ps pulses, on the other hand, is ∼16 mm. Therefore, efficient nonlinear conversion can only take place over about 90 cm of fibre and the pump power must be high enough to achieve sufficient FWM gain over this length. (ii) Our fibres exhibit relatively large wavelength-dependent losses; in particular fibres A and B with the smallest structures exhibit large losses in the blue. Consequently, we observed slightly smaller losses of energy after 30 cm of fibre than after 1 m, as discussed before. (iii) Stimulated Raman scattering competes with FWM. As already mentioned, for orthogonally polarised pump and sidebands, the peak Raman gain and the peak parametric gain are of comparable size. Therefore, a significant fraction of the pump power will be Raman shifted during the FWM process, which leads to a broadening of the pump spectrum and thus to lower FWM conversion efficiency. (iv) Fluctuations of the structural dimensions along the fibre lead to dephasing of pump and sidebands, and thus in turn reduce the energy conversion. (v) Finally, simulations conducted by my colleague Dr. P. Horak show that the nonlinear change of phase matching conditions as power is transferred to the sidebands restricts the conversion efficiency to less than 2/3 for an untapered fibre. A combination of all these effects is thought to have limited the maximum conversion efficiency in our experiments. Nevertheless, we observed up to 20% of the output power in the red and blue regions.

5.3.2.5 Conclusions

We have demonstrated the generation of RGB light from 80 ps pulses of green light. The pump was launched into sub-micrometre secondary cores in the cladding of a PBGF with large air-filling fraction. After 30 cm to 1 m of fibre propagation, discrete red and blue sidebands were observed. Detailed models of the fibre structure indicate that the RGB generation was based on FWM in single, birefringent cores, where the pump light

and the sidebands propagating in orthogonally polarised fundamental modes are phase matched. The observed spectral sidebands contained up to 20% of the total output power. Improving the coupling of the 530 nm pump light into a single secondary core would increase the pump peak power, which would allow for RGB generation in shorter fibre lengths and thus reduce the effects of spatial walk-off, propagation losses, and dephasing due to structural fluctuations. An optimised laser white light source with equal powers in the red, green, and blue spectral regions seems feasible in due course.

Part III

Photonic Bandgap Guiding Fibres

Chapter 6

Modelling ideal and fabricated PBGFs

6.1 Introduction

The historical development of hollow core photonic bandgap fibres (PBGFs), their potential applications and the physical mechanisms allowing guidance in the air core were introduced in Section 1.3. This chapter focuses on the modelling of these fibres. An idealised model aiming at representing as accurately as possible fabricated fibres is first presented and then extensively employed in order to study optical properties, scaling issues and material-dependent effects of PBGFs. Such a model, which can be efficiently implemented and solved, provides useful insights into the physics of PBGFs and has allowed us to obtain fundamental scaling rules to support the fabrication of such fibres. However, as is shown in the second part of the chapter, this model can not be employed to predict accurately the properties of fabricated fibres, for which even small scale imperfections need to be taken into account. With this aim, simulations of a structure extracted from SEM images can be employed. The benefits, potential and main issues associated with this method are presented.

6.2 Modelling ideal fibres

The vast majority of index-guiding fibres present a transversal structure which can be simply described as an arrangement of circular holes on a regular triangular lattice, around a central defect. Also the first hollow-core PBGFs presented a similar cladding, made of circular holes arranged around a more complex core [3]. However it was soon realised, that the size of the bandgap was roughly proportional to the air-filling fraction in the cladding; as a consequence, fabrication techniques allowing the realisation of

fibres with larger and larger air-filling fractions were developed. Increasing the air-filling fraction however resulted in the deformation of the cladding holes into increasingly hexagonal shapes. Although initial studies on PBGFs neglected the true shape of the holes, approximating them with circles (see for example Refs. [109, 116, 119, 121, 220–222]), Mortensen *et al.* realised that for a more accurate modelling the true shape of the holes – hexagonal with rounded corners – needed to be considered [110]. In this section we build on that work and propose an enhanced model containing 4 additional parameters for the accurate description of the glass boundary around the core: these will be essential in the detailed study of surface modes presented in Chapter 7. The model, which contains 8 free-parameters, is then used to study a typical PBGF with 7 missing cells in the core and to compare its properties with those of a 19-cell core fibre. Two studies are finally presented, which analyse the bandgap dependence on both some structural parameters and on the material properties of the glass host employed.

6.2.1 8-parameters model

The typical fabrication process of hollow-core PBGFs requires stacking circular capillaries in such a way as to leave a central cavity which will act as the light guiding defect. Such a preform is then drawn, in a single or in two consecutive steps, using a conventional fibre tower. The use of vacuum during the drawing phase allows the holes to expand, while the entire structure is scaled down to the required size. In such a way it is possible to eliminate the interstitials between the original capillaries and to achieve, in the final fibre, air-filling fractions larger than in the stacked preform. This fabrication procedure has also the effect of forcing the holes of those structures with an air-filling fraction larger than nearly 80% into an increasingly hexagonal shape. Mortensen *et al.* suggested a simple description for the shape of the resulting holes as hexagons with side-to-side distance d, and whose corners are rounded by 6 circles with diameter D_c [110]. Such an elementary unit cell is then placed on a perfect triangular lattice where the distance between the centre of each hole is Λ. In such a way the cladding of most fabricated hollow core PBGFs can be represented quite accurately. N complete rings of holes are then placed around a central core, which is formed by the omission of 7 or 19 holes. The hollow central area of these fibres is typically surrounded by a thin glass boundary, shaped as a dodecahedron as shown in Figure 6.1. In order to represent this interface as accurately as possible, we introduce four additional parameters: D_1 and D_2 are the diameters of two additional circles used to round a number of internal and external corners, while R_c and t_c are the radius and the thickness of the glass boundary, respectively [see the graphical representation in Figure 6.1(c)]. In order to obtain structures as similar as possible to those actually fabricated, the first two parameters (D_1 and D_2) will be fixed, for all the results reported in this thesis, to the value of $D_1 = D_c/\sqrt{3}$ and $D_2 = \Lambda/2$. In contrast, the influence of R_c and t_c on the optical performances of

the fibre will be thoroughly studied in Chapter 7, as these two parameters have been found to have a significant influence on the surface modes (SMs) of the fibre.

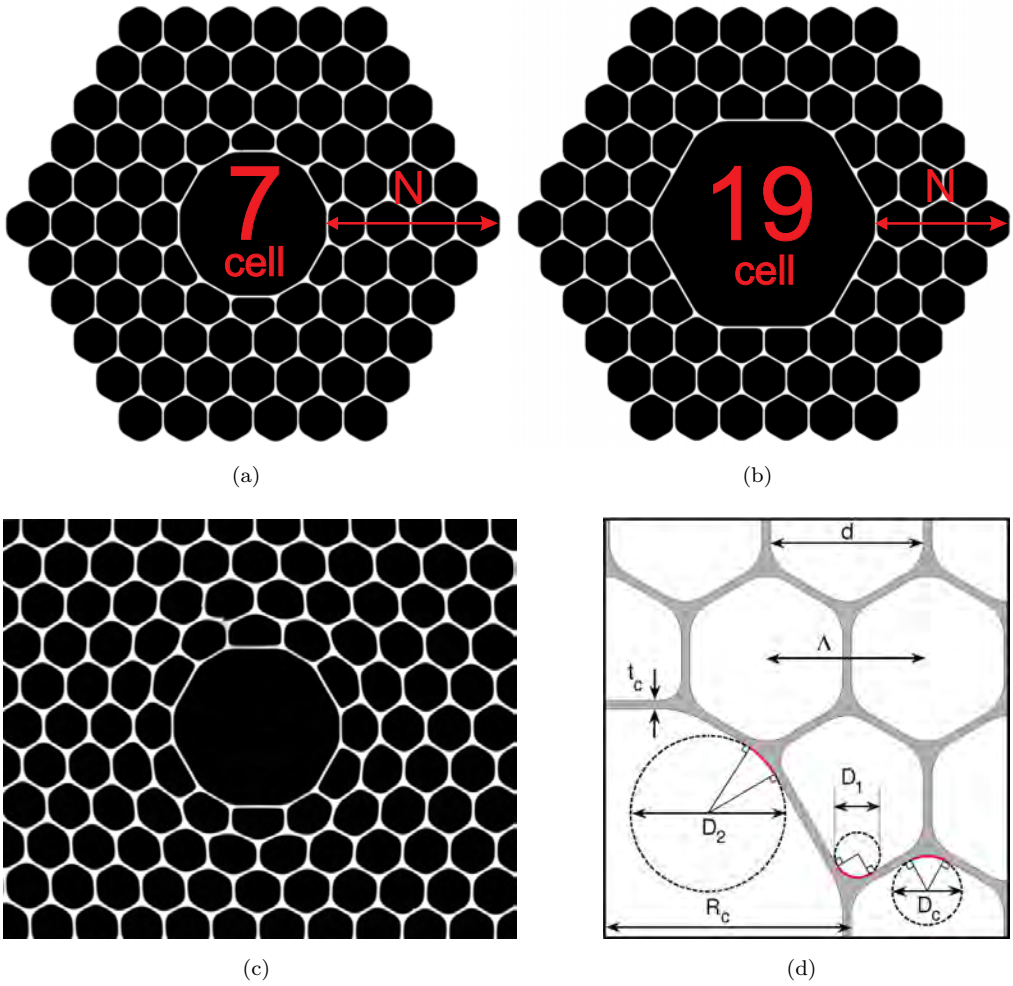

(a) (b)

(c) (d)

FIGURE 6.1: Model of a realistic PBGF: the cladding is composed by hexagonal holes with rounded corners and the hollow core is formed by (a) 7 and (b) 19 missing holes; (c) SEM image of a typical fabricated 7-cell fibre; (d) definition of the 7 parameters used in both models (the number of hole rings N is the 8th free-parameter).

Having introduced the structural model and its 8 free-parameters, the result of an FEM simulation of a typical 7-cell core, silica PBGF is shown in Figure 6.2. The fibre presents structural parameters that are achievable with the current fabrication process: $d/\Lambda = 0.97$, $D_c/d = 0.5$, 7 rings of holes outside the core ($N = 7$), a thickness of the core boundary equal to half the width of a typical strut in the cladding ($t_c = (\Lambda - d)/2$) and a pitch, $\Lambda = 4.33$ μm, all of which generates a fundamental bandgap crossing the air line between $\sim$1.5 μm and $\sim$1.85 μm. The top left box in Figure 6.2 shows the effective index plot of the fibre. The green patched area represents the PBG of the infinitely periodic cladding, calculated by simulating a unit cell with periodic boundary conditions with the FEM, and assuming a glass refractive index of 1.444. Lines and circle markers in this box and all other optical properties in the figure have been obtained by modelling the finite structure surrounded by PMLs with the FEM modal solver described in Section 2.4.4.

Red circles represent modes that are index-guided in the cladding (cladding modes, CM): since they cannot be guided at those wavelength where the PBG exists, their location can be used to identify the upper and lower edges of the PBG. The slight discrepancy between the PBG edges predicted by the two methods (infinitely repeated unit cell and finite structure with a defect) lies in the different mesh used and in the fact that for the finite structure the material dispersion is taken into account through the Sellmeier equation (Equation 2.24). The black line represents the effective index of the two degenerate air guided modes with the largest effective index, which from now on we will (improperly) call fundamental modes (FMs), even if the proper fundamental mode of the fibre would be an index guided mode at a much higher effective index. Blue circles are used to represent the effective index of the higher order modes (HOMs) which are always present in fibres with 7 or 19 cell core size, as can be verified by the density of modes argument reported in Section 1.3.2.1.

The remaining graphs in Figure 6.2 show the wavelength dependence of effective area, confinement loss, group velocity dispersion and percentage of power in the air core. The effective area is between 60 and 70 μm^2 and since the mode is mostly localised in air, by using the formulae reported in Section 1.2.4, this corresponds to a nonlinear coefficient $\gamma \sim 0.002$ $W^{-1}km^{-1}$, nearly three orders of magnitude smaller than for a solid core silica fibre with the same effective area. The decrease of A_{eff} with wavelength can be explained by recurring to the intuitive model presented by Digonnet *et al.* [223], which shows that air-core PBGFs can be reasonably approximated by step-index fibres with the same core dimension and with a wavelength dependent effective numerical aperture (NA). According to the model, the NA only depends on the band edges of the PBG, it is zero at the shortest wavelength at which the air-line crosses the PBG, and it increases with wavelength until reaching its maximum value at the longest wavelength at which the air-line crosses the PBG. The wavelength behaviour of the effective area reflects this trend and it reaches its minimum where the NA is maximum. The confinement loss reaches a minimum value of $\sim 10^{-5}$ dB/m and remains below 0.1 dB/km over a region broader than 200 nm. Note that, due to the tilt of the effective index curve with respect to the air line, the bandgap appears at slightly longer wavelengths than the one measured along the air line with the infinitely periodic cladding model. The dispersion curve shows the typical behaviour that is inherent, from the Kramers-Kronig relations, to any optical structure that has relatively sharp transmission features [93], and it presents extremely large normal and anomalous values at the short and long PBG wavelength edges respectively. The zero dispersion wavelength is off-centred with respect to the bandgap and it appears shifted towards the short-wavelength band edge because of the additional waveguide dispersion contribution [224]. The existence of a range in the transmission gap where the dispersion is large and anomalous appears thus to be a generic feature of these types of fibres. The percentage of power in the core region reaches 97% in the middle of the bandgap; only $\sim 0.5\%$ of the power resides in

the glass, while most of the remaining 2.5% in concentrated in the first ring of air holes.

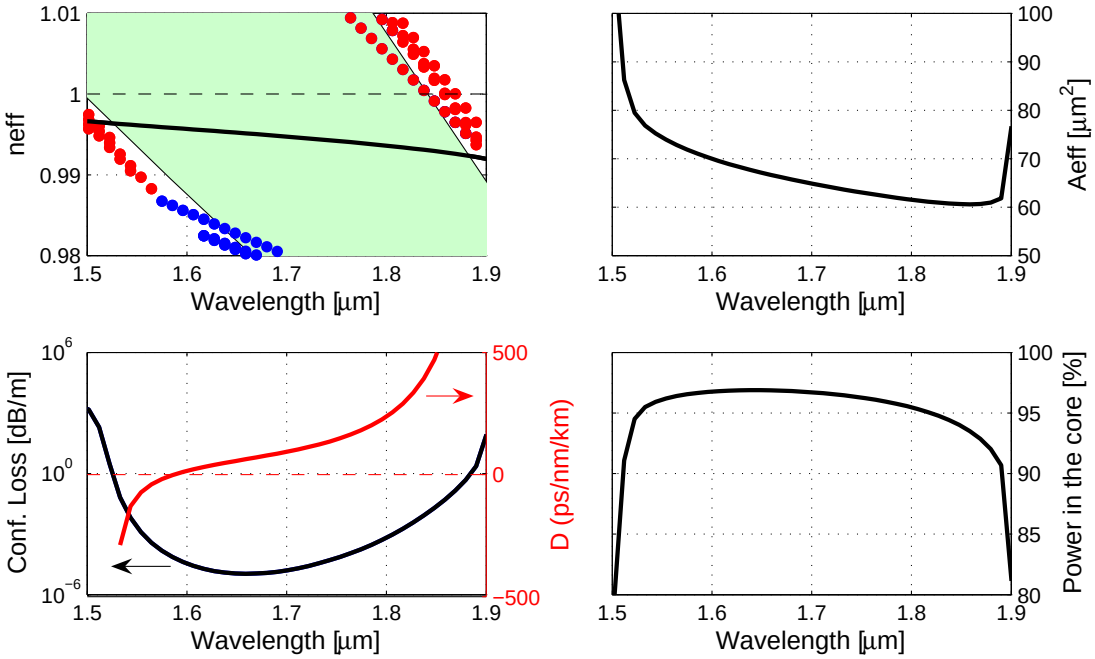

FIGURE 6.2: Simulated optical properties of a PBGF with a 7-cell core; the main structural parameters are $\Lambda = 4.33$ μm, $d/\Lambda = 0.97$, $D_c/d = 0.5$, $t_c = (\Lambda - d)/2$ and $N = 7$. The green patched area in the upper right figure represents the photonic bandgap of the unit cell in the cladding; the black line is the effective index of the air guided mode, red circles represent cladding modes and blue circles higher order modes.

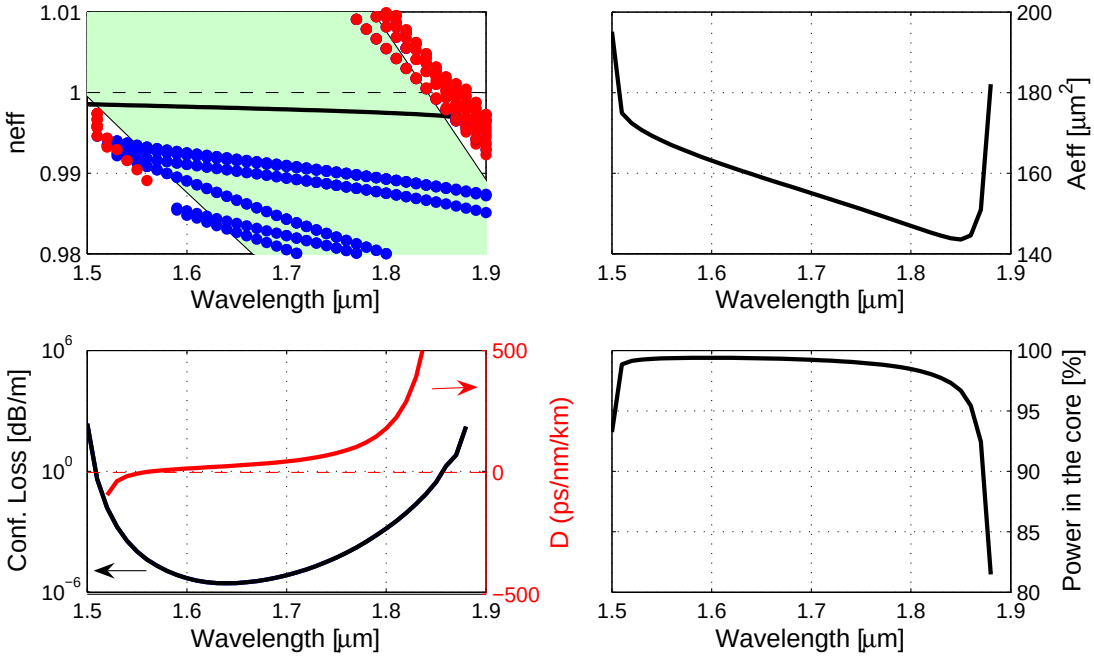

FIGURE 6.3: Simulated optical properties of a PBGF with a 19-cell core; structural parameters and colour codes are the same as in Figure 6.2.

As a means of comparison, Figure 6.3 shows the properties of a similar fibre with exactly the same cladding but with a core formed by the omission of 19 capillaries.

The increase in core area by a factor of roughly $19/7 \cong 2.7$ is matched by a similar increase in effective area ($A_{eff} \sim 160\ \mu m^2$). The larger core has also the effect of increasing the percentage of power in the core region to more than 99% of the total power; the amount of power guided in the glass decreases to less than 0.2%, which corresponds to an even lower nonlinear coefficient, $\gamma = 0.0007\ W^{-1}km^{-1}$. The lower interaction of the FM with the glass makes its effective index curve lie more parallel to the air line than for the 7-cell core case. As a consequence, the resulting bandgap and zero dispersion wavelength are slightly shifted to shorter wavelengths. The dispersion slope at the centre of the bandgap is smaller than for the 7-cell case. Finally, the higher density of modes that one would expect as a result of the larger core is numerically proven by the increased presence of higher order modes (HOMs) in the top-left effective index plot of Figure 6.3 as compared to Figure 6.2.

6.2.2 Bandgap scaling

The fibres studied in the previous section have been presented in order to provide a typical example of the optical properties of realistic PBGFs. These however represent only a subset of the achievable performances: from a fabrication point of view it is extremely important to understand how the various optical properties, and in particular the bandgap position and width, depend upon the size and shape of the holes in the cladding. This section studies the scaling rules that apply to the bandgap of hollow core PBGFs by using FEM simulations of the model presented in the previous Section.

The study by Mortensen *et al.* revealed that a useful quantity to introduce when considering PBGFs is the *air-filling fraction* of the cladding, f. This is defined, for an infinitely periodic cladding, as the ratio between the total area of the air regions to the area of the glass. From geometric considerations f is related to the geometrical parameters by [110]:

$$f = \left(\frac{d}{\Lambda}\right)^2 \left[1 - \left(1 - \frac{\pi}{2\sqrt{3}}\right)\left(\frac{D_c}{d}\right)^2\right]. \tag{6.1}$$

Figure 6.4 shows the values of f for typical values of D_c/d and d/Λ, showing that for circular holes ($D_c/d = 1$) the maximum achievable f is ~92%, corresponding to a non-realisable structure with touching circular air holes. A higher value of f can be obtained tough, if holes with a more hexagonal shape are employed.

The work in Ref. [110] demonstrated that both the normalised upper edge (λ_{up}/Λ) and lower edge (λ_{low}/Λ) of the PBG decrease as the air-filling fraction increases, and this reduction is, to a first approximation, independent on the exact hole shape. Figure 6.5(a) shows a numerical confirmation of this behaviour, calculated for a hole shape described

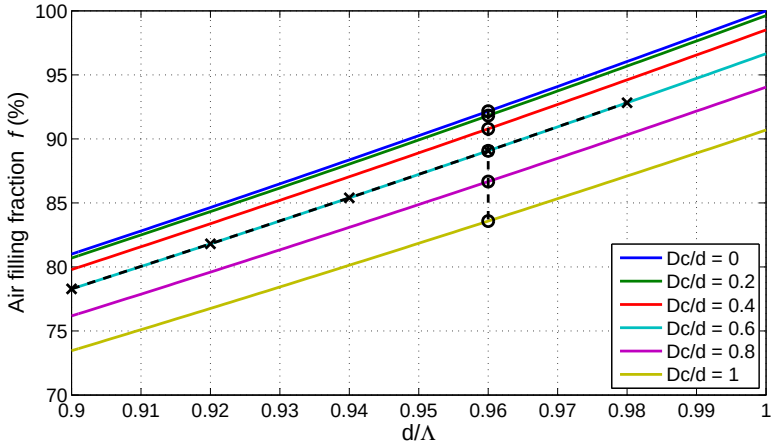

FIGURE 6.4: Air filling fraction f as a function of d/Λ and D_c. Black crosses represent the fibres studied in the scan at a fixed D_c shown in Figure 6.6, while black circles refer to the scan at a fixed d/Λ shown in Figure 6.7. Note that $D_c/d = 0$ corresponds to perfectly hexagonal holes, while for $D_c/d = 1$ the holes are circular.

by $D_c/d = 0.6$ (quite common in fabricated fibres) and assuming $\mathrm{n_{glass}} = n_{\mathrm{Si0_2@1.55\mu m}} = 1.444$. By fitting the quadratic equation

$$\lambda_i/\Lambda = af^2 + bf + c, \qquad i = up \text{ or } low \tag{6.2}$$

to the simulated points, small residuals were obtained for both edges. The values of the best fitting coefficients are reported in Table 6.1. The same study reveals that the relative bandwidth $\Delta\lambda/\lambda_c = (\lambda_{up} - \lambda_{low})/[(\lambda_{up} + \lambda_{low})/2]$ increases more than linearly with f, as is shown in Figure 6.5(b).

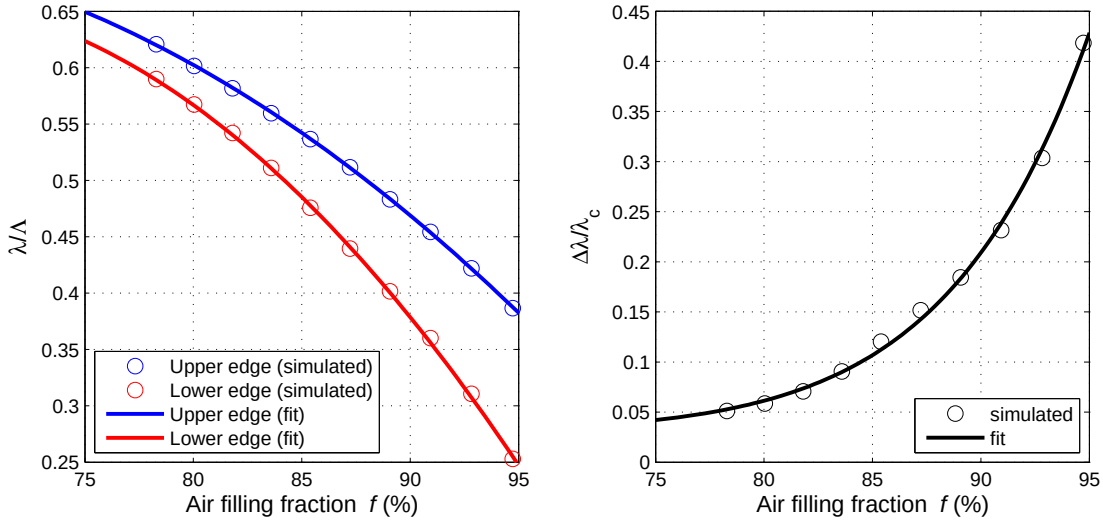

FIGURE 6.5: PBG of a infinitely periodic cladding with $D_c/d = 0.6$ as a function of f: (Left) Normalised upper edge (λ_{up}/Λ) and lower edge (λ_{low}/Λ); (Right) relative bandgap width. Circles represent the simulated points, while the continuous lines are the best fit reported in Equation 6.2 and 6.3.

The simulated values can be fitted by the following polynomial

$$\Delta\lambda/\lambda_c = af^b + c, \tag{6.3}$$

where the values of the best fitting coefficients a, b and c are reported in Table 6.1.

	a	b	c
λ_{up}/Λ	-2.619	3.117	-0.215
λ_{low}/Λ	-4.974	6.574	-1.509
$\Delta\lambda/\lambda_c$	0.850	14.787	0.030

TABLE 6.1: Best fit coefficients.

The relative bandwidth in a PBGF can theoretically exceed 40%, although this would require a rather extreme structure, made such that for more than 95% of its total cross-sectional area is filled with air.

Equation 6.2 and the values of the coefficients reported in Table 6.1 have been used in all the subsequent simulations of the finite PBGF structure to provide an initial estimate of the initial and final wavelengths to be scanned through.

The increase in relative bandwidth with f shown in Figure 6.5(b) suggests that for large-bandwidth applications claddings with the largest possible holes (subject to the required periodicity) need to be fabricated. Large air-filling fractions also bring numerous additional advantages, as can be deduced by the next study, shown in Figure 6.6. Here a 7-cell core fibre is simulated, in which the hole curvature is kept constant at $D_c/d = 0.6$, while d/Λ is scanned at 5 different values, corresponding to the black crosses in Figure 6.4. By combining the study of the resulting periodic cladding unit cell with the results for a finite structure with 6 rings of holes and a 7-cell core, the following observations can be made:

- A larger d/Λ, besides making the PBG wider and centred at shorter wavelengths, makes it also 'shallower', i.e. extending less below the air line; this means that if the core supports multiple modes these will present more closely spaced effective indices and the coupling between them becomes more likely;
- A larger value of f also brings the refractive index of the FM closer to the air line; this needs to be taken into account when setting the guess value around which searching for eigenvalues (see Equation 2.22);
- Most importantly perhaps, a larger d/Λ implies a larger amount of air surrounding the core and a stronger PBG: as a result, the confinement loss experienced by the mode, for the same number of air rings, decreases. The decrease is found to be exponential with d/Λ;

- The fibre's third order dispersion also decreases as the air filling fraction increases;

Finally, note that the agreement between the two simulation methods is excellent for large d/Λ but worsens as the the air-filling fraction decreases. This is probably due to the fact that for small d/Λ the PBG is weaker and the discrepancies between finite and infinite models become more apparent. Increasing the number of rings of holes in the cladding can help in reducing this discrepancy.

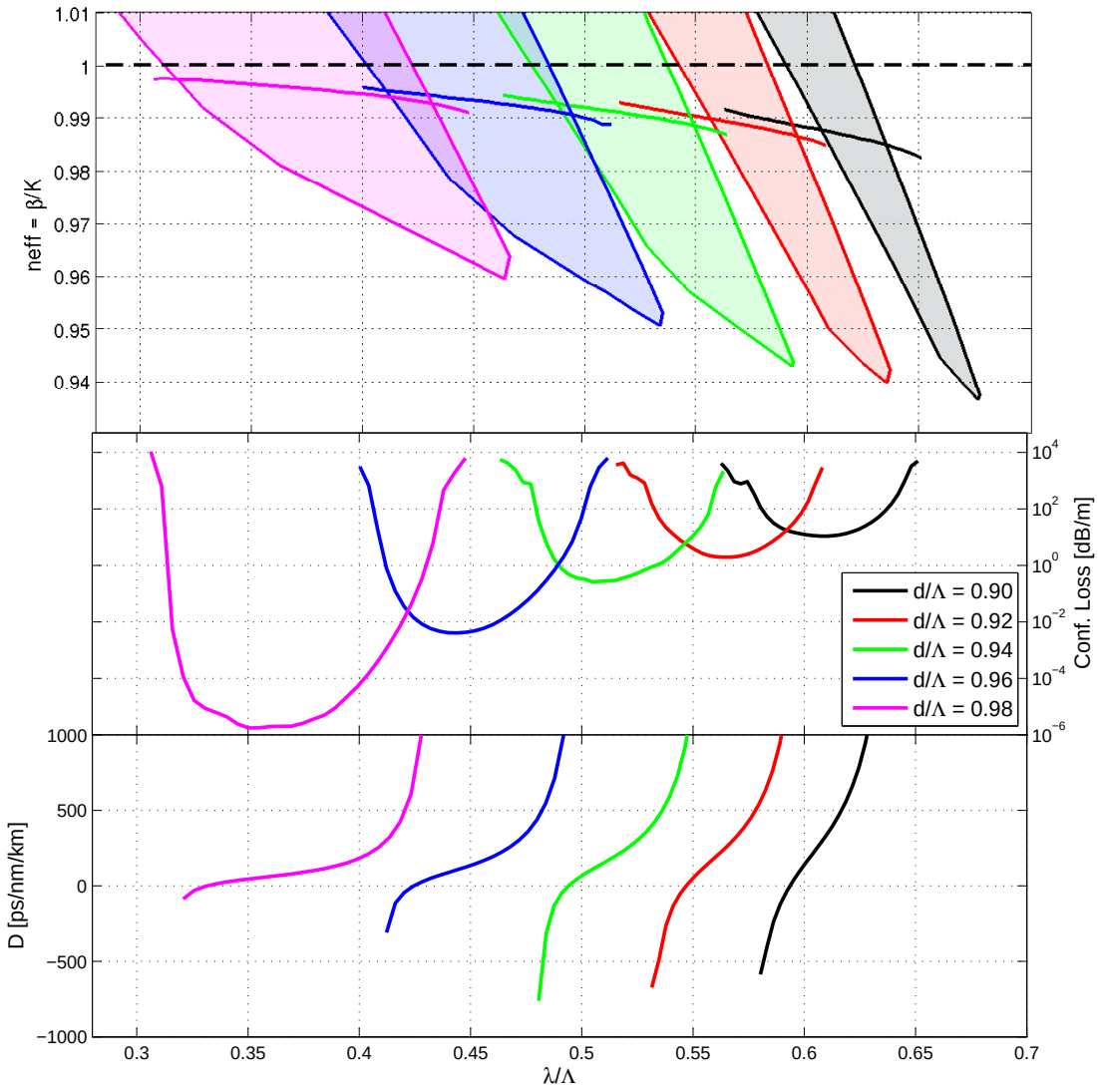

FIGURE 6.6: Photonic bandgap dependence on d/Λ for a 7-cell core fibre: (top) PBG of the periodic unit cell in the cladding (patched areas) and effective index of the air-guided fundamental mode (continuous line); (middle) confinement loss of fibres with 6 rings of holes around the core; (bottom) group velocity dispersion. In these simulations $n_{glass} = 1.444$ and $D_c/d = 0.6$.

As already has been mentioned, the study in Ref. [110] claims that the bandgap position and size depend mainly on f, and in particular the wavelength position decreases with f while its width increases, according to rules similar to those reported in Figure 6.5. This

is indeed true if the hole shape is kept constant, as in the study previously reported. However, if the shape of the holes is modified, the behaviour can be rather different, as it is shown in Figure 6.7, where a 7-cell core PBGF with 6 rings of holes, $d/\Lambda = 0.96$ and different cladding hole shapes are simulated (the scan corresponds to the dark circle markers in Figure 6.4). Under these circumstances, an increase in f is obtained by decreasing the value of D_c/d and thus making the holes more hexagonal, in such a way to decrease the amount of glass at the intersection between three adjacent holes. The resultant bandgap shifts to shorter wavelengths, but, in contrast to the previous case, it also becomes narrower and its confinement loss increases. This clearly confirms a significant dependence of the bandgap on the hole shape which had not been previously recognised. The air-filling fraction alone cannot describe on its own the bandgap generated by a given unit cell, as can be observed by comparing the confinement loss of the fibre with $D_c/d = 0.6$ and $d/\Lambda = 0.98$ in Figure 6.6 with the one of the fibre with $D_c/d = 0$ and $d/\Lambda = 0.96$ in Figure 6.7 which present a similar value of f ($\sim 93\%$).

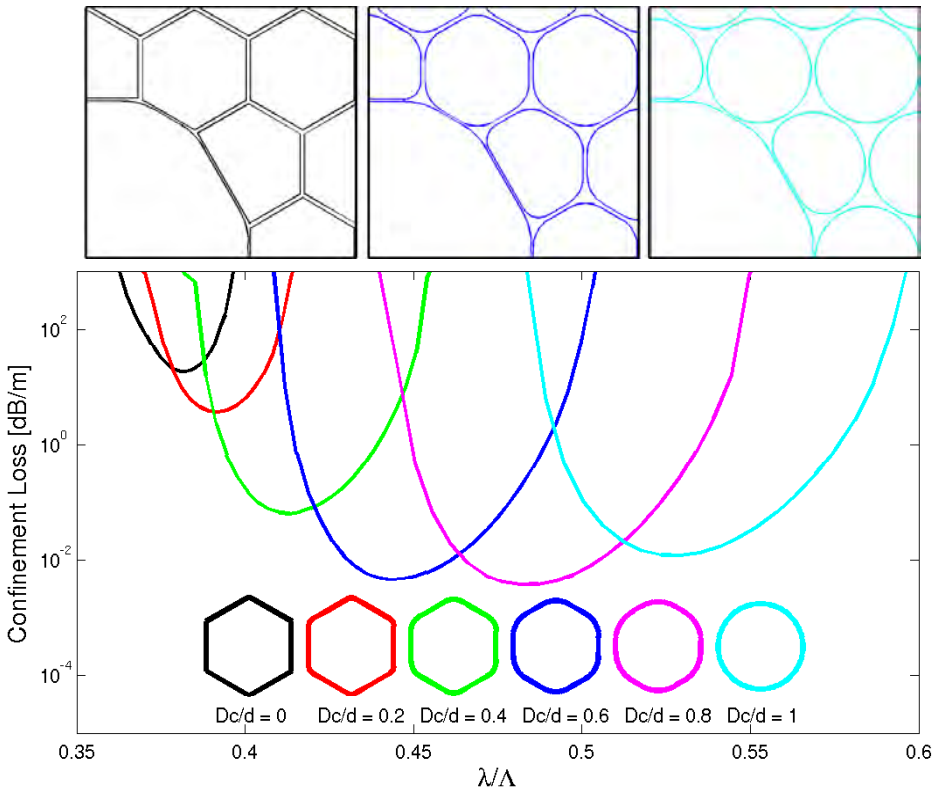

FIGURE 6.7: Photonic bandgap dependence on D_c/d for a 7-cell core PBGF with 6 rings of holes and $d/\Lambda = 0.96$. The shape of the air holes corresponding to the different values of D_c/d is shown in the inset, while the shape of core and first ring of holes for $D_c/d = 0$, 0.6 and 1 is shown at the top.

Additional simulations confirmed that for a given value of f the circular hole shape guarantees the largest and strongest bandgap, as was also previously demonstrated for in-plane photonic bandgaps [225, 226]. In order to achieve with circular holes the same value of f that is achievable with more hexagonal holes however, a larger d/Λ is needed.

If fabrication constraints pose a limit to the maximum achievable d/Λ, the study in Figure 6.7 shows that the widest bandgap is achieved by deviating slightly from the perfectly circular shape and targeting holes with $D_c/d \simeq 0.8$.

6.2.3 Effect of material properties

If the material dispersion is neglected, Maxwell's equations become scale-independent and the central wavelength of a PBG scales rigidly with the dimension of the associated lattice [91]. Under the assumption of neglecting the material dispersion therefore, normalised plots such as the one in Figure 6.6 can be displayed. Within the validity of this assumption, this procedure greatly simplifies the study and design of PBG-based devices, and it has hence been thoroughly employed in all the initial studies on PBGFs (see for example Refs. [112, 227]). Note that neglecting the material dispersion is mandatory with those numerical methods such as the PWE [228] where the frequency ω and not the propagation constant β is the eigenvalue, but it is just an option in our FEM implementation (see Chapter 2 for more details). The usual justification for neglecting the material dispersion in the study of PBGFs is that the mode is mostly concentrated in air and the variation in the refractive index of the glass with wavelength is generally small as compared to the index difference between glass and air. A theoretical study however has recently demonstrated that even for these fibres the material dispersion of silica makes a significant contribution to the total chromatic dispersion [221]. This work however considers a coarse representation of the fibre, for which up to 9% of the power is found to reside in the glass. In order to verify if these results still apply for more realistic fibres with a much lower power in the glass, a 7-cell core PBGF with $d/\Lambda = 0.94$ and $D_c/d = 0.6$ is simulated. The glass refractive index is assumed independent of wavelength and equal to 1.450, 1.444 and 1.438, roughly corresponding to the silica index at the wavelengths of 1, 1.55 and 2 μm respectively. The 3 simulation results are plotted on a normalised axis in Figure 6.8(a), clearly showing that even small percentage variations in the material index are reflected in the final bandgap position. As a conclusion, it is therefore demonstrated that accurate simulations of PBGFs require the inclusion of the material dispersion.

Besides the material dispersion our FEM implementation also allows us to include the effect of material losses, thanks to the use of eigensolvers for complex matrices. These losses can generally be neglected for those applications centred in regions where the glass is highly transparent, such as those involving silica glasses at wavelengths from the visible to the near infrared. However, as was mentioned in Section 1.1.3, multiphonon absorptions in silica are responsible for the rapid increase in loss at wavelengths larger than about 2-3 μm [229]. This conflicts with the fact that the spectral region in the mid-infrared between 2.5 and 5 μm is currently of growing interest, because the development of a new generation of laser sources promises to open this spectral window for

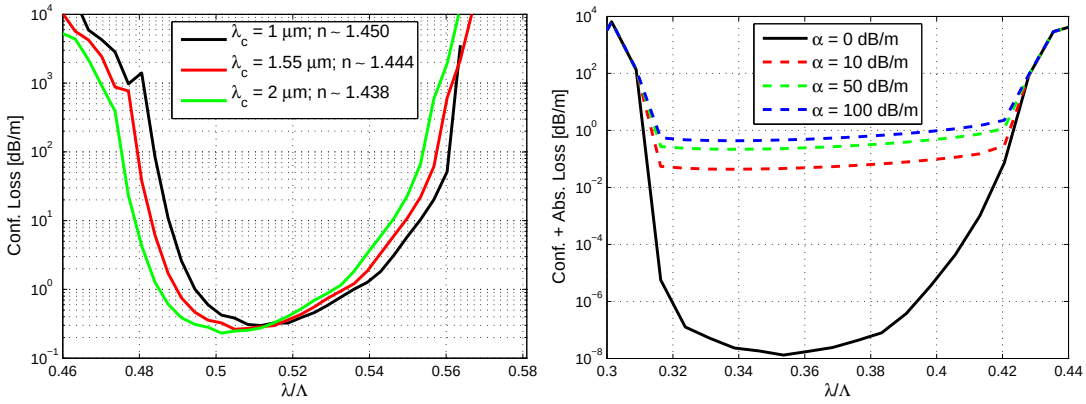

(a) (b)

FIGURE 6.8: Effect of material dispersion and loss: CL of the fundamental air guided mode for a PBGF with (a) $d/\Lambda = 0.94$ and three values of glass refractive index, at $\lambda \sim 1$ μm, $\lambda \sim 1.55$ μm and $\lambda \sim 2$ μm respectively; (b) $d/\Lambda = 0.98$ and increasing values of material absorption loss.

applications in the near future. Moreover many gases exhibit strong molecular absorption at these wavelengths, especially in the wavelength range of 3 to 3.5 μm (e.g. CH_4 has a strong absorption band around 3.3 μm). Thus, the availability and performance of single-mode fibres for this spectral range is of great interest. A possible solution is to employ soft glasses in which the multiphonon absorption edge is itself shifted to longer wavelengths. An alternative solution is to employ silica PBGFs, due to the very small percentage of power that is actually guided in the glass. The simulation results reported in Figure 6.8(b), obtained for a 7-ring fibre with $d/\Lambda = 0.98$ and $D_c/d = 0.6$ indeed confirm that silica PBGFs can be effectively employed in applications at wavelengths up to around 3.5 μm. The simulated total loss, which includes leakage and absorption loss but neglects the effects of bulk and surface scattering, results in less than 0.1 dB/m loss over most of the bandgap, even if the material loss is ~10 dB/m (corresponding to wavelengths around 2.7 μm) and still less than 1 dB/m if the material loss is ~100 dB/m ($\lambda\sim$ 3.5 μm).

The improvement of more than 2 orders of magnitude in the achievable loss showed by these preliminary simulation results encouraged the fabrication of PBGFs at wavelengths longer than 2 μm. One example out of the several fibres fabricated by my colleague Dr. M. N. Petrovich is shown in Figure 6.9(a): the fibre presents a relative hole dimension and shape closely following the previous specifications, and a pitch Λ of 6.45 μm [12].

The fibre transmission was measured using an optical parametric oscillator (OPO), whose output could be tuned in the range 2-3.5 μm. Figure 6.9(b) shows the spectral transmission (normalised to the input power) of a 2 m long sample of PBGF. The bandgap extends from 2 to 2.6 μm, with maximum transmission at 2.35 μm, in good agreement with the theoretical predictions. A region of relatively higher loss is located at about 2.2 μm, and is probably due to absorption from surface hydroxyl impurity. The

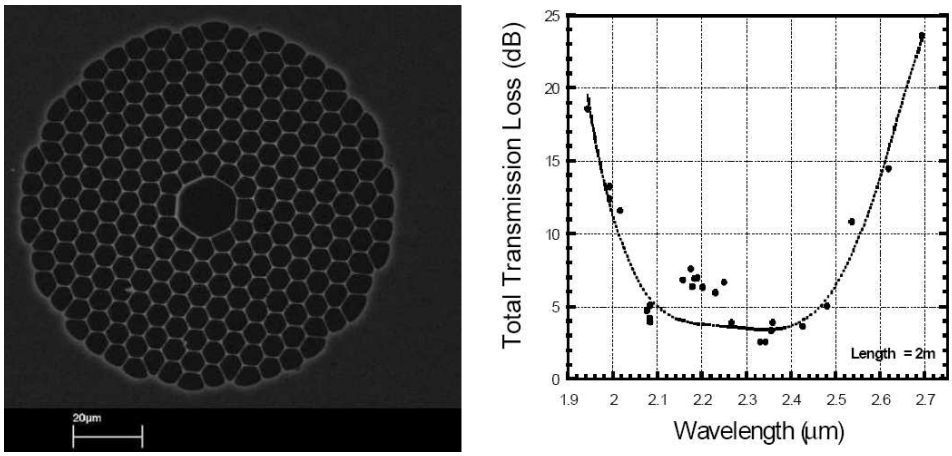

FIGURE 6.9: Fabricated fibre for mid-IR transmission: (a) SEM and (b) measured loss (After Ref. [12]).

transmission loss was measured by the cutback method, yielding a value of 0.8 dB/m at the central wavelength 2.35 μm, higher than the predicted confinement and absorption loss but still more than an order of magnitude smaller than the material loss ($\sim$10 dB/m at those wavelengths).

The fabrication of a silica PBGF with a 19-cell core, with a bandgap centred at even longer wavelengths ($\lambda_c \sim 3.25$ μm) and minimum attenuation loss of 2.6 dB/m was also recently reported [230]. These result confirm that hollow core PBGFs have many potential applications in the mid-IR, offering an alternative to fluoride, tellurite or chalcogenide glass based optical fibres for chemical and biological sensing applications.

6.3 Modelling fabricated fibres

6.3.1 Introduction

Modelling the optical properties of fabricated optical fibres is useful to complement measurement results, evaluate properties that are otherwise difficult to measure, or to predict the effect of small changes in the design parameters through perturbation analysis. Obtaining reliable modelling results for silica hollow core Photonic Bandgap Fibres (PBGF) is a particularly challenging task since the optical properties of these fibres depend critically on both large scale features of the fibre (i.e. the distribution of the air holes within the extended periodic cladding on a length scale of several μm) and on much smaller scale features (i.e. the width of the thin silica struts which are typically of order a few 10s of nanometers).

Two simulation approaches have been so far proposed: the first employs a model of an idealised fibre's cross-section, such as the one presented in Section 6.2.1, and fits its parameters to those of the fabricated fibre [222]; the second models a structure which is directly obtained from an SEM image [13, 231]. In both cases however, no emphasis has been given so far to the achievable precision and reliability of the method. In this section the potentials and limitations of both simulation approaches are explored: the extreme sensitivity of the photonic bandgap to small scale features is highlighted, while the size of the source SEM image and the conductive coating applied for the image acquisition are identified as the primary factors limiting the accuracy of the results.

6.3.2 Simulations using an ideal model

In order to calculate many of the optical properties of a fabricated PBGF it is often adequate to simulate an idealised model of its cross-section, such as the one presented in the previous section. Using this approach, structural imperfections (which, to a first approximation, are irrelevant for many fibre properties) are neglected and symmetries can be exploited, resulting in smaller meshes and shorter simulation times. Some properties of the fibre, such as the PBG position and width or the input coupling efficiency, and other specific properties of the air-guided modes, such as the percentage of power in the air and glass, the group velocity dispersion and an estimate of the scattering loss can all be obtained by this approach.

The model with 8 free-parameters previously described was found to provide an adequate description of the fibre's cross section. Also in the present study, fixing D_1 and D_2 to $D_1 = D_c/\sqrt{3}$ and $D_2 = \Lambda/2$ does not cause significant loss of accuracy. The number of rings of holes N is chosen to match the preform design, while the remaining 5 parameters – hole-to-hole spacing Λ, hole diameter d, hole roundedness D_c, core radius R_c and thickness of its boundary layer t_c – need to be fitted from SEMs of the real structure.

The average measure of Λ can be obtained from a Fourier analysis of the periodic cladding, while the expansion or compression factor of the core can be directly measured from the SEM. Less accurately determined are the values obtained from the SEM for D_c and for the thickness of the struts in the cladding (inversely proportional to d/Λ) and around the core (t_c). The limited size of the bitmap obtained from a typical SEM (1024x768 pixels for our instrument) is the main obstacle, as even on highly magnified images (containing a sufficient number of periodic holes to average their properties) each strut is defined by only a few pixels. Charging effects during the SEM acquisition, sample tilt and the additional thickness of the gold coating layer represent additional uncertainties to be taken into account. On the other hand, as was shown in Section 6.2.2, the PBG position and width are strongly dependent on the air-filling fraction of the cladding, which is ultimately determined by D_c and d/Λ. Small variations in the estimated averaged value of D_c or d/Λ can produce a significant shift in the PBG. For example, Figure 6.10(a) shows a model with 3 slightly different values of d/Λ, used to fit a highly magnified image of a fabricated fibre. The resulting simulated bandgaps are compared with the measured transmission spectra of the real fibre in Figure 6.10(b). The difference between $d/\Lambda = 0.95$ and 0.96, even on a high magnification image of the cladding, is only $\sim$1 pixel, and yet it produces significant shifts in the resulting PBG.

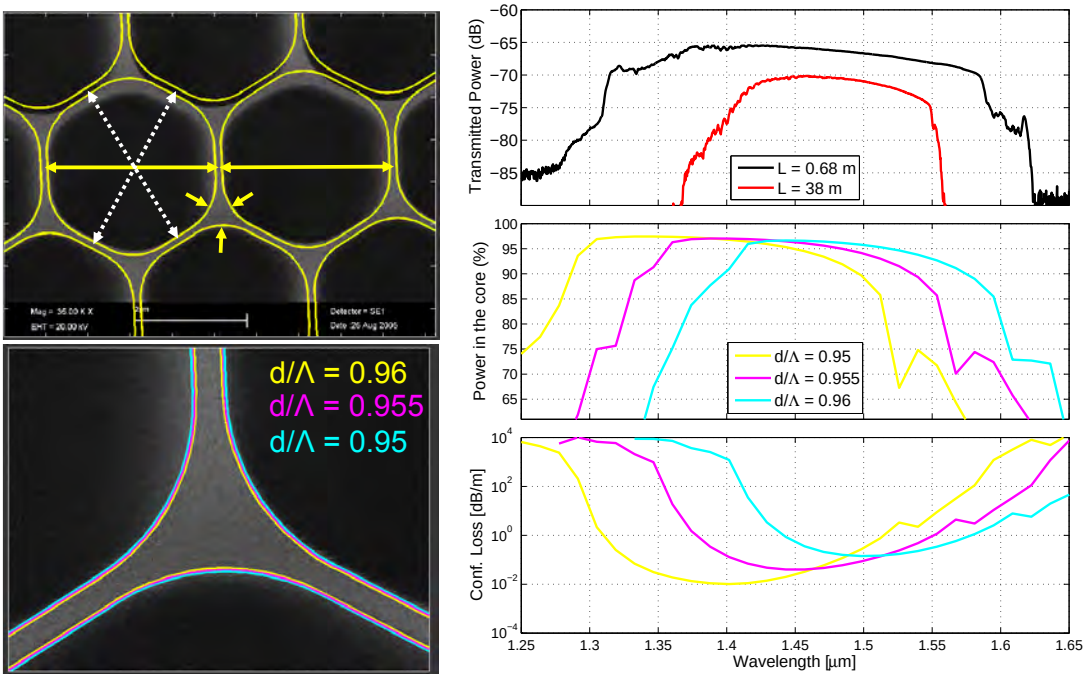

(a) (b)

FIGURE 6.10: Ideal model of a fabricated fibre. (a, top) highly magnified SEM of the cladding and (super-imposed in yellow) best fitting ideal structure; (a, bottom) closeup on a triangular strut and ideal model with 3 values of d/Λ. (b) Comparison between the measured transmission spectrum, simulated percentage of power in the core and confinement loss for the 3 previous values of d/Λ.

By analysing a range of different fibres, it was found that the PBG shift for a change of 1% in d/Λ (corresponding to 1 or 2 pixels on our images) can be as large as 0.02Λ to 0.03Λ (80 to 120 nm for a typical pitch of 4 μm). For this reason we have never been able to reliably predict the PBG size and position of a fibre from its SEM image using this approach. However, we believe that in addition to being a valuable tool for designing the fibres, the idealised model also provide a good estimate of many of the fabricated fibre's properties, providing that the most critical structural parameters are first inferred by fitting the simulated PBG properties to the measured data, rather than directly estimating them from an image.

6.3.3 Simulations using realistic cross-sections

Although the idealised fibre structure provides a simple way for estimating the principal performances of a fibre, it cannot determine those properties, such as birefringence, that result from structural asymmetries. Neither can it predict the exact location of surface modes inside the PBG, which are extremely sensitive to very fine details of the ring surrounding the core in which they are localised, as will be discussed in more detail in the next chapter. Therefore it can sometimes be necessary to simulate the performances of a structure as closely matched as is possible to the SEM of the real fibre's cross-section. The process, already employed in several other projects reported in this thesis, generally involves multiple image-processing stages to eliminate noise, charging effects and to obtain a two-level bitmap, which is then approximated with splines and finally meshed.

Initial attempts at simulating the full structure of the fibre always predicted a PBG at much longer wavelengths than actually measured. A careful analysis of the various simulated fibres permitted us to attribute this mismatch to the limited image size. The 19 periods (Λ) along the diameter of a typical fibre are represented by $\sim$700 pixels along the vertical dimension of the image; this limits the resolution of each individual strut to between 1 and 2 pixels, which is clearly insufficient to obtain accurate results and often led us to underestimate the correct value of d/Λ.

It was however verified that by increasing the magnification by 2-3 times as in Figure 6.11(a) it is possible to determine the hole shapes and positions with sufficient accuracy. Although this approach implies that information about the fibre's confinement loss is lost, since only part of the fibre is represented, the principal modal properties were found not to be significantly affected by neglecting the outer rings of holes. For example the PBG can still be accurately estimated by studying the percentage of power in the core (P_{core}) of the air-guided modes. In Figure 6.11(b) we plot the calculated P_{core} of the structure represented by the yellow contours in Figure 6.11(a). The PBG extends from nearly 1.3 to 1.6 μm. A number of SMs, which are different for the two polarisations and, as will be discussed in the next Chapter, are identifiable as dips in the

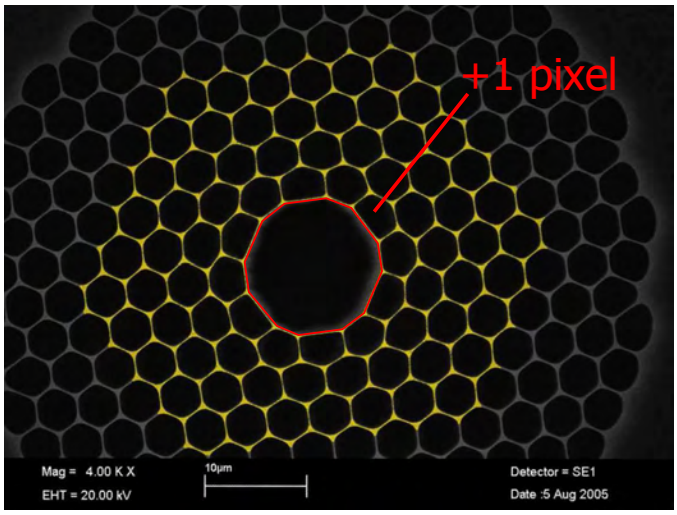

(a)

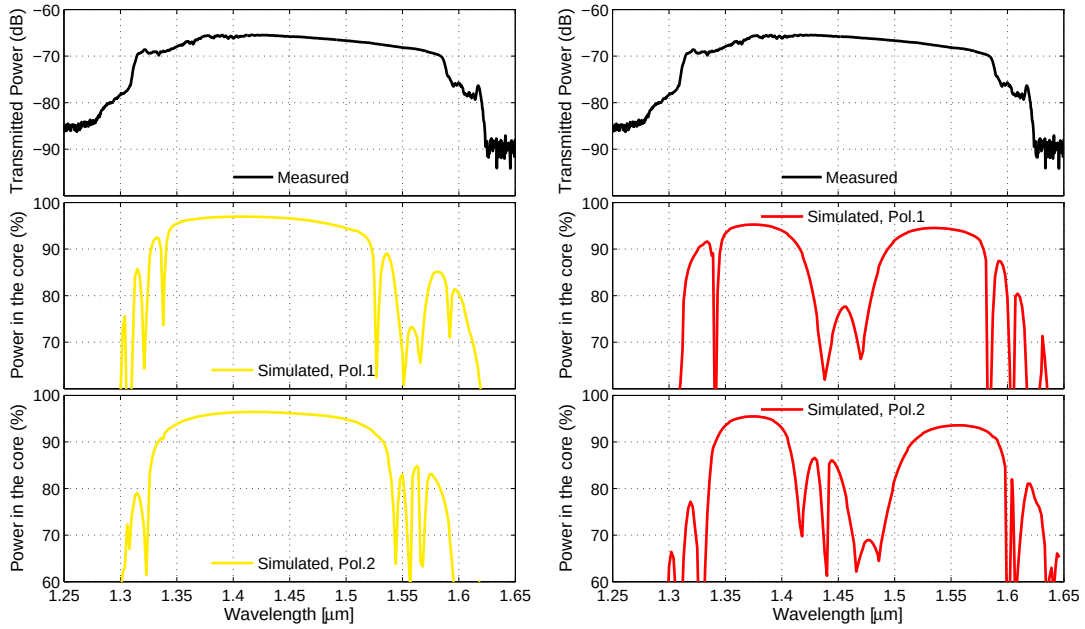

(b) (c)

FIGURE 6.11: Modelling a PBGF from its SEM. (a) High magnification SEM of the fibre, zoomed in around the core and, in yellow, the structure used in the simulations. (b) and (c) Measured spectrum of 0.68 m of the fibre and simulated percentage of power in the core for the two linearly polarised modes, corresponding to the yellow structure (b) and to a structure where the red boundary in (a) has been enlarged by 1 pixel (c).

plot, appear at the edges of the PBG, while only the fundamental and the higher order modes (not shown) are guided within its central region. This is in reasonable agreement with the measured spectrum of a short section of the fibre, shown at the top of the figure. However, due to the nature and localisation of the SMs, their exact position in the PBG is extremely dependant upon the thickness of the interface between the core and the photonic crystal. This dependence is demonstrated in Figure 6.11(c) where we plot the results of a simulation for a similar fibre, in which the thickness of the core boundary

has been expanded by just 1 pixel all around (which is within the resolution error of our SEM measurements). As a result, the SMs around 1.55 μm shift to longer wavelengths and disappear into the continuum of cladding modes, while other SMs emerge from the short wavelength edge and move towards the centre of the PBG.

This example (and similar work on other fabricated fibres) leads us to conclude that by using an SEM image with a strut resolution of at least 3-5 pixels it is possible to accurately predict the width and position of the PBG without having to determine the structural parameters via comparison with experimental data. However, it was found that an even higher image resolution would be required in order to accurately estimate also the position of SMs within the PBG. In order to confirm this, a state-of-the-art scanning electron microscope was employed to obtain images of the previous fibre. This allowed SEMs with a pixel resolution of 3072×2304 to be acquired. One example of the structural contours obtained from such high definition images, to be subsequently used in FEM simulations, is shown by the red lines in Figure 6.12.

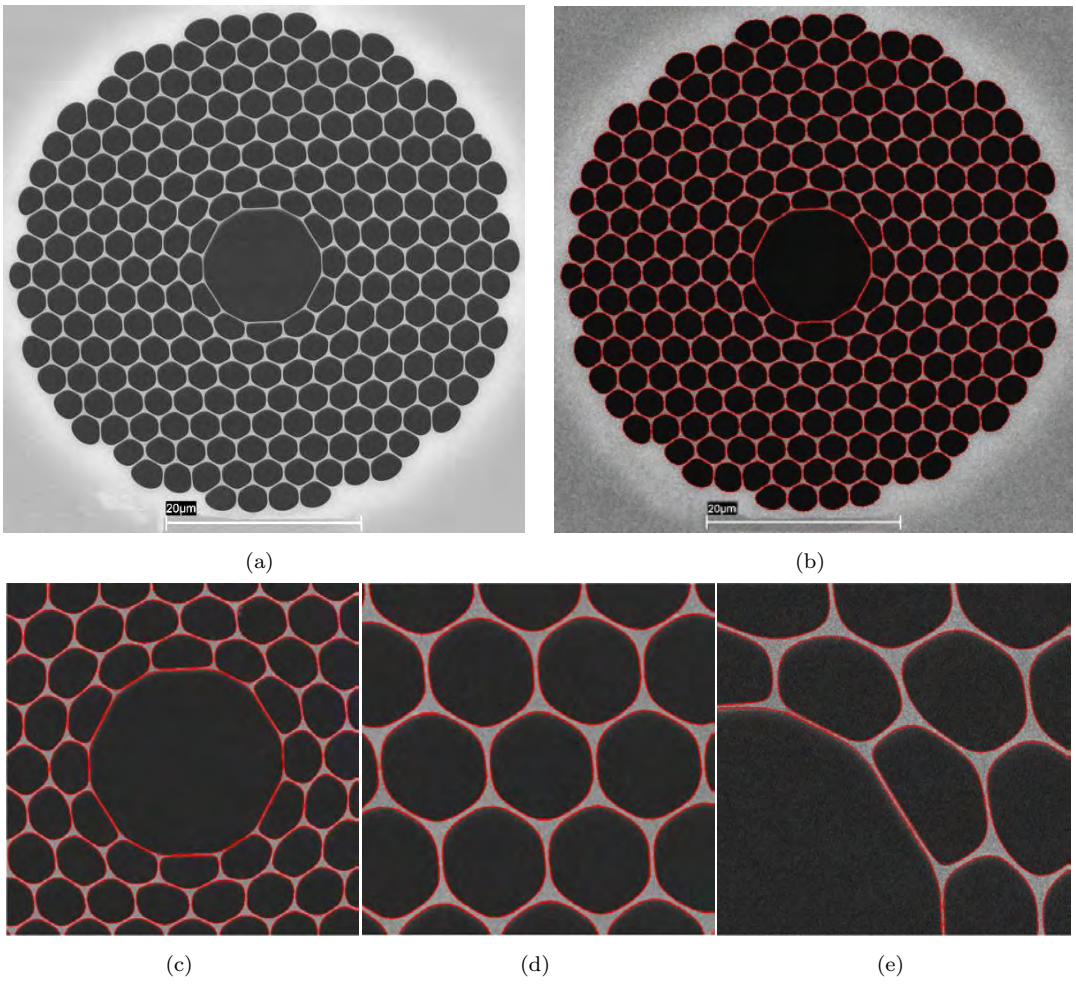

FIGURE 6.12: PBGF modelling from a high definition SEM: (a) SEM of the full structure and (b) overimposed in red the structure to be simulated. (c), (d) and (e) show details of the fibre's cross section and, in red, the contours of the simulated structure (SEM courtesy of M. N. Petrovich).

The high image resolution, its good contrast and the absence of charging effects, achieved as a result of the meticulous work and repeated trials by Dr. M. N. Petrovich, results in the unequivocal representation of each strut in the cladding (∼170 nm wide) by on average 7 pixels, while the thinner core boundary is constituted by ∼4 pixels. The sim-

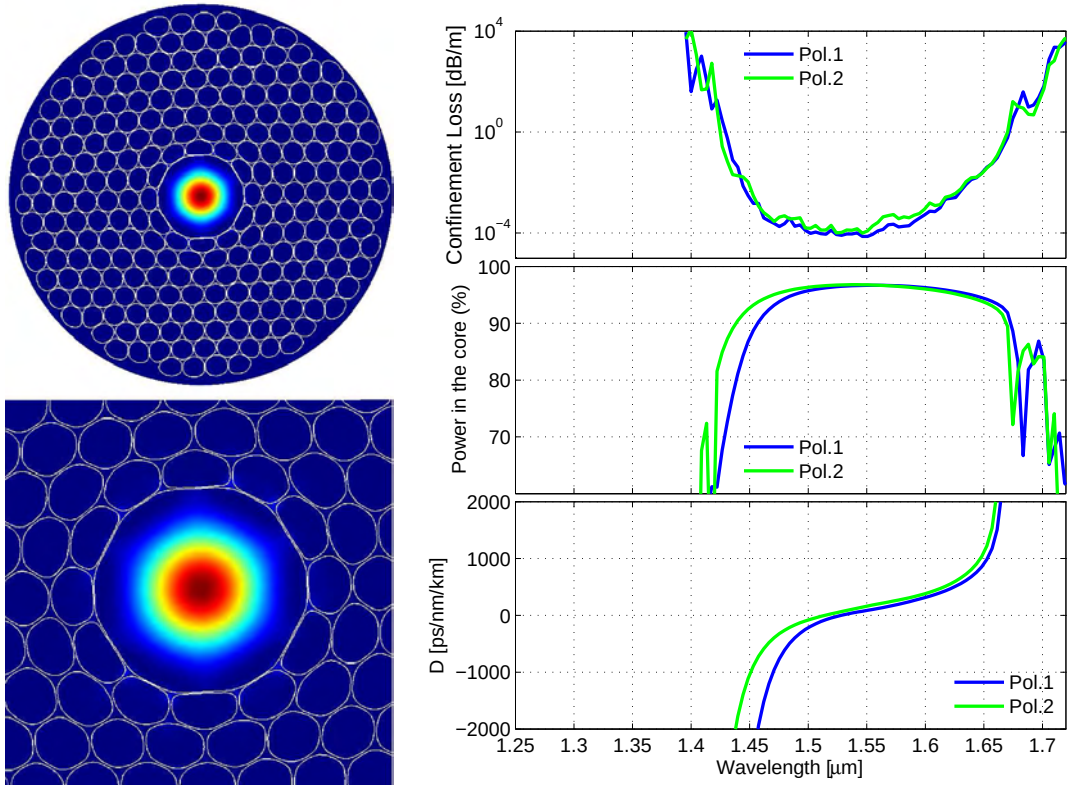

FIGURE 6.13: PBGF modelling from a high definition SEM: (a) Poynting vector of the simulated fundamental air-guided mode; (b) simulated optical parameters for both polarisations.

ulation results for this structure are shown in Figure 6.13. A mesh of 105000 triangular elements, denser in the core area was used, and a scan over 100 wavelengths was conducted, requiring nearly 4 hours of computation time on a dual-core PC with 2.5 GHz processors and 8 GB of memory. For both polarisations of the FM, anticrossing with SMs are only present near the PBG edges, in accord with the transmission measurements. The simulated confinement loss of $\sim 10^{-4}$ dB/m is orders of magnitude smaller than the measured loss of the fibre, indicating that scattering loss is the predominant loss mechanism. The percentage of power in the core, dispersion and birefringence could also be obtained from the same simulation.

Despite these encouraging results in the simulation of the wavelength position of SMs, the resulting PBG was smaller and shifted to longer wavelengths than the measured one, suggesting that the actual hole size had been underestimated (see Figure 6.6 and related discussion). This was attributed to the presence of a gold coating layer, applied to reduce charging effects during the SEM acquisition, and whose thickness, ranging

between 5 and 20 nm and generally difficult to estimate accurately, can influence the simulation results. Additional simulations on samples with thicker coating were then performed, and as expected the resulting PBG was even narrower and centred at longer wavelengths.

6.3.4 Conclusions and future work

The applicability and limitations of two different techniques for modelling real fabricated PBGFs have been thoroughly studied. Ideal, parametrised fibres can be employed to model the fairly regular structures produced with the current technology, although an initial fitting of some structural parameters through comparison with the measured transmission spectrum is recommended. Alternatively, and/or in order to estimate the polarisation properties of the fibre, structures directly extracted from SEMs can be simulated. In this case, the size of the SEM bitmap is identified as one of the main limiting factors in obtaining reliable information about the exact SM position. A good agreement with the measured data can be obtained, provided that high resolution SEM images are employed. The thickness of the coating layer, which can reach up to 25% of the strut thickness, is also another issue to be faced. Ongoing work focuses on the evaluation of other image acquisition techniques, such as the environmental SEM (ESEM), which do not require a conductive coating and hence could help overcoming the issues identified.

Chapter 7

The impact of surface modes

7.1 Introduction

A brief introduction to what surface modes are and why they exist was presented in Section 1.3.2.3; in the previous chapter their presence was claimed to be responsible for dips at certain wavelengths in the amount of power in the core, when modelling real PBGFs. This chapter analyses these modes in more detail.

Surface modes can occur when an infinite photonic crystal is abruptly terminated, as happens for example at the edges of a crystal of finite dimensions. Terminations introduce a new set of boundary conditions, which result in the creation of surface modes that satisfy these conditions and are localised at the termination [232]. In a photonic crystal, the existence of surface modes depends strongly on the location of the termination [91, 232]. For example, in photonic crystals made of dielectric rods in air, surface modes are induced only when the termination cuts through rods: a termination that cuts only through air is too weak to induce surface modes [91]. Similarly, in a PBGF the core acts as a defect that perturbs the crystal and may introduce surface modes at the core's edge. Whether surface modes appear, and how many of them appear, depends on how the photonic crystal is terminated, which determines the magnitude of the perturbation introduced by the defect.

This chapter presents two studies that analyse the dependence between the way in which the photonic crystal in the cladding of a PBGF is terminated and the type and number of associated surface modes. Both studies benefit from the capability offered by the FEM, through the use of nonuniform meshes, to model accurately and efficiently structures with details several orders of magnitude smaller than the average features in the fibre's cross section. The first study focuses on some of the polarisation issues of fabricated PBGFs that had been experimentally observed and it proposes, for the first time, a theoretical explanation. This is based on the presence of asymmetric interactions

with surface modes for the two fundamental modes, resulting from (even very small) asymmetries in the core boundary. The second study systematically searches for core shapes that are at the same time realisable and free of surface modes, and it successfully reveals a design regime with those characteristics.

7.2 Surface modes and polarisation

7.2.1 Introduction

In order to design PBGFs for device and system applications it is essential to establish a detailed understanding of the polarisation properties of such fibres [e.g. birefringence, polarisation-dependent loss (PDL) and polarisation mode dispersion (PMD)], to determine how these properties depend on the fibre structure, and to establish means of controlling these during fabrication, and/or use. One way to limit the coupling between the two nearly degenerate orthogonal fundamental modes (FMs) is to deliberately fabricate highly birefringent, polarisation-maintaining structures. PBGFs with a birefringence one order of magnitude higher than any other fibre structure have been designed and successfully fabricated by introducing a deliberate asymmetry into the air core [233–235]. An alternative, opposite approach is to reduce the birefringence by producing fibres with as symmetrical a structure as is possible, in order to exploit the degeneracy between the two linearly polarised FMs of an idealised symmetric PBGF structure [76]. It has been demonstrated that (unintentional) deformations during the drawing process can lead to significant mode splitting, resulting in beat lengths of the order of a few mm [236]. Subsequent systematic studies have revealed that even in less obviously asymmetric structures significant polarisation dependent phenomena can be observed in the wavelength region where an anticrossing occurs between an air-guided core mode (FM) and a surface-localised mode (SM) [237]. Near-field images of the output mode distribution in such circumstances have shown the presence of spectral regions within the photonic bandgap where one of the two polarisations of the FM appears to interact more strongly with a surface mode than the other [238]. Moreover, an extensive study of the polarisation properties of PBGFs has demonstrated a correlation between a peak in the PDL measurement and the presence of a surface mode inside the bandgap at a wavelength where only one of the two polarisations of the fundamental mode appears to be properly guided [239].

In order to generate a deeper understanding of these experimentally observed phenomena, this section presents a number of simulations of a PBGF in which an incremental asymmetric structural perturbation is applied. These examples allow us to deduce more generally how the fibre's polarisation properties depend on structural deformations. It is demonstrated that many of the recently measured wavelength-dependent polarisation properties of PBGFs, such as beatlength and PDL, can be explained by an asymmetry

associated with the fibre core, combined with the presence of surface modes inside the bandgap.

7.2.2 Structure definition and simulation parameters

The structure considered in this study is the ideal representation of a real, state-of-the-art hollow core PBGF with a 7-cell core presented in Section 6.2.1. The idealised fibre represents closely the fabricated Corning PBGF with 13 dB/km attenuation [231] which has been already repeatedly studied in the literature [13, 222]; both real and idealised fibres are shown in Figure 7.1.

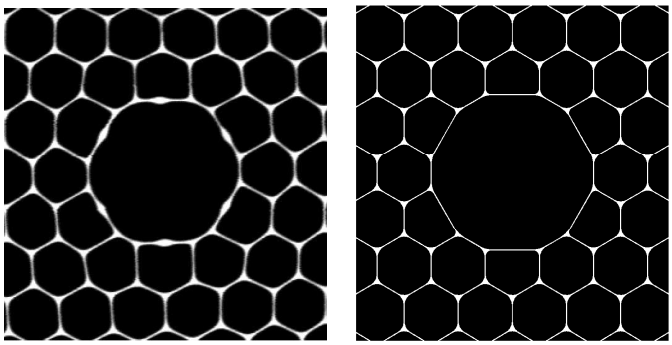

(a) (b)

FIGURE 7.1: (a) SEM image of the Corning PBGF (After [13]); (b) idealised model of the same fibre.

The fibre's hole-to-hole distance is $\Lambda = 4.7$ μm, its relative hole diameter d/Λ is 0.98, and the corners are rounded with circles of diameter $D_c = 0.44\,\Lambda$, $D_1 = D_c/\sqrt{3}$ and $D_2 = \Lambda/2$ [see the definitions in Figure 6.1(c)]. Dielectrics are modelled using the Sellmeier equation for silica and considering n = 1 for air. The bandgap of this idealised structure matches quite closely that of the fibre reported in Ref. [222], extending from nearly 1.35 to 1.8 μm, although the position of the surface modes within the bandgap is somewhat different due to the slightly modified core design.

7.2.3 Results

7.2.3.1 Perfect Structure

The effective index plot in Figure 7.2 shows the dispersion of the modes, either localised in air or on the surface terminating the photonic crystal and whose frequency lies within the photonic bandgap, for the case of a perfectly symmetric, unperturbed structure. One very evident avoided crossing takes place near the middle of the bandgap between pairs of linearly polarised modes (solid blue lines). This involves the degenerate pair of

HE_{11}-like, air-guided, fundamental modes passing through points (a), (b), (g) and (h), and the two degenerate, linearly polarised SMs passing through (e) and (d).

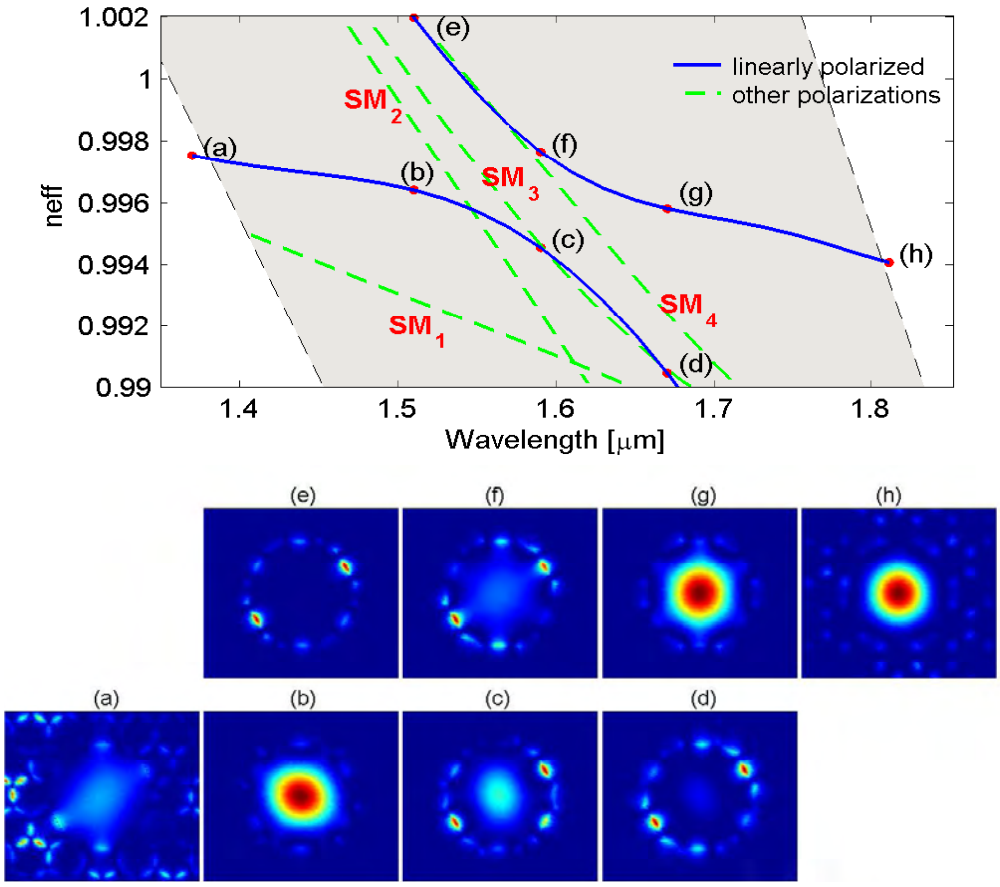

FIGURE 7.2: (Top) Effective index plot for the perfectly symmetric structure. The shaded area represents the bandgap as calculated for an infinite periodic cladding; (Bottom) Poynting vector of a linearly polarised mode: (a) and (h) are at the bandgap edges, while (b)→(d) and (e)→(g) show the mode evolution in the two branches of the anticrossing.

The large separation in effective index between the interacting modes around the avoided crossing at $\lambda = 1.6$ μm is an indication of a large interaction between the modes involved [237]. Besides the SM shown at points (d) and (e), other SMs (represented by dashed green lines) are supported by this structure, but since they belong to different symmetry classes, they do not significantly interact with the linearly polarised fundamental modes, as was confirmed by numerical simulations. The 8 subplots at the bottom of Figure 7.2 show the evolution of the mode's Poynting vector from the short to the long bandgap edge, passing through the central avoided crossing region.

7.2.3.2 Perturbed structure

In order to understand how the PBGF polarisation properties depend upon structural imperfections, we consider the consequence of two different deformations of the fibre

cross-section, as shown in Figure 7.3. The first (deformation A) is obtained by scaling the whole structure in the x direction only, according to

$$(x,\ y) \rightarrow \big(x \cdot [1+\sigma],\ y\big) \tag{7.1}$$

where σ is the percentage scaling factor. Deformation A thus generates an oval fibre with an oval core and a correspondingly modified periodic cladding.

For deformation B we distort only the dodecahedron defining the inner boundaries of the core by compressing it in the x direction and leaving the periodic cladding unaltered. The deformation, which only applies inside the core region, is defined by

$$(x,\ y) \rightarrow \left(x \cdot \left[1-\sigma \cdot \frac{\Lambda - d}{R_c}\right],\ y\right) \tag{7.2}$$

where R_c is the core radius of the unperturbed structure. In this way σ represents the (percentage) thickness variation of the vertical struts around the air core. The thickness of the diagonal struts linearly decreases to that of the (unaltered) horizontal struts.

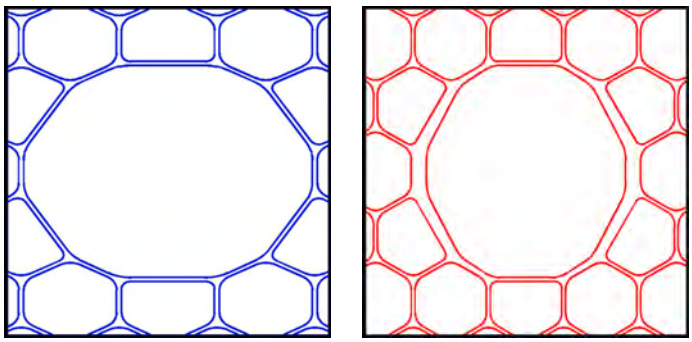

(A) (B)

FIGURE 7.3: Deformation types considered: (A) overall deformation with f = 30%; (B) core deformation with an exaggerated $\sigma = 300\%$ for illustration purposes.

Applying either deformation distorts the silica ring around the core such that the thickness of the vertical struts is scaled by a factor $(1 + \sigma)$ whilst the thickness of the horizontal upper and lower struts remains unchanged. Since this ring is where surface modes are located, it comes as no surprise that for both types of deformation we obtained qualitatively similar anticrossing behaviour for the same value of σ. This can be seen by comparing the effects of deformation A in Figure 7.4(a) and (b) with those of deformation B in Figure 7.5(a) and (b). Deformation A however also distorts the periodic cell, resulting in a narrowing and shifting of the bandgap to longer wavelengths. Moreover it also has the effect of scaling the ratio between the geometric core axes by a factor $(1 + \sigma)$ which is more than 2 orders of magnitude larger than that due to deformation B. As can be seen in Figure 7.4 this has the effect of introducing a large amount of "ordinary" birefringence between the core modes, as previously observed in a fabricated fibre [236]. In order to avoid any effect arising from the deformation of the

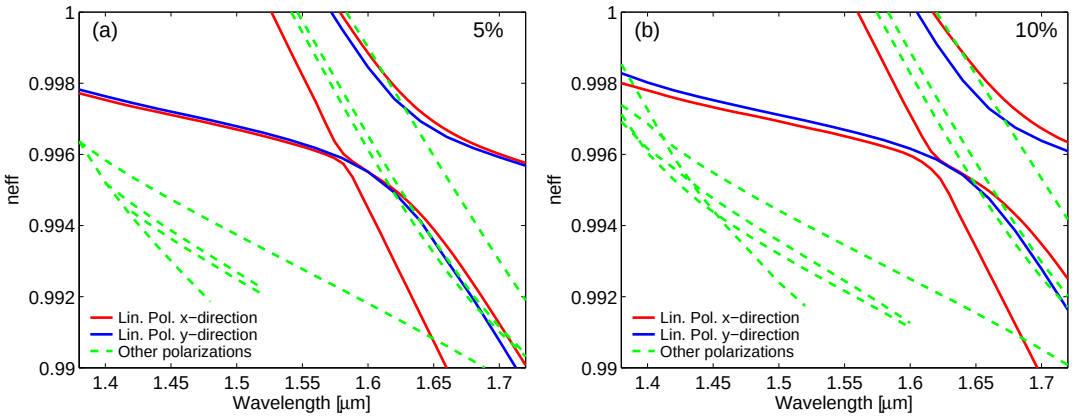

FIGURE 7.4: Effect of deformation A with $\sigma = 5\%$ and $\sigma = 10\%$. Linearly polarised modes are represented with solid lines, while dashed lines are used for any other polarisation type.

bandgap itself and to better identify those polarisation effects arising from coupling to SMs, the rest of the section is focused on the influence of deformation B. The overall conclusions that are presented in the following though, are believed to be applicable to any similar asymmetric deformation of the inner silica ring, including deformation A.

Figure 7.5 shows the effect of applying deformation B with $\sigma = 5\%$, 10%, 20% and 30% to the fibre in Figure 7.1. The unperturbed fibre had a core silica ring thickness of (Λ - d) = 94 nm. Note that the increase in thickness introduced (4.7, 9.4, 18.8 and 28.2 nm respectively) is around 2 orders of magnitude smaller than the wavelength of light and 3 orders of magnitude smaller than the fibre's core. In ordinary waveguiding structures this would represent an almost negligible variation. For example, our calculations show that for an index guiding holey fibre with the same pitch ($\Lambda = 4.7$ μm) and $d/\Lambda = 0.4$, adding 9.4 or 18.8 nm to the pitch length in just the x-direction causes the birefringence to increase from our numerical resolution limit of $\Delta n \leq 1.5{\cdot}10^{-7}$ for the perfect structure to just $3.5{\cdot}10^{-7}$ and $8.7{\cdot}10^{-7}$ respectively.

In hollow core PBGFs however, the termination of the cladding periodicity around the central defect localises a number of surface modes at the photonic crystal termination. These modes, localised in regions of the thin silica ring around the core and exponentially decaying on either side of it [Figure 7.2(e)], are extremely sensitive to the precise level of structural deformation applied, as can be appreciated by studying Figure 7.5(a)-(d). Moreover, through an avoided crossing mechanism [237], the core mode can also become extremely sensitive to small scale structural variations.

From a group representation theory point of view, as a consequence of the deformation, the structure shifts from a symmetry class C_{6v} to C_{2v} (a general random perturbation would destroy any symmetry, but this doesn't change the final result of the present study) [8]. As a result, the 4 non-degenerate symmetry classes which exhibit the full waveguide symmetry in C_{6v} are no longer supported, and the 4 remaining classes become

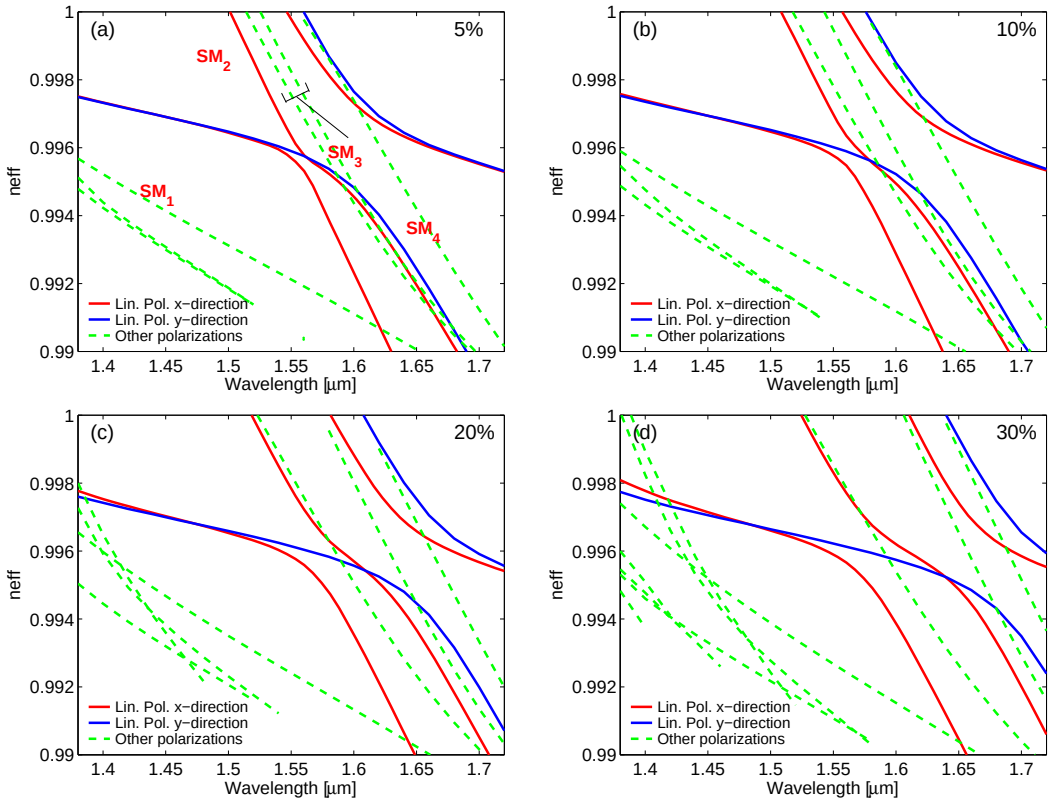

FIGURE 7.5: Effect of deformation B, producing an increase of 5%, 10%, 20% and 30% on the thickness of vertical struts around the core.

non-degenerate. Both these effects can be observed by comparing Figure 7.2 and Figure 7.5(a). In the perfect structure the SM denoted as SM_2 belongs to a class exhibiting the full 6-fold fibre symmetry (using the same nomenclature as for the core modes it would be labelled as HE_{31y}), while SM_3 represents a pair of degenerate surface modes (HE_{21}). After the deformation is introduced, the SM_3 modes are split, while SM_2 is transformed into a linearly polarised mode, interacting with only one of the fundamental modes. Also the linearly polarised SMs which interacted with the FMs in the perfect structure split, causing the avoided crossings for the 2 polarisations to take place at different wavelengths.

Increasing the amount of deformation has a different effect on the 2 polarisations, as can be observed in Figure 7.6.

The SM whose electric field is linearly polarised along the y-axis concentrates its power on the lateral silica struts, whose thickness is progressively increased (Figure 7.6, left). As a result the effective index of the mode increases with the thickness, shifting the avoided crossing to longer wavelengths. A different behaviour can be noticed for the x-polarised modes (Figure 7.6, right). Here the structural perturbation introduces a second linearly polarised surface mode, SM_2, initially very weakly interacting with the FM. As the deformation is increased though, the degree of polarisation (DOP) of SM_2 also progressively increases, resulting in a stronger interaction with the fundamental

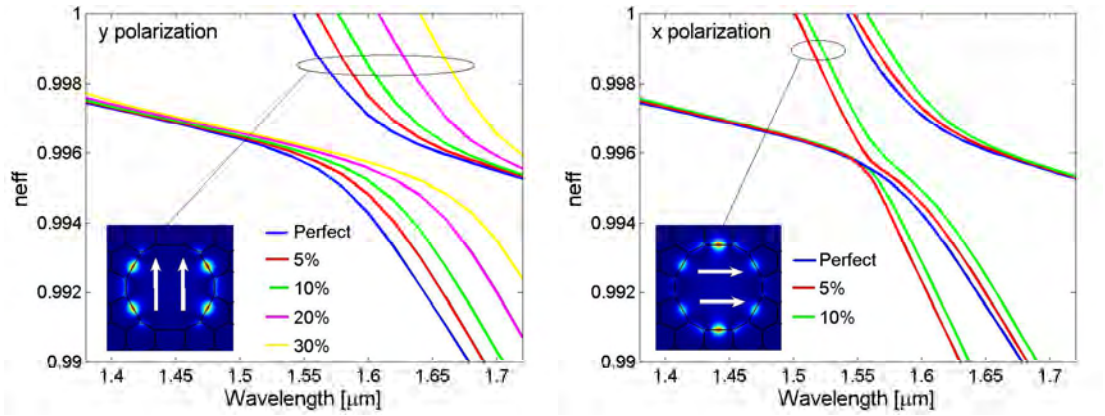

FIGURE 7.6: Effect of core deformation on the mode having the transverse electric field polarised along the y (left) and x axis (right). The insets show the surface mode involved in the anticrossing.

mode. A difference in the wavelength dependent loss for each polarisation will clearly be associated with this behaviour.

According to the coupled mode theory-based model that was proposed in order to evaluate the losses originating from SM-FM interactions, each avoided crossing generates a peak in the loss spectrum [13]. This stems from the fact that near an anticrossing no pure core mode exists: the supermodes existing at those wavelengths (see for example modes (c) and (f) in Figure 7.2) present a large amount of power in the core boundary layer, which can couple quite efficiently to lossy cladding modes in the presence of small structural perturbations along the fibre. The loss peak is approximately Lorentzian in shape: its width is inversely proportional to the difference in propagation constant between the modes involved in the avoided crossing, $\Delta\beta_{ij}$, and its peak value is approximately given by [13]:

$$\text{Loss(dB/m)} \approx \gamma_{\text{i}} \cdot \frac{|\kappa_{\text{ij}}|^2}{(\Delta\beta_{\text{ij}})^2} \tag{7.3}$$

where γ_i is the loss coefficient due to coupling between SM_i and a continuum of leaky cladding modes and $\kappa_{ij} = \Delta n_{min,ij}\,\pi/\lambda_{min,ij}$ describes the coupling between SM_i and FM_j at the avoided crossing wavelength $\lambda_{min,ij}$, where the difference in effective index between the two is $\Delta n_{min,ij}$ [116].

The derivation of the exact γ_i for each SM goes beyond the scope of this study but, as a first approximation, γ_i can be considered as constant for all surface modes, as previously demonstrated in the work by West *et al.* [116], where a good fit to measured loss data was achieved using this assumption. Therefore, in order to acquire a qualitative understanding of the (unweighted) contribution to the overall loss due to the SM-FM interaction, we plot in Figure 7.7 the factor $|\kappa_{ij}|^2/(\Delta\beta_{ij})^2$ for the two polarisations and different levels of distortion.

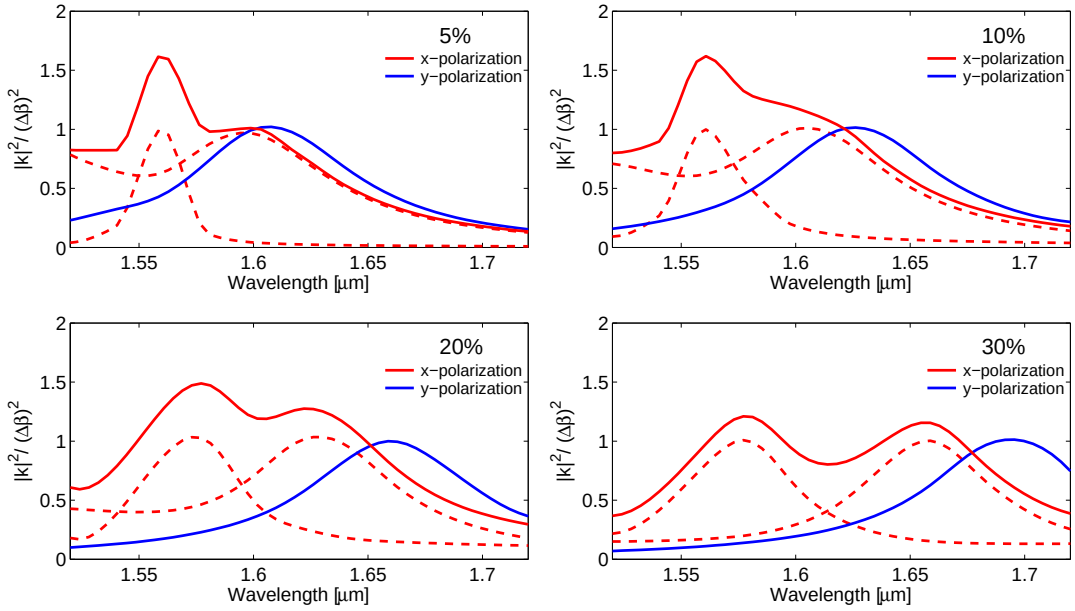

FIGURE 7.7: The set of Lorentzian peaks proportional to the loss induced by avoided crossings in the two polarisations for different levels of structural deformation. The dashed lines represent single peaks while the continuous lines show the total contribution for each polarisation.

From the graphs in Figure 7.7 it can be qualitatively appreciated how even a small-scale perturbation from the perfect structure can introduce significantly different losses for the two polarisation states. This can explain the large value of PDL measured by Wegmuller *et al.* for wavelengths well inside the bandgap in the vicinity of a surface mode [239]. The fibre used in those experiments exhibits a clear core asymmetry and, just as for the fibre studied in Figure 7.5(d) at wavelengths around 1.6 μm, this could well have resulted in an anticrossing between the FM and a SM in just one of the two polarisation states.

To conclude the analysis we calculate the beatlength for a fibre with a distorted core of $\sigma = 10\%$ (Figure 7.8). Far from the anticrossing region, at both shorter and longer wavelengths, only one pair of orthogonal modes is supported in the air core. The beatlength is therefore unequivocally defined, and it presents a strong wavelength dependent behaviour, arising principally from the different wavelength locations of the anticrossing for the two polarisations. This is in accordance with the experimental observation in Ref. [239], where a mean beatlength of 1.1 cm was also measured at a wavelength 70 nm away from an anticrossing.

In the region where avoided crossings for the orthogonal polarisations take place at different wavelengths, i.e. between the vertical dashed lines in Figure 7.8, the definition of beatlength becomes ambiguous. This is due to the presence of two or more modes per polarisation with different propagation constants but similar transverse profiles and

mode overlap with the air core (such as modes (c) and (f) in Figure 7.2). A superposition of those modes is likely to be excited in practical experiments, and therefore, between approximately 1.55 and 1.67 μm, more than one beatlength can be theoretically defined [Figure 7.8 (bottom)], and in principle measured. Generally though, when launching light into these fibres, the coupling is optimised so that the air guided modes are predominantly excited. Under these circumstances we would expect principally the beatlengths corresponding to wavelengths where both interacting modes have a high percentage of power in air to be measurable, such as, in Figure 7.8 (bottom), the region around 1.57 μm for modes x_2 and y_1 (green curve) or around 1.62 μm for x_3 and y_1 (red curve). In practice however, randomly distributed perturbations of the core boundary or 'point-defects' along the fibre length may cause random shifts of the position of the SM within the bandgap, making it difficult to make birefringence or beatlength measurements in the vicinity of the anticrossing, as possibly witnessed during the PBGF birefringence measurements reported by Chen *et al.* [Ref. [234], Fig. 5(a)].

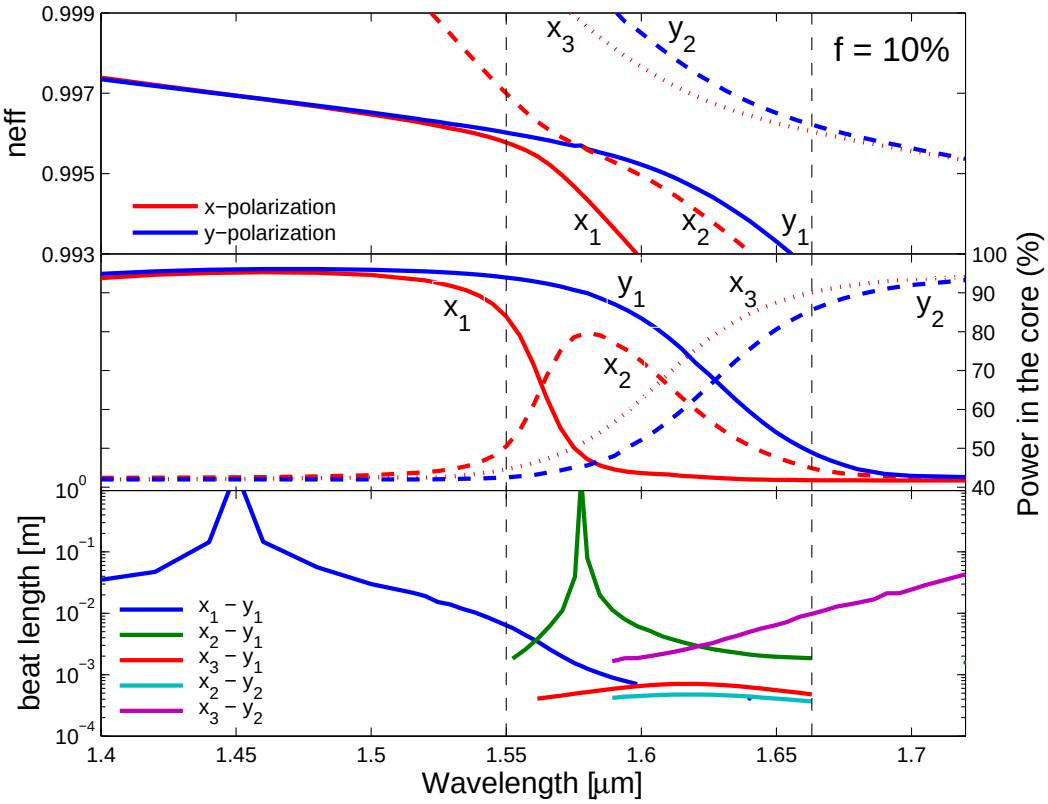

FIGURE 7.8: Effective index (Top) and percentage of the mode in the core (Middle) for the 5 modes involved in three different anticrossings for a fibre with a 10% distortion; (Bottom) Calculated beatlength for various interactions between an x and y polarised mode.

Theoretically calculated values of beatlength as short as a few mm or less for the PBGF in this study may be surprising at first, considering that the structural perturbation

introduced is nearly 1000 times smaller than the period of an otherwise perfectly symmetric structure. This is another consequence of the extreme sensitivity of this type of fibre to structural imperfections at the interface between the defect and the photonic crystal.

7.2.4 Discussion and conclusions

Simulation results for hollow core PBGFs suggest that large and noticeable effects on the fibres' polarisation properties can be produced not only by macroscopic structural deformations, but also by small asymmetries in the shape of the silica ring surrounding the core, where surface modes are located.

Previous experimental observations of anomalous polarisation behaviour in PBGFs, including the measurement of a strongly wavelength dependent beatlength and polarisation dependent loss [239] can be explained by the results presented in this study. Moreover, the observed changes in mode profile as a function of polarisation and wavelength reported in Ref. [238] can be explained by assuming that avoided crossings for the two polarisations occur at slightly different wavelengths due to an asymmetric structural deformation of the core, even when this deformation is small. Under such circumstances, we have shown through a specific example that multiple beatlengths should be theoretically measurable, resulting from the fact that in experiments a superposition of modes with slightly different effective indices would be excited at a given wavelength. We speculate though that due to the presence of 'point defects' or small non-uniformities along the fibre length, a clear measurement of those multiple beatlengths may be problematic [234].

Information about the fibre's birefringence around an anticrossing region may not be important for some applications of PBGFs, particularly if the fibre is operated at wavelengths away from an anticrossing region or it is designed not to have surface modes (see the study presented in the next section). However, in the future, through an improved understanding of anti-crossing behaviour and likely advances in PBGF fabrication, it may be possible to exploit the various phenomena that were described in this section in order to tailor the birefringence and PDL of PBGFs to suit specific applications.

The study presented here highlights the fact that, due to the presence of surface modes, the polarisation properties of hollow core PBGF can be strongly affected by structural features and distortions with length scales around 2-3 orders of magnitude smaller than the cladding periodicity. It is to be appreciated that, for the same reasons, the dispersive properties of such fibres can show a similar level of structural sensitivity. The ability to control the shape of core structures over 3 orders of magnitude could thus represent a key challenge in the future realisation of dispersion-optimised hollow-core PBGFs.

7.3 Design of fibres free of surface-modes

The results reported in the previous section highlighted how interactions between the fundamental core mode and surface modes guided at the core-cladding interface can affect the loss, polarisation properties and also the maximum useable bandwidth of hollow core PBGFs. In this section realistic designs of hollow-core PBGFs are systematically studied in order to identify core shapes that are able to eliminate surface modes from the bandgap altogether. New fibre designs with a fundamental core mode free of anti-crossings with surface modes at all wavelengths within the bandgap are presented; these allow for as wide a low-loss operational bandwidth as possible (which, for the specific fibre analysed in this study, reaches ∼17% of the central gap wavelength).

The results presented in this section are the outcome of a collaborative effort within the Holey Fibre Group at the ORC. My main contributions to this study have been in the initial development of the FEM scripts, in the definition of objectives and methods and in assistance throughout the project in terms of analysis of the results; the bulk of the work however, including the execution of all the simulations and the generation of most of the figures reported, has been carried out by my colleague R. Amezcua-Correa, to whom most of the credit for this work should be attributed.

7.3.1 Introduction

It has already been argued in the previous section how imperfections along the fibre can give rise to coupling of energy between the fundamental air-guided mode (FM) and surface modes (SMs), and then from SMs to cladding modes, resulting in a major source of loss in PBGFs [13, 116]. Moreover, these interactions can drastically reduce the fibre's transmission bandwidth [116, 118], making the presence of surface modes the major limitation in the development of air-silica PBGFs with low-loss and a broad transmission spectrum. Note that, as was shown in Section 6.2.2, the wavelength position and width of the bandgap in these fibres is determined predominantly by the properties of the photonic crystal cladding (which in this study is kept fixed). However, for a given cladding, the useful bandwidth is also determined by the core shape, and in particular whether or not it supports surface modes. Therefore, in order to increase the low-loss transmission window of photonic band gap fibres, it is essential to design core structures that do not support SMs or at least that "push" them towards the bandgap edges. The problem of minimising the impact of surface modes has of course attracted much attention and stimulated several studies in the recent literature. For example, it was proposed that cores formed by introducing a circular defect in a photonic crystal cladding with circular holes can suppress the presence of surface modes, if the defect radius is chosen appropriately [119, 120]. Alternatively, it was suggested that if an appropriate circular silica ring is added at the core-cladding interface, the impact of surface modes

can be reduced [121]. However both these core designs do not resemble real fibres and cannot be readily manufactured with the current fabrication processes. Real fabricated fibres always present a non-circular silica ring at the core-cladding boundary, and often variations in the core size can deform the ring of holes immediately surrounding it. An investigation into the influence of the core design on the overall fibre properties for these realistic structures is therefore needed in order to successfully address the elimination of surface modes [240]. In this section a detailed study of idealised but realistic silica PBGFs structures is presented. The impact that key structural parameters have on the fibre's transmission properties is investigated and a new design regime is identified, where the fundamental core mode is robustly free of anticrossings with surface modes for all frequencies within the bandgap.

7.3.2 Fibre structure and general assumptions

The study is based on PBGFs modelled by using the 8-parameter model presented in Section 6.2.1: the core, with 7 missing holes, is surrounded by a non-circular silica ring of radius R_c and constant thickness t_c, as shown in Figure 6.1(c).

During the fabrication of PBGFs, a reasonable degree of control exists in the determination of the final air-guiding defect, which allows fabricators to modify the size of the core (R_c) and/or the thickness of its boundary (t_c) while maintaining unchanged the cladding structure. For example, the core can be compressed or expanded with respect to its nominal size in the preform by employing appropriate pressures and/or temperatures during the fibre draw, or by using a different pressure for the core relative to that used for the cladding. The surrounding thickness can be modified, for example, by adding an appropriate central capillary during the preform stacking [114]. This study therefore focuses on the effects that these two structural parameters have on the fibre's transmission properties. An assumption in our structural model is that only the first ring of holes is affected by changes in the core shape, while the rest of the cladding is unchanged. This assumption seems justified through a quick visual study of several SEMs of fabricated PBGFs with expanded and compressed cores, such as those shown in Figure 7.9. In Figure 7.9(a) for example (compressed core), the distortion of the structure beyond the first ring is minimal. For the fibre with an expanded core shown in Figure 7.9(c), a certain degree of distortion is observed in the second ring of holes, even though this distortion has little impact on the surface modes, which are localised in the ring around the core. Therefore it is believed that this distortion would not change the conclusions of this study. The corresponding idealised representations of the fibres used for the simulations are shown in Figure 7.9(b) and (d).

The modelled fibre structures strongly resemble the fabricated fibres, suggesting that the designs obtained from this study are feasible. Note that changes in the thickness of the core boundary do not affect the parameter R_c, which is measured from the centre

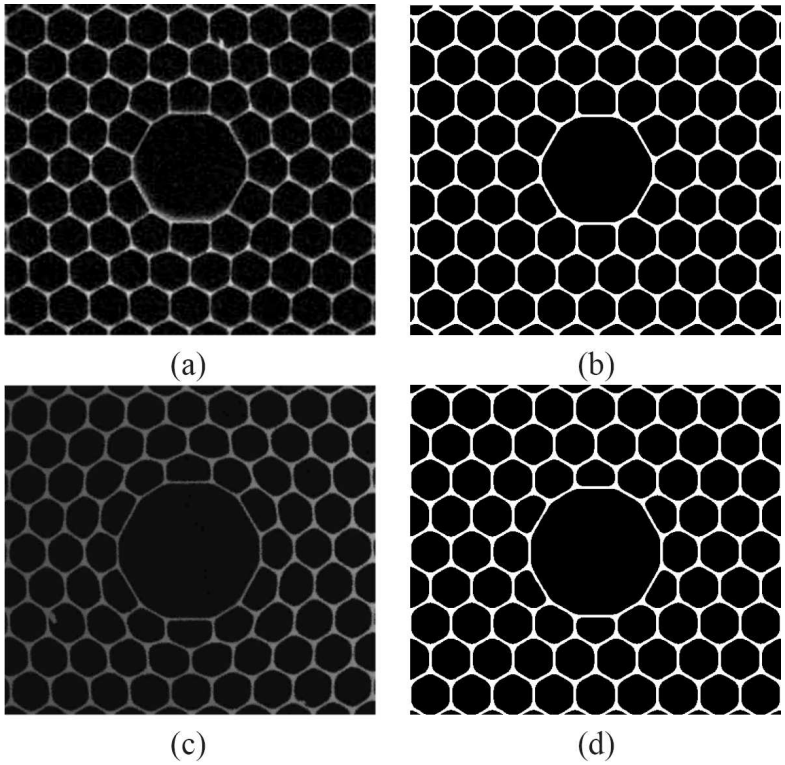

FIGURE 7.9: (a) and (c) SEM images of hollow-core PBGFs fabricated at the ORC (courtesy of Dr. M. N. Petrovich) with compressed and expanded cores respectively. (b) and (d) modelled structures best matching the real fibres, with $d/\Lambda = 0.95$, $D_c/d = 0.58$, normalised ring thickness $T = 1$ and normalised core radius of 94% (b) and 106% (d). (After Ref. [14])

of the fibre to the edge of the first cladding hole. It is useful to introduce a normalised core radius coefficient C as:

$$C = \frac{R_c}{\left(\frac{3\Lambda}{2} - \frac{\Lambda - d}{2}\right)}, \tag{7.4}$$

where values of C smaller than 1 (100%) correspond to fibres with compressed cores and values larger than 100% to fibres with enlarged cores. It is also convenient to consider a parameter T obtained by normalising the thickness of the core boundary t_c to the thickness of the silica struts in the cladding:

$$T = \frac{t_c}{\Lambda - d}. \tag{7.5}$$

Note that by employing the most common fabrication approach involving the use of a central capillary, larger in size and d/Λ than those used in the cladding [114], values of $T \geq 1$ are typically obtained. Figure 7.10 shows some typical structures obtained by modifying C (with $T = 1$) and by changing T (with $C = 100\%$).

In all the following FEM simulations, for the reasons reported in Section 6.2.3, the dielectric properties of silica are directly included in the model through the Sellmeier

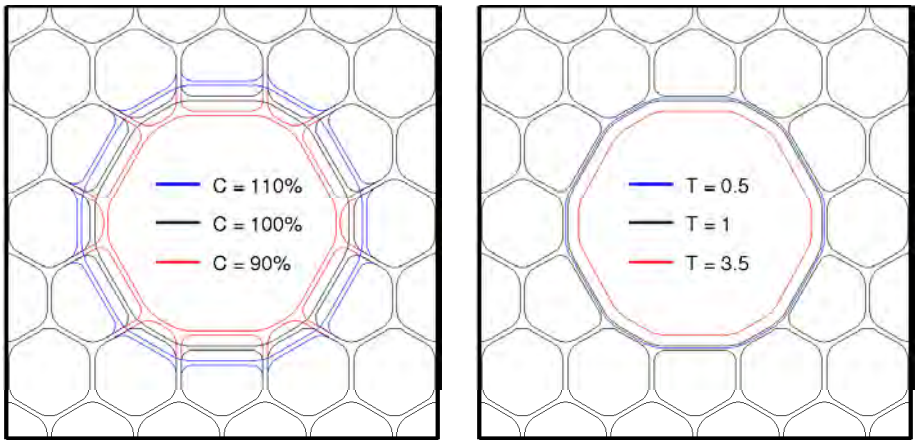

(a) (b)

FIGURE 7.10: Ideal structures resulting from our model with: (a) $T = 1$ and different values of C; (b) $C = 100\%$ and different values of T.

equation. Moreover, since in this study we are only interested in the fundamental air-guided mode and in those surface modes belonging to the same symmetry class and hence interacting with it (as previously observed, modes of different symmetry classes do not interact), than in contrast to the previous study in this chapter, all simulations are conducted on a $\pi/2$ sector of the fibre's cross section. Finally, although the fibres studied here theoretically support higher order, air-guided modes, these will not be analysed at this stage, based on the consideration that they are generally lossier than the FM and therefore the fibres can be effectively considered as single moded.

7.3.3 Methods and results

Once the fibre model had been implemented and tested, and the modifications in the core size had been parameterised through C and T, the values of d/Λ, Λ and D_c/d to be used throughout the study were selected. From the analysis of several SEMs of fabricated PBGFs it was decided that a typical cladding would present $d/\Lambda = 0.95$ and $D_c/d = 0.58$, and therefore these were the values employed in this work as realistic fabrication targets. A hole-to-hole distance $\Lambda = 4.3$ μm was also chosen in order to produce a bandgap centred at around 2 μm, although the results presented here have a more general validity and can be transposed to any other wavelength by simply scaling the structure.

Two parameters were chosen in order to assess the "quality" of each fibre as a function of C and T: the normalised percentage of power in the air core (P_{core}) and the *F-factor* defined by Equation 1.12. The former was found to provide a simple qualitative estimation of the fibre's transmission spectrum, while the second can be employed as an estimate of the likely scattering losses that are present in each fibre.

It was already observed in the previous section how an increase in the fibre's transmission loss is always observed at wavelengths near an avoided crossing [116]. Every SM that appears to anticross with a FM generates a loss dip in the fibre's transmission spectrum [13, 116], thus effectively reducing the fibre's operational bandwidth. The fraction of power in the air core provides a simple way to directly estimate the maximum useful bandwidth, as it peaks at those wavelength regions that are far from anticrossings, it presents dips where interactions with SMs occur [see for example Figure 7.8(middle)] and it falls off rapidly close to the bandgap edges, where the PBG is ineffective at confining the mode.

At wavelengths distant enough from anticrossings, and for fibres with a sufficient number of holes, the dominant loss in PBGFs is the scattering loss due to roughness at the glass/air interfaces (see Section 1.3.2.2). Even though this loss cannot be completely eliminated, it can be reduced by decreasing the intensity of the fundamental core mode at the air-glass interfaces. The *F-factor*, defined in Equation 1.12 as the normalised path integral of the electric field squared calculated on the air-silica boundary, provides a value directly proportional to the minimum loss achievable in the fibre [25]. In the definition of F, the path integral is normalised by the total amount of power in the fibre: therefore a the strong inverse relation between F and $\mathrm{P_{core}}$ exists, as will be further shown in the following simulation results.

In conclusion, the aim of this work is to design core structures that are able to suppress surface modes. By the elimination of SMs the fibre's operational bandwidth is increased and the loss due to mode coupling mechanisms is reduced. In addition, in order to reduce the dominant loss factor at wavelengths where the interaction with surface modes is small, designs that at the same time, if possible, minimise F are also sought.

7.3.3.1 Variation in the thickness of the core boundary

The first part of this study investigates the effects that modifications on the ring thickness have on the fibre's transmission properties. The core size is held constant at an ideal value ($C = 100\%$) and the normalised boundary thickness is scanned by small steps of T in the range $0.175 \leq T \leq 3.5$. For each fibre geometry a wavelength scan through the bandgap (~ 1.9 μm to ~ 2.25 μm) is conducted, and both $\mathrm{P_{core}}$ and the *F-factor* for the various modes are calculated and recorded as a function of λ.

The results are presented in the two-dimensional maps of Figure 7.11 as a function of the normalised ring thickness T and of the wavelength λ. For the design map in Figure 7.11(a), red areas ($\mathrm{P_{core}} \geq 90\%$) represent regions where the fundamental mode is more tightly confined in the core; the yellow diagonal lines ($\mathrm{P_{core}} \sim 60\%$) correspond to anticrossing points between the fundamental and surface modes (note that some lines appear discontinuous in the graph due to the discrete number of T values considered);

green regions (P_{core} ~50%) correspond to wavelengths where the fundamental mode is outside the gap and therefore weakly localised in the core. The regions where the fundamental air-guided mode is no longer supported are shown in blue.

Similarly, the map in Figure 7.11(b) shows the normalised field at the silica-air interfaces, plotted in normalised units of $F\Lambda$: blue areas ($F\Lambda \leq 1$) correspond to regions of high confinement of the fundamental mode, cyan lines (FL $\sim$ 3) to anticrossing points, and red zones to regions where a fundamental air-guided mode is no longer supported.

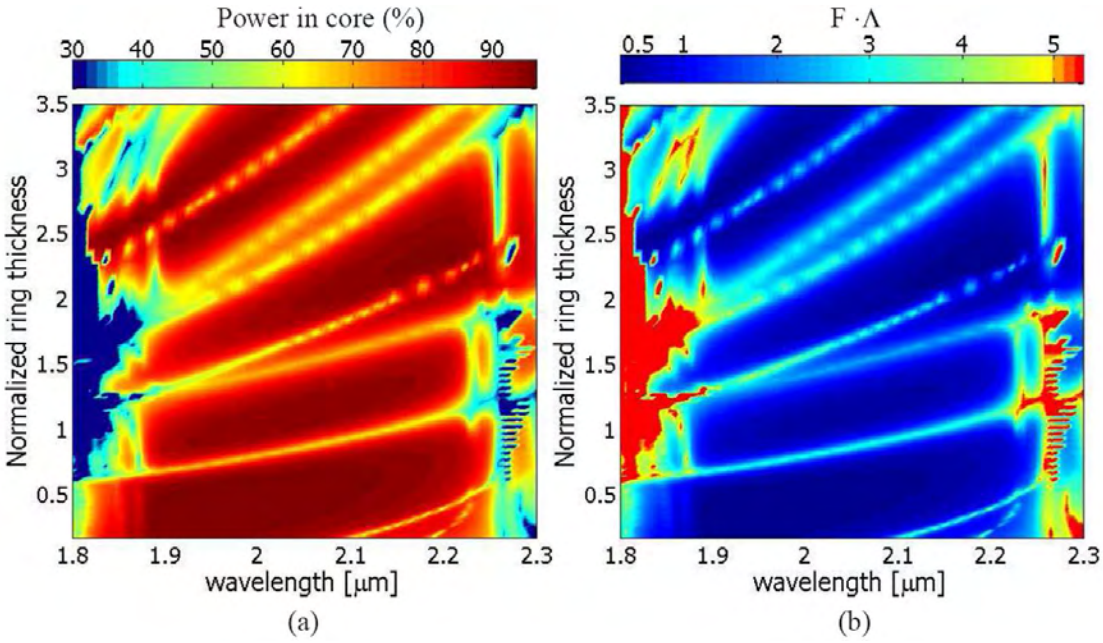

FIGURE 7.11: (a) P_{core} and (b) $F\Lambda$-factor of the fundamental core mode vs. normalised ring thickness and vs. wavelength, for fibres with $C = 100\%$. (After Ref. [14]).

From the maps in Figure 7.11 it can be noticed how the fibre with a core boundary thickness of $T = 0.175$ (the lowest value examined in this study) supports two surface modes, interacting with the FM at $\lambda = 2.1$ μm and $\lambda = 2.19$ μm. Similarly, for most values of T multiple surface modes appear inside the bandgap, in all cases reducing the operational bandwidth of the fibre. However, Figure 7.11 also shows that there are two important design regions for which no surface modes exist inside the bandgap. The first one, which seems to provide the widest possible operational bandwidth, takes place for core surrounds with a thickness of $T \sim 0.5$, while the second regime occurs around $T = 1.15$.

The evolution of the dispersion curve of fundamental and surface modes as the thickness of the core boundary increases from $T = 0.175$ to $T = 0.7$ is presented in Figure 7.12(a) and (b). Solid lines correspond to the effective index of the fundamental air-guided mode, while dashed lines correspond to surface modes. Figure 7.12(c) shows the $F\Lambda$-factor of the fundamental core mode for fibres with $T = 0.4$, 0.5, 0.6 and 0.7. As it can be observed from Figure 7.12(a), an increase in the thickness of the silica ring at

the core-cladding interface (modifying T from 0.175 to 0.4) produces an increase in the effective index of the surface modes, which in turns shifts the anticrossings towards longer wavelengths and increases the fibre's operational bandwidth. Additionally, the strength of the interactions is reduced. As T increases still further, see Figure 7.12(b), the surface modes are progressively "pushed" beyond the longest edge of the bandgap, where they become indistinguishable from the continuum of cladding modes. As a result, the fundamental mode of a PBGF with $T = 0.6$ is completely free of anticrossings with surface modes. Increasing the thickness still further results in a new surface mode appearing on the short wavelength side of the gap, along with a related decrease in the operational bandwidth of the fibre.

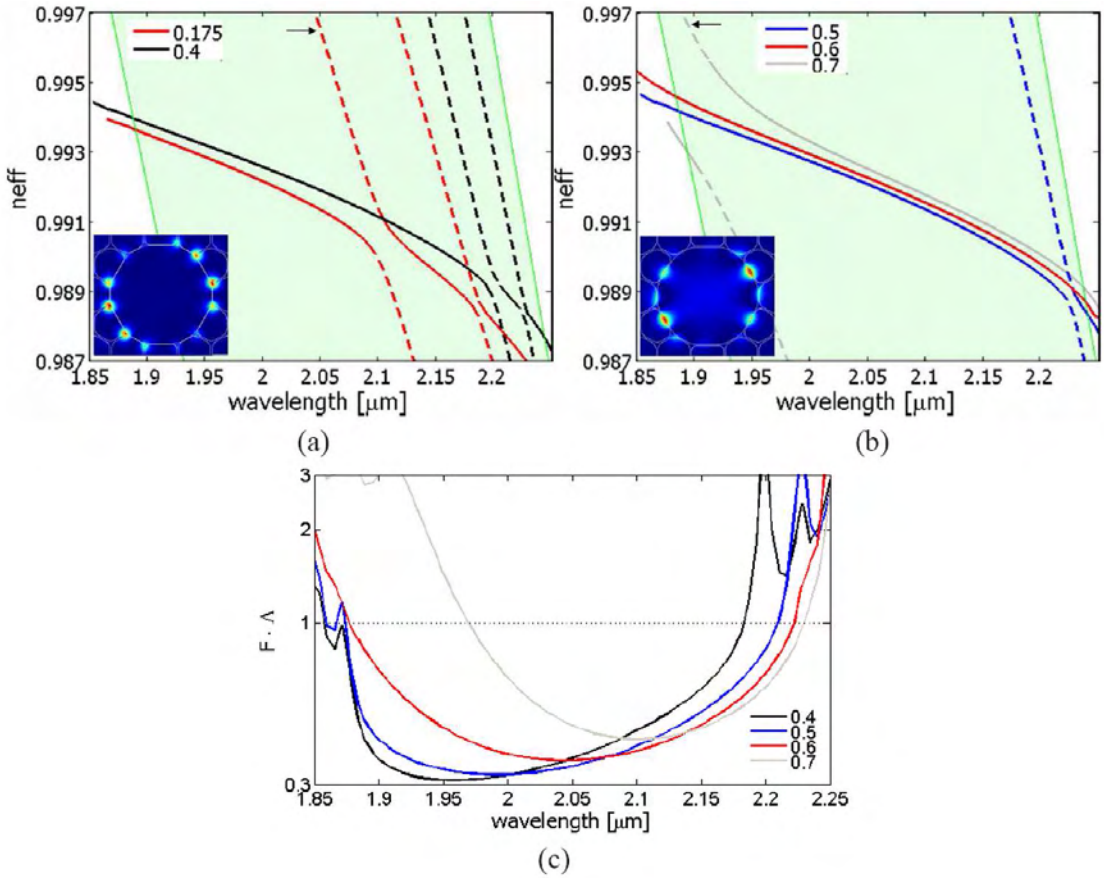

FIGURE 7.12: Dispersion curves of the fundamental mode (solid lines) and surface modes (dashed lines) for fibres with (a) $T = 0.175$ and 0.4, (b) $T = 0.5$, 0.6 and 0.7. Insets show the mode profiles of the surface modes indicated by the arrows. (c) $F\Lambda$-factor of the FM for fibres with $T = 0.4$, 0.5, 0.6 and 0.7. (After Ref. [14]).

The appearance of this design region free of surface modes can be explained as follows. Termination of the cladding in such a way to create an air core with no additional silica ring (i.e. for $T = 0$) generates surface modes whose intensity maxima are located at the "corners" of the photonic crystal (i.e. in the thicker portion of silica separating three adjacent holes), as described by Kim, Digonnet *et al.* [119–121]. The profile of a surface mode localised at the corners of the photonic crystal is shown in the inset of Figure 7.12(a), and it corresponds to the mode indicated by an arrow. However, if

a silica ring of thickness $T = 0.7$ is added, the structure is perturbed strongly enough to support a new type of surface mode, which concentrates its energy at the thin silica struts of the core boundary, see the inset in Figure 7.12(b). During these studies though, we found that between these two fibre designs there is an intermediate design regime that induces a perturbation that is too weak to support surface modes of the second type but strong enough to shift surface modes of the first type outside the bandgap. The factor $F\Lambda$ for the fundamental mode of a fibre with $T \leq 0.6$ is approximately equal to unity in the vicinity of the short wavelength edge of the bandgap ($\lambda \sim 1.88$ μm), see Figure 7.12(c) and Figure 7.11(b), and it remains below unity across most of the bandgap, when no surface modes are present. We therefore set $F\Lambda < 1$ as the criterion to measure the useful bandwidth of the fibres, and define the *operational bandwidth* as the maximum continuous wavelength range for which this condition is satisfied within the bandgap. Using this definition the operational bandwidth is shown in Figure 7.13 as a function of the normalised core thickness. In Figure 7.13(a) the operational bandwidth is normalised with respect to the central gap wavelength, $\lambda_c = 2.05$ μm, while in Figure 7.13(b) the same results are normalised with respect to the bandgap width measured at the airline (equal to ∼330 nm). As expected, PBGF structures with rings of thickness in the range of approximately $0.45 \leq T \leq 0.65$ are optimal for broadband transmission, providing a wide operational bandwidth of more than 15% of the central gap wavelength. Figure 7.13(b) shows that fibres in this new design regime have an operational bandwidth of over 90% of the gap width at the airline. The maximum operational bandwidth is ∼17% of λ_c (105% of the bandgap width at the airline) for a fibre with a ring of $T = 0.575$. Note that this new design regime drastically reduces the impact of surface modes as compared with a more conventional core design of $T = 1$: in this latter regime an operational bandwidth of only 9% of λ_c is obtained, due to the presence of SMs close to the PBG edges.

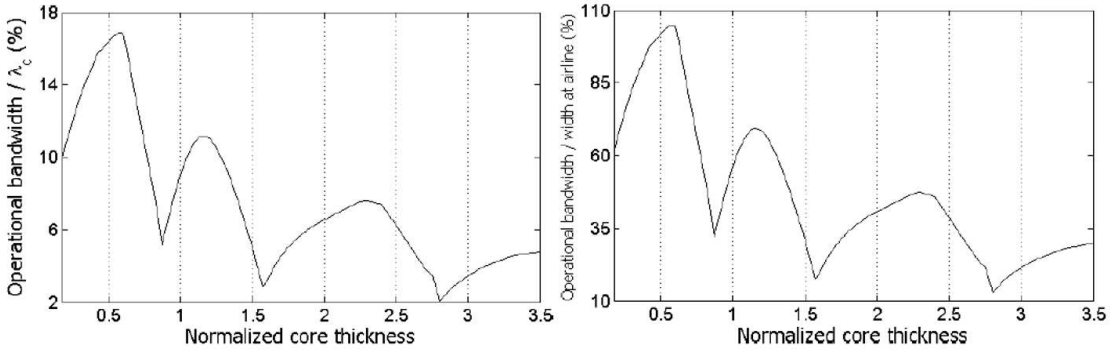

FIGURE 7.13: (a) Operational bandwidth normalised with respect to the central gap wavelength $\lambda_c = 2.05$ μm, and (b) normalised with respect to the bandgap width measured at the airline, equal to 330 nm. (After Ref. [14]).

Finally, to conclude this analysis, a plot summarising the two maps in Figure 7.11 is shown in Figure 7.14: for each different ring thickness the minimum $F\Lambda$ factor and the maximum amount of power in the core across all wavelengths in the bandgap are plotted.

Three design regimes are found, where the confinement of the fundamental mode in the core and the factor $F\Lambda$ are maximised and minimised respectively. These correspond to the thin ring region centred round $T = 0.5$, an intermediate region around $T = 1.15$ and the antiresonant region studied by Roberts *et al.* [25, 114] around $T = 2.5$. Note that for this particular fibre the antiresonant region does not seem to offer particular advantages, even though, as it will be shown in the following, for other fibre designs it can offer the possibility of reducing the scattering loss [114]. For the particular fibre analysed, with $C = 100\%$, the thin ring design presents at the same time the widest operational bandwidth and the lowest scattering loss ($F\Lambda$-factor), and should therefore be considered as the preferred fabrication target.

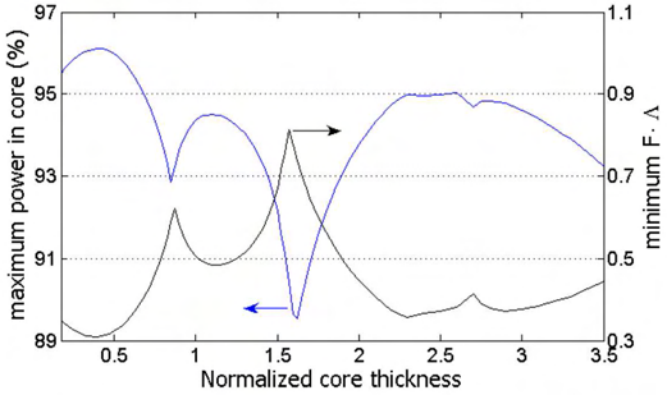

FIGURE 7.14: (blue) Maximum of the core-confined energy and (black) minimum $F\Lambda$-factor of the fundamental core mode vs. normalised ring thickness. (After Ref. [14]).

7.3.3.2 Variation in the core size

In this final part the effects that compressing or expanding the core produce on the fibre's transmission properties are studied. To do so, the fibre's core was modified by scanning the expansion coefficient C from 94% to 106% in 1.5% intervals. For each core radius the thickness of the core boundary T was varied in the range previously discussed. Nine contour maps for the percentage of power in the core of the fundamental air guided mode as a function of C were thus obtained. As the core is expanded, the amount of power in the central air region increases (red regions of the contour maps become darker). It was found that the number and position of surface modes in fibres with thick core surrounds ($T > 2$) is strongly dependent on the size of the core. Conversely, surface modes supported by fibres with thin core surrounds ($T < 0.6$) are nearly independent on the core size. This behaviour is more evident when comparing the contour maps for the fibres with the smallest ($C = 94\%$) and largest ($C = 106\%$) core analysed, shown in Figure 7.15(a) and (b) respectively: the lower part of the maps remains almost unchanged while the upper part presents evident differences.

The maximum P_{core}, the minimum $F\Lambda$ and the operational bandwidth are presented as a function of the normalised ring thickness and for different core radii in Figure 7.16(a),(b)

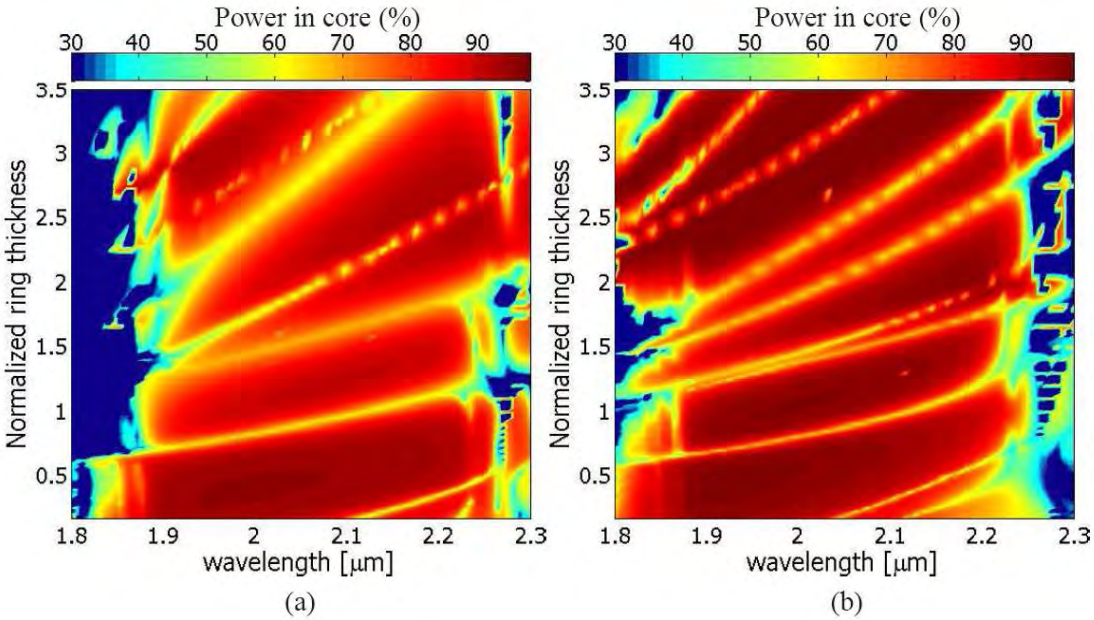

FIGURE 7.15: Contour maps of P_{core} of the FM for fibres with the (a) smallest ($C = 94\%$) and (b) largest ($C = 106\%$) core analysed. (After Ref. [14]).

and (c) respectively. Changes of the core radius do not drastically shift the position of the three design regimes, found for $C = 100\%$, in which the mode confinement is maximised and F is minimised. The effect of antiresonances (T around 2.5-3) become more evident for larger cores, i.e. $C = 103\%$ and 106%. Despite the presence of surface modes, fibres with large cores and antiresonant core surrounding are likely to present the lowest loss amongst the fibres analysed; however they do offer a rather narrow operational bandwidth. Moreover, in these fibres the actual size of the core has a large impact on the minimum achievable value of F. In contrast, it was found that the thin ring design regime (T around 0.5) is robust against the size of the hollow-core, see Figure 7.16(c). This is important as it relaxes the requirement for a precise control of the size of the core during the fabrication process. Additionally, for all the simulated core sizes, thin ring designs are found to offer the widest operational bandwidth and generally quite a low scattering loss. If the cores are not too expanded ($C < 103\%$), thin ring designs even present lower F values than designs with antiresonant core surrounds.

7.3.4 Conclusion

Through numerical simulations it was demonstrated that a careful choice of the thickness of the silica ring around the core and of the size of the air core allows the design of realistic PBGFs with a fundamental air-guided mode free of anticrossings with surface modes at all wavelengths within the bandgap. The best fibres were found to be those presenting a silica ring surrounding the core with a thickness around half the thickness of the cladding struts. These designs offer the widest operational bandwidth and should thus be preferred when fabricating fibres for broadband operation. Furthermore, it was

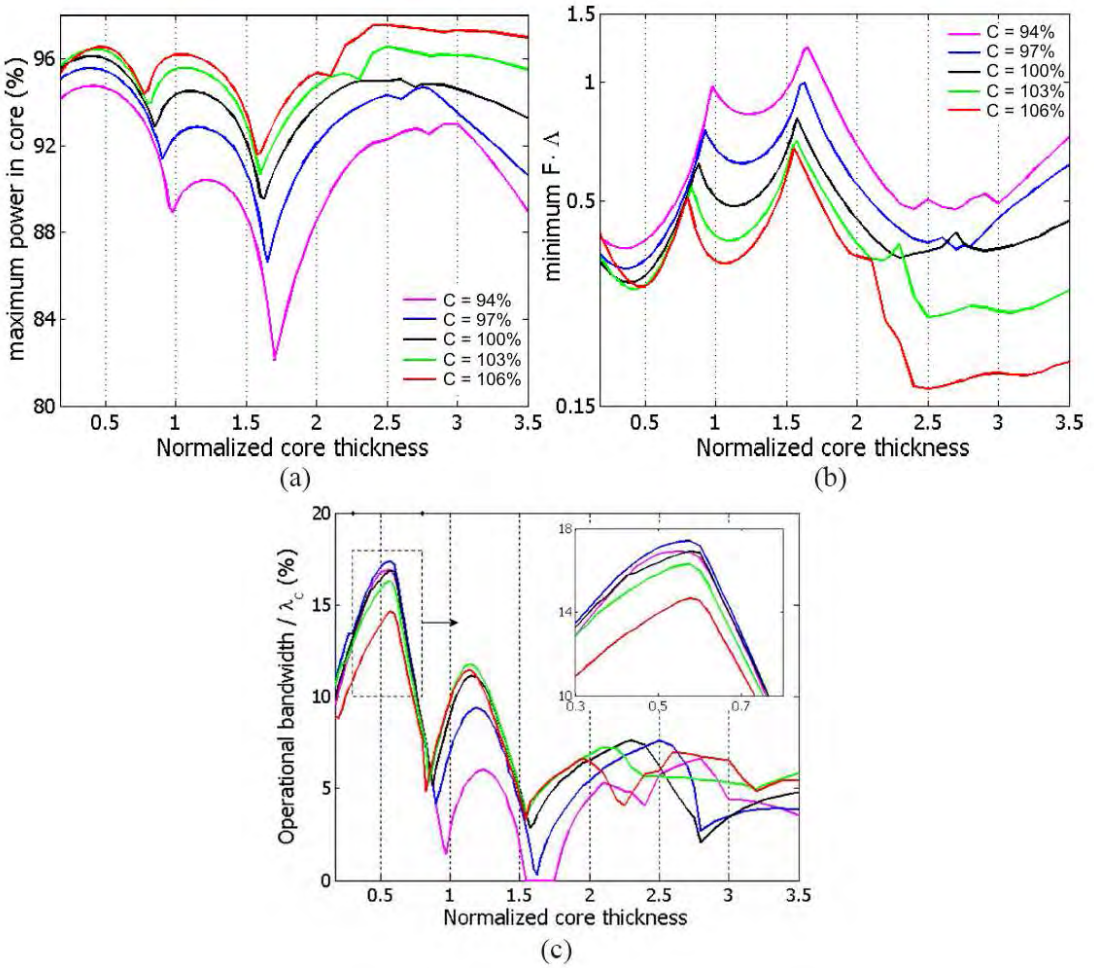

FIGURE 7.16: (a) Maximum fraction of power in the core, (b) minimum $F\Lambda$, and (c) operational bandwidth normalised with respect to the central wavelength, $\lambda_c = 2.05$ μmfor different values of the normalised core thickness T and for $C = 94\%$, 97%, 100%, 103% and 106%. (After Ref. [14]).

demonstrated that the suggested designs are robust in eliminating surface modes, as variations in the core size affect their operational bandwidth only marginally. These results can be transposed to other wavelengths by scaling the structures. Several fibres with different cladding parameters have also been studied, demonstrating that these conclusions are independent of the cladding type. Initial studies of fibres with a 19-cell core suggest that the design regime presented here also maximises the useful bandwidth of these fibres [241].

Finally, the approach chosen to model the fibres suggests that the optimum design is indeed realisable. Thicknesses of the central silica ring close to the optimum ($T \sim 0.5$) can be obtained simply by modifying the fabrication process and avoiding the use of the central capillary in the fibre preform. A preliminary validation of these results was obtained by characterising several fibres fabricated with this method, including those analysed in Section 6.3, and observing that no sign of interactions with surface modes in the central part of the bandgap could be detected.

Chapter 8

Conclusions and future directions

Interest in the field of optical waveguides has received an enormous boost by the recent introduction of microstructured optical fibres, which, in the space of only a few years, have assumed a significant role in many scientific and commercial applications. The potential for accessing unprecedented optical regimes and novel physical effects stems from the higher index contrasts, a larger flexibility in the choice of glasses and in the way the air holes can be topologically arranged to form the fibre's cross section, as compared to conventional fibres. This enhanced design flexibility has increased the demand for efficient modelling tools, able to analyse a large number of designs and determine the best ones for a specific application, or to thoroughly scan certain design spaces in order to understand the ultimate performance limits of these fibres. Accurate modelling can also provide support for experimental activities and allow the understanding of physical effects that might be difficult to observe experimentally. This thesis has established the FEM to be a versatile and efficient modelling method for the electromagnetic modelling of MOFs. I have employed FEM modelling for the purpose of: (i) designing optimum fibres for a range of specific applications with the practical fabrication constraints in mind; (ii) analysing fabricated fibres and extrapolating the optical performances at other structural scales; (iii) understanding experimentally observed phenomena; and (iv) identifying fundamental limits of these fibres. Close interaction with fabricators and experimentalists within the silica and compound glass MOF groups at the ORC has allowed frequent experimental confirmations of the numerical accuracy of the model implemented, and it has contributed to improve our current understanding of the potential and limitations of MOFs. This concluding chapter summarises the work presented in this thesis and suggests some future directions.

8.1 Summary of this work

Since electromagnetic propagation in mixed dielectric structures with a complex transverse profile cannot be studied analytically, several numerical methods have been developed over the years to model the main optical properties of MOFs. The preliminary work in this thesis has concerned the analysis and comparison of the various methods.

The FEM was identified as one of the most complete and efficient methods for the modelling of MOFs. Besides allowing the direct inclusion of the material dispersion into the calculations and the direct estimation of confinement losses, it also permits cross sections of any shape and topology to be studied, as required in the study of fabricated fibres; furthermore, in order to reduce computation time, symmetries in the fibre's transverse profile can be also exploited. In addition, the use of libraries of routines for sparse matrices, highly optimised over more than 40 years of use in aerospace and structural engineering design, makes the FEM the most efficient method amongst those that I have tested, enabling the computation time to be improved by up to an order of magnitude. The calculation of the fundamental mode of typical MOFs is obtained in minutes, rather than hours, and it can be performed on an ordinary desktop computer with no requirement for supercomputing facilities. This high efficiency was key to the routine execution of inverse design methods for the search of the optimum solution, frequently employed throughout the thesis. Finally, the possibility of using unequal meshes, denser in those areas where the field changes more rapidly, or where small structural details need to be accurately described, allows the study of structures, such as those presented by realistic PBGFs, where details on length scales differing by orders of magnitude determine the detailed optical performance of the fibre. A commercial FEM package for the solution of general PDEs has been adapted to the harmonic analysis of high frequency electromagnetic waves in both index guiding and photonic bandgap guiding MOFs.

Two approaches to design fibres with required optical properties are explored in this thesis, either through the use of property maps or through the use of inverse design methods. The first approach involves pre-calculating optical maps, in which the contour plots of many optical properties are overlaid. This method has been applied to the design of various hexagonally stacked HFs with circular holes. In the thesis the maps are employed in order to: (i) acquire a more fundamental understanding of the applicability of HFs for DWDM data transmission, and determine two structural designs and corresponding applications where HFs have the potential to compete with conventional fibres; (ii) design a fibre with optimum dispersion characteristics for SC generation around 1 μm; (iii) design optimum tapering paths in highly nonlinear fibres made of different glasses, in order to enhance the Brillouin threshold while maintaining an overall near-zero dispersion.

Optical maps provide invaluable assistance in the fibre design, whenever they can be applied. However, their use is limited to structures with a restricted number of free-parameters and they are generally computationally rather demanding. A second approach to design optimum fibres, involving the use of specific inverse design methods, is therefore explored. The Nelder-Mead or Downhill Simplex method (DSM) and the Genetic Algorithm (GA) are applied to the dispersion optimisation of nonlinear fibres. Despite a simple coding, the Simplex method represents an efficient way to locate the minimum of rather smooth multi-dimensional objective functions. It was therefore employed to optimise 2 and 3 free-structural parameters in the search for SF57 nonlinear SEST fibres that presented nearly zero and flat dispersion at telecom wavelengths and a negligible confinement loss. Fabrication of the resulting best fibres was subsequently targeted by my colleagues and, although the ORC fire (30/10/2005) prevented the fabrication of a fibre closely matching the specifications, fibres close enough to the target were found to possess a novel combination of high nonlinearity and low dispersion [182, 242], and one of them was employed for the demonstration of efficient and broadband Four-Wave Mixing at telecom wavelengths [243]. A second inverse technique, more suited for exhaustive searches in those design problems with several free-parameters, where multiple false minima may occur, is the Genetic Algorithm. A GA was applied to the design of nonlinear silica HFs with a flat dispersion between 1.5 and 1.6 μm. The best fibres, presenting a cross section with holes of different sizes and up to 6 free-parameters, were found to have an extremely small theoretical dispersion ($D = 0 \pm 0.1$ ps/nm/km) over the full wavelength range of interest; furthermore, the tolerance required on the most critical structural parameters in order to achieve these values was found to be compatible with the present fabrication technology.

The FEM modal solver was then used to model a fabricated suspended core HF in order to confirm its measured dispersion and nonlinear coefficient and to establish the fibre's behaviour at different wavelengths and for other core dimensions. The study suggests interesting applications for this fibre, which also benefits from a novel and simplified method of preform fabrication through ultrasonic drilling. These applications include use within evanescent-wave chemical sensing of gases and liquids, as a dispersion compensating fibre, or as a polarisation maintaining highly nonlinear fibre.

Efficient generation of white/RGB light, currently a hot topic amongst the optical community for application, for example, in portable projectors, has been also targeted. I analyse two possible approaches to achieve it: through SC generation at visible wavelengths, and through a parametric process in birefringent, phase-matched waveguides. The waveguide requirement for the efficient generation of supercontinuum light at visible wavelengths has been studied, and it was demonstrated that fibre geometries allowing the required zero dispersion wavelengths in the visible are indeed possible, even though not all waveguide shapes are suitable. The large amount of waveguide dispersion that is necessary to compensate for the large and normal material dispersion in the visible

can be obtained by core shapes with a large convexity and high rotational symmetry. A holey fibre with hexagonal symmetry and large air filling fraction has been designed for this application, and its fabrication is amongst the next targets of the fabrication group at the ORC. FEM modelling is also employed to understand the parametric mechanism underlying the experimentally observed generation of RGB light: when ps pulses of green light were launched into sub-micrometre secondary cores in the cladding of a PBGF, discrete red and blue sidebands were observed after 30 cm to 1 m of fibre propagation. Detailed models of the fibre structure indicate that the RGB generation is based on FWM in single, birefringent cores, where the pump light and the sidebands propagating in orthogonally polarised fundamental modes are phase matched. From this study, an optimised white light laser source with equal powers in the red, green, and blue spectral regions seems feasible in due course.

The second part of this thesis is concerned with the modelling of PBGFs. Beside the modal FEM solver already employed for index guiding fibres, two further FEM-based programs for the calculation of photonic bandgaps and of photonic density of states were also developed for a more complete analysis of these fibres. A model of the cross-section of realistic fibres is developed and employed to study the typical properties of fibres with 7 and 19 cell cores, to devise scaling rules for the bandgap and for the air-guided modes, and to analyse the contribution of the glass attenuation and dispersion to the overall optical performance of the fibre. Even though more than 90% of the optical power guided in the fundamental mode resides in air, simulations show that the glass dispersion needs to be taken into account for accurate results. On the other hand, the material losses are highly reduced, and the study also shows that chemical and biological sensing applications in the mid-IR could be targeted using silica hollow core fibres, despite the large intrinsic loss of the glass above 2 μm.

Applicability and limitations of two different techniques for modelling real fabricated PBGFs have been thoroughly studied. Ideal, parametrised fibres can be employed to model the fairly regular structures produced with the current technology, although an initial fitting of some structural parameters through comparison with the measured transmission spectrum is recommended. Alternatively, and/or in order to estimate the polarisation properties of the fibre, structures directly extracted from SEMs can be simulated. In this case, the size of the SEM bitmap is identified as one of the main limiting factors in obtaining accurate predictions. It is demonstrated that a good agreement with the measured data in terms of spectral position and width of the bandgap can be obtained, provided that high resolution SEM images are employed. The thickness of the coating layer, which can reach up to 25% of the strut thickness for certain fibres of interest, is also another issue to be faced.

The polarisation properties of hollow core PBGFs are analysed in order to propose an explanation for a number of unusual experimentally observed effects, such as a strongly wavelength dependent beatlength and polarisation dependent loss, or the difference in

mode profile observed for the two polarisations at certain wavelengths. This thesis suggests that all of these effects are caused by small asymmetries in the shape of the silica ring surrounding the core, where surface modes are located. Under such circumstances, an avoided crossing between FM and SM takes place at slightly different wavelengths for the two polarisations, giving rise to the observed phenomena, as well as multiple beatlengths that should, in principle, be measurable. The study highlights the fact that the amount of distortion of the thin core boundary required to cause noticeable effects is around 2-3 orders of magnitude smaller than the cladding periodicity. This makes the simulation of these effects and their practical elimination particularly difficult.

Finally, the design of realistic silica PBGFs with the widest bandwidth and the lowest loss is targeted. It is demonstrated that, through a careful choice of the thickness of the core boundary and of the size of the core defect, the fundamental air-guided mode can be free of anticrossings with surface modes at all wavelengths within the bandgap. The optimum fibres present an air core surrounded by a silica ring with nearly halved thickness with respect to the cladding struts. This design offers the widest operational bandwidth and should therefore be targeted when fabricating fibres for broadband operation. Furthermore, it is demonstrated that the suggested designs are robust in eliminating surface modes, as variations in the core size affect their operational bandwidth only marginally. By appropriately scaling the structures these results can be transposed to any other wavelength. Experimental confirmation of these theoretical results has come through the characterisation of several fibres, fabricated according to these design rules. As opposed ro most of the other fibres reported in the literature, our fibres show no sign of interactions with surface modes in the central part of the bandgap.

8.2 Future work

The reported work on the use of the optical maps has demonstrated the wide applicability of this approach to a vast range of design problems. The maps can be used, in the future, to understand the key properties and to design other types of MOFs, which can be parametrised on a two dimensional space. For example, one dimensional *"Bragg fibres"*, either index guiding [186] or photonic bandgap guiding guiding [187] can be studied, where the period of the spacing between alternating dielectric rings and the index difference between the two materials could be set as free-parameters. The maps have also been proved invaluable in the design of tapers with a controlled change in the optical properties along the length, and numerous future studies can be envisaged in this area. Besides the reported enhancement of the Brillouin threshold with associated dispersion control, tapered HFs can also allow, for example, a specific dispersion profile along the length; this could be suitable for extra-wideband SC generation or for soliton compression [244]. Carefully designed tapers could also allow, at the same time, a

reduction in the effective area and in the dispersion, which would allow very high soliton compression to be achieved [185].

The inverse design approaches implemented in the thesis have also quite a large applicability to many structural fibre designs, as documented by a number of studies recently published [198, 199]. However, a parametrisation of the structures to be optimised is required. A method able to search through all possible structures without any pre-defined parametrisation would therefore represent an obvious improvement of these methods. A possible candidate is the Level-Set method, which represents the arbitrary interface between two media as the zero-contour of a curve in a higher dimensional space [200]. As a result, the method is able to evolve the interface to any possible shape, and even modify the initial topology. Kao *et al.* have shown that the level set method can be combined with a generalised gradient descent method in order to find the best structures that maximise the photonic bandgap width for planar propagation [201]. Differently from the planar case, where a scalar approximation of Maxwell's equations is allowed though, most MOFs require a full vector solution, which clearly complicates the analytical formulation of the generalised gradient and poses a serious challenge to the implementation of such a method.

In the study of fabricated photonic bandgap fibres, ongoing work focuses on the evaluation of other image acquisition techniques, such as the environmental SEM (ESEM), which do not require a conductive coating and are expected to provide a significant improvement in the accuracy of the FEM simulations from an SEM image. This would facilitate a deeper understanding of the FM–SM interactions and could help designing fibres where the interaction with surface modes is exploited rather avoided. For example, it may be possible to exploit the different anticrossing wavelengths between FM and SM in the orthogonal polarisations in order to tailor the birefringence (as suggested by Roberts *et al.* [245]) and PDL of PBGFs to suit specific applications. The ability to control and exploit the anticrossing between FMs and SMs may also be the key to realise dispersion-optimised hollow-core PBGFs, that may find important applications as low-loss, low-nonlinearity transmission fibres for telecommunications or in extremely high power pulse compression and amplification schemes.

Appendix A

Brillouin nonlinearity within optical fibres

Brillouin scattering in an optical fibre results from the interaction between a guided light wave and an acoustic wave, the latter of which can either be guided or anti-guided depending upon the core structure of the fibre [246]. Thermally excited acoustic phonons initiate a periodic modulation of the refractive index as they travel along the fibre length. Brillouin scattering occurs when the pump lightwave is diffracted in a backward direction by this moving grating, giving rise to frequency shifted Stokes and anti-Stokes waves via the Doppler effect. This process can be stimulated when the interference between the pump and Stokes waves reinforces the acoustic wave through electrostriction. Note that the longitudinal components of the relevant waves are responsible for this reinforcement. The resultant frequency shift ν_B of the scattered light is determined by the time taken for the acoustic wave to travel between the adjacent interference peaks,

$$\nu_B(z) = \frac{2n_{\text{eff}}(z) \cdot v_A}{\lambda} \tag{A.1}$$

where v_A is the acoustic velocity within the fibre, $\mathrm{n_{eff}(z)}$ the effective modal index, and λ the vacuum wavelength of the pump lightwave. The quantity $\nu_B(z)$ is referred to as the Brillouin frequency shift (BFS) and its dependence on the longitudinal coordinate z is only true in the case of longitudinally varying fibres. The attenuation of sound waves in silica determines the shape of the Brillouin gain spectrum (BGS). It has been shown that the exponential decay of the acoustic waves results in a Lorenzian spectral shape for the BGS [6]:

$$g_B(\nu, z) = g_{B0} \frac{(\Delta\nu_B/2)^2}{(\nu - \nu_B(z))^2 + (\Delta\nu_B/2)^2} \tag{A.2}$$

where $\Delta\nu_B$ is the full width at half maximum (FWHM). This is related to the decay time constant Γ of the sound wave via $\Delta\nu_B = \Gamma/2\pi$. Thus, the BGS peaks at a frequency shifted by $\nu_B(z)$ from the optical pump frequency. The peak value of the gain coefficient g_{B0} is referred to as the Brillouin gain coefficient (BGC) [47],

$$g_{B0} = \frac{4\pi^2\gamma_e^2}{n\nu_A c\lambda^2\rho_0\Gamma} = \frac{4\pi\gamma_e^2}{\nu_B c\lambda^3\rho_0\Delta\nu_B} \tag{A.3}$$

where γ_e is the electrostriction constant, ρ_0 the density of the material, and c the velocity of light in vacuum.

When pump light with power $I_p(0)$ is launched into a fibre, the evolution of the Stokes wave $I_S(\nu, z)$ with frequency shift $\nu_B(z)$ at the coordinate z is given by:

$$\frac{dI_s(\nu,z)}{dz} = -g_B(\nu,z)\frac{I_P(z)}{A_{\text{eff}}}I_s(\nu,z) + \alpha I_s(\nu,z) \tag{A.4}$$

where α is the loss coefficient, A_{eff} is the effective core area, and the signs have been chosen to represent a Stokes wave propagating along the negative z-direction, counter-directionally to the pump wave. If pump depletion is disregarded and only the pump attenuation loss is considered, by solving the separable first order ODE in (A.4) the power in the Stokes wave at z = 0 can be obtained as:

$$I_s(\nu,0) = I_s(\nu,z)e^{\left(-\alpha L + \frac{I_P(0)}{A_{\text{eff}}}G(\nu)\right)} \tag{A.5}$$

where $G(\nu)$ is the effective gain coefficient:

$$G(\nu) = \int_0^L g_B(\nu,z)\cdot e^{-\alpha z}dz. \tag{A.6}$$

It is evident how the SBS efficiency is maximum at a frequency ν_{max} for which $G(\nu)$ is maximised. For a fibre with a uniform BFS along the length, $g_B(\nu_B, z) = g_{B0}$ for any z and the effective gain coefficient becomes

$$G(\nu_B) = G_0 = g_{B0}L_{\text{eff}} \tag{A.7}$$

where L_{eff} is the effective interaction length given by $L_{\text{eff}} = [1 - \exp(-\alpha L)/\alpha]$. On the other hand, for a fibre with a z-dependent BFS, the effective gain coefficient $G(\nu)$ is smaller than G_0 because $g_B(\nu_B(z), z) \leq g_{B0}$.

A commonly used formula for evaluating the SBS threshold (defined as the pump power at which the Stokes power equals the input power) is [6]

$$P_{th} \cong 21\frac{KA_{\text{eff}}}{G(\nu_{max})} \tag{A.8}$$

where K is the polarisation factor (K = 1 for polarisation maintaining fibres, otherwise K = 2). From Equation A.9 it is evident how the SBS threshold increases when G(ν_{max}) is reduced by applying a nonuniform BFS distribution along the fibre. The increase in SBS threshold, P_{inc} (dB) is given by

$$P_{inc} = 10\ log_{10}\left[\frac{g_{B0}L_{\text{eff}}}{G(\nu_{max})}\right] = 10\ log_{10}(\sigma) \tag{A.9}$$

where σ is a suppression factor that can be easily evaluated by numerically integrating Equation A.6.

When the acoustic waves are also guided within the optical fibre, several acoustic modes may be involved in the Brillouin scattering process [246]. This can be expressed by summing the individual contributions from different acoustic interactions as

$$g(\nu) = \sum_i g_b^i(\nu) \tag{A.10}$$

Therefore, the Brillouin nonlinearity within any optical fibre can be best characterised by measuring the BFS ν_B, the BGB $\Delta\nu_B$, and the BGC g_{B0} for each peak.

There are two primary ways of experimentally characterising the Brillouin characteristics of a fibre. The most commonly used method is to pump the fibre using a narrow linewidth high power laser source and then to observe the backscattered Brillouin signal. By heterodyning the spontaneous backscattered signal, the BGS can be estimated. However, although very convenient and straightforward to implement, this approach suffers from some practical drawbacks. First, most high power pump sources (typically an amplified DFB laser) contain a large amount of ASE noise, and this may result in errors in the measurement of the observed SBS threshold (i.e. the process can be seeded by ASE and artificially low threshold estimates are obtained. Secondly, when this technique is extended to allow distributed measurements [i.e. using Brillouin optical time domain reflectometry (BOTDR)], the pump has to be pulsed and thus the finite bandwidth of the pump pulses may ultimately limit the spectral resolution of the measurement - the higher the spatial resolution required the lower the spectral resolution of the measurement.

The second main approach, used in all the measurements in Section 3.4, relies upon a direct measurement of Brillouin amplification, where a weak probe beam is amplified by the Brillouin gain induced by a counter-propagating pump beam. In order to produce an accurate measurement of the BGS it is essential to achieve accurate, adjustable control

of the frequency spacing between the pump and probe signal wavelengths. Nikles *et al.* have shown that this can be achieved by using an electro-optic phase modulator (EOM) to generate a well-defined side band component separated, by the applied RF-frequency, from the pump wavelength [179]. By physically splitting the pump and probe signals and passing them in a bidirectional fashion through the fibre under test (e.g. in a Sagnac configuration), it is possible to accurately measure the Brillouin gain properties of the fibre. A schematic of the experimental setup used for the pump probe measurement is shown in Figure A.1. A CW-external cavity laser diode with a linewidth of 100kHz is used as a source. The laser output is split into two beams that serve as a probe and pump beams, respectively. The probe beam is phase modulated by an electro-optic modulator (EOM) that is driven by a microwave generator. The generated (lower frequency) sideband serves as a tunable probe around 10GHz below the carrier frequency (see inset). The pump beam is amplified by a booster amplifier. These two beams are coupled into the fibre under test which is fusion-spliced at both ends into the measurement system. The Brillouin amplification takes place as a result of the counter-propagating geometry. The probe beam was extracted from the Sagnac loop using a circulator. The amplified side band was then filtered from the extracted signal using a fibre Bragg grating (FBG) filter with a 3dB bandwidth of 6GHz and high (>40dB) extinction ratio. The combination of the FBG filter and the circulator allows us to efficiently extract the probe signal and to significantly reduce the beat noise due to the adjacent sidebands.

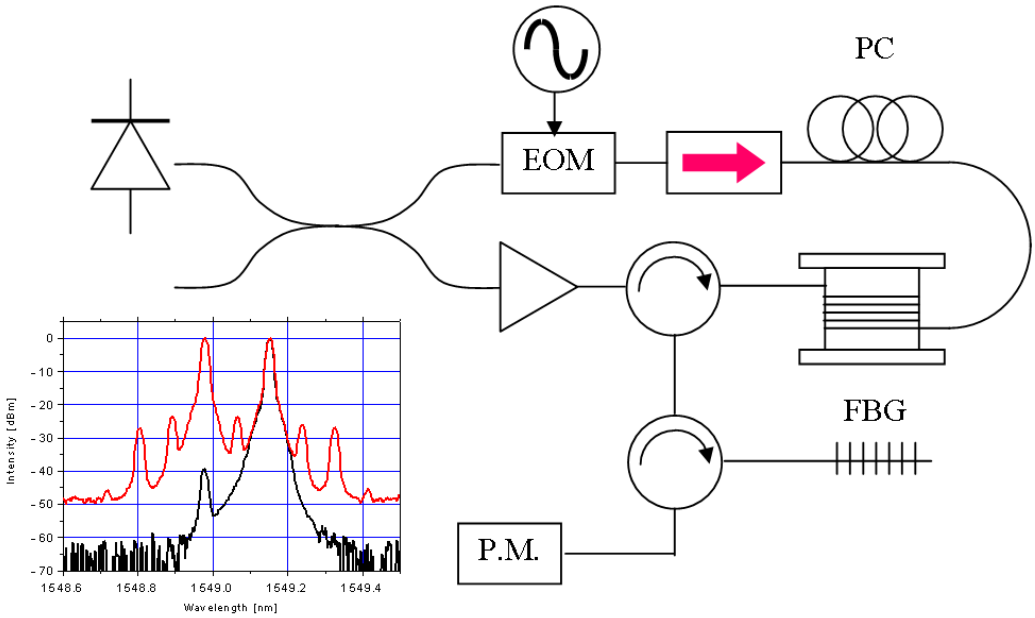

FIGURE A.1: Setup for the pump probe measurements (scheme and measurement results courtesy of Dr. K. Furusawa). EOM is the electro-optic modulator; FBG is the fibre Bragg grating used to filter the Brillouin backscattered signal and P.M. is the power meter.

Appendix B

Phase matching curves calculation

Third-order parametric processes such as Four Wave Mixing (FWM) involve, in general, nonlinear interaction amongst four optical waves. In quantum-mechanical terms, FWM occurs when photons from one or more waves are annihilated and new photons are created at different frequencies such that both the total energy and momentum are conserved during the parametric interaction. The most frequently observed form of FWM, which is also responsible for the phenomena observed in Section 5.3.2.4, corresponds to the case in which two photons at frequencies ω_1 and ω_2 are annihilated with the simultaneous creation of two photons at frequencies ω_3 and ω_4, such that:

$$\omega_3 + \omega_4 = \omega_1 + \omega_2. \tag{B.1}$$

The efficiency of the process is maximised if the following phase matching condition is satisfied:

$$\begin{aligned} \Delta k &= k_3 + k_4 - k_1 - k_2 \\ &= (n_3\omega_3 + n_4\omega_4 - n_1\omega_1 - n_2\omega_2)/c = 0. \end{aligned} \tag{B.2}$$

where n_i is the effective index for the i-th mode at the frequency ω_i and c is the speed of light.

The partially degenerate case, where $\omega_1 = \omega_2 = \omega_P$, is the most relevant for optical fibres. Physically it manifests itself as an energy transfer from a strong pump wave to two waves, upshifted (anti-Stokes) and downshifted (Stokes) from the pump frequency. If only the pump wave is incident at the fibre and the phase matching condition is satisfied, the Stokes and anti-Stokes waves can be generated from noise at frequencies ω_S and ω_A, respectively.

In order to calculate the phase matching curves for the process, the effective index curves for all the modes involved need to be calculated. All the processes analysed in Section 5.3.2.4 require the pump to be guided in one optical mode [with effective index $n_I(\omega)$] and both Stokes and anti-Stokes signals, for symmetry reasons, in the same, different mode [with effective index $n_{II}(\omega)$].

By studying the four coupled amplitude equations describing the FWM process and by making the approximation of an *undepleted pump*, the equations describing the energy conservation and the phase matching condition corresponding to the maximum parametric gain can be written as [6]:

$$2\omega_P = \omega_A + \omega_S \tag{B.3}$$

$$(2n_I(\omega_P)\cdot\omega_P - n_{II}(\omega_S)\cdot\omega_S - n_{II}(\omega_A)\cdot\omega_A)/c - 2\gamma P_0 = 0 \tag{B.4}$$

where $\gamma = n_2\omega/(cA_{eff})$ is the nonlinear parameter of the fibre, P_0 is the pump power and the last term in (B.4) describes the contribution of self and cross phase modulation to the total phase mismatch [6].

The overall phase matching curves can therefore be calculated using the following algorithm:

1. Calculate n_I and n_{II} with the FEM for the two modes of interest and for a discrete number of frequencies;
2. Interpolate the results to obtain $n_I(\omega)$ and $n_{II}(\omega)$ for any ω;
3. Fix ω_P;
4. Choose a value of ω_S and calculate the corresponding ω_A from (B.3);
5. Evaluate $n_I(\omega_P)$, $n_{II}(\omega_S)$, $n_{II}(\omega_A)$ and $\Delta K(\omega_P, \omega_S, \omega_A)$, defined as

$$\Delta K(\omega_P, \omega_S, \omega_A) = [2n_I(\omega_P)\cdot\omega_P - n_{II}(\omega_S)\cdot\omega_S - n_{II}(\omega_A)\cdot\omega_A]/c - 2\gamma P_0;$$

6. if $\Delta K \neq 0$, repeat points 4. and 5. with a different value of ω_S. Eventually, the values of ω_S and ω_A for which $\Delta K = 0$ represent the phase matched frequencies for a given ω_P. (Note that this procedure can be easily implemented, for example, using the `fzero` function in `Matlab`);
7. Change ω_P and repeat points 4. to 7. for all other frequencies of interest.

Bibliography

[1] P. Kaiser and H. W. Astle, "Low-loss single-material fibers made from pure fused silica," *The Bell Syst. Tech. J.*, vol. 53, no. 6, pp. 1021–1039, 1974.

[2] J. C. Knight, T. A. Birks, P. S. Russell, and D. M. Atkin, "All-silica single-mode optical fiber with photonic crystal cladding," *Optics Letters*, vol. 21, no. 19, pp. 1547–1549, 1996.

[3] R. F. Cregan, B. J. Mangan, J. C. Knight, T. A. Birks, P. S. Russell, P. J. Roberts, and D. C. Allan, "Single-mode photonic band gap guidance of light in air," *Science*, vol. 285, no. 5433, pp. 1537–1539, 1999.

[4] V. Finazzi, "A theoretical study into the fundamental design limits of devices based on one and two-dimensional structured fibres," Ph.D. dissertation, Optoelectronics Research Centre, University of Southampton, 2003.

[5] M. Feng, A. K. Mairaj, D. W. Hewak, and T. M. Monro, "Nonsilica glasses for holey fibers," *Journal Of Lightwave Technology*, vol. 23, no. 6, pp. 2046–2054, 2005.

[6] G. P. Agrawal, *Nonlinear fiber optics*, 3rd ed. Academic Press, 2001.

[7] See the Schott website at www.schott.com.

[8] P. R. McIsaac, "Symmetry-induced modal characteristics of uniform waveguides. I. Summary of results," *IEEE Transactions on Microwave Theory and Techniques*, vol. MTT-23, no. 5, pp. 421–429, 1975.

[9] T. P. White, B. T. Kuhlmey, R. C. McPhedran, D. Maystre, G. Renversez, C. M. de Sterke, and L. C. Botten, "Multipole method for microstructured optical fibers. I. Formulation," *Journal of the Optical Society of America B*, vol. 19, no. 10, pp. 2322–2330, 2002.

[10] T. Hasegawa, T. Nagashima, and N. Sugimoto, "Z-scan study of third-order optical nonlinearities in bismuth-based glasses," *Optics Communications*, vol. 250, no. 4-6, pp. 411–415, 2005.

[11] D. Beasley, D. R. Bull, and R. R. Martin, "An overview of genetic algorithms: Part 1, Fundamentals." *University Computing*, vol. 15, no. 2, pp. 58–74, 1993.

[12] M. N. Petrovich, A. Van Brakel, F. Poletti, K. Mukasa, E. Austin, V. Finazzi, P. Petropoulos, E. O'Driscoll, M. Watson, T. DelMonte, T. M. Monro, J. P. Dakin, and D. J. Richardson, "Microstructured fibres for sensing applications," in *Photonic Crystals and Photonic Crystal Fibers for Sensing Applications*, ser. Proc. SPIE, vol. 6005, 2005, p. 60050E.

[13] D. C. Allan, N. F. Borrelli, M. T. Gallagher, D. Muller, C. M. Smith, N. Venkataraman, J. A. West, P. Zhang, and K. W. Koch, "Surface modes and loss in air-core photonic band-gap fibers," in *Photonic Crystal Materials and Devices*, ser. Proc. SPIE, vol. 5000, 2003, pp. 161–174.

[14] R. Amezcua-Correa, N. G. R. Broderick, M. N. Petrovich, F. Poletti, and D. J. Richardson, "Optimizing the usable bandwidth and loss through core design in realistic hollow-core photonic bandgap fibers," *Optics Express*, vol. 14, no. 17, pp. 7974–7985, 2006.

[15] J. Hecht, *City of light: the story of fiber optics.* Oxford University Press, 1999.

[16] K. C. Kao and G. A. Hocham, "Dielectric fiber surface waveguides for optical frequencies," in *Proceedings IEE*, vol. 113, July 1966, pp. 1151–1158.

[17] F. P. Kapron, D. B. Keck, and R. D. Maurer, "Radiation losses in glass optical waveguides," *Applied Physics Letters*, vol. 17, no. 10, pp. 423–425, 1970.

[18] T. Miya, Y. Terunuma, T. Hosaka, and T. Miyashita, "Ultimate low-loss single-mode fiber at 1.55 micron," *Electronics Letters*, vol. 15, no. 4, pp. 106–108, 1979.

[19] T. A. Birks, P. J. Roberts, P. S. J. Russell, D. M. Atkin, and T. J. Shepherd, "Full 2-D photonic bandgaps in silica/air structures," *Electronics Letters*, vol. 31, no. 22, pp. 1941–1943, 1995.

[20] E. Yablonovitch, "Inhibited spontaneous emission in solid-state physics and electronics," *Physical Review Letters*, vol. 58, no. 20, pp. 2059–2062, 1987.

[21] S. John, "Strong localization of photons in certain disordered dielectric superlattices," *Physical Review Letters*, vol. 58, no. 23, pp. 2486–2489, 1987.

[22] J. C. Knight, J. Broeng, T. A. Birks, and P. S. J. Russell, "Photonic band gap guidance in optical fibers," *Science*, vol. 282, no. 5393, pp. 1476–8, 1998.

[23] S. E. Barkou, J. Broeng, and A. Bjarklev, "Silica-air photonic crystal fiber design that permits waveguiding by a true photonic bandgap effect," *Optics Letters*, vol. 24, no. 1, pp. 46–48, 1999.

[24] K. Tajima, J. Zhou, K. Kurokawa, and K. Nakajima, "Low water peak photonic crystal fibers," in *Proc. European Conference on Optical Communications (ECOC)*, 2003, paper Th 4.1.6.

[25] P. J. Roberts, F. Couny, H. Sabert, B. J. Mangan, D. P. Williams, L. Farr, M. W. Mason, A. Tomlinson, T. A. Birks, J. C. Knight, and P. S. J. Russell, "Ultimate low loss of hollow-core photonic crystal fibres," *Optics Express*, vol. 13, no. 1, pp. 236–244, 2005.

[26] T. M. Monro, Y. D. West, D. W. Hewak, N. G. R. Broderick, and D. J. Richardson, "Chalcogenide holey fibres," *Electronics Letters*, vol. 36, no. 24, pp. 1998–2000, 2000.

[27] K. M. Kiang, K. Frampton, T. M. Monro, R. Moore, J. Tucknott, D. W. Hewak, D. J. Richardson, and H. N. Rutt, "Extruded singlemode non-silica glass holey optical fibres," *Electronics Letters*, vol. 38, no. 12, pp. 546–547, 2002.

[28] V. V. R. K. Kumar, A. K. George, J. C. Knight, and P. S. Russell, "Tellurite photonic crystal fiber," *Optics Express*, vol. 11, no. 20, pp. 2641–2645, 2003.

[29] H. Ebendorff-Heidepriem, P. Petropoulos, S. Asimakis, V. Finazzi, R. C. Moore, K. Frampton, F. Koizumi, D. J. Richardson, and T. M. Monro, "Bismuth glass holey fibers with high nonlinearity," *Optics Express*, vol. 12, no. 21, pp. 5082–5087, 2004.

[30] M. A. van Eijkelenborg, M. C. J. Large, A. Argyros, J. Zagari, S. Manos, N. Issa, I. Bassett, S. Fleming, R. C. McPhedran, C. M. de Sterke, and N. A. P. Nicorovici, "Microstructured polymer optical fibre," *Optics Express*, vol. 9, no. 7, pp. 319–327, 2001.

[31] G. Barton, M. A. van Eijkelenborg, G. Henry, M. C. J. Large, and J. Zagari, "Fabrication of microstructured polymer optical fibres," *Optical Fiber Technology*, vol. 10, no. 4, pp. 325–335, 2004.

[32] A. Argyros, M. A. van Eijkelenborg, M. C. J. Large, and I. M. Bassett, "Hollow-core microstructured polymer optical fiber," *Optics Letters*, vol. 31, no. 2, pp. 172–174, 2006.

[33] X. Feng, T. M. Monro, P. Petropoulos, V. Finazzi, and D. Hewak, "Solid microstructured optical fiber," *Optics Express*, vol. 11, no. 18, pp. 2225–2230, 2003.

[34] F. Luan, A. K. George, T. D. Hedley, G. J. Pearce, D. M. Bird, J. C. Knight, and P. S. J. Russell, "All-solid photonic bandgap fiber," *Optics Letters*, vol. 29, no. 20, pp. 2369–2371, 2004.

[35] T. A. Birks, D. M. Bird, T. D. Hedley, J. M. Pottage, and P. S. J. Russell, "Scaling laws and vector effects in bandgap-guiding fibres," *Optics Express*, vol. 12, no. 1, pp. 69–74, 2004.

[36] A. Argyros, T. A. Birks, S. G. Leon-Saval, C. M. B. Cordeiro, F. Luan, and P. S. J. Russell, "Photonic bandgap with an index step of one percent," *Optics Express*, vol. 13, no. 1, pp. 309–314, 2005.

[37] G. Bouwmans, L. Bigot, Y. Quiquempois, F. Lopez, L. Provino, and M. Douay, "Fabrication and characterization of an all-solid 2D photonic bandgap fiber with a low-loss region (¡ 20 db/km) around 1550 nm," *Optics Express*, vol. 13, no. 21, pp. 8452–8459, 2005.

[38] P. Yeh, A. Yariv, and C. S. Hong, "Electromagnetic propagation in periodic stratified media.1. general theory," *Journal of the Optical Society of America*, vol. 67, no. 4, pp. 423–438, 1977.

[39] P. Yeh, A. Yariv, and E. Marom, "Theory of bragg fiber," *Journal of the Optical Society of America*, vol. 68, no. 9, pp. 1196–1201, 1978.

[40] Y. Fink, J. N. Winn, S. H. Fan, C. P. Chen, J. Michel, J. D. Joannopoulos, and E. L. Thomas, "A dielectric omnidirectional reflector," *Science*, vol. 282, no. 5394, pp. 1679–1682, 1998.

[41] B. Temelkuran, S. D. Hart, G. Benoit, J. D. Joannopoulos, and Y. Fink, "Wavelength-scalable hollow optical fibres with large photonic bandgaps for co2 laser transmission," *Nature*, vol. 420, no. 6916, pp. 650–653, 2002.

[42] G. Vienne, Y. Xu, C. Jakobsen, H. J. Deyerl, J. B. Jensen, T. Sorensen, T. P. Hansen, Y. Y. Huang, M. Terrel, R. K. Lee, N. A. Mortensen, J. Broeng, H. Simonsen, A. Bjarklev, and A. Yariv, "Ultra-large bandwidth hollow-core guiding in all-silica bragg fibers with nano-supports," *Optics Express*, vol. 12, no. 15, pp. 3500–3508, 2004.

[43] T. M. Monro, P. J. Bennett, N. G. R. Broderick, and D. J. Richardson, "Holey fibers with random cladding distributions," *Optics Express*, vol. 25, no. 4, pp. 206–208, 2000.

[44] A. W. Snyder and J. D. Love, *Optical waveguide theory*, 2nd ed. Kluwer academic publisher, 2000.

[45] J. C. Flanagan, R. Amezcua Correa, F. Poletti, J. R. Hayes, N. G. Broderick, and D. J. Richardson, "Parasitic modes in large mode area microstructured fibers," in *Proc. Optical Fiber Communication Conference (OFC)*, 2007, paper OML4.

[46] B. J. Mangan, J. Arriaga, T. A. Birks, J. C. Knight, and P. S. Russell, "Fundamental-mode cutoff in a photonic crystal fiber with a depressed-index core," *Optics Letters*, vol. 26, no. 19, pp. 1469–1471, 2001.

[47] R. W. Boyd, *Nonlinear optics*, 2nd ed. Academic Press, 2003.

[48] C. C. Wang, "Empirical relation between linear third-order nonlinear optical susceptibilities," *Physical Review B*, vol. 2, no. 6, pp. 2045–2048, 1970.

[49] X. Feng, T. M. Monro, V. Finazzi, R. C. Moore, K. Frampton, P. Petropoulos, and D. J. Richardson, "Extruded singlemode, high-nonlinearity, tellurite glass holey fibre," *Electronics Letters*, vol. 41, no. 15, pp. 835–837, 2005.

[50] J. Y. Y. Leong, P. Petropoulos, J. H. V. Price, H. Ebendorff-Heidepriem, S. Asimakis, R. C. Moore, K. E. Frampton, V. Finazzi, X. Feng, T. M. Monro, and D. J. Richardson, "High-nonlinearity dispersion-shifted lead-silicate holey fibers for efficient 1-μm pumped supercontinuum generation," *Journal of Lightwave Technology*, vol. 24, no. 1, pp. 183–190, 2006.

[51] X. Feng, A. K. Mairaj, D. W. Hewak, and T. M. Monro, "Towards high-index glass based monomode holey fibre with large mode area," *Electronics Letters*, vol. 40, no. 3, pp. 167–169, 2004.

[52] P. Falkenstein, C. D. Merritt, and B. L. Justus, "Fused preforms for the fabrication of photonic crystal fibers," *Optics Letters*, vol. 29, no. 16, pp. 1858–1860, 2004.

[53] G. Y. Zhou, Z. Y. Hou, S. G. Li, and L. T. Hou, "Fabrication of glass photonic crystal fibers with a die-cast process," *Applied Optics*, vol. 45, no. 18, pp. 4433–4436, 2006.

[54] P. Russell, "Photonic crystal fibers," *Science*, vol. 299, no. 5605, pp. 358–362, 2003.

[55] T. P. Hansen, J. Broeng, S. E. B. Libori, E. Knudsen, A. Bjarklev, J. R. Jensen, and H. Simonsen, "Highly birefringent index-guiding photonic crystal fibers," *IEEE Photonics Technology Letters*, vol. 13, no. 6, pp. 588–590, 2001.

[56] N. A. Mortensen, M. D. Nielsen, J. R. Folkenberg, A. Petersson, and H. R. Simonsen, "Improved large-mode-area endlessly single-mode photonic crystal fibers," *Optics Letters*, vol. 28, no. 6, pp. 393–395, 2003.

[57] J. Limpert, O. Schmidt, J. Rothhardt, F. Roser, T. Schreiber, A. Tunnermann, S. Ermeneux, P. Yvernault, and F. Salin, "Extended single-mode photonic crystal fiber lasers," *Optics Express*, vol. 14, no. 7, pp. 2715–2720, 2006.

[58] T. A. Birks, J. C. Knight, and P. S. J. Russell, "Endlessly single-mode photonic crystal fiber," *Optics Letters*, vol. 22, no. 13, pp. 961–963, 1997.

[59] F. Brechet, J. Marcou, D. Pagnoux, and P. Roy, "Complete analysis of the characteristics of propagation into photonic crystal fibers by the finite element method," *Optical Fiber Technology: Materials, Devices and Systems*, vol. 6, no. 2, pp. 181–91, 2000.

[60] M. Koshiba, "Full-vector analysis of photonic crystal fibers using the finite element method," *IEICE Transactions on Electronics*, vol. E85C, no. 4, pp. 881–888, 2002.

[61] N. A. Mortensen, J. R. Folkenberg, M. D. Nielsen, and K. P. Hansen, "Modal cutoff and the V parameter in photonic crystal fibers," *Optics Letters*, vol. 28, no. 20, pp. 1879–81, 2003.

[62] B. T. Kuhlmey, R. C. McPhedran, and C. Martijn de Sterke, "Modal cutoff in microstructured optical fibers," *Optics Letters*, vol. 27, no. 19, pp. 1684–1686, 2002.

[63] J. R. Folkenberg, N. A. Mortensen, K. P. Hansen, T. P. Hansen, H. R. Simonsen, and C. Jakobsen, "Experimental investigation of cutoff phenomena in nonlinear photonic crystal fibers," *Optics Letters*, vol. 28, no. 20, pp. 1882–1884, 2003.

[64] J. C. Knight, J. Arriaga, T. A. Birks, A. Ortigosa-Blanch, W. J. Wadsworth, and P. S. Russell, "Anomalous dispersion in photonic crystal fiber," *IEEE Photonics Technology Letters*, vol. 12, no. 7, pp. 807–809, 2000.

[65] J. K. Ranka, R. S. Windeler, and A. J. Stentz, "Visible continuum generation in air-silica microstructure optical fibers with anomalous dispersion at 800 nm," *Optics Letters*, vol. 25, no. 1, pp. 25–27, 2000.

[66] W. J. Wadsworth, J. C. Knight, A. Ortigosa-Blanch, J. Arriaga, E. Silvestre, and P. S. J. Russell, "Soliton effects in photonic crystal fibres at 850 nm," *Electronics Letters*, vol. 36, no. 1, pp. 53–55, 2000.

[67] J. H. V. Price, W. Belardi, T. M. Monro, A. Malinowski, A. Piper, and D. J. Richardson, "Soliton transmission and supercontinuum generation in holey fiber, using a diode pumped ytterbium fiber source," *Optics Express*, vol. 10, no. 8, pp. 382–387, 2002.

[68] T. A. Birks, D. Mogilevtsev, J. C. Knight, and P. St. J. Russell, "Dispersion compensation using single-material fibers," *IEEE Photonics Technology Letters*, vol. 11, no. 6, pp. 674–676, 1999.

[69] F. Poli, A. Cucinotta, M. Fuochi, S. Selleri, and L. Vincetti, "Characterization of microstructured optical fibers for wideband dispersion compensation," *Journal of the Optical Society of America A*, vol. 20, no. 10, pp. 1958–1962, 2003.

[70] A. Ferrando, E. Silvestre, P. Andres, J. J. Miret, and M. V. Andres, "Designing the properties of dispersion-flattened photonic crystal fibers," *Optics Express*, vol. 9, no. 13, pp. 687–697, 2001.

[71] W. H. Reeves, J. C. Knight, P. S. J. Russell, and P. J. Roberts, "Demonstration of ultra-flattened dispersion in photonic crystal fibers," *Optics Express*, vol. 10, no. 14, pp. 609–613, 2002.

[72] K. P. Hansen, "Dispersion flattened hybrid-core nonlinear photonic crystal fiber," *Optics Express*, vol. 11, no. 13, pp. 1503–1509, 2003.

[73] K. M. Hilligsoe, T. V. Andersen, H. N. Paulsen, C. K. Nielsen, K. Molmer, S. Keiding, R. Kristiansen, K. P. Hansen, and J. J. Larsen, "Supercontinuum generation in a photonic crystal fiber with two zero dispersion wavelengths," *Optics Express*, vol. 12, no. 6, pp. 1045–1054, 2004.

[74] G. B. Ren, Z. Wang, S. Q. Lou, and S. S. Jian, "Mode classification and degeneracy in photonic crystal fibers," *Optics Express*, vol. 11, no. 11, pp. 1310–1321, 2003.

[75] A. Ferrando, E. Silvestre, J. J. Miret, P. Andres, and M. V. Andres, "Vector description of higher-order modes in photonic crystal fibers," *Journal of the Optical Society of America A*, vol. 17, no. 7, pp. 1333–1340, 2000.

[76] M. T. Steel, T. P. White, C. M. De Sterke, R. C. McPhedran, and L. C. Botten, "Symmetry and degeneracy in microstructured optical fibers," *Optics Letters*, vol. 26, no. 8, pp. 488–90, 2001.

[77] P. R. McIsaac, "Symmetry-induced modal characteristics of uniform waveguides. II. Theory," *IEEE Transactions on Microwave Theory and Techniques*, vol. MTT-23, no. 5, pp. 429–433, 1975.

[78] A. Ortigosa-Blanch, J. C. Knight, W. J. Wadsworth, J. Arriaga, B. J. Mangan, T. A. Birks, and P. S. J. Russell, "Highly birefringent photonic crystal fibers," *Optics Letters*, vol. 25, no. 18, pp. 1325–1327, 2000.

[79] K. Saitoh and M. Koshiba, "Single-polarization single-mode photonic crystal fibers," *IEEE Photonics Technology Letters*, vol. 15, no. 10, pp. 1384–1386, 2003.

[80] T. Okuno, M. Onishi, T. Kashiwada, S. Ishikawa, and M. Nishimura, "Silica-based functional fibers with enhanced nonlinearity and their applications," *IEEE Journal of Selected Topics in Quantum Electronics*, vol. 5, no. 5, pp. 1385–1391, 1999.

[81] N. G. R. Broderick, H. L. Offerhaus, D. J. Richardson, R. A. Sammut, J. Caplen, and L. Dong, "Large mode area fibers for high power applications," *Optical Fiber Technology*, vol. 5, no. 2, pp. 185–196, 1999.

[82] V. Finazzi, T. Monro, and D. Richardson, "Small-core silica holey fibers: nonlinearity and confinement loss trade-offs," *Journal of the Optical Society of America B*, vol. 20, no. 7, pp. 1427–36, 2003.

[83] J. Laegsgaard, N. A. Mortensen, and A. Bjarklev, "Mode areas and field-energy distribution in honeycomb photonic bandgap fibers," *Journal of the Optical Society of America B*, vol. 20, no. 10, pp. 2037–2045, 2003.

[84] R. Hainberger and S. Watanabe, "Impact of the wavelength dependence of the mode field on the nonlinearity coefficient of PCFs," *IEEE Photonics Technology Letters*, vol. 17, no. 1, pp. 70–72, 2005.

[85] M. D. Nielsen, J. R. Folkenberg, N. A. Mortensen, and A. Bjarklev, "Bandwidth comparison of photonic crystal fibers and conventional single-mode fibers," *Optics Express*, vol. 12, no. 3, pp. 430–435, 2004.

[86] J. C. Baggett, T. M. Monro, and D. J. Richardson, "Mode area limits in practical single-mode fibers," in *Proc. Conference on Lasers and Electro-Optics (CLEO)*, vol. 1, 2005, pp. 62–64.

[87] M. D. Nielsen, J. R. Folkenberg, and N. A. Mortensen, "Singlemode photonic crystal fibre with effective area of 600 μm^2 and low bending loss," *Electronics Letters*, vol. 39, no. 25, pp. 1802–1803, 2003.

[88] W. S. Wong, X. Peng, J. M. McLaughlin, and L. Dong, "Breaking the limit of maximum effective area for robust single-mode propagation in optical fibers," *Optics Letters*, vol. 30, no. 21, pp. 2855–2857, 2005.

[89] J. M. Fini, "Bend-resistant design of conventional and microstructure fibers with very large mode area," *Optics Express*, vol. 14, no. 1, pp. 69–81, 2006.

[90] T. P. White, R. C. McPhedran, C. M. de Sterke, L. C. Botten, and M. J. Steel, "Confinement losses in microstructured optical fibers," *Optics Letters*, vol. 26, no. 21, pp. 1660–1662, 2001.

[91] J. D. Joannopoulos, R. D. Meade, and J. N. Winn, *Photonic crystals: molding the flow of light*. Princeton University Press, 1995.

[92] J. D. Shephard, J. D. C. Jones, D. P. Hand, G. Bouwmans, J. C. Knight, P. S. Russell, and B. J. Mangan, "High energy nanosecond laser pulses delivered single-mode through hollow-core PBG fibers," *Optics Express*, vol. 12, no. 4, pp. 717–723, 2004.

[93] D. G. Ouzounov, F. R. Ahmad, D. Muller, N. Venkataraman, M. T. Gallagher, M. G. Thomas, J. Silcox, K. W. Koch, and A. L. Gaeta, "Generation of megawatt optical solitons in hollow-core photonic band-gap fibers," *Science*, vol. 301, no. 5640, pp. 1702–1704, 2003.

[94] F. Luan, J. C. Knight, P. S. J. Russell, S. Campbell, D. Xiao, D. T. Reid, B. J. Mangan, D. P. Williams, and P. J. Roberts, "Femtosecond soliton pulse delivery at 800 nm wavelength in hollow-core photonic bandgap fibers," *Optics Express*, vol. 12, no. 5, pp. 835–840, 2004.

[95] D. G. Ouzounov, C. J. Hensley, A. L. Gaeta, N. Venkateraman, M. T. Gallagher, and K. W. Koch, "Soliton pulse compression in photonic band-gap fibers," *Optics Express*, vol. 13, no. 16, pp. 6153–6159, 2005.

[96] J. Limpert, T. Schreiber, S. Nolte, H. Zellmer, and A. Tunnermann, "All fiber chirped-pulse amplification system based on compression in air-guiding photonic bandgap fiber," *Optics Express*, vol. 11, no. 24, pp. 3332–3337, 2003.

[97] C. J. S. De Matos, J. R. Taylor, T. P. Hansen, K. P. Hansen, and J. Broeng, "All-fiber chirped pulse amplification using highly-dispersive air-core photonic bandgap fiber," *Optics Express*, vol. 11, no. 22, pp. 2832–2837, 2003.

[98] C. J. S. De Matos and J. R. Taylor, "Chirped pulse raman amplification with compression in air-core photonic bandgap fiber," *Optics Express*, vol. 13, no. 8, pp. 2828–2834, 2005.

[99] C. J. S. De Matos, R. E. Kennedy, S. V. Popov, and J. R. Taylor, "20-kw peak power all-fiber 1.57-μm source based on compression in air-core photonic bandgap fiber, its frequency doubling, and broadband generation from 430 to 1450 nm," *Optics Letters*, vol. 30, no. 4, pp. 436–438, 2005.

[100] F. Benabid, J. C. Knight, G. Antonopoulos, and P. S. J. Russell, "Stimulated Raman scattering in hydrogen-filled hollow-core photonic crystal fiber," *Science*, vol. 298, no. 5592, pp. 399–402, 2002.

[101] F. Benabid, J. C. Knight, and P. S. Russell, "Particle levitation and guidance in hollow-core photonic crystal fiber," *Optics Express*, vol. 10, no. 21, pp. 1195–1203, 2002.

[102] F. Benabid, F. Couny, J. C. Knight, T. A. Birks, and P. S. J. Russell, "Compact, stable and efficient all-fibre gas cells using hollow-core photonic crystal fibres," vol. 434, no. 7032, pp. 488–491, 2005.

[103] J. Tuominen, T. Ritari, H. Ludvigsen, and J. C. Petersen, "Gas filled photonic bandgap fibers as wavelength references," *Optics Communications*, vol. 255, no. 4-6, pp. 272–277, 2005.

[104] T. Ritari, J. Tuominen, H. Ludvigsen, J. C. Petersen, T. Sorensen, T. P. Hansen, and H. R. Simonsen, "Gas sensing using air-guiding photonic bandgap fibers," *Optics Express*, vol. 12, no. 17, pp. 4080–4087, 2004.

[105] A. A. Maradudin and A. R. McGurn, "Out-of-plane propagation of electromagnetic-waves in a 2-dimensional periodic dielectric medium," *Journal of Modern Optics*, vol. 41, no. 2, pp. 275–284, 1994.

[106] M. Plihal and A. A. Maradudin, "Photonic band structure of two-dimensional systems: The triangular lattice," *Physical Review B*, vol. 44, no. 16, pp. 8565–8571, 1991.

[107] R. D. Meade, K. D. Brommer, A. M. Rappe, and J. D. Joannopoulos, "Existence of a photonic band-gap in 2 dimensions," *Applied Physics Letters*, vol. 61, no. 4, pp. 495–497, 1992.

[108] P. R. Villeneuve and M. Piche, "Photonic band-gaps in 2-dimensional square and hexagonal lattices," *Physical Review B*, vol. 46, no. 8, pp. 4969–4972, 1992.

[109] J. Broeng, S. E. Barkou, T. Sondergaard, and A. Bjarklev, "Analysis of air-guiding photonic bandgap fibers," *Optics Letters*, vol. 25, no. 2, pp. 96–98, 2000.

[110] N. Mortensen and M. Nielsen, "Modeling of realistic cladding structures for air-core photonic bandgap fibers," *Optics Letters*, vol. 29, no. 4, pp. 349–351, 2004.

[111] A. W. Snyder and C. Pask, "Incoherent illumination of an optical fiber," *Journal of the Optical Society of America*, vol. 63, no. 7, pp. 806–812, 1973.

[112] K. Saitoh and M. Koshiba, "Leakage loss and group velocity dispersion in air-core photonic bandgap fibers," *Optics Express*, vol. 11, no. 23, pp. 3100–3109, 2003.

[113] P. J. Roberts, F. Couny, H. Sabert, B. J. Mangan, T. A. Birks, J. C. Knight, and P. S. J. Russell, "Loss in solid-core photonic crystal fibers due to interface roughness scattering," *Optics Express*, vol. 13, no. 20, pp. 7779–7793, 2005.

[114] P. J. Roberts, D. P. Williams, B. J. Mangan, H. Sabert, F. Couny, W. J. Wadsworth, T. A. Birks, J. C. Knight, and P. S. J. Russell, "Realizing low loss air core photonic crystal fibers by exploiting an antiresonant core surround," *Optics Express*, vol. 13, no. 20, pp. 8277–8285, 2005.

[115] J. C. Baggett, M. N. Petrovich, J. R. Hayes, V. Finazzi, F. Poletti, R. Amezcua, N. G. R. Broderick, D. J. Richardson, T. M. Monro, P. L. Salter, G. Proudley, and E. J. O'Driscoll, "Microstructured fibers for high power applications," in *Nanophotonics for Communication: Materials and Devices II*, ser. Proc. SPIE, vol. 6017, 2005, p. 601709.

[116] J. A. West, C. M. Smith, N. F. Borrelli, D. C. Allan, and K. W. Koch, "Surface modes in air-core photonic band-gap fibers," *Optics Express*, vol. 12, no. 8, pp. 1485–1496, 2004.

[117] B. J. Mangan, L. Farr, A. Langford, P. J. Roberts, D. P. Williams, F. Couny, M. Lawman, M. Mason, S. Coupland, R. Flea, H. Sabert, T. A. Birks, J. C. Knight, and P. S. J. Russell, "Low loss (1.7 dB/km) hollow core photonic bandgap fiber," in *Proc. Optical Fiber Communucation Conference (OFC)*, 2004, paper PDP24.

[118] P. J. Roberts, F. Couny, T. A. Birks, J. C. Knight, P. S. J. Russell, B. J. Mangan, H. Sabert, D. P. Williams, and L. Farr, "Achieving low loss and low nonlinearity in hollow core photonic crystal fibers," in *Proc. Conference on Lasers and Electro-Optics (CLEO)*, vol. 2, 2005, pp. 1240–1242.

[119] M. J. F. Digonnet, H. K. Kim, J. Shin, S. Fan, and G. Kino, "Simple geometric criterion to predict the existence of surface modes in air-core photonic-bandgap fibers," *Optics Express*, vol. 12, no. 9, pp. 1864–1872, 2004.

[120] H. K. Kim, J. Shin, S. Fan, M. J. F. Digonnet, and G. S. Kino, "Designing air-core photonic-bandgap fibers free of surface modes," *IEEE Journal of Quantum Electronics*, vol. 40, no. 5, pp. 551–556, 2004.

[121] H. K. Kim, M. J. F. Digonnet, G. S. Kino, J. Shin, and S. Fan, "Simulations of the effect of the core ring on surface and air-core modes in photonic bandgap fibers," *Optics Express*, vol. 12, no. 15, pp. 3436–3442, 2004.

[122] M. D. Nielsen, N. A. Mortensen, J. R. Folkenberg, and A. Bjarklev, "Mode-field radius of photonic crystal fibers expressed by the V parameter," *Optics Letters*, vol. 28, no. 23, pp. 2309–2311, 2003.

[123] M. D. Nielsen, N. A. Mortensen, M. Albertsen, J. R. Folkenberg, A. Bjarklev, and D. Bonacinni, "Predicting macrobending loss for large-mode area photonic crystal fibers," *Optics Express*, vol. 12, no. 8, pp. 1775–1779, 2004.

[124] M. Koshiba and K. Saitoh, "Applicability of classical optical fiber theories to holey fibers," *Optics Letters*, vol. 29, no. 15, pp. 1739–1741, 2004.

[125] K. Saitoh and M. Koshiba, "Empirical relations for simple design of photonic crystal fibers," *Optics Express*, vol. 13, no. 1, pp. 267–274, 2005.

[126] T. M. Monro, D. J. Richardson, N. G. R. Broderick, and P. J. Bennett, "Holey optical fibers: an efficient modal model," *Journal of Lightwave Technology*, vol. 17, no. 6, pp. 1093–1102, 1999.

[127] E. Silvestre, M. V. Andres, and P. Andres, "Biorthonormal-basis method for the vector description of optical-fiber modes," *Journal of Lightwave Technology*, vol. 16, no. 5, pp. 923–928, 1998.

[128] A. Ferrando, E. Silvestre, J. J. Miret, P. Andres, and M. V. Andres, "Full-vector analysis of a realistic photonic crystal fiber," *Optics Letters*, vol. 24, no. 5, pp. 276–278, 1999.

[129] S. G. Johnson and J. D. Joannopoulos, "Block-iterative frequency-domain methods for Maxwell's equations in a planewave basis," *Optics Express*, vol. 8, no. 3, pp. 173–190, 2001.

[130] G. J. Pearce, T. D. Hedley, and D. M. Bird, "Adaptive curvilinear coordinates in a plane-wave solution of maxwell's equations in photonic crystals," *Physical Review B*, vol. 71, no. 19, p. 195108, 2005.

[131] R. Kotynski, M. Antkowiak, F. Berghmans, H. Thienpont, and K. Panajotov, "Photonic crystal fibers with material anisotropy," *Optical and Quantum Electronics*, vol. 37, no. 1-3, pp. 253–264, 2005.

[132] D. Mogilevtsev, T. A. Birks, and P. S. J. Russell, "Group-velocity dispersion in photonic crystal fibers," *Optics Letters*, vol. 23, no. 21, pp. 1662–1664, 1998.

[133] ——, "Localized function method for modeling defect modes in 2-D photonic crystals," *Journal of Lightwave Technology*, vol. 17, no. 11, pp. 2078–2081, 1999.

[134] T. M. Monro, D. J. Richardson, N. G. R. Broderick, and P. J. Bennett, "Modeling large air fraction holey optical fibers," *Journal of Lightwave Technology*, vol. 18, no. 1, pp. 50–56, 2000.

[135] L. Poladian, N. A. Issa, and T. M. Monro, "Fourier decomposition algorithm for leaky modes of fibres with arbitrary geometry," *Optics Express*, vol. 10, no. 10, pp. 449–454, 2002.

[136] N. A. Issa and L. Poladian, "Vector wave expansion method for leaky modes of microstructured optical fibers," *Journal of Lightwave Technology*, vol. 21, no. 4, pp. 1005–1012, 2003.

[137] M. D. Feit and J. A. Fleck, "Computation of mode eigenfunctions in graded-index optical fibers by the propagating beam method," *Applied Optics*, vol. 19, no. 13, pp. 2240–2246, 1980.

[138] K. Saitoh and M. Koshiba, "Full-vectorial imaginary-distance beam propagation method based on a finite element scheme: Application to photonic crystal fibers," *IEEE Journal of Quantum Electronics*, vol. 38, no. 7, pp. 927–933, 2002.

[139] R. Scarmozzino, A. Gopinath, R. Pregla, and S. Helfert, "Numerical techniques for modeling guided-wave photonic devices," *IEEE Journal of Selected Topics in Quantum Electronics*, vol. 6, no. 1, pp. 150–162, 2000.

[140] B. T. Kuhlmey, T. P. White, G. Renversez, D. Maystre, L. C. Botten, C. M. de Sterke, and R. C. McPhedran, "Multipole method for microstructured optical fibers. II. Implementation and results," *Journal of the Optical Society of America B*, vol. 19, no. 10, pp. 2331–2340, 2002.

[141] T. P. White, R. C. McPhedran, L. C. Botten, G. H. Smith, and C. M. de Sterke, "Calculations of air-guided modes in photonic crystal fibers using the multipole method," *Optics Express*, vol. 9, no. 13, pp. 721–732, 2001.

[142] A. Hochman and Y. Leviatan, "Analysis of strictly bound modes in photonic crystal fibers by use of a source-model technique," *Journal of the Optical Society of America A*, vol. 21, no. 6, pp. 1073–1081, 2004.

[143] ——, "Calculation of confinement losses in photonic crystal fibers by use of a source-model technique," *Journal of the Optical Society of America B*, vol. 22, no. 2, pp. 474–480, 2005.

[144] M. Koshiba and K. Saitoh, "Numerical verification of degeneracy in hexagonal photonic crystal fibers," *IEEE Photonics Technology Letters*, vol. 13, no. 12, pp. 1313–1315, 2001.

[145] A. Cucinotta, S. Selleri, L. Vincetti, and M. Zoboli, "Perturbation analysis of dispersion properties in photonic crystal fibers through the finite element method," *Journal of Lightwave Technology*, vol. 20, no. 8, pp. 1433–1442, 2002.

[146] J. K. Ranka, R. S. Windeler, and A. J. Stentz, "Optical properties of high-delta air-silica microstructure optical fibers," *Optics Letters*, vol. 25, no. 11, pp. 796–798, 2000.

[147] M. Szpulak, W. Urbanczyk, E. Serebryannikov, A. Zheltikov, A. Hochman, Y. Leviatan, R. Kotynski, and K. Panajotov, "Comparison of different methods for rigorous modeling of photonic crystal fibers," *Optics Express*, vol. 14, no. 12, pp. 5699–5714, 2006.

[148] J. Jin, *The finite element method in electromagnetics*, 2nd ed. New York: John Wiley & Sons, 2002.

[149] M. Koshiba and Y. Tsuji, "Curvilinear hybrid edge/nodal elements with triangular shape for guided-wave problems," *Journal of Lightwave Technology*, vol. 18, no. 5, pp. 737–743, 2000.

[150] J. P. Berenger, "A perfectly matched layer for the absorption of electromagnetic waves," *Journal of Computational Physics*, vol. 114, no. 2, pp. 185–200, 1994.

[151] Z. Sacks, D. Kingsland, R. Lee, and J.-F. Lee, "A perfectly matched anisotropic absorber for use as an absorbing boundary condition," *IEEE Transactions on Antennas and Propagation*, vol. 43, no. 12, pp. 1460–1463, 1995.

[152] K. Saitoh and M. Koshiba, "Full-vectorial finite element beam propagation method with perfectly matched layers for anisotropic optical waveguides," *Journal of Lightwave Technology*, vol. 19, no. 3, pp. 405–413, 2001.

[153] F. L. Teixeira and W. C. Chew, "Systematic derivation of anisotropic PML absorbing media in cylindrical and spherical coordinates," *IEEE Microwave and Guided Wave Letters*, vol. 7, no. 11, pp. 371–373, 1997.

[154] M. Kuzuoglu and R. Mittra, "Investigation of nonplanar perfectly matched absorbers for finite-element mesh truncation," *IEEE Transactions on Antennas and Propagation*, vol. 45, no. 3, pp. 474–486, 1997.

[155] J. C. Baggett, "Bending losses in large mode area holey fibres," Ph.D. dissertation, Optoelectronics Research Centre, University of Southampton, 2004.

[156] P. J. Bennett, T. M. Monro, and D. J. Richardson, "Toward practical holey fiber technology: fabrication, splicing, modeling, and characterization," *Optics Letters*, vol. 24, no. 17, pp. 1203–1205, 1999.

[157] T. Izawa, "Early days of VAD process," *IEEE Journal of Selected Topics in Quantum Electronics*, vol. 6, no. 6, pp. 1220–1227, 2000.

[158] P. J. Roberts, F. Couny, H. Sabert, B. J. Mangan, T. A. Birks, J. C. Knight, and P. S. J. Russell, "Loss in solid-core photonic crystal fibers due to interface roughness scattering," *Optics Express*, vol. 13, no. 20, pp. 7779–7793, 2005.

[159] K. Kurokawa, K. Tajima, K. Tsujikawa, K. Nakajima, T. Matsui, I. Sankawa, and T. Haibara, "Penalty-free dispersion-managed soliton transmission over a 100-km low-loss PCF," *Journal of Lightwave Technology*, vol. 24, no. 1, pp. 32–37, 2006.

[160] K. Nakajima, J. Zhou, K. Tajima, K. Kurokawa, C. Fukai, and I. Sankawa, "Ultrawide-band single-mode transmission performance in a low-loss photonic crystal fiber," *Journal of Lightwave Technology*, vol. 23, no. 1, pp. 7–12, 2005.

[161] K. Tajima, J. Zhou, K. Nakajima, and K. Sato, "Ultralow loss and long length photonic crystal fiber," *Journal of Lightwave Technology*, vol. 22, no. 1, pp. 7–10, 2004.

[162] M. D. Nielsen, C. Jacobsen, N. A. Mortensen, J. R. Folkenberg, and H. R. Simonsen, "Low-loss photonic crystal fibers for transmission systems and their dispersion properties," *Optics Express*, vol. 12, no. 7, pp. 1372–1376, 2004.

[163] M. D. Nielsen and N. A. Mortensen, "Photonic crystal fiber design based on the V-parameter," *Optics Express*, vol. 11, no. 21, pp. 2762–2768, 2003.

[164] K. Mukasa, F. Poletti, K. Imamura, N. Kumano, T. Yagi, and D. J. Richardson, "A high performance GeO2/SiO2 NZ-DSF and the prospects for future improvement using holey fiber technology," in *Proc. European Conference on Optical Communications (ECOC)*, vol. 2, 2005, pp. 161–162.

[165] D. M. Taylor, C. R. Bennett, T. J. Shepherd, L. F. Michaille, M. D. Nielsen, and H. R. Simonsen, "Demonstration of multi-core photonic crystal fibre in an optical interconnect," *Electronics Letters*, vol. 42, no. 6, pp. 331–332, 2006.

[166] T. Matsui, J. Zhou, K. Nakajima, and I. Sankawa, "Dispersion-flattened photonic crystal fiber with large effective area and low confinement loss," *Journal of Lightwave Technology*, vol. 23, no. 12, pp. 4178–4183, 2005.

[167] N. Florous, K. Saitoh, and M. Koshiba, "The role of artificial defects for engineering large effective mode area, flat chromatic dispersion, and low leakage losses in photonic crystal fibers: Towards high speed reconfigurable transmission platforms," *Optics Express*, vol. 14, no. 2, pp. 901–913, 2006.

[168] A. B. Rulkov, M. Y. Vyatkin, S. V. Popov, J. R. Taylor, and V. P. Gapontsev, "High brightness picosecond all-fiber generation in 525-1800nm range with picosecond Yb pumping," *Optics Express*, vol. 13, no. 2, pp. 377–381, 2005.

[169] J. M. Harbold, F. O. Ilday, F. W. Wise, T. A. Birks, W. J. Wadsworth, and Z. Chen, "Long-wavelength continuum generation about the second dispersion zero of a tapered fiber," *Optics Letters*, vol. 27, no. 17, pp. 1558–1560, 2002.

[170] T. V. Andersen, K. M. Hilligsoe, C. K. Nielsen, J. Thgersen, K. P. Hansen, S. R. Keiding, and J. J. Larsen, "Continuous-wave wavelength conversion in a photonic crystal fiber with two zero-dispersion wavelengths," *Optics Express*, vol. 12, no. 17, pp. 4113–4122, 2004.

[171] M. H. Frosz, P. Falk, and O. Bang, "The role of the second zero-dispersion wavelength in generation of supercontinua and bright-bright soliton-pairs across the zero-dispersion wavelength," *Optics Express*, vol. 13, no. 16, pp. 6181–6192, 2005.

[172] M. L. V. Tse, P. Horak, F. Poletti, N. G. R. Broderick, J. H. V. Price, J. R. Hayes, and D. J. Richardson, "Supercontinuum generation at 1.06 μm in holey fibers with dispersion flattened profiles," *Optics Express*, vol. 14, no. 10, pp. 4445–4451, 2006.

[173] K. P. Hansen, J. R. Falkenberg, C. Peucheret, and A. Bjarklev, "Fully dispersion-controlled triangular core photonic crystal fiber," in *Proc. Optical Fiber Communication Conference (OFC)*, 2003, paper PD2-1.

[174] A. Hirose, Y. Takushima, and T. Okoshi, "Suppression of stimulated Brillouin scattering and Brillouin crosstalk by frequency-sweeping spread-spectrum scheme," *Journal of Optical Communications*, vol. 12, no. 3, pp. 82–85, 1991.

[175] X. P. Mao, R. W. Tkach, A. R. Chraplyvy, R. M. Jopson, and R. M. Derosier, "Stimulated Brillouin threshold dependence on fiber type and uniformity," *IEEE Photonics Technology Letters*, vol. 4, no. 1, pp. 66–69, 1992.

[176] K. Shiraki, M. Ohashi, and M. Tateda, "SBS threshold of a fiber with a Brillouin frequency shift distribution," *Journal of Lightwave Technology*, vol. 14, no. 1, pp. 50–57, 1996.

[177] J. H. Lee, Z. Yusoff, W. Belardi, M. Ibsen, T. M. Monro, and D. J. Richardson, "Investigation of Brillouin effects in small-core holey optical fiber: lasing and scattering," *Optics Letters*, vol. 27, no. 11, pp. 927–929, 2002.

[178] K. Furusawa, Y. Yusoff, F. Poletti, T. M. Monro, N. G. R. Broderick, and D. J. Richardson, "On the Brillouin characterization of holey optical fibers," *Optics Letters*, vol. 31, no. 17, pp. 2541–2543, 2006.

[179] M. Nikles, L. Thevenaz, and P. A. Robert, "Brillouin gain spectrum characterization in single-mode optical fibers," *Journal of Lightwave Technology*, vol. 15, no. 10, pp. 1842–1851, 1997.

[180] P. Dainese, P. S. J. Russell, N. Joly, J. C. Knight, G. S. Wiederhecker, H. L. Fragnito, V. Laude, and A. Khelif, "Stimulated Brillouin scattering from multi-GHz-guided acoustic phonons in nanostructured photonic crystal fibres," *Nature Physics*, vol. 2, no. 6, pp. 388–392, 2006.

[181] J. H. Lee, T. Tanemura, K. Kikuchi, T. Nagashima, T. Hasegawa, S. Ohara, and N. Sugimoto, "Experimental comparison of a Kerr nonlinearity figure of merit including the stimulated Brillouin scattering threshold for state-of-the-art nonlinear optical fibers," *Optics Letters*, vol. 30, no. 13, pp. 1698–1700, 2005.

[182] J. Y. Y. Leong, S. Asimakis, F. Poletti, P. Petropoulos, X. Feng, R. C. Moore, K. E. Frampton, T. M. Monro, H. Ebendorff-Heidepriem, W. H. Loh, and D. J. Richardson, "Towards zero dispersion highly nonlinear lead silicate glass holey fibres at 1550 nm by structured-element-stacking," in *Proc. European Conference on Optical Communications (ECOC)*, vol. 6, 2005, pp. 45–46.

[183] T. Nagashima, T. Hasegawa, S. Ohara, and N. Sugimoto, "Dispersion shifted Bi2O3-based photonic crystal fiber," in *Proc. European Conference on Optical Communications (ECOC)*, 2006, paper We1.3.2.

[184] C. Jauregui, H. Ono, P. Petropoulos, and D. J. Richardson, "Four-fold reduction in the speed of light at practical power levels using Brillouin scattering in a 2-m Bismuth-oxide fiber," in *Proc. Optical Fiber Communication Conference (OFC)*, 2006, paper PDP2.

[185] M. L. V. Tse, P. Horak, F. Poletti, and D. J. Richardson, "Designing dispersion and mode area decreasing holey fibers for soliton compression," in *Proc. Conference on Lasers and Electro-Optics (CLEO)*, 2007, paper (submitted).

[186] X. Feng, T. M. Monro, P. Petropoulos, V. Finazzi, and D. J. Richardson, "Extruded single-mode high-index-core one-dimensional microstructured optical fiber with high index-contrast for highly nonlinear optical devices," *Applied Physics Letters*, vol. 87, no. 8, p. 81110, 2005.

[187] S. Fevrier, R. Jamier, J. M. Blondy, S. L. Semjonov, M. E. Likhachev, M. M. Bubnov, E. M. Dianov, V. F. Khopin, M. Y. Salganskii, and A. N. Guryanov, "Low-loss singlemode large mode area all-silica photonic bandgap fiber," *Optics Express*, vol. 14, no. 2, pp. 562–569, 2006.

[188] J. A. Nelder and R. Mead, "A simplex method for function minimization," *Computer Journal*, vol. 7, pp. 308–313, 1965.

[189] T. Okuno, M. Hirano, T. Kato, M. Shigematsu, and M. Onishi, "Highly nonlinear and perfectly dispersion-flattened fibres for efficient optical signal processing applications," *Electronics Letters*, vol. 39, no. 13, pp. 972–974, 2003.

[190] W. H. Reeves, , J. C. Knight, P. S. J. Russell, P. J. Roberts, and B. J. Mangan, "Dispersion-flattened photonic crystal fibers at 1550 nm," in *Proc. Optical Fiber Communication Conference (OFC)*, 2003.

[191] K. Saitoh, M. Koshiba, T. Hasegawa, and E. Sasaoka, "Chromatic dispersion control in photonic crystal fibers: application to ultra-flattened dispersion," *Optics Express*, vol. 11, no. 8, pp. 843–852, 2003.

[192] F. Poli, A. Cucinotta, S. Selleri, and A. H. Bouk, "Tailoring of flattened dispersion in highly nonlinear photonic crystal fibers," *IEEE Photonics Technology Letters*, vol. 16, no. 4, pp. 1065–1067, 2004.

[193] G. Renversez, B. Kuhlmey, and R. McPhedran, "Dispersion management with microstructured optical fibers: ultraflattened chromatic dispersion with low losses," *Optics Letters*, vol. 28, no. 12, pp. 989–991, 2003.

[194] J. Skaar and K. M. Risvik, "A genetic algorithm for the inverse problem in synthesis of fiber gratings," *Journal of Lightwave Technology*, vol. 16, no. 10, pp. 1928–1932, 1998.

[195] E. Kerrinckx, L. Bigot, M. Douay, and Y. Quiquempois, "Photonic crystal fiber design by means of a genetic algorithm," *Optics Express*, vol. 12, no. 9, pp. 1990–1995, 2004.

[196] J. H. Holland, *Adaptation in natural and artificial systems: an introductory analysis.* University of Michigan Press, 1975.

[197] D. E. Goldberg, *Genetic algorithms in search, optimization and machine learning.* Addison-Wesley, New York, 1989.

[198] T. Fujisawa, K. Saitoh, K. Wada, and M. Koshiba, "Chromatic dispersion profile optimization of dual-concentric-core photonic crystal fibers for broadband dispersion compensation," *Optics Express*, vol. 14, no. 2, pp. 893–900, 2006.

[199] S. K. Varshney, T. Fujisawa, K. Saitoh, and M. Koshiba, "Novel design of inherently gain-flattened discrete highly nonlinear photonic crystal fiber raman amplifier and dispersion compensation using a single pump in c-band," *Optics Express*, vol. 13, no. 23, pp. 9516–9526, 2005.

[200] J. A. Sethian, *Level Set Methods and Fast Marching Methods: Evolving Interfaces in Computational Geometry, Fluid Mechanics, Computer Vision, and Materials Science*, 2nd ed. Cambridge University Press, 1999.

[201] C. Y. Kao, S. Osher, and E. Yablonovitch, "Maximizing band gaps in two-dimensional photonic crystals by using level set methods," *Applied Physics B*, vol. 81, no. 2-3, pp. 235–244, 2005.

[202] K. Mukasa, M. N. Petrovich, F. Poletti, A. Webb, J. R. Hayes, A. Van Brakel, R. Amezcua Correa, L. Provost, J. Sahu, P. Petropoulos, and D. J. Richardson, "Novel fabrication method of highly-nonlinear silica holey fibres," in *Proc. Conference on Lasers and Electro-Optics (CLEO)*, 2006, paper CMC5.

[203] T. M. Monro, D. J. Richardson, and P. J. Bennett, "Developing holey fibres for evanescent field devices," *Electronics Letters*, vol. 35, no. 14, pp. 1188–1189, 1999.

[204] B. Culshaw, F. Muhammad, G. Stewart, S. Murray, D. Pinchbeck, J. Norris, S. Cassidy, M. Wilkinson, D. Williams, I. Crisp, R. Vanewyk, and A. Mcghee, "Evanescent wave methane detection using optical fibres," *Electronics Letters*, vol. 28, no. 24, pp. 2232–2234, 1992.

[205] T. M. Monro, W. Belardi, K. Furusawa, J. C. Baggett, N. G. R. Broderick, and D. J. Richardson, "Sensing with microstructured optical fibres," *Measurement, Science & Technology*, vol. 12, no. 7, pp. 854–858, 2001.

[206] Y. L. Hoo, W. Jin, H. L. Ho, D. N. Wang, and R. S. Windeler, "Evanescent-wave gas sensing using microstructure fiber," *Optical Engineering*, vol. 41, no. 1, pp. 8–9, 2002.

[207] Y. L. Hoo, W. Jin, C. Z. Shi, H. L. Ho, D. N. Wang, and S. C. Ruan, "Design and modeling of a photonic crystal fiber gas sensor," *Applied Optics*, vol. 42, no. 18, pp. 3509–3515, 2003.

[208] W. Belardi, J. H. Lee, K. Furusawa, Z. Yusoff, P. Petropoulos, M. Ibsen, T. M. Monro, and D. J. Richardson, "A 10 Gbit/s tuneable wavelength converter based on four-wave mixing in highly nonlinear holey fibre," in *Proc. European Conference on Optical Communications (ECOC)*, 2002, paper PD1.

[209] S. Coen, A. H. L. Chau, R. Leonhardt, J. D. Harvey, J. C. Knight, W. J. Wadsworth, and P. S. J. Russell, "Supercontinuum generation by stimulated raman scattering and parametric four-wave mixing in photonic crystal fibers," *Journal of the Optical Society of America B*, vol. 19, no. 4, pp. 7537–64, 2002.

[210] G. Derra, H. Moench, E. Fischer, H. Giese, U. Hechtfischer, G. Hensler, A. Koerber, U. Niemann, F. C. Noertemann, P. Pekarski, J. Pollmann-Retsch, A. Ritz, and U. Weichmann, "UHP lamp systems for projection applications," *Journal of Physics D-Applied Physics*, vol. 38, no. 17, pp. 2995–3010, 2005.

[211] P. A. Champert, V. Couderc, P. Leproux, S. Fevrier, V. Tombelaine, L. Labonte, P. Roy, C. Froehly, and P. Nerin, "White-light supercontinuum generation in normally dispersive optical fiber using original multi-wavelength pumping system," *Optics Express*, vol. 12, no. 19, pp. 4366–4371, 2004.

[212] S. G. Leon-Saval, T. A. Birks, W. J. Wadsworth, P. S. J. Russell, and M. W. Mason, "Supercontinuum generation in submicron fibre waveguides," *Optics Express*, vol. 12, no. 13, pp. 2864–2869, 2004.

[213] M. Rusu, S. Kivisto, C. B. E. Gawith, and O. Okhotnikov, "Red-green-blue (RGB) light generator using tapered fiber pumped with a frequency-doubled Yb-fiber laser," *Optics Express*, vol. 13, no. 21, pp. 8547–8554, 2005.

[214] J. C. Travers, S. V. Popov, and J. R. Taylor, "Extended blue supercontinuum generation in cascaded holey fibers," *Optics Letters*, vol. 30, no. 23, pp. 3132–3134, 2005.

[215] J. M. Dudley, L. Provino, N. Grossard, H. Maillotte, R. S. Windeler, B. J. Eggleton, and S. Coen, "Supercontinuum generation in air-silica microstructured fibers with nanosecond and femtosecond pulse pumping," *Journal of The Optical Society of America B*, vol. 19, no. 4, pp. 765–771, 2002.

[216] F. Brunner, E. Innerhofer, S. V. Marchese, T. Sudmeyer, R. Paschotta, T. Usami, H. Ito, S. Kurimura, K. Kitamura, G. Arisholm, and U. Keller, "Powerful red-green-blue laser source pumped with a mode-locked thin disk laser," *Optics Letters*, vol. 29, no. 16, pp. 1921–1923, 2004.

[217] S. Coen, A. H. L. Chan, R. Leonhardt, J. D. Harvey, J. C. Knight, W. J. Wadsworth, and P. S. J. Russell, "White-light supercontinuum generation with 60-ps pump pulses in a photonic crystal fiber," *Optics Letters*, vol. 26, no. 17, pp. 1356–1358, 2001.

[218] A. Tonello, S. Pitois, S. Wabnitz, G. Millot, T. Martynkien, W. Urbanczyk, J. Wojcik, A. Locatelli, M. Conforti, and C. De Angelis, "Frequency tunable polarization and intermodal modulation instability in high birefringence holey fiber," *Optics Express*, vol. 14, no. 1, pp. 397–404, 2006.

[219] R. J. Kruhlak, G. K. L. Wong, J. S. Y. Chen, S. G. Murdoch, R. Leonhardt, J. D. Harvey, N. Y. Joly, and J. C. Knight, "Polarization modulation instability in photonic crystal fibers," *Optics Letters*, vol. 31, no. 10, pp. 1379–1381, 2006.

[220] J. Riishede, N. A. Mortensen, and J. Laegsgaard, "A 'poor man's approach' to modelling micro-structured optical fibres," *Journal of Optics A: Pure and Applied Optics*, vol. 5, no. 5, pp. 534–538, 2003.

[221] J. Laegsgaard, N. A. Mortensen, J. Riishede, and A. Bjarklev, "Material effects in air-guiding photonic bandgap fibers," *Journal of the Optical Society of America B*, vol. 20, no. 10, pp. 2046–2051, 2003.

[222] K. Saitoh, N. Mortensen, and M. Koshiba, "Air-core photonic band-gap fibers: the impact of surface modes," *Optics Express*, vol. 12, no. 3, pp. 394–400, 2004.

[223] M. J. F. Digonnet, H. K. Kim, G. S. Kino, and S. H. Fan, "Understanding air-core photonic-bandgap fibers: Analogy to conventional fibers," *Journal of Lightwave Technology*, vol. 23, no. 12, pp. 4169–4177, 2005.

[224] J. Jasapara, T. H. Her, R. Bise, R. Windeler, and D. J. DiGiovanni, "Group-velocity dispersion measurements in a photonic bandgap fiber," *Journal of the Optical Society of America B*, vol. 20, no. 8, pp. 1611–1615, 2003.

[225] T. Baba and T. Matsuzaki, "Theoretical calculation of photonic gap in semiconductor 2-dimensional photonic crystals with various shapes of optical atoms," *Japanese Journal of Applied Physics*, vol. 34, no. 8B, pp. 4496–4498, 1995.

[226] R. Padjen, J. M. Gerard, and J. Y. Marzin, "Analysis of the filling pattern dependence of the photonic bandgap for 2-dimensional systems," *Journal of Modern Optics*, vol. 41, no. 2, pp. 295–310, 1994.

[227] J. Riishede, J. Laegsgaard, J. Broeng, and A. Bjarklev, "All-silica photonic bandgap fibre with zero dispersion and a large mode area at 730 nm," *Journal of Optics A: Pure and Applied Optics*, vol. 6, no. 7, pp. 667–670, 2004.

[228] S. G. Johnson, M. Ibanescu, M. Skorobogatiy, O. Weisberg, T. D. Engeness, M. Soljacic, S. A. Jacobs, J. D. Joannopoulos, and Y. Fink, "Low-loss asymptotically single-mode propagation in large-core omniguide fibers," *Optics Express*, vol. 9, no. 13, pp. 748–779, 2001.

[229] O. Humbach, H. Fabian, U. Grzesik, U. Haken, and W. Heitmann, "Analysis of OH absorption bands in synthetic silica," *Journal on Non-crystalline Solids*, vol. 203, pp. 19–26, 1996.

[230] J. D. Shephard, W. N. MacPherson, R. R. J. Maier, J. D. C. Jones, D. P. Hand, M. Mohebbi, A. K. George, P. J. Roberts, and J. C. Knight, "Single-mode mid-IR guidance in a hollow-core photonic crystal fiber," *Optics Express*, vol. 13, no. 18, pp. 7139–7144, 2005.

[231] C. M. Smith, N. Venkataraman, M. T. Gallagher, D. Muller, J. A. West, N. F. Borreill, D. C. Allan, and K. W. Koch, "Low-loss hollow-core silica/air photonic bandgap fibre," *Nature*, vol. 424, no. 6949, pp. 657–659, 2003.

[232] F. Ramos-Mendieta and P. Halevi, "Surface electromagnetic waves in two-dimensional photonic crystals: Effect of the position of the surface plane," *Physical Review B*, vol. 59, no. 23, pp. 15 112–15 120, 1999.

[233] K. Saitoh and M. Koshiba, "Photonic bandgap fibers with high birefringence," *IEEE Photonics Technology Letters*, vol. 14, no. 9, pp. 1291–1293, 2002.

[234] X. Chen, M.-J. Li, N. Venkataraman, M. T. Gallagher, W. A. Wood, A. M. Crowley, J. P. Carberry, L. A. Zenteno, and K. W. Koch, "Highly birefringent hollow-core photonic bandgap fiber," *Optics Express*, vol. 12, no. 16, pp. 3888–3893, 2004.

[235] M. S. Alam, K. Saitoh, and M. Koshiba, "High group birefringence in air-core photonic bandgap fibers," *Optics Letters*, vol. 30, no. 8, pp. 824–826, 2005.

[236] G. Bouwmans, F. Luan, J. Knight, P. S. J. Russell, L. Farr, B. J. Mangan, and H. Sabert, "Properties of a hollow-core photonic bandgap fiber at 850 nm wavelength," *Optics Express*, vol. 11, no. 14, pp. 1613–1620, 2003.

[237] T. D. Engeness, M. Ibanescu, S. G. Johnson, O. Weisberg, M. Skorobogatiy, S. Jacobs, and Y. Fink, "Dispersion tailoring and compensation by modal interactions in omniguide fibers," *Optics Express*, vol. 11, no. 10, pp. 1175–1196, 2003.

[238] G. Humbert, J. C. Knight, G. Bouwmans, P. S. Russell, D. P. Williams, P. J. Roberts, and B. J. Mangan, "Hollow core photonic crystal fibers for beam delivery," *Optics Express*, vol. 12, no. 8, pp. 1477–1484, 2004.

[239] M. Wegmuller, M. Legre, N. Gisin, T. P. Hansen, C. Jacobsen, and J. Broeng, "Experimental investigation of the polarization properties of a hollw core photonic bandgap fiber for 1550 nm," *Optics Express*, vol. 13, no. 5, pp. 1457–1467, 2005.

[240] G. J. Pearce, J. M. Pottage, D. M. Bird, P. J. Roberts, J. C. Knight, and P. S. J. Russell, "Hollow-core pcf for guidance in the mid to far infra-red," *Optics Express*, vol. 13, no. 18, pp. 6937–6946, 2005.

[241] R. Amezcua Correa, N. G. Broderick, M. N. Petrovich, F. Poletti, and D. J. Richardson, "Comparison of mode properties of 7 and 19 cells core hollow-core photonic crystal fibers," in *Proc. Optical Fiber Communication Conference (OFC)*, 2007, paper OML5.

[242] J. Y. Y. Leong, S. Asimakis, F. Poletti, P. Petropoulos, X. Feng, R. C. Moore, K. E. Frampton, T. M. Monro, H. Ebendorff-Heidepriem, W. H. Loh, and D. J. Richardson, "Nonlinearity and dispersion control in small core lead silicate holey fibers by structured element stacking," in *Proc. Optical Fiber Communication Conference (OFC)*, 2006, paper OTuH1.

[243] S. Asimakis, P. Petropoulos, F. Poletti, J. J. Y. Leong, R. Moore, K. Frampton, X. Feng, W. H. Loh, and D. J. Richardson, "Towards efficient and broadband four-wave mixing using short-length dispersion tailored lead silicate holey fibers," *Optics Express*, vol. 17, no. 2, pp. 596–601, 2007.

[244] M. L. Tse, P. Horak, J. H. V. Price, F. Poletti, F. He, and D. J. Richardson, "Pulse compression at 1.06 μm in dispersion-decreasing holey fibers," *Optics Letters*, vol. 31, no. 23, pp. 3504–3506, 2006.

[245] P. J. Roberts, D. P. Williams, H. Sabert, B. J. Mangan, D. M. Bird, T. A. Birks, J. C. Knight, and P. S. Russell, "Design of low-loss and highly birefringent hollow-core photonic crystal fiber," *Optics Express*, vol. 14, no. 16, pp. 7329–7341, 2006.

[246] N. Shibata, K. Okamoto, and Y. Azuma, "Longitudinal acoustic modes and Brillouin-gain spectra for GeO_2-doped-core single-mode fibers," *Journal of The Optical Society of America B*, vol. 6, no. 6, pp. 1167–1174, 1989.

List of Publications

Journal papers

F. Poletti, V. Finazzi, T. M. Monro, N. G. R. Broderick, V. Tse, and D. J. Richardson, "Inverse design and fabrication tolerances of ultra-flattened dispersion holey fibers," *Optics Express*, vol. 13, no. 10, pp. 3728–3736, 2005.

F. Poletti, N. G. R. Broderick, D. J. Richardson, and T. M. Monro, "The effect of core asymmetries on the polarization properties of hollow core photonic band gap fibers," *Optics Express*, vol. 13, no. 22, pp. 9115–9124, 2005.

M. L. V. Tse, P. Horak, F. Poletti, N. G. R. Broderick, J. H. V. Price, J. R. Hayes, and D. J. Richardson, "Supercontinuum generation at 1.06 μm in holey fibers with dispersion flattened profiles," *Optics Express*, vol. 14, no. 10, pp. 4445–4451, 2006.

K. Furusawa, Z. Yusoff, F. Poletti, T. M. Monro, N. G. R. Broderick, and D. J. Richardson, "Brillouin characterization of holey optical fibers," *Optics Letters*, vol. 31, no. 17, pp. 2541–2543, 2006.

M. L. Tse, P. Horak, J. H. V. Price, F. Poletti, F. He, and D. J. Richardson, "Pulse compression at 1.06 μm in dispersion-decreasing holey fibers," *Optics Letters*, vol. 31, no. 23, pp. 3504–3506, 2006.

R. Amezcua-Correa, N. G. R. Broderick, M. N. Petrovich, F. Poletti, and D. J. Richardson, "Optimizing the usable bandwidth and loss through core design in realistic hollow-core photonic bandgap fibers," *Optics Express*, vol. 14, no. 17, pp. 7974–7985, 2006.

A. Webb, F. Poletti, D. J. Richardson, and J. Sahu, "Suspended-core holey fibre for evanescent-field sensing," *Optical Engineering Letters*, vol. 46, no. 010503, 2007.

S. Asimakis, P. Petropoulos, F. Poletti, J. J. Y. Leong, R. Moore, K. Frampton, X. Feng, W. H. Loh, and D. J. Richardson, "Towards efficient and broadband Four-Wave Mixing using short-length dispersion tailored lead silicate holey fibers," *Optics Express*, vol. 15, no. 2, pp. 596–601, 2007.

P. Dupriez, F. Poletti, P. Horak, M. N. Petrovich, Y. Jeong, J. Nilsson, D. J. Richardson, and D. N. Payne, "Efficient white light generation in secondary cores of holey fibers," *Optics Express*, vol. 15, no. 7, pp. 3729–3736, 2007.

Conference Papers

F. Poletti, V. Finazzi, T. M. Monro, N. G. R. Broderick, and D. J. Richardson, "Ultra-flattened dispersion holey fibers: genetic algorithm design and fabrication tolerances," in *Proc. Conference on Lasers and Electro-Optics (CLEO)*, 2005, vol. 1, pp. 387–389.

K. Mukasa, F. Poletti, J. C. Baggett, V. Finazzi, K. Imamura, I. Shimotakahara, T. Yagi, and D. J. Richardson, "Development of Transmission Fibre for Long-Haul High-Capacity Transmission," in *Proc. 10th Optoelectronics and Communications Conference (OECC)*, 2005, paper 5D2-1 (invited).

K. Mukasa, F. Poletti, K. lmamura, N. Kumano, T. Yagi, and D. J. Richardson, "A high performance GeO_2/SiO_2 NZ-DSF and the prospects for future improvement using holey fiber technology," in *Proc. European Conference on Optical Communication (ECOC)*, 2005, vol. 2, pp. 161-162.

P. Petropoulos, F. Poletti, J. J. Y. Leong, T. M. Monro, H. Ebendorff-Heidepriem, H. V. Finazzi, M. L. Tse, X. Feng, S. Asimakis, N. G. Broderick, and D. J. Richardson, "High nonlinearity holey fibers: design, fabrication and applications," in *Proc. CLEO/Pacific Rim*, 2005, pp. 1566-1568, (invited).

J. C. Baggett, M. N. Petrovich, J. R. Hayes, V. Finazzi, F. Poletti, R. Amezcua, N. G. R. Broderick, D. J. Richardson, T. M. Monro, P. L. Salter, G. Proudley, and E. J. O'Driscoll, "Microstructured fibers for high power applications," in *Nanophotonics for Communication: Materials and Devices II*, 2005, Proc SPIE 6017, 601709 (invited).

M. N. Petrovich, A. Van Brakel, F. Poletti, K. Mukasa, E. Austin, V. Finazzi, P. Petropoulos, E. O'Driscoll, M. Watson, T. DelMonte, T. M. Monro, J. P. Dakin, and D. J. Richardson, "Microstructured fibres for sensing applications," in *Photonic Crystals and Photonic Crystal Fibers for Sensing Applications*, 2005, Proc. SPIE 6005, 60050E (invited).

J. Y. Y. Leong, S. Asimakis, F. Poletti, P. Petropoulos, X. Feng, R. C. Moore, K. E. Frampton, T. M. Monro, H. Ebendorff-Heidepriem, W. H. Loh, and D. J. Richardson, "Towards zero dispersion highly nonlinear lead silicate glass holey fibres at 1550 nm by structured-element-stacking," in *Proc. European Conference on Optical Communication (ECOC)*, 2005, pp. 45-46, (postdeadline).

D. J. Richardson, F. Poletti, J. J. Y. Leong, X. Feng, H. E. Heidepreim, H. V. Finazzi, K. E. Frampton, S. Asimakis, R. C. Moore, J. C. Baggett, J. R. Hayes, M. N. Petrovich, M. L. Tse, R. Amezcua, J. V. H. Price, N. G. R. Broderick, P. Petropoulos, and T. M. Monro, "Advances in microstructured fiber technology," in *Proc. 4th IEEE/LEOS Workshop on Fibres and Optical Passive Components*, 2005, pp. 1-9, (invited).

F. Poletti, K. Furusawa, Z. Yussoff, P. Petropoulos, N. G. R. Broderick, T. M. Monro, and D. J. Richardson, "Brillouin suppression through longitudinal structural variation in high nonlinearity silica holey fibers," in *Proc. Optical Fiber Communication Conference (OFC)*, 2006, paper OWI10.

F. Poletti, M. N. Petrovich, R. Amezcua-Correa, N. G. Broderick, T. M. Monro, and D. J. Richardson, "Advances and limitations in the modeling of fabricated photonic bandgap fibers," in *Proc. Optical Fiber Communication Conference (OFC)*, 2006, paper OFC2.

M. L. V. Tse, P. Horak, F. Poletti, N. G. R. Broderick, J. H. V. Price, J. R. Hayes, and D. J. Richardson, "A systematic study of supercontinuum generation at 1.06 μm in holey fibers with dispersion flattened profiles," in *Proc. Optical Fiber Communication Conference (OFC)*, 2006, paper OThQ5.

J. Y. Y. Leong, S. Asimakis, F. Poletti, P. Petropoulos, X. Feng, R. C. Moore, K. E. Frampton, T. M. Monro, H. Ebendorff-Heidepriem, W. H. Loh, and D. J. Richardson, "Nonlinearity and dispersion control in small core lead silicate holey fibers by structured element stacking," in *Proc. Optical Fiber Communication Conference (OFC)*, 2006, paper OTuH1.

R. Amezcua-Correa, N. G. R. Broderick, M. N. Petrovich, F. Poletti, D. J. Richardson, V. Finazzi, and T. M. Monro, "Realistic designs of silica hollow-core bandgap fibers free of surface," in *Proc. Optical Fiber Communication Conference (OFC)*, 2006, paper OFC3.

K. Mukasa, M. N. Petrovich, F. Poletti, A. Webb, J. R. Hayes, A. Van Brakef, R. Amezcua Correa, L. Provost, J. Sahu, P. Petropoulos, and D. J. Richardson, "Novel fabrication method of highly-nonlinear silica holey fibres," in *Proc. Conference on Lasers and Electro-Optics (CLEO)*, 2006, paper CMC5.

J. H. V. Price, T. M. Monro, H. Ebendorff-Heidepriem, F. Poletti, V. Finazzi, J. Y. Y. Leong, P. Petropoulos, J. C. Flanagan, G. Brambilla, X. Feng, and D. J. Richardson, "Non-silica microstructured optical fibers for mid-IR supercontinuum generation from 2 μm – 5 μm," in *Fiber Lasers III: Technology, Systems, and Applications*, 2006, Proc. SPIE 6102, 61020A (invited).

F. Poletti, P. Petropoulos, N. G. Broderick, and D. J. Richardson, "Design of Highly Nonlinear Bismuth-Oxide Holey Fibres with Zero Dispersion and Enhanced Brillouin Suppression," in *Proc. European Conference on Optical Communication (ECOC)*, 2006, paper Tu4.3.2.

S. Asimakis, P. Petropoulos, F. Poletti, J. Y. Y. Leong, H. Ebendorff-Heidepriem, R. C. Moore, K. E. Frampton, X. Feng, W. H. Loh, T. M. Monro, and D. J. Richardson, "Efficient four-wave-mixing at 1.55 microns in a short-length dispersion shifted lead silicate holey fibre," in *Proc. European Conference on Optical Communication (ECOC)*, 2006, paper Th1.3.3.

N. G. Broderick, R. Amezcua Correa, F. Poletti, J. C. Flanagan, D. J. Richardson, and M. N. Petrovich, "Modelling applications of photonic bandgap fibres," in *Photonics 2006*, 2006 (invited).

J. C. Flanagan, R. Amezcua Correa, F. Poletti, J. R. Hayes, N. G. Broderick, and D. J. Richardson, "Parasitic modes in large mode area microstructured fibers," in *Proc. Optical Fiber Communication Conference (OFC)*, 2007, Paper OML4.

R. Amezcua Correa, N. G. Broderick, M. N. Petrovich, F. Poletti, and D. J. Richardson, "Comparison of Mode Properties of 7 and 19 Cells Core Hollow-Core Photonic Crystal Fibers," in *Proc. Optical Fiber Communication Conference (OFC)*, 2007, paper OML5.

K. Mukasa, F. Poletti, M. N. Petrovich, N. G. Broderick, R. Amezcua Correa, M. A. F. Roelens, and D. J. Richardson, "Using photonic bandgap fiber for extending the reach in non-repeatered transmission systems," in *Proc. Optical Fiber Communication Conference (OFC)*, 2007, Paper OML1.

M. L. Tse, P. Horak, F. Poletti, and D. J. Richardson, "Designing dispersion and mode area-decreasing holey fibers for soliton compression," *submitted to CLEO*, 2007.

P. Horak, P. Dupriez, F. Poletti, M. N. Petrovich, Y. Jeong, J. Nilsson, D. J. Richardson, and D. N. Payne, "RGB generation in secondary cores of microstructured fibers," *submitted to CLEO Europe*, 2007.

P. Horak, M. L. Tse, F. Poletti, and D. J. Richardson, "Soliton compression in short lengths of microstructured fibres," *submitted to CLEO Europe*, 2007.